

Characterization of porosity & C-S-H in cement pastes by ^1H NMR

THÈSE N° 6339 (2014)

PRÉSENTÉE LE 3 OCTOBRE 2014

À LA FACULTÉ DES SCIENCES ET TECHNIQUES DE L'INGÉNIEUR
LABORATOIRE DES MATÉRIAUX DE CONSTRUCTION
PROGRAMME DOCTORAL EN SCIENCE ET GÉNIE DES MATÉRIAUX

ÉCOLE POLYTECHNIQUE FÉDÉRALE DE LAUSANNE

POUR L'OBTENTION DU GRADE DE DOCTEUR ÈS SCIENCES

PAR

Arnaud Charles Albert MULLER

acceptée sur proposition du jury:

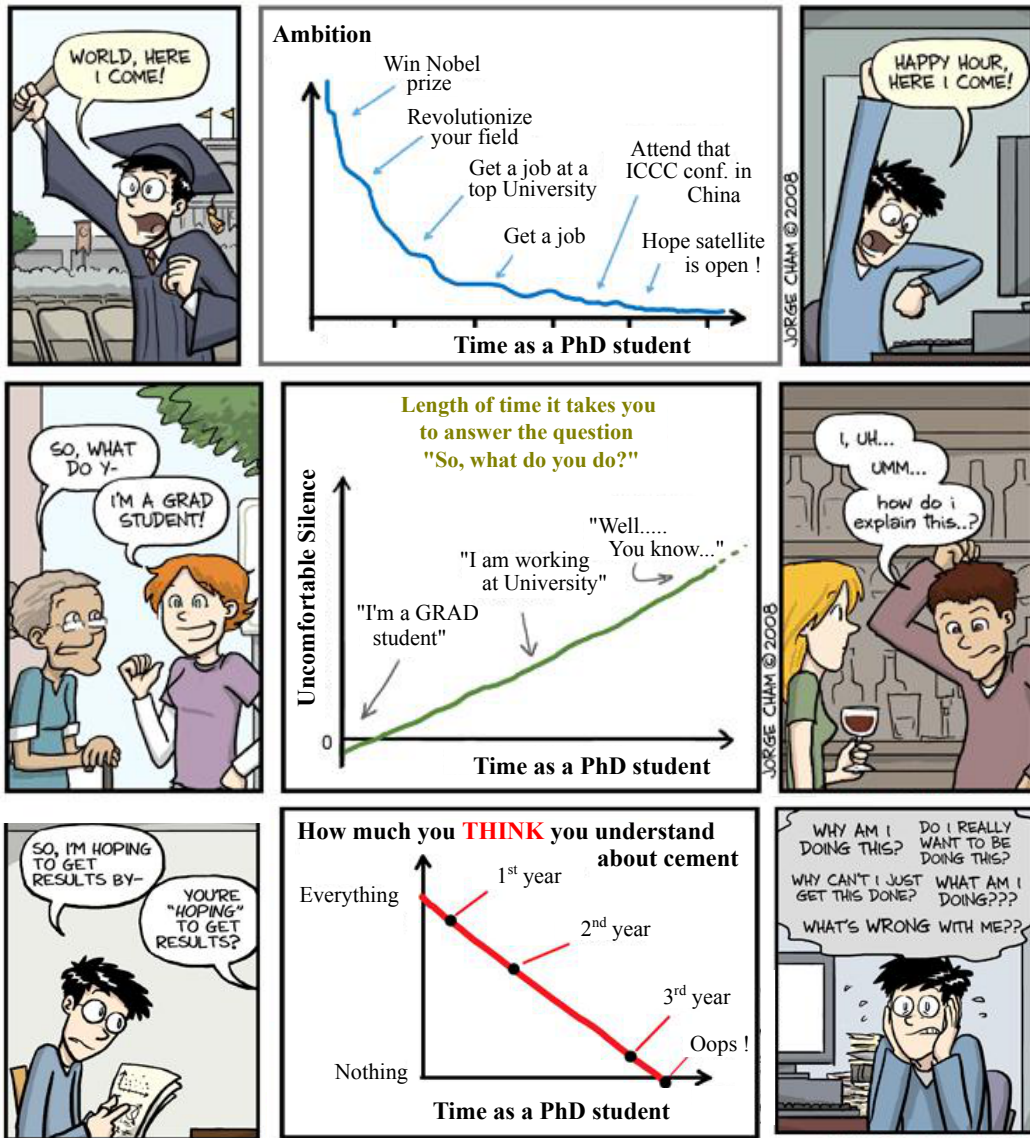
Prof. F. Nüesch, président du jury
Prof. K. Scrivener, Prof. P. J. McDonald, directeurs de thèse
Dr P. Bowen, rapporteur
Prof. H. Jennings, rapporteur
Dr J. S. Mitchell, rapporteur



ÉCOLE POLYTECHNIQUE
FÉDÉRALE DE LAUSANNE

Suisse
2014

Life is different before...
...and after the PhD.



WWW.PHDCOMICS.COM

— A.C.A. Muller...

Acknowledgements

Je voudrais tout d'abord remercier sincèrement le Professeur Karen Scrivener, ma directrice de thèse, pour m'avoir donné l'opportunité de réaliser ma thèse dans son laboratoire ainsi que pour sa confiance et son soutien au cours de ces années de doctorat. Ses conseils et sa supervision ont contribué à la qualité de cette thèse. Je tenais aussi à remercier Karen pour l'organisation des ski-séminaires, lab-hike et autre souper de Noël, autant d'activités qui contribuent à l'ambiance collective mais aussi au plaisir d'effectuer une thèse dans son laboratoire.

J'adresse le même niveau de remerciements au Professeur Peter McDonald, mon co-directeur de thèse, qui a apporté son enthousiasme et ses compétences scientifiques à ce travail. J'ai beaucoup appris au côté de Peter, notamment sur la rigueur scientifique et l'analyse de résultats.

Cette thèse, financée par l'Union Européenne*, est l'une des 15 thèses TRANSCEND du programme "Initial Training Network" du consortium Nanocem. Prendre part à un projet d'une telle envergure, regroupant des professeurs et des entreprises de nombreux pays européens, a été une très grande opportunité pour moi. A travers de nombreux cours et meetings, j'y ai développé mes qualités de chercheur. J'y ai rencontré des gens incroyables et je voudrais en premier citer tous les étudiants TRANSCEND. L'organisation de séjours au ski et les nombreux voyages qui ont suivi les meetings restent des souvenirs très forts. Quelques mots particuliers pour Agata (your hotel in Aldershot is nice), Vadim (I will remember Belarus for ever), Merlin (When do we go punting?) and Elena (keep singing). Je remercie également tous les gens avec qui j'ai eu des interactions au sein de Nanocem, scientifiques ou sociales, et tout particulièrement Marie-Alix Dalang-Secrétan pour son accompagnement dévoué tout au long de ce programme TRANSCEND. Je remercie Mette Geiker, Professeur à NTNU Trondheim, qui m'a accueilli au sein de son laboratoire pendant quelques mois pour mon "secondment". J'adresse un remerciement spécial à Agata Gajewicz avec qui j'ai travaillé en tandem durant ces 4 années de thèse. Son aide concernant les expériences de résonance nucléaire magnétique a été précieuse et la rédaction d'articles en commun une "sympathique" expérience. Plus qu'une collègue, Agata est maintenant une amie.

*This project is part of a Marie Curie ITN funded by the European Union Seventh Framework Programme (FP7 / 2007–2013) under grant agreement n°264448.

Acknowledgements

Je voudrais également remercier tous mes collègues du LMC qui ont contribué, de près ou de loin, à ce travail et à la bonne ambiance du laboratoire: Bizzo, Pawel, François, Elise, Berta, Théo, Mo, Aslam, Lili, Alain, Amélie.....Hadi, Christophe, Cyrille, Ruben et Aurélie (Post-doc géniaux).....et tous ceux que j'oublie. Le temps est passé très vite. Je n'oublie pas les secrétaires Sandra Lapalud, Anne-Sandra Hoffer et Maude Rigoli, tous responsables du bon fonctionnement du laboratoire. Je tenais à remercier aussi tous les techniciens du LMC, et particulièrement Lionel, mon coach personnel de course à pied. Merci pour les 1237 km de course parcourus ensemble au bord du lac, et particulièrement pour ton plan d'entraînement drastique qui m'a mené à ma meilleure performance en marathon. Ton humour et ta bonne humeur au quotidien y ont aidé.

Et voici un paragraphe spécial pour mes collègues (et amis) de bureau: John Rossen, Mathieu Antoni et Olga Chowanec. Il est vrai de penser que son bureau est le meilleur de tous les bureaux mais le MXG-239 a été tout de même particulier. Entre les livraisons pour John et les valises d'argiles cubaines (pour Mathieu), l'animation n'a pas manqué. La présence féminine d'Olga en début de thèse a été plus qu'appréciée et non content de passer dans un bureau à 3, tu as laissé un vide derrière toi (surtout les dessiccateurs :-). Merci à vous 3 pour ces moments de vie incroyables et Vive le "Faculty Club".

Je remercie bien entendu ma famille proche, mes parents (Antoine et Dominique) et mon frère Yannick, pour leur soutien continu durant ce doctorat. Et je me dois de mentionner les gâteaux de ma tante Marie-Thérèse, qui à chaque passage en Alsace, contribuaient à une petite fraction du travail de cette thèse.

D'un point de vu plus scientifique maintenant, je remercie John Rossen pour les mesures TEM et son expertise dans l'analyse SEM-EDX. Je remercie également Jørgen Skibsted pour les mesures de "solid-state NMR", Mathieu Antoni pour les calculs GEMS et Wu Min pour son aide dans l'analyse DVS. J'aimerais remercier également Ruben Snellings, pour son aide répéter à l'obtention d'analyses DRX fiables.

Je tiens à remercier Merlin Etzold et Abdel Perez Hernandez pour leur aide dans la rédaction des résumés en allemand et espagnol respectivement.

Je remercie aussi mes rapporteurs de thèse, Hamlin Jennings and Johnathan Mitchell et Paul Bowen pour leurs commentaires et leur persévérance dans la lecture (complète) de ce document.

Ce dernier paragraphe pour mentionner la réalisation de la vidéo "Minute Cement", avec la collaboration de John Rossen au scénario et au montage vidéo. Funny time Johnny.

Lausanne, 12 septembre 2014

— A.C.A. Muller.

Abstract

The aim of this thesis is to investigate the porosity of cementitious material and the way to measure it experimentally. Porosity is related to the strength of the material and underpins most degradation phenomena that lead to the deterioration of structures.

Many studies focus on characterising the porosity of cement-based materials and different techniques exist. For most of them, the water is first removed from the pore network prior to testing, a procedure that can alter the structures of calcium-silicate-hydrates (C–S–H). In this work, nuclear magnetic resonance (^1H NMR) relaxometry was used to characterise the different pore populations in hydrating cementitious pastes. ^1H NMR has the advantage over other techniques that it is non-destructive, non-invasive and that *in-situ* measurements can be made. As ^1H hydrogen is the probe, the NMR technique possesses potentially a size resolution of one atom-atom distance.

White cement pastes cured at 20 °C were first studied throughout the hydration and with variation of the water-to-cement ratio (w/c). Water in crystalline solid phases, C–S–H interlayer, C–S–H gel and capillary pores were distinguished and quantified based on the analysis of ^1H NMR relaxation data. A plateau of the gel pore formation was observed. Combined with X-ray diffraction measurements, calculations allowed C–S–H density and chemical composition to be found. At 28 days of hydrations, the density of the C–S–H layers including the interlayer water in between is typically $\rho_x = 2.74 \pm 0.02 \text{ g/cm}^3$ for all pastes at 20 °C. This density however dropped down to $\rho_x = 2.45 \pm 0.05 \text{ g/cm}^3$ when the paste was cured at 10 °C. On the other hand, the $\text{Ca}/(\text{Si}+\text{Al})$ of the C–S–H is robust to the curing temperature but dependent on the w/c . At 28 days for $w/c = 0.40$, the C–S–H has $\text{Ca}/(\text{Si}+\text{Al}) \approx 1.70 \pm 0.04$. Based on the ^1H NMR signals, a Powers Brownyard type's diagram was achieved.

In addition to the study of plain white cement pastes, the influence of silica fume and slag on the C–S–H parameters was investigated by ^1H NMR. The addition of 10% of silica fume did not change much the water content and the density of the C–S–H. However, the $\text{Ca}/(\text{Si}+\text{Al})$ went down compared to plain pastes with $\text{Ca}/(\text{Si}+\text{Al}) = 1.33 \pm 0.04$ at 28 days of hydration. The addition of 40% of slag led to a decrease in the C–S–H gel pore content.

The size of the C–S–H interlayer pores, C–S–H gel pores and capillary pores was calculated

from NMR data. It did not vary significantly between the different mixes under study. C–S–H interlayer space is ≈ 1 nm and C–S–H gel pores ≈ 2.5 nm. The capillary pores quickly reached ≈ 8 nm in diameter. The size of these capillary pores is smaller than usually reported by other techniques. It is considered in this work as the spaces between the growing C–S–H needles and defined as "interhydrate pores".

The NMR results were compared to porosity results obtained by dynamic sorption isotherm, scanning electron microscopy (SEM) and mercury intrusion porosimetry (MIP). None of these techniques is able to measure the C–S–H interlayer pores. As compared to NMR, the analysis of the desorption isotherm gives a good estimate of the C–S–H gel pores in terms of size and absolute amount. The porosity estimated by SEM showed similar trend as the NMR capillary pores but highly underestimated its amount. MIP is able to quantify accurately the amount of capillary pores in cementitious materials if the samples are prepared by solvent exchange and the data are correctly analysed. The pore entry size measured by the MIP are shifted to bigger size by 3 to 4 \times compared to the other measurement techniques.

Keywords: ^1H NMR, porosity, C–S–H, density, chemical composition

Résumé

Le but de cette thèse était d'étudier la porosité des matériaux cimentaires et la façon dont on la mesure expérimentalement. La plupart des mécanismes de dégradation du béton sont intimement reliés à la porosité, qui influence les résistances et la durabilité du matériau.

Beaucoup d'études sont consacrées à la porosité des pâtes de ciment et de nombreuses méthodes existent pour la quantifier. Pour la plupart d'entre elles, l'eau est dans un premier temps retirée du réseau poreux ce qui peut endommager de manière irréversible les silicates de calcium hydratés (C-S-H). Dans ce travail, la résonance magnétique nucléaire du proton (^1H RMN) a été utilisée pour caractériser l'état de l'eau dans les pâtes de ciment hydratées. Cette technique a l'avantage d'être non destructive, non invasive et permet de réaliser des mesures *in-situ* au cours de l'hydratation. Comme l'atome d'hydrogène est la cible de la mesure, la ^1H RMN possède potentiellement une résolution d'une interaction atomique.

Différentes pâtes de ciment blanc curées scellées à 20 °C ont été étudiées au cours de l'hydratation et en variant le ratio eau/ciment (e/c). L'eau des phases cristallines, dans les inter-feuillets des C-S-H, dans les pores de gel des C-S-H et dans les pores capillaires a été distinguée et quantifiée séparément par ^1H RMN. La quantité des pores de gel atteint rapidement un plateau pour chaque pâte étudiée. Combinées avec des mesures parallèles faites par X-Ray diffraction, les données de ^1H RMN permettent de calculer la densité et la composition chimique des C-S-H. Après 28 jours d'hydratation, la densité des feuillets de C-S-H incluant l'eau qui réside entre eux est typiquement de $\rho_x = 2.74 \pm 0.02 \text{ g/cm}^3$. Cependant, cette densité est dépendante de la température de cure avec $\rho_x = 2.45 \pm 0.05 \text{ g/cm}^3$ à 10 °C. La composition chimique des feuillets de C-S-H quant à elle est indépendante de la température mais sensible aux variations du ratio e/c . A 28 jours de cure pour la pâte de ciment mélangée à $e/c = 0.40$, le rapport $\text{Ca}/(\text{Si}+\text{Al})$ des C-S-H est approximativement de 1.70 ± 0.04 . Le diagramme de Powers and Brownnyard a été refait à partir de ces différents résultats.

Dans un second temps, l'influence de la fumée de silice et des laitiers de hauts fourneaux sur les C-S-H a été étudiée par ^1H RMN. L'addition de 10% de fumée de silice en remplacement du ciment n'a pas changé la densité des C-S-H. Cependant, le ratio $\text{Ca}/(\text{Si}+\text{Al})$ a été diminué jusque $\text{Ca}/(\text{Si}+\text{Al}) = 1.33 \pm 0.04$ à 28 jours d'hydratation. L'ajout de laitiers conduit à une diminution de la teneur en eau de gel des C-S-H.

La taille des différents pores a été calculée à partir des données de RMN. L'inter-feuillet des C-S-H a une taille de approximativement 1 nm, celle des gel de C-S-H 2.5 nm et celle des pores capillaires 8 nm. Ces différentes tailles sont à peu près équivalentes pour tous les mélanges étudiés. La taille des pores capillaire est plus petite qu'habituellement mesurée par d'autres techniques. Cette taille est considéré comme étant la distance entre les aiguilles de C-S-H.

Les résultats de RMN ont été comparés à ceux obtenus par isotherme d'absorption d'eau, par microscope électronique a balayage (MEB) et par l'intrusion au mercure (MIP). Aucune de ces techniques n'est capable de mesurer l'eau inter-feuillet des C-S-H. A comparer à la RMN, l'isotherme d'absorption d'eau mesure de façon adéquate les pores de gel des C-S-H. La porosité estimée par le MEB suit les mêmes tendances que celle mesurée par ^1H RMN mais le MEB largement sous-estime le volume de pores. Le MIP mesure avec précision la quantité de pores capillaires à condition que l'échantillon soit préparé par un échange de solvant et que l'analyse soit correctement effectuée.

Mots clefs : ^1H RMN, porosité, C-S-H, densité, composition chimique

Zusammenfassung

In dieser Arbeit wird die Porosität von Zementmaterialien untersucht. Diese experimentelle Studie umfasst sowohl die Porosität an sich als auch die Messmethode. Die Porosität von Zementmaterialien beeinflusst die Festigkeit und die meisten Korrosionsprozesse in Zementmaterialien.

Verschiedene Techniken wurden zur Untersuchung der Porosität von Zementmaterialien in einer Vielzahl von Studien genutzt. Für die meisten dieser Methoden muss das Porenwasser entfernt werden, was wiederum das Porennetzwerk und die Struktur der Calcium-Silikat-Hydrate (C-S-H) verändern kann. In der vorliegenden Arbeit wurde Kern-Spin-Resonanz (^1H NMR) Relaxometrie genutzt um die verschiedenen Porenräume in hydratisierenden Zementleimen zu charakterisieren. Die verwendete NMR Methode erlaubt zerstörungsfreie *in-situ* Messungen, was ein wichtiger Vorteil gegenüber anderen Methoden ist. Die Methode verwendet das dominante Wasserstoffisotop als Sonde, was ihr eine potentielle Auflösung von einer atomaren Distanz gibt.

Zunächst wurde die Hydratation von weißem Zement mit verschiedenen Wasser-Zement-Verhältnissen (w/z) untersucht. ^1H NMR erlaubt es, dass in kristallinen Phasen gebundene Wasser, das Wasser im Interlayer-Porenraum, im Gel-Porenraum und im Kapillarporenraum zu unterscheiden und quantitativ zu bestimmen. Der Anteil der Gel-Poren erreichte ein Plateau. Die Einbindung von Röntgenstreuungsmessungen erlaubte die Berechnung der C-S-H Dichte und der gemittelten Summenformel. Nach einer Hydratationszeit von ungefähr 28 Tage betrug die Dichte des C-S-H typischerweise $\rho_x = 2.74 \pm 0.02 \text{ g/cm}^3$ für Proben, die bei 20°C hydratisiert wurden. Für jene, die bei 10°C reagierten, fiel dieser Wert auf $\rho_x = 2.45 \pm 0.05 \text{ g/cm}^3$. Das Ca/(Si+Al)-Verhältnis ist jedoch temperaturunabhängig, zeigt aber eine Abhängigkeit vom Wasser-Zement-Wert. Für $w/z = 0.4$ ist $\text{Ca}/(\text{Si}+\text{Al}) \approx 1.70 \pm 0.04$. Anhand der NMR Daten wurde ein Diagramm nach Powers und Brownyard erstellt.

Diese Methode wurde auch angewandt um den Einfluss von Silikatstaub und Hochofenschlacke auf C-S-H zu untersuchen. Die Zugabe von 10% Silikatstaub hatte nur geringen Einfluss auf den Wassergehalt und die Dichte von C-S-H. Das Ca/(Si+Al)-Verhältnis verringerte sich jedoch auf $\text{Ca}/(\text{Si}+\text{Al}) \approx 1.33 \pm 0.04$ nach 28 Tagen Hydratation. Die Zugabe von 40% Hochofenschlacke führte zu einer Verringerung des Gelporenvolumens.

Die charakteristische Größe der C–S–H Interlayerporen, der C–S–H Gelporen und der Kapillarporen wurde anhand der NMR Daten berechnet. Diese waren für die untersuchten Mischungen weitestgehend konstant. Für den Interlayerporenraum wurde eine Größe von ≈ 1 nm gefunden, die Gelporen sind bei ca. ≈ 2.5 nm. Die Größe der Kapillarporen erreichte schnell 8 nm. Dieser Wert ist kleiner als jene Werte, die mit anderen Methoden typischerweise bestimmt werden. Diese Längenskala wird in dieser Arbeit mit dem verbleibenden Raum zwischen C–S–H nadeln verknüpft.

Die NMR Ergebnisse wurden mit Porositätsmessungen verglichen, die mit dynamischen Sorptionsmessungen, Rasterelektronenmikroskopie (REM) und Quecksilberporosimetry erhalten wurden. Keine dieser Techniken vermag die C–S–H Interlayerporen zu erfassen. Verglichen mit NMR, die dynamischen Sorptionsmessungen geben gute Ergebnisse sowohl im Hinblick auf die Porengröße und das Volumen. REM zeigt die selben Trends wie NMR, misst jedoch deutlich geringere Porositäten. Quecksilberporosimetry vermag den Anteil der Kapillarporen genau zu bestimmen, wenn die Proben mit Lösungsmittelaustausch vorbereitet wurden. Die gemessenen Größen für die Poreneingänge sind jedoch um einen Faktor von drei oder vier größer als die anderen Messmethoden.

Schlüsselworte: ^1H NMR, Porosität, Dichte, Chemische Zusammensetzung

Resumen

El objetivo de esta tesis es la investigación de la porosidad de los materiales cementicios y la manera de medirla experimentalmente. La porosidad está relacionada con la resistencia del material y es la causa de la mayoría de los fenómenos de degradación que derivan en el deterioro de las estructuras.

Muchos estudios se han centrado en la caracterización de la porosidad de los materiales cementicios y existen diferentes técnicas para su evaluación. En la mayoría, se extrae el agua de la red de poros antes de realizar el ensayo, un procedimiento que puede alterar las estructuras calcio-silicato-hidratos (C-S-H). En este trabajo se utilizó la relaxometría por resonancia magnética nuclear (^1H RMN) para caracterizar las diferentes poblaciones de poros en pastas de cemento hidratado. ^1H RMN tiene como ventaja sobre las demás técnicas que es un procedimiento no destructivo, no invasivo y que las mediciones pueden hacerse *in-situ*. Como la muestra es ^1H , la ^1H RMN tiene una resolución igual a la distancia entre átomos.

Primeramente se prepararon diferentes pastas de cemento blanco con diferente relación agua cemento (*a/c*), curadas a 20 °C, las que fueron estudiadas durante todo el proceso de hidratación. Se pudieron distinguir y cuantificar, basados en los datos de relajación de ^1H RMN, el agua de las fases sólidas cristalinas, la presente entre las capas de C-S-H, en el gel C-S-H y en los poros capilares. Se pudo observar un máximo en la formación de los poros de gel a partir del cual su número no varía. Combinando estos resultados con los de difracción de rayos X se pudo calcular la densidad y composición química del C-S-H. A los 28 días de hidratación, la densidad de las capas de C-S-H incluyendo el agua entre capas es del orden de $\rho_x = 2.74 \pm 0.02 \text{ g/cm}^3$ para todas las pastas curadas a 20 °C. Sin embargo la densidad bajó al $\rho_x = 2.45 \pm 0.05 \text{ g/cm}^3$ cuando la pasta fue curada a 10 °C. Por otra parte, la relación $\text{Ca}/(\text{Si}+\text{Al})$ de la C-S-H no depende de la temperatura de curado, pero sí de la *a/c*. A los 28 días, para *a/c* = 0.40, la relación $\text{Ca}/(\text{Si}+\text{Al})$ es de $\approx 1.70 \pm 0.04$. A partir de las señales de ^1H RMN se obtuvo un diagrama tipo Powers Brownyard.

Además del estudio de pastas de cemento blanco puras, mediante la técnica ^1H RMN se investigó la influencia de la adición de humo de sílice y de escoria en los parámetros de la C-S-H. La adición de un 10% de humo de sílice no tuvo un efecto significativo en el contenido de agua y la densidad de la C-S-H. Sin embargo, la relación $\text{Ca}/(\text{Si}+\text{Al})$ fue menor en compa-

ración con pastas puras con un valor de $\text{Ca}/(\text{Si}+\text{Al})= 1.33 \pm 0.04$ a los 28 días de hidratación. La adición de 40% de escoria produjo una disminución en el contenido de poros del gel C-S-H.

A partir de los datos de ^1H RMN fueron calculados, el tamaño de los poros entre las capas de C-S-H, de los poros del gel C-S-H y de los poros capilares. No hubo una variación significativa entre las diferentes mezclas bajo estudio. El espacio entre las capas de C-S-H es de ≈ 1 nm y el poros del gel ≈ 2.5 nm. Los poros capilares rápidamente alcanzaron un diámetro de ≈ 8 nm. El tamaño de estos poros resultó menor al que generalmente reportan otras técnicas. En este trabajo los poros son considerados como los espacios entre las agujas de C-S-H en crecimiento y definidos como "poros intehidratos".

Los resultados de ^1H RMN fueron comparados con los resultados de porosidad obtenidos mediante la isoterma de absorción dinámica, microscopía electrónica de barrido (SEM) y porosimetría por inmersión de mercurio (MIP). Ninguna de estas técnicas es capaz de medir los poros entre las capas de C-S-H. En comparación con ^1H RMN, el análisis mediante la isoterma de desorción brinda una buena estimación de los poros del gel C-S-H en términos de tamaño y cantidad absoluta. La porosidad estimada por SEM mostró una tendencia similar a la estimada por ^1H RMN pero cualitativamente indeterminada. Mediante MIP se puede cuantificar con precisión la cantidad de poros capilares en los materiales cementicios siempre que las muestras sean primero preparadas mediante intercambio de disolvente y los datos sean analizados correctamente. El valor del tamaño de los poros medido por MIP tiende a ser de 3 a 4 veces mayor a los obtenidos con otras técnicas de medición.

Palabras Clave: ^1H RMN, porosidad, C-S-H, densidad, composición química

Contents

Acknowledgements	i
Abstract (English/Français/Deutsch/Español)	iii
List of figures	xv
List of tables	xix
Glossary	xxi
1 Introduction and literature review	1
1.1 Overall context	2
1.2 Aims of the thesis	3
1.3 Concepts related to porosity in porous media	3
1.4 Water states and roles	4
1.5 Porosity of cement-based materials	4
1.5.1 Basic cement hydration	4
1.5.2 The different categories of porosity in cement pastes	6
1.5.3 Powers and Brownyard's model	7
1.5.4 Pore structure and properties of C–S–H hydrates	9
1.6 Different methods to characterise porosity	11
1.6.1 Dynamic vapour sorption experiment	12
1.6.2 Mercury Intrusion Porosimetry	14
1.6.3 Scanning Electron Microscopy	15
1.6.4 Nuclear Magnetic Resonance	17
1.7 The impact of drying on porosity results	17
2 ¹H NMR technique	19
2.1 Introduction to NMR	20
2.1.1 Basics of NMR and relaxation phenomena	20
2.1.2 Different methods of pulse sequences	24
2.1.3 Calculation of pore size	28
2.2 NMR Literature in the context of cement	30
2.2.1 Simple relaxation experiments	30
2.2.2 Exchange experiments	32

2.2.3	NMR cryoporometry	33
3	Materials and methods	35
3.1	Cements	36
3.2	Generic sample casting	36
3.3	¹ H NMR: pulse sequences, parameters and analysis	37
3.3.1	Quad-echo pulse sequence	38
3.3.2	CPMG pulse sequence	42
3.4	Other methods	44
3.4.1	X-ray diffraction (XRD)	44
3.4.2	Chemical shrinkage	44
3.4.3	Isothermal calorimetry	44
3.4.4	Scanning electron microscopy (SEM)	45
3.4.5	Transmission electron microscopy (TEM)	45
3.4.6	Thermo-gravimetric analysis (TGA)	46
3.4.7	Solid-state ²⁹ Si MAS NMR	46
3.4.8	Relative humidity measurement	46
3.4.9	Water dynamic vapour sorption (DVS)	46
3.4.10	Mercury intrusion porosimetry	48
4	NMR study of plain white cement pastes	49
4.1	Mixes under study	51
4.2	Experimental results	51
4.2.1	Isothermal calorimetry	51
4.2.2	¹ H NMR signal assignment	52
4.2.3	¹ H NMR experimental error	55
4.2.4	Evolution of NMR signal amplitude during the hydration (<i>w/c</i> = 0.40)	56
4.2.5	Evolution of <i>T</i> ₂ relaxation times during the hydration (<i>w/c</i> = 0.40)	57
4.2.6	Pore size interpretation	57
4.2.7	NMR responses for <i>w/c</i> = 0.32 and <i>w/c</i> = 0.48	59
4.2.8	Chemical shrinkage volume	62
4.3	Theory - calculations based on NMR signals	64
4.3.1	Mass and volume paste composition	64
4.3.2	C–S–H chemical composition	65
4.4	Analytical results - C–S–H characteristics	68
4.4.1	C–S–H density	68
4.4.2	C–S–H Chemical composition	73
4.4.3	Specific surface area of the C–S–H interlayer and gel pores	76
4.5	Mass and volume composition diagram	76
4.6	Sensitivity analysis	78
4.7	Desorption isotherm at 20 °C	79
4.7.1	Sample preparation and experimental procedure	79
4.7.2	Effective water-to-cement ratio	79

4.7.3	Solid and liquid NMR components after 28 days of underwater cure . . .	79
4.7.4	Desorption isotherm results	80
4.7.5	Analysis of the results - C-S-H characteristics	82
4.7.6	Pore size by amplitude model	82
4.8	Sealed white cement paste cured at 10 °C	83
4.8.1	Experimental results	83
4.8.2	Analytical results - C-S-H characteristics	86
4.8.3	Discussion	87
4.9	General discussion	88
5	NMR study of blended systems	91
5.1	The influence of 10% of silica fume	92
5.1.1	Introduction on silica fume	92
5.1.2	Mix under study	92
5.1.3	Theory - modifications of the calculation for the silica fume	93
5.1.4	NMR results	94
5.1.5	Hydration kinetics	95
5.1.6	Degree of reaction of alite and belite	98
5.1.7	Degree of reaction of silica fume	99
5.1.8	Crystalline phases: ettringite and Portlandite content	102
5.1.9	Chemical shrinkage	104
5.1.10	Calculation of the C-S-H parameters	104
5.1.11	SEM and TEM microscopy	107
5.1.12	Discussion and conclusions	109
5.2	The addition of slag	111
5.2.1	Mixes under study	111
5.2.2	Experimental results	111
6	Comparison with other measurement techniques	115
6.1	Desorption isotherms	116
6.1.1	Experimental procedure	116
6.1.2	Results	116
6.1.3	Discussion	119
6.2	Scanning electron microscopy	120
6.2.1	Experimental procedure	120
6.2.2	Image analysis	121
6.2.3	Results	124
6.2.4	Discussion	124
6.3	Mercury intrusion porosimetry	126
6.3.1	Experimental procedure	126
6.3.2	White cement pastes with different <i>w/c</i> at 28 days of sealed hydration . .	126
6.3.3	White cement paste at <i>w/c</i> as a function of hydration time	132
6.3.4	White cement paste cured under water for 28 days	134

6.3.5	The influence of drying on MIP results	136
6.3.6	Conclusions	138
7	Conclusions and perspectives	139
A	Appendix - ¹H NMR experimental details	143
A.1	Before starting	144
A.2	Signal acquisition	145
A.3	What can affect the acquisition?	146
A.4	What ways of testing do we have?	148
A.5	Signal processing	150
A.6	Issues with the measurement of	156
A.7	Matlab codes	158
B	Appendix - Oxides composition of white cements, silica fume and slag	163
C	Appendix - Particle size distribution (cement, slag and quartz)	165
	Bibliography	177
	List of publication	179
	Curriculum Vitae	181

List of Figures

1.1	Organigram of the 15 TRANSCEND projects with their links	2
1.2	Schematic representation of heat released during ordinary cement hydration .	5
1.3	SEM BSE micrograph of an OPC paste and Schematic illustration of hollow grains	5
1.4	Schematic representation of the different categories of pores in OPC	6
1.5	Powers' schematic vision of hydrated cement pastes	7
1.6	Powers' cement composition diagram as a function of water-to-cement ratio .	8
1.7	Volume composition diagram based on Powers' equations	8
1.8	Schematic representation of Tobermorite, taken as a C-S-H analogue	9
1.9	The different vision of the porosity of C-S-H	10
1.10	Range of size probed by different techniques	11
1.11	Comparison of pore categories between different author	12
1.12	Example of sorption isotherm data	14
1.13	SEM BSE micrograph of an OPC paste and a SEM typical grey level histogram .	16
1.14	SEM BSE micrograph of an OPC paste at 10,000 × magnification	16
1.15	Comparison between different drying methods	18
2.1	Representation of the spins in the rotating frame exposed to different pulses . . .	20
2.2	Nuclear spins illustrating the dipole-dipole interaction	21
2.3	T_1 recovery of the spins	22
2.4	Schematic rates of relaxation T_1 and T_2 in cement paste	23
2.5	Free induction decays	24
2.6	Carr-Purcell-Gill-Meiboom (CPMG) pulse sequence	25
2.7	Inverse recovery pulse sequence	26
2.8	Quad-echo pulse sequence	27
2.9	Amplitude model	29
2.10	First attempt to calculate the PSD in cement pastes based on ^1H NMR	31
2.11	T_1 - T_2 spectrum showing exchange between gel pores and capillary pores	33
2.12	T_2 - T_2 spectrum	33
3.1	Quad-Echo pulse sequence	38
3.2	QE raw signals for mature cement paste and for pure ettringite or CH	40
3.3	QE solid and liquid amplitudes as a function of τ	41
3.4	Example of T_2 decay and the associated inverse Laplace transform	43

3.5	Sorption and desorption branches for the reference material MCM41	47
3.6	Example of MIP reproducibility	48
4.1	Calorimetry results for white cement pastes with $w/c = 0.32, 0.40$ and 0.48 . . .	51
4.2	Evolution of the NMR signal during hydration for the $w/c = 0.40$ paste	52
4.3	Evolution of the different NMR signal fractions ($w/c = 0.40$)	56
4.4	Evolution of the T_2 relaxation times for $w/c=0.40$	57
4.5	Tobermorite structure viewed along and perpendicular to the silicate chains . .	58
4.6	T_2 distribution map of different pastes with $w/c = 0.32, 0.40,$ and 0.48	59
4.7	NMR amplitudes and T_2 for $w/c = 0.32$	60
4.8	NMR amplitudes and T_2 for $w/c = 0.48$	60
4.9	Measure of the “internal” relative humidity of samples	61
4.10	Change in C–S–H water signals by the creation of solid layer(s) into gel pores .	62
4.11	Chemical shrinkage and re-wetting experiments	63
4.12	Graphical representation of the C–S–H based on ^1H NMR data	68
4.13	C–S–H density as a function of the degree of hydration ($w/c = 0.40$)	69
4.14	Volume of cement consumed and volume of C–S–H layers created	70
4.15	Influence of surface water to the C–S–H density	71
4.16	C–S–H density as a function of w/c at 28 days of hydration	72
4.17	Capillary and gel absolute water contents for $w/c = 0.32, 0.40$ and 0.48	72
4.18	Chemical composition of the C–S–H for the $w/c = 0.40$ paste	73
4.19	Chemical composition of the C–S–H as a function of w/c	74
4.20	SEM BSE micrograph of $w/c = 0.40$ paste after 28 days of hydration	75
4.21	SEM-EDX quantification of 28 days old pastes with different w/c	75
4.22	Mass and volume composition of cement paste based on NMR data	77
4.23	Spectrum of the different liquid water populations measured by CPMG	80
4.24	NMR desorption isotherm results	81
4.25	schematic representation of the C–S–H for different RH	81
4.26	Evolution of the different NMR signal amplitudes with hydration time at 10°C .	83
4.27	Chemical shrinkage for the paste with $w/c = 0.40$ cured at 10°C	85
4.28	C–S–H density as a function of time at 10°C	86
4.29	SFEG micrographs showing the C–S–H growing as needles	89
5.1	Evolution of the different water populations for the WC/SF paste	95
5.2	Calorimetry results for the WC/SF paste	96
5.3	Degree of reaction of alite and belite calculated from XRD	98
5.4	Degree of reaction for silica fume measured by ^{29}Si MAS NMR	100
5.5	^{29}Si MAS NMR spectra for WC/SF paste as a function of hydration time	101
5.6	Mass of ettringite as a function of time measured by XRD	102
5.7	Mass of Portlandite as a function of time from NMR, XRD and TGA	103
5.8	Chemical shrinkage results for the WC/SF paste	104
5.9	Results of C–S–H parameters for the WC/SF pastes	105
5.10	Mass and volume compositions of the WC/SF paste	107

5.11	TEM micrograph of the WC/SF paste	109
5.12	XRD results for different pastes containing slag	112
5.13	NMR results for slag systems	112
5.14	Comparison of the XRD results and I_{solid} for different contents of slag	114
6.1	Water desorption isotherm results, being compared to NMR	116
6.2	Pore size distribution calculated from desorption isotherm	118
6.3	Change in porosity for different magnifications	120
6.4	Average grey level histograms for the sealed white cement pastes	122
6.5	Derivative plot of the estimated porosity with variation of the grey level	123
6.6	Pore volume calculated by SEM and compared to NMR	124
6.7	Comparison between SEM and TEM micrographs	125
6.8	MIP cumulative pore volumes at 28 days of hydration for different w/c	126
6.9	First derivative of the MIP pore volumes for different w/c	128
6.10	Comparison between the capillary porosity between MIP and NMR	129
6.11	Comparison between the MIP pore size distribution and that of NMR	131
6.12	Evolution of cumulative pore volumes as a function of hydration age	132
6.13	Evolution of the capillary pores as seem by MIP and NMR	133
6.14	Comparison between the NMR pore volumes and those measured by MIP	134
6.15	MIP of underwater cured sample	135
6.16	First derivative of the MIP data for the underwater cured paste	135
6.17	MIP results for different drying methods	136
6.18	Quantification of the impact on drying on MIP results	137
7.1	Change in C–S–H water signals by the creation of solid layer(s) into gel pores	141
A.1	Home-made syringe for inserting cement paste at the bottom of NMR tubes	144
A.2	Empty tube signal	147
A.3	Pulses recored by an oscilloscope	148
A.4	NMR results for copper sulfate solutions	149
A.5	Effect of the $\tau = 15 \mu\text{s}$ data point on QE results	151
A.6	Effect of the parameter α on the ILT peak deconvolution	152
A.7	Example of “wrong” deconvolution having an artefact peak	153
A.8	Deconvolution of the CPMG decay between the different populations	154
A.9	Generated data, Fourier transform and ILT deconvolution	155
A.10	Illustration of the condensation issue for saturated sample	157
C.1	Typical particle size distribution for white cement, slag and quartz	165

List of Tables

1.1	Molecule size and associated BET SSA values of a mature OPC paste	14
3.1	Phases composition of the three white cement batches used in this work	36
3.2	Comparison between ignited water mass and the initial water mass	37
4.1	CH and ettringite mass fractions measured by XRD and TGA	54
4.2	Calculated errors in % for the four aforementioned options	55
4.3	Sensitivity study of C–S–H parameters	78
4.4	TGA and XRD results for the plain white cement paste sealed cured at 10 °C	84
4.5	Comparison of different C–S–H variables between 10 °C and 20 °C	87
5.1	Fitting parameters for the cumulative heat flows from calorimetry	97
5.2	Fitting parameters for the degree of reaction of alite and belite from XRD	99
5.3	²⁹ Si MAS NMR results	101
5.4	SEM-EDX and TEM-EDX Ca/(Si+Al) results	108
5.5	The different mixes under study with slag contents ranging from 0 to 40%	111
7.1	C–S–H parameters as a function of <i>w/c</i> at 28 days of hydration	140
A.1	τ values as calculated with Equation A.1 and the aforementioned parameters	149
A.2	Peak area for the different populations presented in Figure A.6	153
B.1	Oxides composition of the binders	163

Glossary

Cement chemistry notation is used throughout this thesis to refer to the compositional oxides:

C = CaO	F = Fe ₃ O ₃	N = Na ₂ O
S = SiO ₂	\$ = SO ₃	K = K ₂ O
H = H ₂ O	<u>C</u> = CO ₃	
A = Al ₂ O ₃	M = MgO	

This leads to the following abbreviations for anhydrous and hydrates phases:

C ₃ S	3 CaO · SiO ₂	Tricalcium silicate (Alite)
C ₂ S	2 CaO · SiO ₂	Dicalcium silicate (Belite)
C ₃ A	3 CaO · Al ₂ O ₃	Tricalcium aluminate
C ₄ AF	4 CaO · Al ₂ O ₃ · Fe ₂ O ₃	Ferrite
C\$H ₂	CaSO ₄ · 2 H ₂ O	Gypsum
C\$H _{1/2}	CaSO ₄ · $\frac{1}{2}$ H ₂ O	Bassanite
C\$	CaSO ₄	Anhydrite
<u>CC</u>	CaCO ₃	Calcium carbonate
CH	Ca(OH) ₂	Calcium hydroxide (Portlandite)
C-S-H	CaO-SiO ₂ -H ₂ O	Calcium silicate hydrate
AFt	3 CaO · Al ₂ O ₃ · 3 CaSO ₄ · 32 H ₂ O	Ettringite
AFm	3 CaO · Al ₂ O ₃ · CaSO ₄ · 12 H ₂ O	Tricalcium monosulfo aluminate

The following abbreviations are also used:

AMU	Atomic Mass Units
BET	Brunauer-Emeth-Tarr
BJH	Barrett-Joyner-Halenda
BSE	BackScattered-Electron
DVS	Dynamic Vapour Sorption
EDX	Energy Dispersive X-Ray Spectroscopy
ILT	Inverse Laplace Transform

MIP	Mercury Intrusion Porosimetry
NMR	Nuclear Magnetic Resonance
OPC	Ordinary Portland Cement
PSD	Pore Size Distribution
SEM	Scanning Electron Microscopy
SSA	Specific Surface Area
TEM	Transition Electron Microscopy
TGA	ThermoGravimetric Analysis
WC	White Cement
WC/SF	White Cement / Silica Fume mix
XRD	X-Ray Diffraction
XRF	X-Ray Fluorescence

1 Introduction and literature review

Contents

1.1 Overall context	2
1.2 Aims of the thesis	3
1.3 Concepts related to porosity in porous media	3
1.4 Water states and roles	4
1.5 Porosity of cement-based materials	4
1.5.1 Basic cement hydration	4
1.5.2 The different categories of porosity in cement pastes	6
1.5.3 Powers and Brownyard's model	7
1.5.4 Pore structure and properties of C-S-H hydrates	9
1.6 Different methods to characterise porosity	11
1.6.1 Dynamic vapour sorption experiment	12
1.6.2 Mercury Intrusion Porosimetry	14
1.6.3 Scanning Electron Microscopy	15
1.6.4 Nuclear Magnetic Resonance	17
1.7 The impact of drying on porosity results	17

The motivations for the present study and the research objectives are presented in this chapter. It gives an overview about porosity in cement pastes and describes the methods used to assess porosity and their limitations.

1.1 Overall context

Concrete is the most widely used material in the world. This is linked to its price, its mechanical performances and its possibilities for casting *in-situ* (in any geometry). Concrete works are generally designed and used from 40 to 100 years but a fraction of them require maintenance or reconstruction far before the predicted end of service life. Damages observed in concrete structures are often due to the penetration of an external agent that modifies the initial state of the material. The ability of the material to withstand these phenomena is called durability. The penetration of aggressive elements into concrete is therefore conditioned by the accessible porosity, closely associating durability with pore network.

The current interest for research in the field of cement is fuelled by the substantial contribution of cement production (due to the enormous volumes) to global CO₂ production, currently 5-8%, and the requirement to reduce this by the incorporation of supplementary cementitious materials (SCMs). These supplementary products can react themselves and/or modify the reaction of the clinker component. Hence, there is not a single microstructure but a multitude. Better quantitative characterisation of the pore network is therefore important to ensure the durability of concrete.

This thesis is one of the 15 **TRANSCEND** theses in the Initial Training Network under the consortium Nanocem. These 15 projects focus on the description and prediction of water transport in cementitious materials. From a scientific standpoint, this translates as water transport and permeability properties of cementitious systems and the name TRANSCEND originates from **TRAN**SPORT for **CON**crete which is **Eco** friendly, **iN**novative and **Durable**.

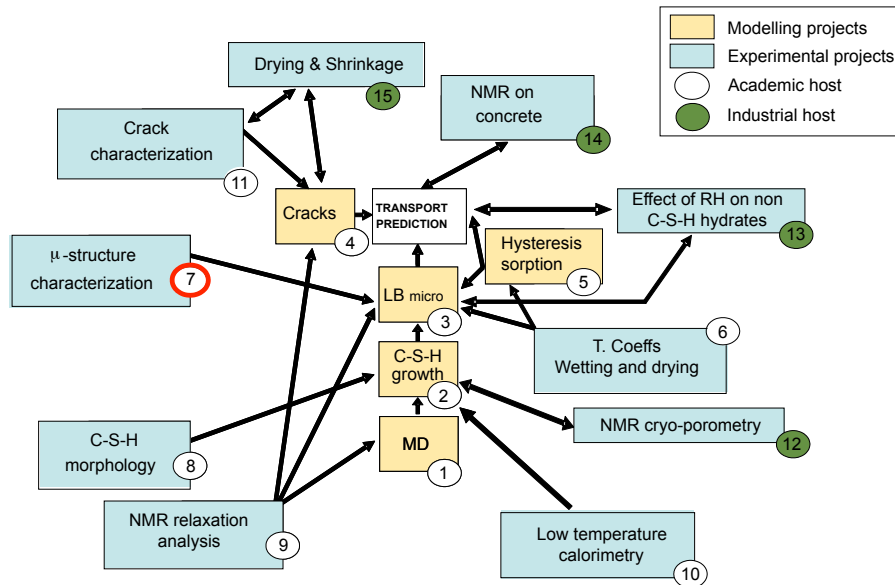


Figure 1.1 – Organigram of the 15 TRANSCEND projects and their links between each other. My thesis project is the project number 7.

TRANSCEND aims to understand and describe the evolution of transport properties across all scales from the atomistic to the structural level. This specific thesis was proposed to bring a better understanding of porosity of cementitious material across different binders by the use of different techniques. A schematic representation of the different TRANSCEND projects and the way they interact with each other is presented in Figure 1.1. This project is the project number 7 originally named “ μ -structure characterisation”. For more information about the other TRANSCEND projects, please go to the website: <http://www.nanocem.org/index.php?id=282>.

1.2 Aims of the thesis

The porosity of cement-based material is defined in literature in many ways and authors do not agree about the separation in categories. The three most accepted categories are “compaction/air voids”, “capillary porosity” and “gel porosity”. However micro/meso/macro terms are often used. The main issue is the disagreement about the size ranges. These confusions come from the intrinsic material complexity and the dispersion of results between many different characterisation methods. No one investigation method accurately covers the whole range of pore size existing in cementitious material and the data from overlapping zones (when they exist) often do not agree.

A lot of factors can influence porosity measurements and each characterisation technique has its own limitations. Moreover, most porosity measurement methods require a pre-drying, which may permanently alter the microstructure and may lead to further difficulties in understanding the true porosity of the material.

Part of this work focuses on fundamental understanding of porosity and its development over time. The relatively new technique of ^1H nuclear magnetic resonance (^1H NMR) provides the basis of this study. Plain cement pastes and the influence of different SCMs on the porosity are studied. The results obtained by NMR are then compared to the other characterization techniques usually used in the field. In that context, the main objective of the work is to bring a better description of the pore network of cement-based materials.

1.3 Concepts related to porosity in porous media

Hardened cement pastes are heterogeneous materials whose porosity forms a complex interconnected network across a wide range of sizes. Hence, the pore structure has been described in many ways:

- The first characteristic value is the **relative pore volume** (in %), which represents the volume fraction of non-solid elements with respect to the total volume.
- The **pore size distribution** (PSD) gives the relative pore volume as a function of pore size. This concept becomes ambiguous in an interconnected pore network.

- **Specific surface area** (SSA) is another variable used to describe porous media. It represents the solid surface in contact with the porosity. It comes as a complement to the other characteristic values and describes the complexity of solid particles.
- Some concepts linked to the transport properties of the materials are also considered. The **connectivity** of the pores is probably the most important one of these concepts; a non-connected pore network does not transport ionic species in contrast to a connected pore structure.

1.4 Water states and roles

For cement-based materials, water usually represents more than half of the total volume when mixed with cement. This is conventionally expressed as water-to-cement ratio, noted w/c , in mass. When the reactions start, hydrates form at the expense of anhydrous cement and water. Hence, the volume of water determines the starting porosity which is progressively filled with hydration products. Since water in pores underpins most degradation phenomena, it is often the point of interest.

From a general standpoint, water in hydrated cement pastes can be divided into two main categories. The first one refers to structural water associated within crystalline phases such as Portlandite or ettringite (AFt). This kind of water is called “**non-evaporable water**” because these H_2O molecules can only be removed when the material is heated up above $100\text{ }^\circ\text{C}$. However, it is increasingly clear that some structural water is removed from most phases below $100\text{ }^\circ\text{C}$. The second category is called “**evaporable water**” as it can be taken out of cement samples at ambient temperatures in a dry environment.

Evaporable water itself can be divided into two subcategories depending on its physical state. In a fully saturated pore volume, several layers of water molecules are adsorbed on the pore surfaces by attractive forces. This particular state of water is called “**physically bound water**” and the intensity of cohesive forces depends on the adsorbed thickness and the geometry of the cavity. The other water molecules fall into the second subcategory of evaporable water called “**free water**”. It is located in the middle of wide enough pores ($> 2\text{ nm}$ in diameter) and can contribute to the cement reaction process.

1.5 Porosity of cement-based materials

1.5.1 Basic cement hydration

Basic cement hydration involves the dissolution of clinker phases in water and the formation of solid hydration products by precipitation. Dissolution of cement particles releases ions into the pore solution which then combine with water to form mainly calcium silicate hydrates (C–S–H) and calcium hydroxide (CH in cement notation, also called Portlandite). C–S–H hydrates represent approximately half of the solid phases by mass in a mature OPC paste. As

such, the state of mechanical properties in a cement or concrete sample depends heavily on the C-S-H.

The hydration is a complex process known to follow several stages. Isothermal calorimetry is able to identify the different phenomena occurring during cement reactions as most processes are exothermic. Figure 1.2 shows a schematic calorimetry curve of cement reactions illustrating the subdivision of the early hydration into different stages. There is (I) an initial dissolution period, (II) an induction period of a few hours followed by (III) a important precipitation of hydrates.

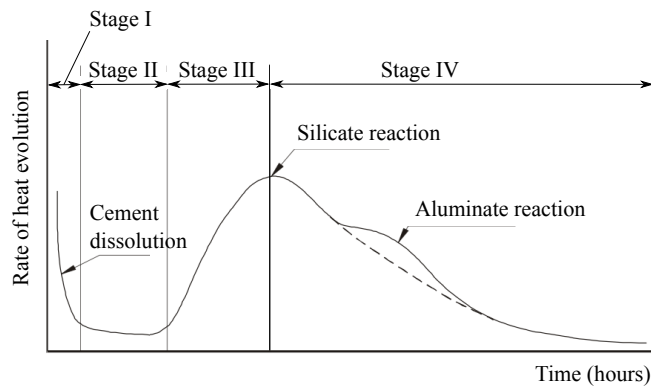


Figure 1.2 – Schematic representation of heat released during ordinary cement hydration, adapted from [1]. Stage I: dissolution; Stage II: induction period; Stage III: acceleration period; Stage IV: deceleration period.

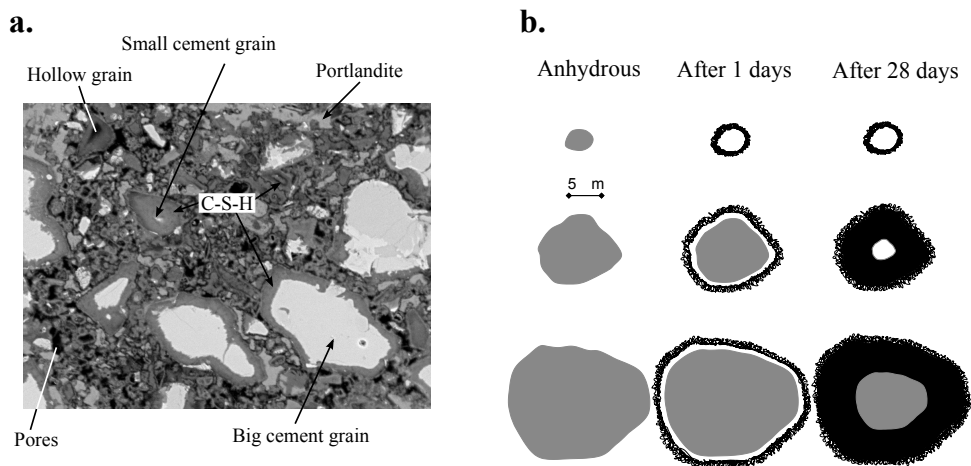


Figure 1.3 – (a) SEM BSE micrograph of an OPC paste at 7 days of hydration. (b) Schematic illustration of the formation of hydration shells according to grain size (from [2]).

Hydrates precipitate on surfaces. The first hydrates cover cement grains and further grow

into the available space. Figure 1.3a shows a SEM micrograph of a typical cement paste microstructure at 7 days of hydration. All cement grains are surrounded by a shell of C–S–H. As the cement grains dissolve, this might leave a hollow shell ($\approx 1\mu\text{m}$) between the first formed hydrate layer and the remaining unreacted particle [2] (Figure 1.3b). Small cement grains hydrate completely in the first stages and remain as hollow shells of hydration product. However, big grains further hydrate which forms denser hydration products and which fill in the gap between shell and grain.

1.5.2 The different categories of porosity in cement pastes

In literature, three main categories of pores are often quoted for hydrated ordinary cement pastes. They can be classified by size from the biggest to the smallest:

The first category is the **compaction/air voids**. Their size can vary between a few μm to a few mm. Air voids can be created during mixing but they can also be triggered by the use of specific chemical products called air entrainment agents. Compaction/air voids are the wider spaces in the porosity of cement pastes (Figure 1.4).

The second category is the **capillary porosity**. There is a common consensus for capillary pores to be the remaining spaces which are not occupied by hydration products or unreacted cement grains. Even if the total content of capillary porosity goes down with increasing hydration, some of them originate from chemical shrinkage: the bulk volume of hydration products is smaller than the volume of the initial components used in the chemical reaction (at around 8% for conventional cements [3]). Capillary cavities are usually reported to be $> 10\text{ nm}$ to a few μm .

The last category is the **gel pores**. *Gel pores* are the intrinsic porosity of C–S–H hydrate (or C–S–H gel) and are considered by many authors to be a part of it (Figure 1.4). “*Gel pores*” is a generic term defining all pores within C–S–H. *Gel pores* are known to be of nanometre size and completely saturated with water. Section 1.5.4, p. 9 describes more in detail the assumed physical properties of C–S–H nano-hydrates.

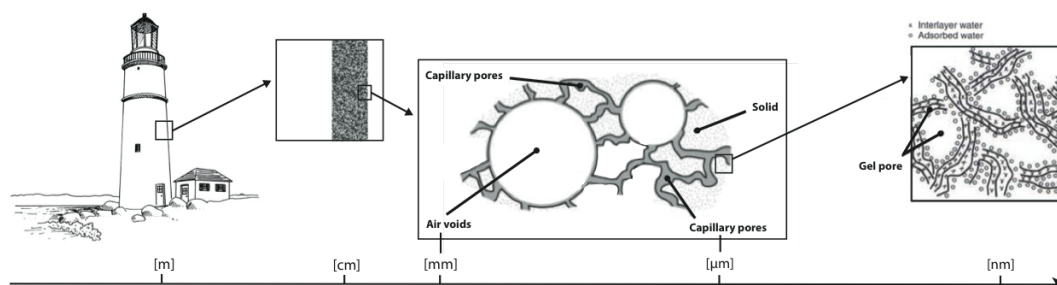


Figure 1.4 – Schematic representation of the different categories of pores in ordinary Portland cement pastes.

1.5.3 Powers and Brownyard's model

The first complete description of porosity and hydration of cement pastes was proposed by Powers and Brownyard (PB) in the 1950s [4]. Powers and Brownyard published a seminal work about cement hydration processes based on a careful study of water states with the help of water sorption isotherms. They reported the way the initial water reacts and how water locations evolve throughout the hydration. They distinguished **water in hydration products** (being C–S–H plus other crystalline phases), and water in so-called “**capillary pores**” which represent the free spaces not occupied by cementitious particles.

Hydrated cement paste is described as big capillary cavities in between hydration products. A schematic is shown in Figure 1.5. C–S–H gel is “fibrous particles” - “*Bundles of such fibres seem to form a cross-linked network containing some more or less amorphous interstitial material*” [5]. They stated the atomic structure of C–S–H to be highly disorganized and comparable to tobermorite crystal structure [6]. They gave the chemical composition of C–S–H as $3 \text{CaO} \cdot 2 \text{SiO}_2 \cdot 3 \text{H}_2\text{O}$ with an intrinsic porosity of 28% by volume.

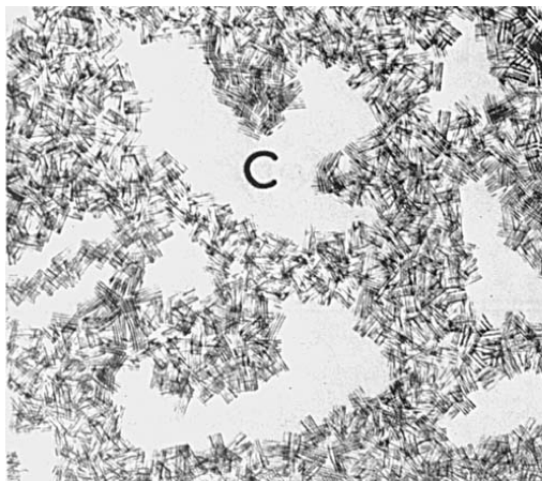


Figure 1.5 – Powers' schematic vision of hydrated cement pastes. “C” represents capillary cavities entrapped in between C–S–H gel [5].

The initial water-to-cement ratio has an impact on the amount of cement that can react but also highly influences the capillary pore content of the final material. Figure 1.6, adapted from one of Powers' paper [5], illustrates this phenomenon when increasing the water-to-cement ratio from $w/c = 0.20$ to $w/c = 0.80$. In a reference mass composition of pure OPC fresh paste right after mixing, the water is already considered by PB as capillary porosity. As the hydration progresses, the volume of solid products increases and consequently the capillary porosity (remaining free water) decreases. As every chemical reaction, it ends with depletion of one of the reagents. For $w/c > 0.40$ sealed pastes, excess water will remain as capillary pores when the cement will have fully reacted. It needs to be reminded that other capillary pores exist due to chemical shrinkage.

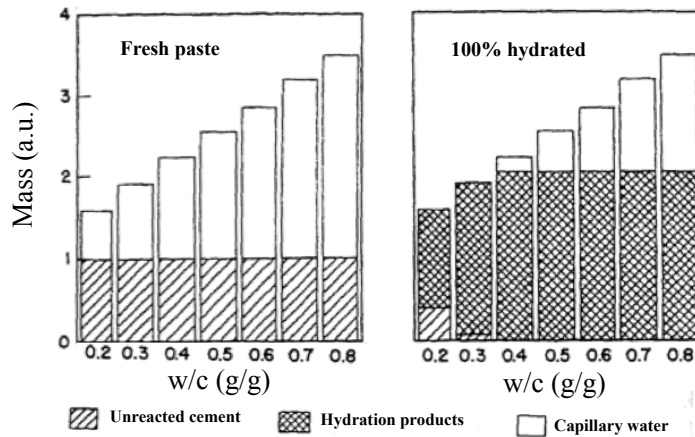


Figure 1.6 – Powers’ cement composition diagram as a function of water-to-cement ratio, adapted from [5].

In Powers’ work, the complete reaction of 1 g of OPC requires 0.23 g of water and, in the saturated condition, holds 0.21 g of gel water in the C–S–H. Full cement hydration demands a minimum water-to-cement ratio of 0.38. Below this ratio, the initial “capillary water” amount is totally used for solid products formation. Above a water-to-cement ratio of 0.38, a part of the initial water will not be used and continues to exist in the microstructure as capillary porosity. In PB’s model, the paste composition can be derived from a set of equations predicting the variation of the different components as a function of degree of cement hydration (Figure 1.7). For instance, the volume fraction of capillary porosity can be calculated by $f_{cap} = f_0 - 1.13 \times \alpha \times (1 - f_0)$ where f_0 is the initial volume fraction of water and α the degree of hydration of cement. Powers’ model remains a reference in the field.

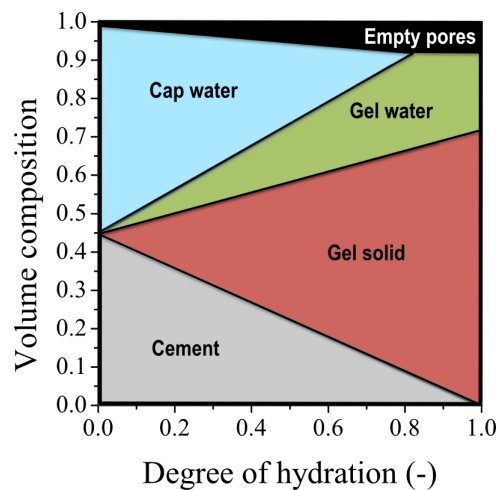


Figure 1.7 – Volume composition diagram based on Powers’ equations for a OPC paste as a function of cement reaction at $w/c = 0.40$.

1.5.4 Pore structure and properties of C–S–H hydrates

Calcium silicate hydrate (C–S–H), the active component of cement, is a disordered nano-scale material comprised of layers of calcium and oxygen, with SiO_2 tetrahedra attached and interspersed by water and further Ca ions (Figure 1.8). Due to the importance of C–S–H as the binder phase of Portland cement it has been widely studied over many decades. Notwithstanding extensive effort, the morphology, density and composition of C–S–H continue to be the subject of active debate in the literature [7, 8, 9, 10]. The primary reason is the diversity of compositions and morphologies and that C–S–H structure may evolve over long periods of time. Secondly, until very recently, there has not been an experimental method available that is able to adequately characterise as-prepared C–S–H without removing the water: a procedure that damages the very nano-scale structures that are of interest.

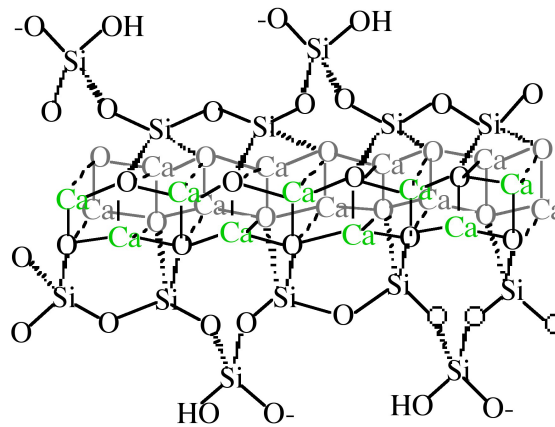


Figure 1.8 – Schematic representation of Tobermorite, taken as a C–S–H analogue. Image taken from [11].

There are various models in the literature which intend to describe the structure of C–S–H gels. The first, already mentioned in this chapter, was proposed by Powers and Brownnyard in 1948 [4]. C–S–H consists of several straight layers making colloidal size particles and assumed to incorporate a large amount of water. PB refer to *gel pores* when speaking about the water of the C–S–H. PB only see water in interlayers within C–S–H. Adsorbed water is reported on the outside surface of C–S–H hydrates facing capillary pores.

The second model for the C–S–H pore structure came from Feldman and Sereda (FS) in 1970 [12]. This model was based on sorption isotherms and the evolution of mechanical properties (mainly Young's modulus) during isotherm experiments. As for Powers and Brownnyard, Feldman and Sereda also represent thin solid sheets based on the tobermorite structure. However, FS do not have an ordered layered structure. The model shows irregular array of single layers which may come together and form interlayer spaces (Figure 1.9b). Further irregularities of C–S–H layers create larger pores of a wide range of size which, but not quoted so, are extensions of the capillary pores. It was the first attempt to describe another cavity than the interlayer

porosity within the C–S–H. Physically adsorbed water is reported on the outside surface of the C–S–H layer facing capillary pores.

Wittmann [13] in 1978 conceived C–S–H as solid tiles with water in between (Figure 1.9c). As for Feldman and Sereda, there is the appearance of a bigger nanometric space in the structure. However, this bigger space is a result of packing more than structure irregularities as in FS’s model.

Jennings in 2008 [7] proposed the nucleation of colloidal particles of C–S–H within the pore solution leading to a morphology arising from coalesced or flocculated particles (colloidal model). Based on small angle neutron scattering experiments, Jennings’s model assimilates the elementary blocks of C–S–H to globules. The size of a globule is 4.2 nm across. As globules contain experimentally water, they are still considered as being internally a tobermorite-like structure with disordered calcium silicate layers with water between. The layers are reported to entrap very small gel pores, called **intraglobular pores** (IGP), which are mainly present inside globules. At this level, the model has some similarities to FS’s model. However, Jennings stated that the C–S–H matrix is made of packed globules generating new interlayers but also **small gel pores** (SGP, Figure 1.9d). On the upper scale, globules flocculates pack and form **larger gel pores** (LGP). SGP measure between 1 nm and 3 nm wide while LGP measure between 3 nm and 12 nm. The LGP tend to disappear with time, and so in that sense they are not part of the C–S–H being formed.

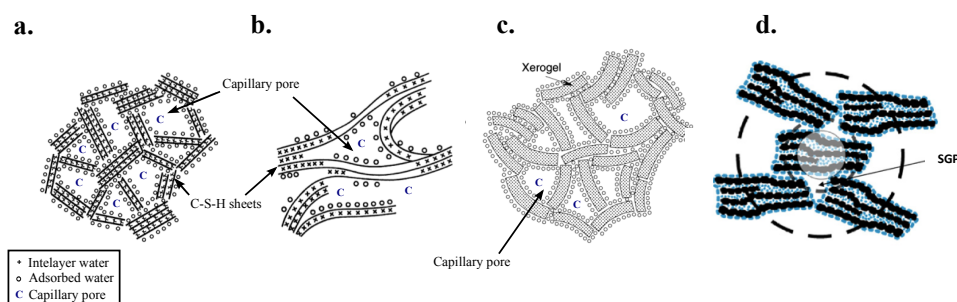


Figure 1.9 – The different vision of the porosity of C–S–H. (a) from Powers and Brownyard 1948 [4]; (b) from Feldman and Sereda 1970 [12], (c) from Wittmann 1978 [13] and (d) from Jennings 2008 [7].

The common feature in all these models is the presence of structural layers with interlayer spaces (often mentioned as interlayer water) and bigger spaces in between layer stacks. The combination of both is usually quoted in literature as C–S–H. The primary reason for the appearance of conceptually different models is the lack of experimental methods to probe the details of the C–S–H structure. Notwithstanding, the different models have many similarities even if they were made for different purposes.

In addition of the complexity of representing the structure of C–S–H, Scrivener *et al.* in 1989 [14] identified based on SEM micrograph two broad types of C–S–H in cement pastes, a more and a less dense phase. These are sometimes attributed to C–S–H that forms in spaces within

and between the confines of the original anhydrous cement particles referred to as inner and outer product respectively. Comparison between the development of the specific surface area measured by neutron scattering and the parallel development of the degree of hydration suggested strongly that two types of C–S–H are present in cement paste [15]. Following that, Jennings and co-workers [16, 17] developed a model to predict capillary porosity, porosity accessible to nitrogen, and specific surface area of hydrating cement pastes. One of the key elements of this model was the division of C–S–H into two types, a high- and a low-density C–S–H. Richardson [18] identified different morphologies of C–S–H by TEM: a fine-scale homogeneous morphology for the inner product and two distinct morphologies for outer product, a fibrillar-like structure and a foil-like structure that appear to correlate with the C/S ratio. The foil-like structure preferentially forms below a C/S ratio of about 1.5.

Growth mechanisms are likely to play a crucial role in the structure of C–S–H. Several authors have proposed mechanisms of C–S–H nucleation and growth but this point will not be further discussed in the thesis.

1.6 Different methods to characterise porosity

The characteristic values of porosity can be measured by different techniques, which have their own advantages, disadvantages, artefacts and degree of precision/accuracy. The widely used techniques are dynamic vapour sorption (DVS), mercury intrusion porosity (MIP), Scanning Electron Microscopy (SEM) and Nuclear Magnetic Resonance (NMR). Other techniques to measure porosity, not discussed in this thesis, are also available such as pycnometry experiments or small-angle neutron scattering. Figure 1.10 shows a summary of the range of sizes that the different techniques are able to cover. No technique is able to measure the entire network of pore sizes present in cement-based materials.

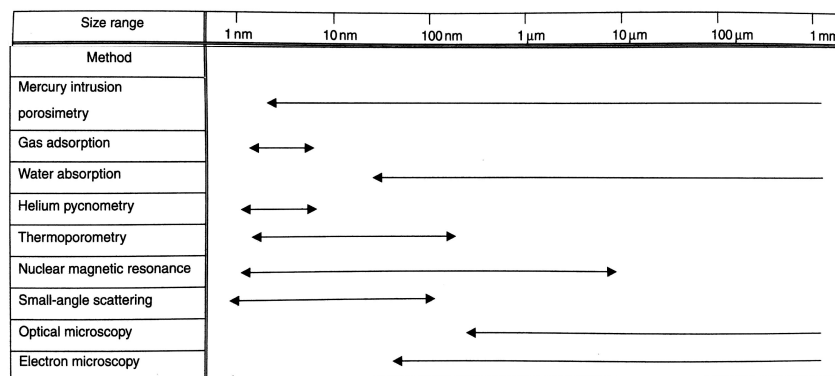


Figure 1.10 – Range of size probed by different techniques, from [19].

Many porosity measurement techniques study the behaviour of a penetrating into the pore network and therefore require a pre-drying. This drying step may damage the microstructure

and lead to an inaccurate picture of the porosity. In addition to the difficulties of measuring at once the whole pore size distribution of cement paste, interpretation of data and assignment to distinct pore categories has been difficult. Figure 1.11 is a summary of the categories reported by different authors. It can be seen that terms like micro, meso and macro pores appear. Sometimes the different categories are well separated from each other and sometimes the lower limit of C-S-H pores is not defined.

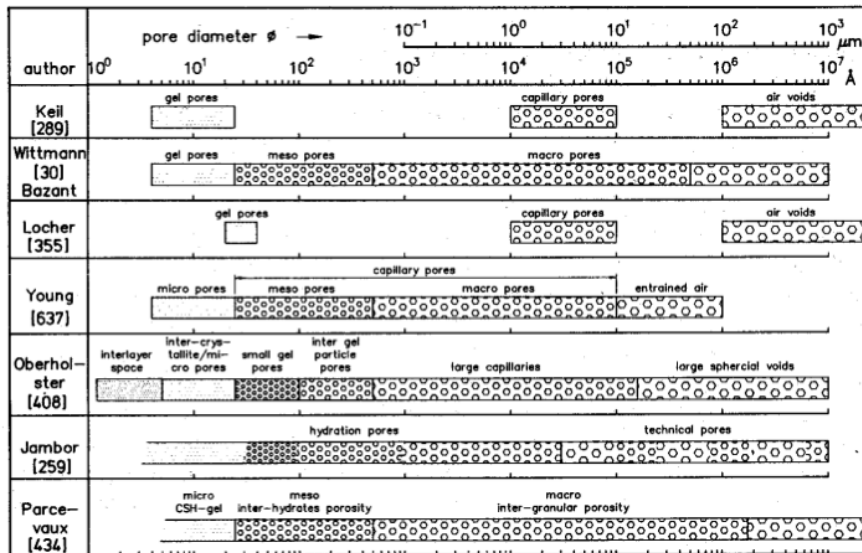


Figure 1.11 – Comparison of pore categories between different authors, from [20].

The goal of this section is to give a broad description of different techniques and the way they probe porosity.

1.6.1 Dynamic vapour sorption experiment

The sorption isotherm experiment has been the most popular technique for the study of pore structure. It is the technique with by far the most published results. A sorption isotherm is obtained by measuring the mass of a sample exposed to a gas and equilibrating at target relative pressures. The experiment is done at constant temperature, often 20 °C, and often uses water as the adsorbate. Cement-based materials are mainly probed as powders with relative pressure steps of 10% ranging from 0% to full saturation. A full water sorption isotherm usually takes weeks to be achieved as the equilibration of the sample to constant mass might be very long to reach with such a complex pore network. Nitrogen sorption can also be carried out for which the experiment is faster.

The shape of the isotherm depends on the microstructure under study *i.e.* mainly on the distribution of pore sizes. Data from sorption isotherms are usually presented as in Figure 1.12, plotting the water content of the sample as a function of relative humidity, or relative vapour

pressure in the case of nitrogen. The figure is taken from Yunping *et al.* [21] where they show results for samples with three water-to-cement ratios.

Numerous mechanisms play a role in the global absorption of vapour into cement pore structure including various diffusion processes and capillary liquefaction. Phenomena of adsorption can be interpreted with the “BET Theory” [22] which, from a few geometrical assumptions, relates relative gas pressures to adsorbed layers on surfaces and further in the absorption to pore sizes. This theory applies very well for low partial pressures (noted ϕ) when no capillary water is present. Above $\phi > 40-45\%$, the physics become more complex. Barret *et al.* [23] proposed the “BJH” model which is based on the assumption that there are two types of liquid existing simultaneously in pores due to different binding mechanisms: adsorption on surfaces and capillary liquefaction on the top. Equally, Nielsen [24] proposed the “BET-modified” equation. Using these models, it is possible to calculate from sorption isotherm data:

- the SSA of the C–S–H
- the total accessible pore volume
- and the pore size distribution of the materials.

The fit parameters of the existing models are however very sensitive at high relative pressures and the calculated pore size tends toward infinity when ϕ goes to 100%. The study of micrometre size pores by sorption experiments then becomes impracticable. Notwithstanding, Powers in 1948 based all his widely accepted work [4] on sorption isotherm data. He calculated precisely water characteristic of C–S–H at $3 \times V_m$, where V_m is the amount of water required to cover all solid surfaces by a monolayer thickness of molecule. More discussion about Powers’ model can be found in the section 1.5.3, p. 7. When several cycles are carried out, a so-called hysteresis appears showing that the absorption path is different than the desorption path over the range of capillary liquefaction ($\phi > 40-45\%$). This leads to another degree of uncertainty when calculating the micro-pore distribution of cement-based materials [25].

Water vapour is widely used as the adsorbate in case of cement but researchers have also used other gases, for which the calculated pore volumes and SSA are often lower than in case of water (Table 1.1). The substantial difference between water and nitrogen SSA vapour isotherms has evoked a lot of debate in the research community. Molecules sizes and their affinity with cement material are mentioned and indicate that water molecules can enter extremely fine zones where nitrogen cannot. A good experimental support to this theory was done on 11% relative humidity stabilized samples by Feldman and Chang-Yi [26]. They showed that different adsorbate molecules give the same pycnometry results when the C–S–H interlayer remains filled. The volume measured is called “free water porosity” and does not include a significant fraction of the C–S–H pores. Litvan [27] said that differences between water and nitrogen SSA results are not especially a molecule deficiency or ability but also a

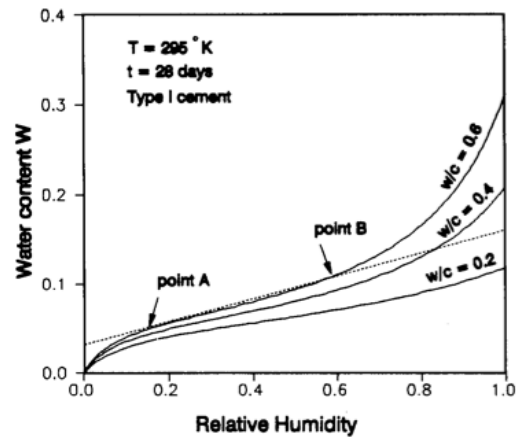


Figure 1.12 – Example of sorption isotherm data, from [21]. Information about the mixes are in the figure.

consequence of poor drying. Depending on preparation, nitrogen surface areas of the same paste were found in the range from $69.6 \text{ m}^2/\text{g}$ to $249.4 \text{ m}^2/\text{g}$.

Table 1.1 – Molecule size and associated BET SSA values of a mature OPC paste with $w/c = 0.40$ exposed to different gasses from [28].

Sorptive Gas	Cross-sectional area nm^2	Surface Area m^2/g of dry paste
H_2O	0.114	202.6
N_2	0.162	79.4
CH_3OH	0.181	62.5
$\text{C}_3\text{H}_7\text{OH}$	0.277	45.0
C_6H_{12}	0.390	44.5

1.6.2 Mercury Intrusion Porosimetry

The MIP test is the second most widely used technique to characterize the pore structure of a cement-based material due to its ready availability and relative speed of measurement [29]. The principle is to force non-wetting mercury into pores at increasing pressures. The intruded volume is recorded at each step of pressure and, by mean of the Washburn equation (Equation 1.1), the intruded volume versus pressure P is converted to pore volume versus pore entry diameter (d). In the Washbrun equation are assumed:

- the surface tension of the mercury (γ)
- a constant contact angle (θ) between the mercury and the solid surface
- and cylindrical pores

$$d = \frac{-4\gamma \cos(\theta)}{P} \quad (1.1)$$

Specific surface area, pore entry size distribution and total pore volume can be obtained for MIP data. The results are presented in cumulative volume or derivative volume as a function of pore radius. Despite its extensive use, the interpretation of the MIP results is controversial. Amongst the criticisms is the fact that MIP does not measure the pore size itself but pore entry size. In consequence, the possible “ink-bottle” effects lead to an overestimation of small pores and an underestimation of big pores [30]. If the only path towards a big pore is a smaller one, the volume of the big cavity will be evaluated at the small pore intrusion pressure, thus resulting in the inaccurate measurement. As an indicator of this phenomenon, a threshold is noticed during the intrusion process. Winslow and Diamond [31] interpret this threshold pore size as the minimum radius that is geometrically continuous throughout the whole hydrated cement paste. This threshold pore diameter is considered by some authors as the only valuable information from MIP measurements. Recently, Zhou *et al.* [32] claimed suppressing the “ink-bottle” effect by cycling the mercury pressurization–depressurization. They found larger pores than those measured by standard MIP. Despite all the aforementioned drawbacks, the MIP method is able to probe volumes of a wide range of sizes ranging from 2 nm up to μm cavities. The measurement is quick (circa 2 hours) and is relatively robust when multiple repetitions are done.

1.6.3 Scanning Electron Microscopy

SEM imaging has been widely used for more than 30 years to study the microstructure of cementitious materials [14]. A backscattered electron (BSE) image of a flat and polished section exhibits the different phases that compose a hydrated cement paste. The sample is bombarded with an electron beam and BSE are detected, giving information about the atomic weight of the elements. In that sense, BSE SEM imaging relates the chemical contrast of volumes being probed. The porosity, filled with epoxy resin, appears in black due to its very low atomic mass. A typical image of a mature cement paste is presented in Figure 1.13a.

The SEM technique is a powerful tool to observe cement microstructure. Portlandite, C–S–H and anhydrous phases can be distinguished. It allows direct observation of pores and in that sense, gives a visual idea about pore distribution. However, magnification limits of standard SEM are usually not sufficient to quantify pores smaller than 100 nm (Figure 1.14). One of the critical aspects of this technique is the sample preparation. The sample is first dried and then embedded in epoxy resin for later polishing. The polishing force may alter the microstructure and generates cracks. Another issue associated with porosity measured by SEM is the determination of the grey level limit between pores and hydration products. Different methods exist to determine the upper limit of pores on the greyscale histogram of cementitious materials. The first one can be seen on Figure 1.13b and was proposed by

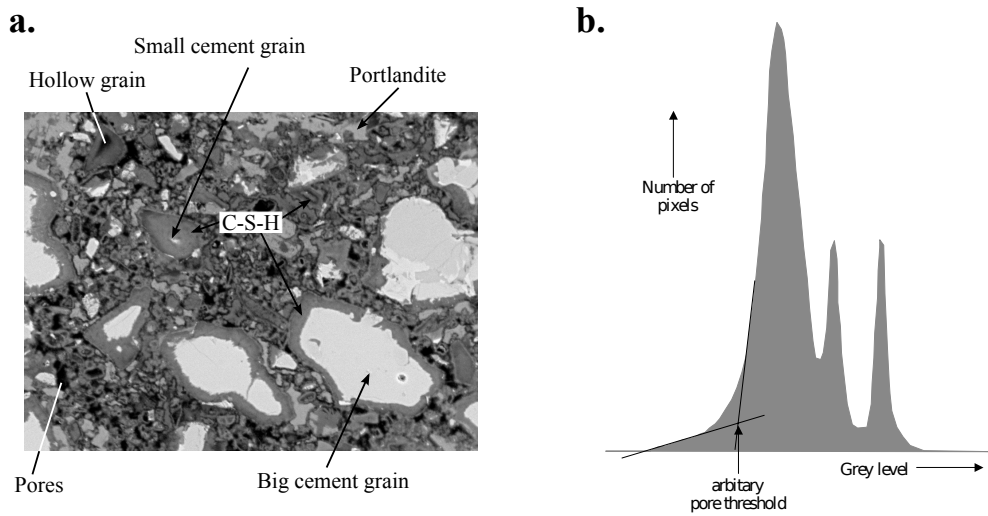


Figure 1.13 – (a) SEM BSE micrograph of an OPC paste at 7 days of hydration. (b) Grey level histogram of backscattered images. Example of pore threshold segmentation taken from [2].

Scrivener [2] in 2004. The threshold is determined by the intersection of tangents drawn on the pore region and the C-S-H peak. The second method called the “overflow” method was proposed by Wong *et al.* [33] in 2006. It follows the same principle but the tangents are drawn on the cumulative greyscale histogram. Despite these studies, the separation between pores and the rest of the cementitious matrix during image analysis is not obvious.

Image analysis and pore volume estimation supposes that surface features are representative of the 3D volume. Also, a significant number of images needs to be taken and analysed to be representative, typically 20×20 images at 2400X magnification which correspond to 10 mm^2 .

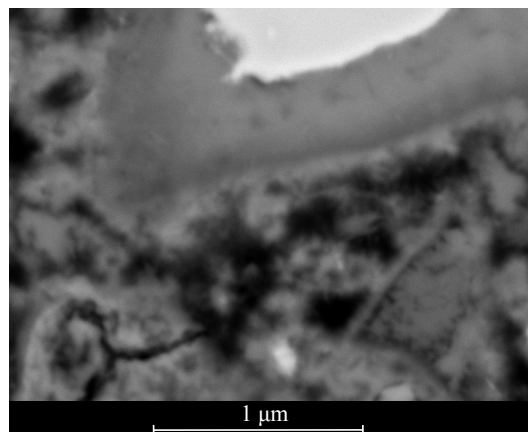


Figure 1.14 – SEM BSE micrograph of an OPC paste at $10,000 \times$ magnification.

1.6.4 Nuclear Magnetic Resonance

For more than 20 years, NMR has been used in cement field to quantify porosity without water removal. In principle, NMR has no limitation in pore size determination but this technique remains difficult for cement-based material. Intrinsically, these materials are complex inhomogeneous systems leading to a rapid dephasing of nuclear spins and rapid signal decay. Iron oxides accentuate this phenomenon by interfering with the applied magnetic field. Therefore, NMR signal from cement samples becomes much weaker as compared to other materials and the critical point of this technique remains the signal analysis. However, NMR avoids the impact of drying and in that respect has a huge potential for future research on cement pore networks. As the NMR technique is the main focus of this thesis, a whole chapter is devoted to the method and I refer the reader to it for further details.

1.7 The impact of drying on porosity results

The influence of environmental conditions during cement paste hydration is very important. Specimens are usually cured either under water or in water vapour saturated air. These controlled environments preserve samples from drying and many procedures were developed to remove it out of the microstructure prior to testing. All drying techniques have their individual advantages and disadvantages depending on application. They are broadly ranked from more damaging for the microstructure to less damaging:

The first category involves direct water evaporation. It entails oven drying or the use of dry vacuum and it is considered as the most damaging treatment for the microstructure. The temperatures used for oven drying range from 40 °C to 110 °C and the higher the temperature the higher the damage. When liquid water progressively goes out of the pores, menisci form generating capillary stresses and drying shrinkage. The morphologies of phases are subject to change. Oven drying may induce cracking of the sample and it can remove a part of the *non-evaporable* water linked to ettringite (from 60 °C), gypsum (from 80 °C) and C-S-H gel (which partially dehydrates below 105 °C). However, oven drying methods are still widely used by researchers because they are rather quick.

Freeze-drying is another method employed to remove water from a porous sample. The sample is quenched in liquid nitrogen and then the ice being formed is sublimated with the help of low relative pressures. In that sense, it avoids the liquid water state so there are no capillary meniscus stresses. However, the temperatures generally used are not low enough to freeze the water in the smallest pores and the first formed ice crystals may drain water from surrounding pores causing damage. In parallel, the high vacuum period must be continued for long period in order to take out most of the water and it can dehydrate phases like AFm (monosulfoaluminate) and AFt (ettringite). Freeze drying is preferentially used for early age pastes and considered less damaging than oven drying.

The last category concerns solvent exchange methods. Samples are immersed in large amount

of solvent so water in pores gets progressively replaced. A common time for replacement is 7 days. After the immersion, the low surface tension of most solvents allows pores to be evacuated without major capillary stresses, preserving the fine structure of C–S–H hydrates. Despite this, water removal is never considered to occur without impact but among the others, solvent exchange is one of the least damaging drying methods.

Drying has been investigated and discussed widely in literature. Gallé [34] compared 4 drying methods measuring the weight loss over 7 days of treatment (Figure 1.15). He points out differences concerning the total porosity and the threshold pore access diameter seen by MIP (0.03 μm for the freeze drying method against 0.17 μm for the oven drying at 105 °C). The oven drying mass loss at 105°C is probably overestimated by the evaporation of chemically bound water. Gallé makes the assumption that for freeze and vacuum drying, residual water remains in the smallest porosity. Moukwa and Aictin [35] confirmed this hypothesis and highlighted residual water for sublimated pastes particularly for dense and low permeable materials. In parallel, Moukwa and Aictin show that MIP total pore volume is higher for oven dried samples compare to freeze dried samples, creating pores in the range of 0.02-0.1 μm .

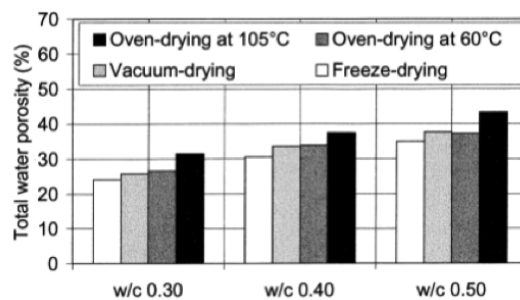


Figure 1.15 – Comparison between different drying methods, from [34].

Fonseca and Jennings [36] also compare different drying processes and their impact on C–S–H morphology using environmental SEM imaging on 3 days C_3S pastes. The slower the drying, the bumpier the aspect is and the lower the specific surface area becomes. Hunt *et al.* [37] also reported that a rapidly dried paste has a larger nitrogen surface area than a slowly dried one.

2 ^1H NMR technique

Contents

2.1 Introduction to NMR	20
2.1.1 Basics of NMR and relaxation phenomena	20
2.1.2 Different methods of pulse sequences	24
2.1.3 Calculation of pore size	28
2.2 NMR Literature in the context of cement	30
2.2.1 Simple relaxation experiments	30
2.2.2 Exchange experiments	32
2.2.3 NMR cryoporometry	33

One of the easiest molecules to probe in NMR experiments is water because it has two hydrogen atoms. Liquid water is present in many materials and often in complex pore structures. For the past 40 years, ^1H nuclear magnetic resonance (NMR) has been used to quantify the porosity of cement samples without water removal. In principle, NMR experiments provide a greater level of detail concerning the state of water in the microstructure than other techniques as it can probe water in pores of any size. NMR avoids the impact of drying and in that respect has a huge potential for better understanding of the cement pore network.

This chapter goes through the basic principles of ^1H NMR relaxation phenomena and describes the way to measure them experimentally. It focuses on ^1H NMR specifically applied to cement, from a state of the art to the methodology used in the thesis.

2.1 Introduction to NMR

2.1.1 Basics of NMR and relaxation phenomena

Many atomic nuclei possess angular momentum or “spin” and NMR is a quantum mechanical phenomenon of nuclear spin. However, a classic picture in terms of nuclear magnetic moments is sufficient for this work.

General relaxation phenomena in NMR experiments occur because an excess energy and phase coherence is given to the nuclei by a preceding excitation pulse(s). The term “relaxation” includes the release of this energy and (in the long term), the return of spins to thermal equilibrium.

A spin $\frac{1}{2}$ nucleus such as ^1H can exist in one of two states commonly called spin “up” and spin “down” which are randomly oriented in the matter. When exposed to a static magnetic field (noted \mathbf{B}_0), there are slightly more spins “up” aligned with the field following a Boltzmann distribution. This gives rise to a bulk nuclear magnetisation along \mathbf{B}_0 resulting in a vector sum \mathbf{M} of all nuclei (spin isochromats; shown as $\mathbf{M}_{z'}$ in the lab frame in Figure 2.1a). If the nuclear spins are disturbed from this alignment, they precess about \mathbf{B}_0 at what is called the Larmor frequency ω_L with

$$\omega_L = \gamma B_0 \quad (2.1)$$

where γ is the gyromagnetic ratio of the nuclei, $\approx 2\pi \times 42.57 \text{ MHz/T}$ for ^1H .

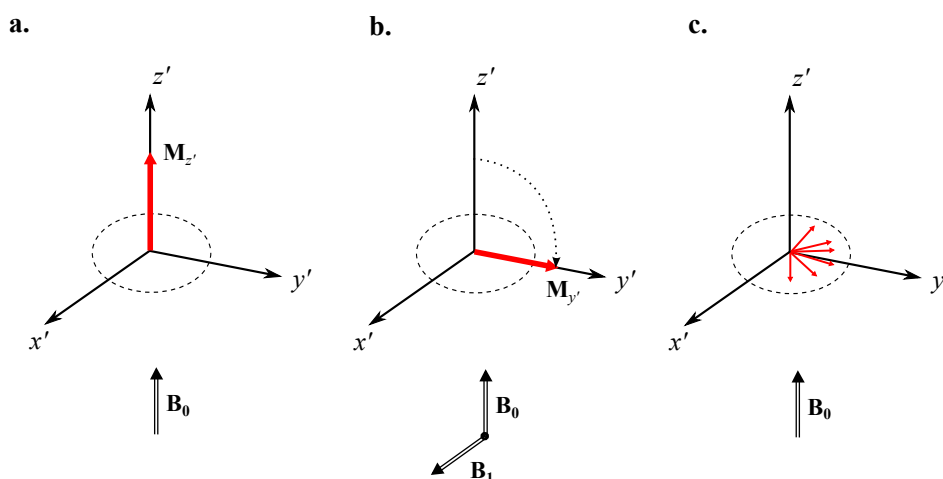


Figure 2.1 – In the rotating frame (a) spins exposed to a static magnetic field \mathbf{B}_0 ; (b) exposed to a P_{90} radio frequency field \mathbf{B}_1 and (c) slightly after the end of the \mathbf{B}_1 pulse.

In a rotating frame rotating about \mathbf{B}_0 at the same frequency, \mathbf{B}_0 is transformed away and only small inhomogeneities of field $\Delta\mathbf{B}_0$ remain. When an oscillating electromagnetic field (\mathbf{B}_1) is applied at the Larmor frequency perpendicularly to the existing static field \mathbf{B}_0 , a coherent precession of the nuclei is observed. This phenomenon is equivalent to a field of magnetisation as $|B_1| \ll |B_0|$ and $|B_1| \gg |\Delta B_0|$. If \mathbf{B}_1 is applied as a 90° radio frequency pulse ($\pi/2$, also noted P_{90} along the x' axis of the rotating frame), the rotation ends up being along the y' -axis. As a result, \mathbf{M} has been flipped from the z' -direction to the y' -direction (Figure 2.1b). At this moment in time, the nuclear spins are aligned with each other in the x' - y' plane and the equilibrium Boltzmann distribution is disturbed.

At the end of the P_{90} pulse, the spins start to precess in the x' - y' plane around \mathbf{B}_0 at slightly different rates due to $\Delta\mathbf{B}_0$ and dephase from the y' direction (Figure 2.1c). The speed and the direction of the dephasing vary as a function of local magnetic disturbances. Two main phenomena contribute to the dephasing. The first one concerns the magnet quality which may create small \mathbf{B}_0 inhomogeneities at the micrometric scale ($\Delta\mathbf{B}_0^{\text{magnet}}$). The spins dephase due to this mechanism in a time $T_2^{\text{inhom.}}$. The second mechanism is the magnetic influence of the surrounding nuclei ($\Delta\mathbf{B}_0^{\text{other nuclei}}$) *i.e.* the true sample T_2 , which is then related to the total loss of coherence, T_2^* , as in Equation 2.2. The true sample T_2 depends on both the distance r and the angle θ between the nuclei (Figure 2.2).

$$\frac{1}{T_2^*} = \frac{1}{T_2^{\text{true}}} + \frac{1}{T_2^{\text{inhom.}}} \quad (2.2)$$

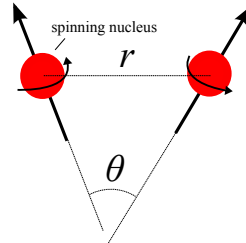


Figure 2.2 – Nuclear spins illustrating the dipole-dipole interaction.

T_2 , known as transverse or spin-spin relaxation time, hence represents the **loss of magnetization in the x' - y' plane** due to dipole-dipole interactions between nuclei. It is a direct interaction of the magnetic fluctuations between spins without energy transfer to the lattice. Although the observed signal is lost in time $\sim T_2$ due to loss of coherence, the spins still remain in the x' - y' plane. A new experiment cannot be conducted until they realign with the z' -direction, a process that takes a few T_1 to complete fully. Hence, a recovery time must be left between the start of repeat experiments.

T_1 , known as longitudinal or spin-lattice relaxation time, is another type of relaxation time which is measured with specific pulse sequences such as the inverse recovery (section 2.1.2, p. 26) or the saturation recovery. The mechanisms leading to T_1 are different from those for T_2 even though both represent the rate of nuclear relaxation of the spins. T_1 represents the time required to **recover** the initial Boltzmann distribution of the **longitudinal magnetization \mathbf{B}_0** (Figure 2.3).

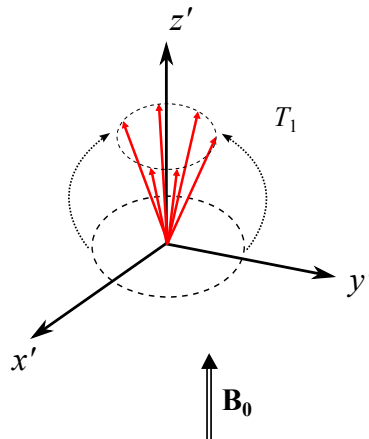


Figure 2.3 – T_1 recovery of the spins.

The main event contributing to relaxation (both T_1 and T_2) for liquids in porous media is the interactions of molecules at the liquid-solid interface. This process happens by energy exchange with the surrounding lattice (neighbouring molecules) by translations, rotations and internal motions. In cements, the primary ^1H relaxation mechanism is interaction of ^1H spins with surface Fe^{3+} paramagnetic impurity. Korb and co-workers [38, 39] have shown how the relaxivity may be calculated given the surface density of paramagnetic Fe^{3+} impurities. Korb *et al.* [38] developed a theoretical explanation of this spin-lattice relaxation by considering the interaction of water molecules walking on pore surfaces containing low concentration of paramagnetic ions. They proposed a surface residence time τ_s and a surface hopping time τ_m and found the spin-lattice relaxation time to be strongly dependent on the frequency of the NMR spectrometer used.

Even if T_1 and T_2 are both representative of the relaxation characteristics of the samples probed, they are obtained by different pulse sequences and involve different atomistic processes. While T_1 is a magnetization gain in the z' -direction and depends on high frequency motions, T_2 is a loss of coherence in the x' - y' plane and depends on low frequency motions. T_1 recovery is always slower (or equal in the case of bulk water) than T_2 . McDonald *et al.* [40] reported that $T_1 = 4 \times T_2$ at 20 MHz NMR frequency for water in hydrated cement samples. The Figure 2.4 illustrates schematically this difference.

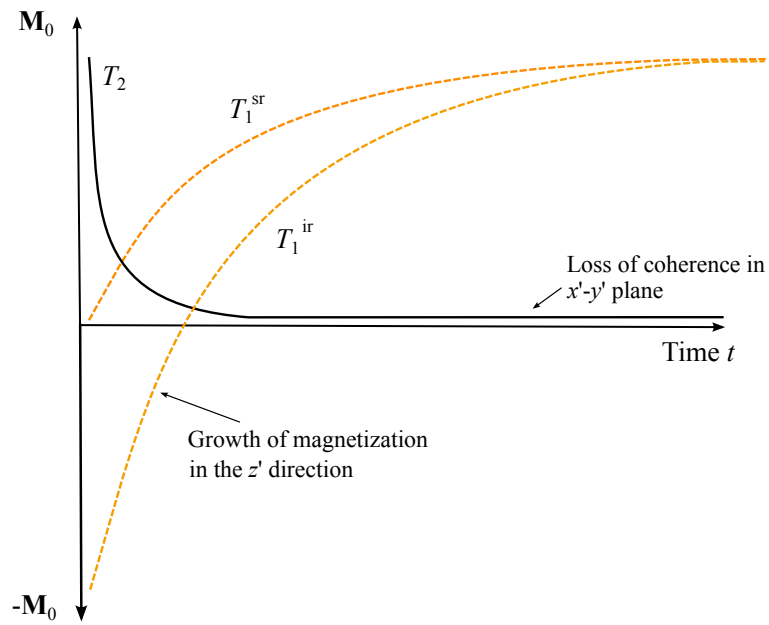


Figure 2.4 – Schematic rates of relaxation T_1 and T_2 in cement paste.

2.1.2 Different methods of pulse sequences

Free induction decay

The simplest experiment to carry out with an NMR magnet is a single 90° pulse aligned along the x' -axis of the rotating frame (Figure 2.1b). In the environmental magnetic field \mathbf{B}_0 , hydrogen nuclear spins are hence rotated to the y' -axis which initiates the free precession of the spins on the x' - y' plane (Figure 2.1c). A signal is detected (called free induction decay or FID) which decreases exponentially (Figure 2.5) as spins progressively dephase and eventually relax. This signal decay is known as the spin-spin relaxation time T_2^* .

As the coil that generates the pulses also records the signal, an intrinsic dead time is observed in all NMR spectrometers. This dead time varies from magnet to magnet and is usually of the order of a few μs .

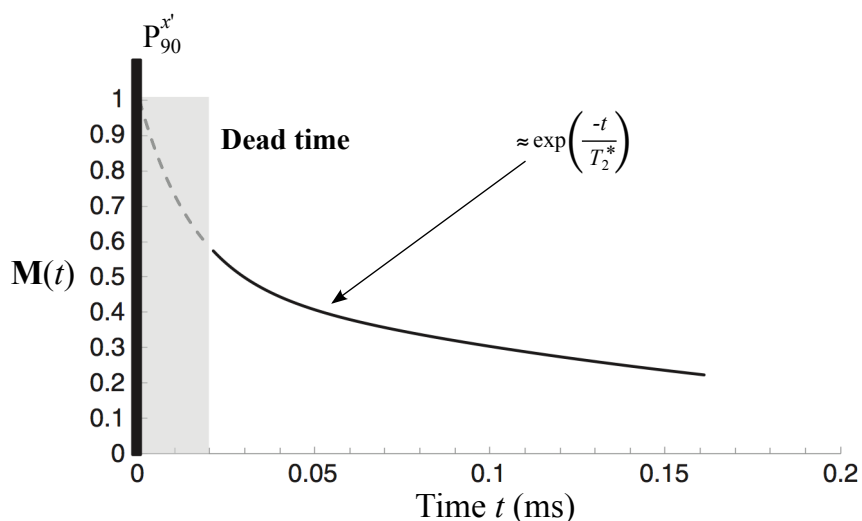


Figure 2.5 – Free induction decays, adapted from [41].

T_2 and the Carr-Purcell-Meiboom-Gill (CPMG) pulse sequence

The CPMG pulse sequence was first proposed by Carr and Purcell in 1954 [42] and modified by Meiboom and Gill in 1958 [43]. This pulse sequence is composed of $P_{90}^{x'} \tau P_{180}^{y'} 2\tau P_{180}^{y'} 2\tau P_{180}^{y'} 2\tau$, etc (Figure 2.6). It has the advantage to overcome the magnetic field inhomogeneities on the dephasing of spins due to magnetic field inhomogeneities ($\Delta B_0^{\text{magnet}}$) and directly measures the true sample T_2 (caused by $\Delta B_0^{\text{other nuclei}}$). The influence of $\Delta B_0^{\text{magnet}}$ and $\Delta B_0^{\text{other nuclei}}$ are separated out by the use of 180° pulses as in Figure 2.6. This causes that spins reverse their instantaneous phase angles and start to precess back into phase. Since the magnet inhomogeneities $\Delta B_0^{\text{magnet}}$ are coherent, the inversion of the precession cancel these variations out when the spins rephase. The best in-phase states are achieved at time 2τ from the start of the pulse sequence and hereafter every 2τ (so-called echoes). The signal envelope of these different echoes is the T_2 spin-spin relaxation decay due to interactions between magnetized protons. For bulk liquid water made of one relaxing component, this decay decreases exponentially according to $\exp(-t/T_2)$ where t is the experimental time and T_2 the characteristic relaxation time of the probed bulk water volume.

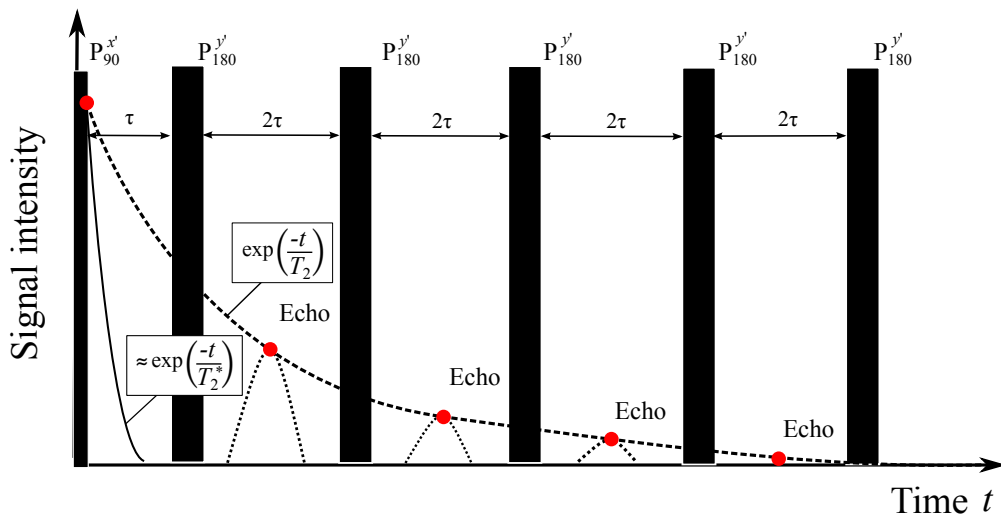


Figure 2.6 – Carr-Purcell-Meiboom-Gill (CPMG) pulse sequence.

T_1 : the inverse recovery (IR) and the saturation recovery (SR) pulse sequences

The IR pulse sequence (Figure 2.7) involves different relaxation mechanisms as described p. 22. It consists of a $P_{180}^{x'}$ and a $P_{90}^{x'}$ separated by a time interval τ . The first $P_{180}^{x'}$ inverts the initial magnetization through to the “ $-z'$ ” direction, resulting in a vector $-\mathbf{M}_{z'}$. After the $P_{180}^{x'}$, the spins progressively relax due to interaction with the lattice and recover toward the low energy state $\mathbf{M}_{z'}$ in equilibrium with \mathbf{B}_0 . A $P_{90}^{x'}$ pulse is used to flip the spins that have already relaxed toward the y' -direction, and hence to measure the spin recovery in the time interval τ . The relaxation rate $1/T_1$ is then obtained by varying the time interval τ over a suitable range to capture the regain of $\mathbf{M}_{z'}$ magnetization.

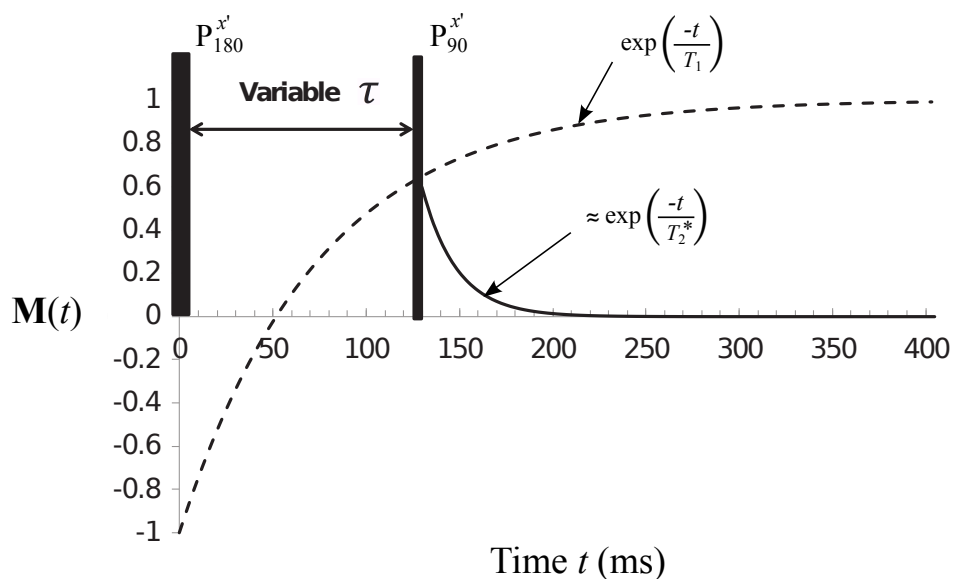


Figure 2.7 – Inverse Recovery pulse sequence, adapted from [44].

The saturation recovery pulse sequence is another way to measure T_1 . It destroys any coherence between the nuclei and saturates the bulk magnetisation to zero before it progressively recovers towards the equilibrium. SR is similar to the IR expect that it starts with a P_{90} so that the magnetization recovers from the x' - y' plane ($\mathbf{M}_{z'} = 0$) rather than along z' ($\mathbf{M}_{z'} = -\mathbf{M}_0$).

Solid signal and the Quadrature-echo (Quad-echo or QE) pulse sequence

The QE pulse sequence [45] is another experiment that can be carried out by NMR (Figure 2.8). QE allows very fast relaxing components such as hydrogen atoms strongly bound to other atoms in solids (noted solid-spins) to be measured and quantified. Such ^1H protons usually have a relaxation time of the order of a few μs and decay mainly within dead time of standard spectrometers. The QE pulse sequence is composed of two P_{90} phase shift separated by a short time τ , so $P_{90}^{x'} \tau P_{90}^{y'}$. While hydrogen atoms in liquid water are not sensitive to the second P_{90} (because it is aligned with the magnetisation), fast relaxing protons with static dipolar interactions become refocused showing a Gaussian type of echo shape. It hence allows the signal of solid-spins to partially recover [45]. To achieve such an experiment, τ must be comparable to the relaxation time of the spins of interest.

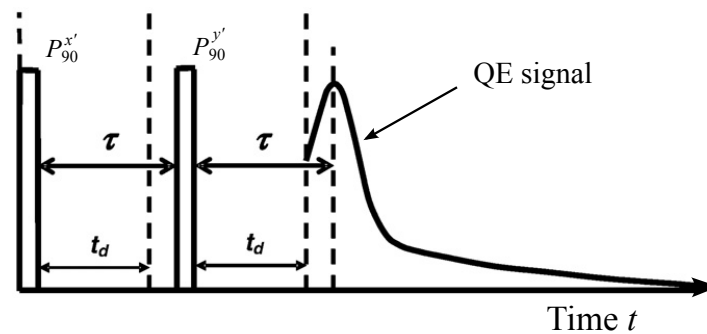


Figure 2.8 – Quad-echo pulse sequence, adapted from [44].

2.1.3 Calculation of pore size

Researchers have studied the relationship between relaxation rates obtained by NMR and pore sizes. Two main models exist known as the fast exchange model and the amplitude model.

Fast exchange model

Brownstein and Tarr [46], and Cohen and Mendelson [47] related longitudinal (spin-lattice) and transverse (spin-spin) relaxation times T_1 and T_2 to the surface-to-volume ratio of pores. This fast exchange model (sometimes called fast diffusion model) supposes the existence of two distinct magnetic species within a pore: a surface layer of water with a fast relaxation rate and a bulk water volume with a much slower relaxation rate [48]. Water molecules are considered in fast exchange between surface and bulk regions on the timescale of the experiment. The global rate of relaxation which is experimentally observed T_2 (or T_1) is, according to the fast exchange model, a weighted average between the fast surface rate of relatively few nuclei and the slow bulk rate of the majority as

$$\frac{1}{T_2} = \frac{1}{T_2^{\text{surf}}} + \frac{1}{T_2^{\text{bulk}}} \quad (2.3)$$

which associate the volume fraction of pore fluid with surface properties to that of pore fluid with bulk properties. T_2^{bulk} of pure bulk water is of the order of 3 s while the relaxation time of surface water T_2^{surf} is usually between 1-10 μs . Hence, the rate of relaxation of bulk fluid becomes negligible compared to the rate of relaxation of surface fluid. If T_2 is the relaxation rate attributed to the pore, the last term of Equation 2.3 can be neglected. The volume fraction of surface water, f_s , can be expressed as in Equation 2.4,

$$\frac{1}{T_2} \approx \frac{S\varepsilon}{V} \times \frac{1}{T_2^{\text{surf}}} \approx \frac{S}{V} \times \lambda \quad \text{with} \quad \lambda = \frac{\varepsilon}{T_2^{\text{surf}}} \quad \Rightarrow \quad T_2 \approx \frac{d}{2} \times \lambda^{-1} \quad (2.4)$$

where S is the surface of the pore, V its volume and ε represents the nuclear dipole-dipole interaction range. For planar pores of area A and ignoring edge effects, $S = 2 \times A$ and $V = A \times d$, where d is the pore width or "size". Hence $V/S = d/2$. The observed relaxation time T_2 is related to d through the parameter λ , which is known as the surface relaxivity parameter. This parameter is assumed constant through the sample as a consequence of the supposed homogeneity of surface properties. ε is expected to be of one intermolecular distance (0.28 nm in the case of the water molecule). The characteristic relaxation T_2^{surf} of surface water layer depends on many parameters such as critically Fe_3^+ surface density, temperature, pore fluid composition and magnetic field strength. T_2^{surf} can be obtained either experimentally by drying the sample out to a monolayer coverage or theoretically by *ab initio* calculations.

In 1990, the fast exchange model was carefully confirmed by D'Orazio *et al.* [49] in unsaturated porous silica glass. It was applied to cement for the first time by Halperin *et al.* [50] in 1994.

Amplitude model

The second model for pore size calculation uses the signal amplitudes during progressive drying of the sample [44]. This amplitude model is based on the fact that the signal intensity is proportional to the mass of water. When a pore is full of water, surface layers are in rapid exchange with the bulk pore fluid and all ^1H appear as one liquid component with a single relaxation time (Figure 2.9). During the progressive drying of a pore, the bulk signal amplitude decreases more rapidly than the total signal whilst a short relaxation component arises from water left immobile on surfaces, both with constant and well defined T_1 and T_2 . The gradient of both amplitudes as a function of water content allows surface-to-volume ratio of the pore to be evaluated and hence pore size/thickness to be found. The main advantage of this method is that it does not require a calibration factor as for the fast exchange model.

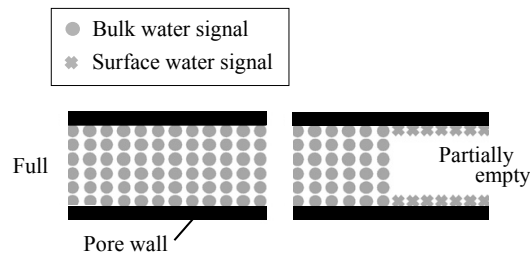


Figure 2.9 – Amplitude model, adapted from [44].

2.2 NMR Literature in the context of cement

A recent review was published by Valori *et al.* on NMR applied to cement [41]. However, a more detailed literature section is needed for this work. The main contributions of NMR to cement microstructure are mentioned in a chronological order.

2.2.1 Simple relaxation experiments

There is long history of applying NMR to cement. Blinc *et al.* [51] first studied in 1978 the hydration of C_3S and commercial Portland cement mixed with distilled H_2O at a water-to-solid ratio of 0.42 by weight. They followed the evolution of T_1 and T_2 relaxation times of the main liquid volume from 10 minutes after mixing up to 28 days of hydration. They identified an induction period (≈ 3 hours) followed by a rapid decrease in characteristic T_1 and T_2 relaxation times. The T_1 and T_2 values then stabilized beyond 24 hours for both binders. They found $T_2 = 0.5$ ms at later ages for the C_3S paste.

The next significant study was done by Schreiner *et al.* [52] in 1985 using inversion recovery, Carr-Purcell and FID pulse sequences on hydrating Portland cements. In addition of following the evolution of relaxation times during the hydration, they quantified for the first time different magnetization fractions: (1) H_2O in micropores at $T_1 = 5$ ms which slightly decreases in amount beyond 10 hours of hydration; (2) a solid gel component at around $T_1 = 1$ ms which at 10 hours already represents more than 50% of the 1H protons and which is described as structural water of C-S-H gel and (3) a solid magnetization component with a growing spin-spin relaxation time representing protons of solid OH groups such in $Ca(OH)_2$. This latter population increases in amount with hydration time.

Lasic and co-authors [53] identified in 1988 up to 5 different hydrogen components within solidifying cement pastes using T_1 decays. They distinguish 1H protons in CH, in aluminate crystalline phases, protons in adsorbed water, protons in C-S-H gel structure and protons in the vicinity of paramagnetic centres. This study showed the first evidences of growing C-S-H water by NMR.

Also in 1988, Miljkovic *et al.* [54] used FID to separate out the signal arising from tightly bound 1H protons (“solid-like” with characteristic constant $T_2 = 10 \mu s$) from “liquid-like” protons. The liquid-like T_2 decreased beyond 8 hours of hydration as already observed in [51]. Miljkovic *et al.* [54] showed that signal arising from solid-like protons grows at the expense of signal from liquid-like protons throughout the hydration process. They also point out a correlation between the liquid-like T_2 and the amount of water used in the mix proportions.

Halperin *et al.* [50] in 1994 presented for the first time an inversion of the CPMG decay into a pore volume distribution function with the help of the fast exchange model [46]. Pore sizes of cement-based materials were calculated for the first time. They reported two principal pore populations of mobile water which are interpreted as “open gel” pores and capillary pores

(Figure 2.10). The capillary water diminished in amount with hydration time in favour of the open gel water. The size of the capillary reservoir decreased down to 12 nm at 7 days of hydration while the size of the open gel pores stayed constant at around 2.5 nm. In addition, the specific surface area of never dried C–S–H was calculated for the first time. This value converged asymptotically to 225 m²/g of cement.

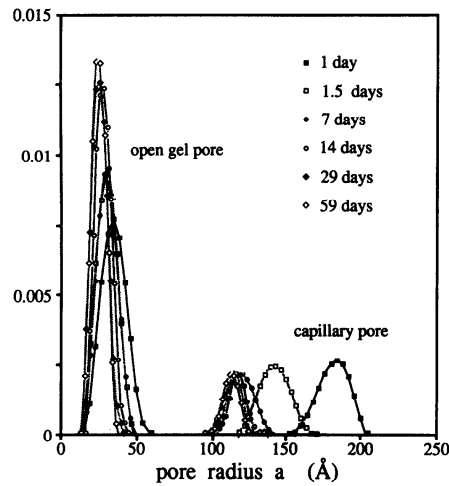


Figure 2.10 – First attempt to calculate the pore size distribution in cement pastes based on ¹H NMR, from [50].

Later in 2000, Greener *et al.* [55] monitored the spin-spin relaxation time T_2 during hydration of cement pastes. They used both FID and CPMG pulse sequences. The former was fit by the sum of one or two Gaussians and one exponential and the latter by a multi-exponential function. The Gaussian part of the signal with $T_2 = 18 \mu\text{s}$ was attributed to solid-like hydrogen being in CH platelets and ettringite. Solid protons are again monitored at constant T_2 as in [54]. Contrary to the study of Lasic *et al.* [53], no distinction was made between the different crystalline phases and the solid compound was taken as a whole signal. From the CPMG liquid signal, Greener *et al.* identified bulk water with the longest T_2 , C–S–H gel pore water with intermediate T_2 and C–S–H interlayer water signal (short T_2), which was only seen and resolved from the CPMG decay curve beyond 10 hours of hydration. This is the first time that two growing hydrogen populations within C–S–H gel were reported. In addition, they see for old pastes the appearance of a very long T_2 component which they attributed to the release of water due to the transformation of AFt into AFm. As in [51], the changes in T_2 initiate at around 3 hours of hydration which is consistent with conventional setting times. No quantification of water in the different environments was done.

Barberon *et al.* [56] set up a methodology and developed an associated model to calculate the specific surface area of reactive porous materials using the frequency dependence of T_1 . This experiment works only for very young pastes (< 12 hours of hydration) when the relaxation

rates are still long due to the need to rapidly switch the magnetic field on and off in T_1 time. They studied mortars mixed at $w/c = 0.38$ which were measured at intervals during the first 12 hours of hydration. By exploring the range of low frequency, they were able to separate out the surface component $1/T_{1\text{-surf}}$ from the bulk component $1/T_{1\text{-bulk}}$, allowing to probe the surface area of the material. They found a linear relationship between the calculated surface area and the degree of reaction of cement (α) and reported $100 \text{ m}^2/\text{g}$ for $\alpha = 0.14$ (~ 12 hours of hydration). This value is very similar to the one reported by Halperin *et al.* [50] based on the fast exchange model in discrete pores [46, 47].

Plassais and co-worker [57] in 2005 used NMR at high frequencies (100, 300 and 500 MHz) to study the hydration of synthesized C_3S . They confirm that ^1H at surfaces are in fast exchange with the pore bulk and give discrete pore sizes in a range 2-500 nm. They find fractal dimension of the arising hydration products at $D_f = 2.6$.

Even if common features are found between authors about the different relaxing components in cement pastes, no absolute consensus was achieved for a long time. There are numerous reasons and difficulties that arise from the intrinsic complexity of the method, the different types of machine used (frequency, pulse length, dead time) and the analysis of the data being the deconvolution of multi-exponential decay curves. The first assignment of relaxation components consistent with the current understanding was achieved by Holly *et al.* in 2007 [58]. They studied the influence of curing temperature from 2°C to 100°C on the hydration of white cement pastes mixed at $w/c = 0.42$. To study water kinetics, FID and CPMG were carried out. They found three components in the CPMG spin-spin T_2 decay: (1) capillary water being initially mixing water filling interstitial regions between cement grains ($T_2 \sim 1 \text{ ms}$ beyond 4 days of hydration); (2) C-S-H gel water with characteristic T_2 between 200 and 500 μs and (3) C-S-H interlayer water with $T_2 \sim 100 \mu\text{s}$. As in [55], they state that hydrogen protons in crystalline phases such as Portlandite and gypsum yield a characteristic Gaussian line shape with T_2 of 15–25 μs . The Gaussian shape intensity is quantified using the FID decay.

2.2.2 Exchange experiments

McDonald *et al.* [40] in 2005 combined two consecutive pulse sequences T_1 - T_2 in order to obtain a two-dimensional relaxation spectrum. The raw relaxation data were analysed using a 2-D inverse Laplace transform (ILT). White cement pastes mixed at $w/c = 0.40$ were measured at 1, 2, 7 and 14 days of hydration. Off-diagonal cross-peaks highlight chemical exchange of water between what were thought to be “gel pores” and “capillary pores” (Figure 2.11). The exchange of water decreases with hydration time and when 10% of silica fume was added in replacement of cement.

Monteilhet *et al.* [39] also studied water exchange in between pores by doing T_2 - T_2 correlation. The advantage over the T_1 - T_2 experiment [40] is the symmetry of the off-diagonal peaks on both sides of the central pattern (Figure 2.12). In contrast to T_2 - T_2 , T_1 - T_2 shows

one off-diagonal peak at long T_1 and short T_2 that can be confused with a solid signal while its symmetrical peak becomes negative and leads to inversion artefacts using the Venkataraman algorithm [59]. The assignment of pore exchange in T_2 - T_2 then becomes unambiguous. Monteilhet *et al.* identify an exchange of water between C-S-H interplanar spacing (calculated at circa 1.0 - 1.7 nm) and a bigger reservoir assigned to spaces between packets of C-S-H sheets comprising gel pores (7 to 30 nm). The exchange rate was found to be 5 ms^{-1} .

The T_2 - T_2 experiment was also performed on synthetic C-S-H by Valori *et al.* in 2010 [60]. The purpose of this study was to show that the C-S-H bimodal pore size distribution and the water exchange seen between them [40] does not arise from different paramagnetic concentrations *i.e.* from pores of different surface relaxivity. The synthetic C-S-H with no Fe^{3+} showed, as for C-S-H in white cement pastes, two populations of pores between which water exchanges. Relaxation times are shifted to higher values and sharper peaks are observed compared to cement pastes due to the absence of Fe_3^+ .

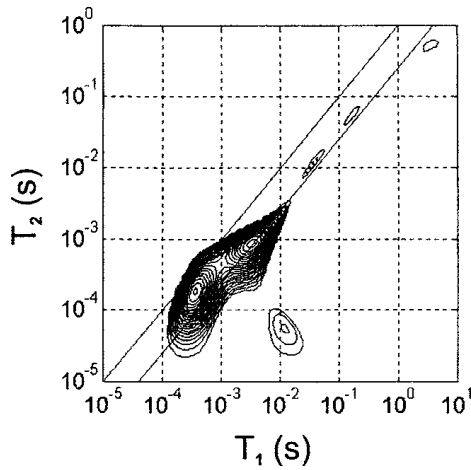


Figure 2.11 – T_1 - T_2 spectrum showing exchange between gel pores and capillary pores, from [40].

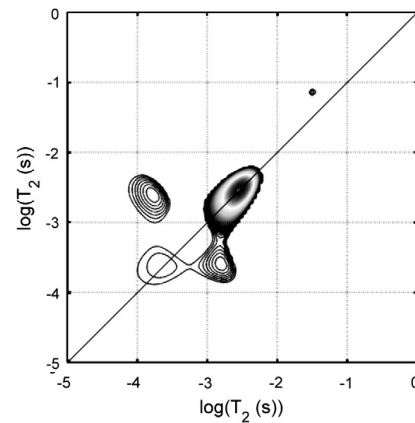


Figure 2.12 – T_2 - T_2 spectrum, from [60].

2.2.3 NMR cryoporometry

Some researchers have combined NMR experiment with freezing a part of the pores. The idea is to follow the NMR signal intensity as a function of temperature, the melting/freezing temperature of water being depressed due to its confinement in small pores according to the Gibbs-Thomson equation. Usually, samples are first frozen down to $-100 \text{ }^\circ\text{C}$ and progressively warmed up to above $0 \text{ }^\circ\text{C}$. The heating rate is usually a few $^\circ\text{C} / \text{hour}$ for a total experimental time of at least 12 hours.

The first known application of NMR cryoporometry on cement was Jehng in 1996 [61]. While capillary pores are completely frozen below $\sim 50\text{-}60 \text{ }^\circ\text{C}$, gel water of C-S-H is not significantly

affected even at -100 °C. However, a shift in T_2 is observed for the gel pores with increase of temperature.

Valckenborg *et al.* [62] performed NMR cryoporometry on mortar samples hydrated for 1 year. The research was conducted studying the transversal T_2 relaxation time. No liquid water was observed by NMR below -70 °C. The melting of “dense gel pores” (1 nm in size) is observed from -60 °C during the warming up of the sample. “Open gel pores” (1-10 nm in size) start melting at -20 °C and large capillary pores from -10 °C. The melting of these different populations is progressive.

3 Materials and methods

Contents

3.1 Cements	36
3.2 Generic sample casting	36
3.3 ¹H NMR: pulse sequences, parameters and analysis	37
3.3.1 Quad-echo pulse sequence	38
3.3.2 CPMG pulse sequence	42
3.4 Other methods	44
3.4.1 X-ray diffraction (XRD)	44
3.4.2 Chemical shrinkage	44
3.4.3 Isothermal calorimetry	44
3.4.4 Scanning electron microscopy (SEM)	45
3.4.5 Transmission electron microscopy (TEM)	45
3.4.6 Thermo-gravimetric analysis (TGA)	46
3.4.7 Solid-state ²⁹ Si MAS NMR	46
3.4.8 Relative humidity measurement	46
3.4.9 Water dynamic vapour sorption (DVS)	46
3.4.10 Mercury intrusion porosimetry	48

Experiments were carried out on cement pastes using different techniques. This section aims to describe the experimental procedures and parameters that led to the results presented.

3.1 Cements

White cement was used as the primary binder in this work. Three different batches of white cement were provided by Aalborg Portland. The main reactive components did not vary much with approximately 67% C₃S; 20% C₂S and 3.5% C₃A. All other anhydrous phases including C₄AF were found to be ≤ 1% of the total mass for the three batches. Detailed compositions quantified by XRD are presented in Table 3.1. The associated XRFs and a typical particle size distribution for these cements can be found in Annex B and Annex C respectively. The cement has a density of 3.15 g/cm³.

Table 3.1 – Phases composition (in wt%) of the three white cement batches used in this work. This was obtained by XRD and Rietveld quantification. The error is estimated at ±1%.

Phases	Batch 1	Batch 2	Batch 3
C ₃ S	66.89	66.85	65.78
C ₂ S	20.00	19.73	21.95
C ₃ A	3.51	3.62	3.54
C ₄ AF	1.00	0.78	0.26
Portlandite	1.02	0.70	1.63
Anhydrite	2.28	2.58	—
Bassanite	2.11	2.10	2.35
Lime	0.31	—	—
Gypsum	—	—	2.28
Amorphous	2.89	3.64	2.20
Total	100.00	100.00	100.00

The study of plain white cement pastes was done using batch 1, in which the sulfate phases were $2.3 \pm 1\%$ anhydrite (CaSO₄) and $2.1 \pm 1\%$ bassanite (CaSO₄ · $\frac{1}{2}$ H₂O). The batch 2 with similar composition was used for the study of white cement with 10% silica fume (section 5.1, p. 92) and the batch 3 was used for the slag study (section 5.2, p. 111). In the batch 3, gypsum was added into the mix proportions as replacement of anhydrite.

3.2 Generic sample casting

Typically 80 g of anhydrous powder was mixed at the desired water-to-cement mass ratio, *w/c*, in plastic containers for 2 minutes at 1,600 rpm using a paste mixer LABORTECHNIK RW 20.n. Samples were then cured in a controlled temperature environment (mostly in sealed conditions at 20 °C) in glass NMR tubes and in larger containers for parallel experiments.

In addition to ¹H NMR, experiments were carried out throughout the hydration using X-ray diffraction with Rietveld analysis (XRD), chemical shrinkage experiments, isothermal calorimetry, scanning electron microscopy with energy dispersive X-ray (SEM-EDX), transmission electron microscopy with energy dispersive X-ray (TEM-EDX), thermo-gravimetric analysis (TGA), solid-state ²⁹Si MAS NMR, water dynamic vapour sorption and mercury intrusion porosimetry.

3.3 ^1H NMR: pulse sequences, parameters and analysis

As for previous studies using ^1H NMR, white cement was preferred in order to slow down relaxation phenomena (due to low iron content) and simplify the analysis. After casting, aliquots about 0.35 cm^3 of paste were deposited directly into NMR tubes and tightly sealed with parafilm[®]. A glass rod was included to reduce the free air volume and to prevent water from leaving the sample by evaporation. To quantify the water that might have leaved the sample throughout the hydration, hydrated sealed pastes with different w/c at the age of 28 days were heated up to $1000\text{ }^\circ\text{C}$. Table 3.2 shows the comparison between the water mass quantified experimentally and the initial water contents. Little water was lost over 28 days of sealed hydration.

Table 3.2 – Comparison between the water mass lost on ignition and the initial water mass for different samples after 28 days of hydration.

Mixing w/c	Measured w/c
0.320	0.317
0.400	0.398
0.480	0.477

^1H NMR measurements were made on a Bruker Minispec NMR spectrometer operating at 7.5 MHz. The 90° pulse length was $2.9\text{ }\mu\text{s}$ and the intrinsic dead time of the machine was 15-16 μs . The glass NMR tubes were provided by Bruker BioSpin AG to ensure their purity regarding NMR experiments. The internal diameter of the tube was 8 mm and the sample height was kept below 10 mm to remain in the most homogeneous part of the magnetic field. Samples were periodically measured as prepared in tubes, in a temperature controlled NMR probe. Measurements were mainly done at $20\text{ }^\circ\text{C}$ and some at $10\text{ }^\circ\text{C}$.

In view of the existing knowledge about NMR on cement (*cf.* previous chapter), both Quad-echo [45] and CPMG [43] echo measurements were carried out to measure T_2 . Quad-echo was used to quantify the amount of chemically bound water in the sample, also called “solid water”. The CPMG sequence was used to further subdivide the liquid water into different components.

Residual ^1H in the NMR probe and adsorbed on the tube surfaces can influence and disrupt the sample signal. Hence and for each experiment, a “blank” (empty probe signal) was previously acquired and subtracted from the sample signal amplitude at each echo time (*cf.* Annex A, p. 143).

As for most oscillating signals, the data comprise two components ($\mathbf{M}_{x'}$ and $\mathbf{M}_{y'}$). After subtraction of the blank, the data were subsequently phased according to Equation 3.1 using

the third data point ($i = 3$) for the calculation of θ .

$$\mathbf{M}(t) = \cos(\theta) \times \mathbf{M}_{y'}(t) + \sin(\theta) \times \mathbf{M}_{x'}(t) \quad \text{with} \quad \theta(i) = \arctan \left[\frac{\mathbf{M}_{x'}(i)}{\mathbf{M}_{y'}(i)} \right] \quad (3.1)$$

3.3.1 Quad-echo pulse sequence

The Quad-echo pulse sequence (Figure 3.1) was used in this work to measure cement pastes from mixing up to 1 year of hydration. There is a lot of literature on the shape of the solid signal from rigid coupled hydrogen which depends on the molecular configuration [45, 63]. For solid hydrogen in Portland cement pastes (mainly within $\text{Ca}(\text{OH})_2$ and ettringite), a Gaussian fitting was preferred following the work of McDonald *et al.* [44].

QE signals were recorded as a function of pulse gap τ , which was varied between 15, 19, 24, 30, 37 and 45 μs . The data were then deconvoluted into a Gaussian and an exponential decay part using

$$\mathbf{M}(t, \tau) = A_{\text{solid}}(\tau) \times \exp \left[\frac{-(t - t_c)^2}{\sigma} \right] + A_{\text{liquid}}(\tau) \times \exp \left(\frac{-t}{T_2^*} \right) \quad (3.2)$$

where t is the experimental time taken from the end of the $P_{90}^{x'}$, t_c is the centre of the Gaussian and σ its width.

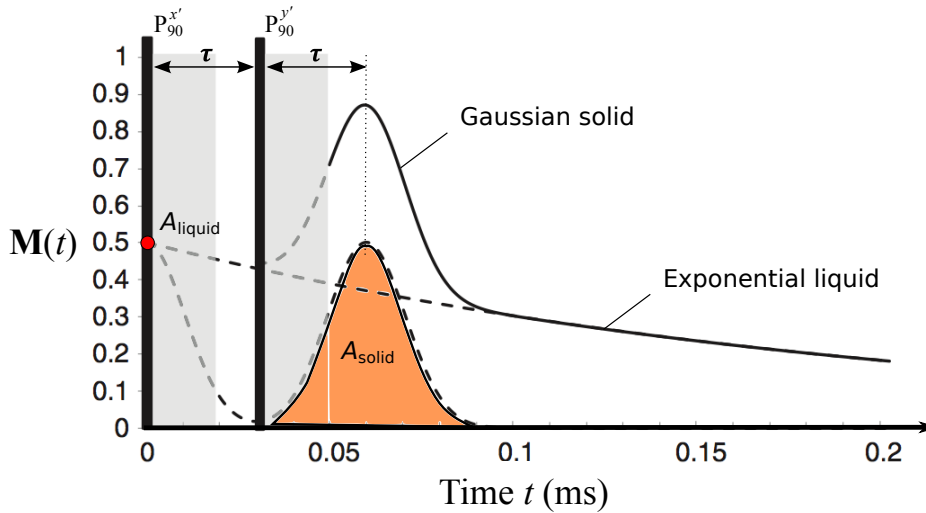


Figure 3.1 – Quad-Echo pulse sequence.

The exponential intensity A_{liquid} is attributed to mobile water within the sample and is only very weakly, nearly not, pulse gap dependent. The Gaussian intensity A_{solid} , of a very short time constant $\sim 10 \mu\text{s}$, is assigned to water in crystalline solid phases [44, 58] and decays when increasing pulse gap interval τ .

Figure 3.2 (left hand side) shows QE signals recorded for a mature white cement paste for $\tau = 15 \mu\text{s}$, $\tau = 30 \mu\text{s}$ and $\tau = 45 \mu\text{s}$. While the exponential constant of the signal is equivalent for all τ values, there is a decrease of the Gaussian intensity part when increasing τ and a shift to maintain the centre at " $2\tau + P_{90}$ time length" from the end of the first P_{90}^x . In order to ensure that bound hydrogen in crystalline phases only and solely contribute to the NMR in the Gaussian peak, synthesized ettringite and Portlandite were separately measured at low relative humidity. The pure ettringite was provided by Luis Baquerizo, one of the 15 TRANSCEND students who worked at Holcim in Switzerland. Results are presented in Figure 3.2 (right hand side) for different τ values. As supposed, no liquid exponential component is seen. At the echo times used, no significant "wobble" due to the classic "Pake doublet" [64] of dipolar coupled spin pairs was seen in the time domain data.

As signal decay occurs in a relative short time, there is always some uncertainties while measuring quadrature echoes. Errors might come from the timing of the pulse sequence, the fact that the pulse lengths are finite, the proximity of the dead time of the spectrometer and some possible group delays of filters. The data are here used the way they are with no manipulation.

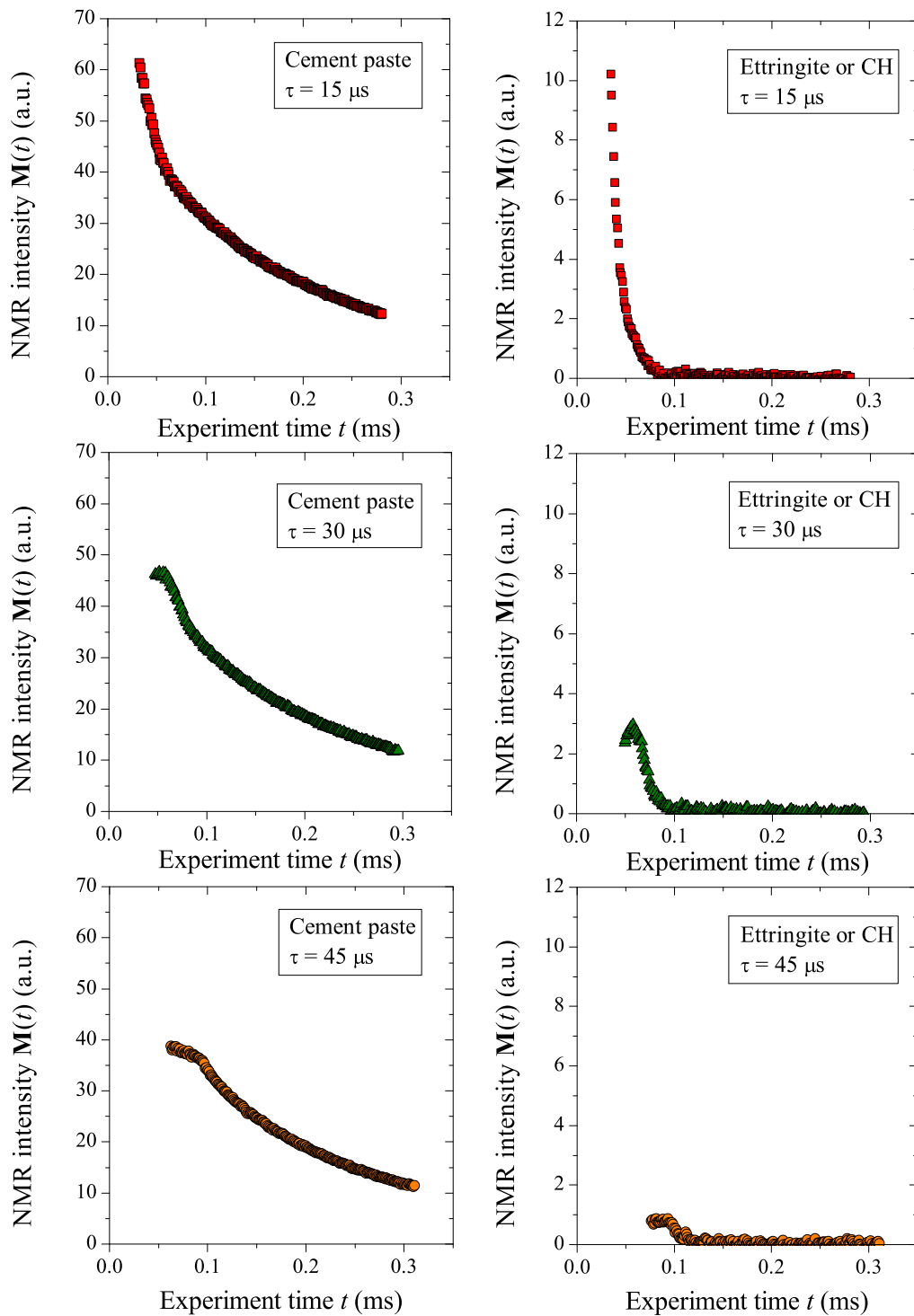


Figure 3.2 – QE raw signals for mature cement paste (left hand side) and for pure ettringite or CH (right hand side) for different values of τ . The time 0 is located at the end of the first $P_{90}^{x'}$.

To elucidate and quantify the fraction of solid-like hydrogen in the sample, the Gaussian fraction of the signal was back extrapolated to zero pulse gap *i.e.* free from relaxation phenomena using a Gaussian fit. An illustration of the A_{solid} and A_{liquid} amplitudes as a function of pulse gap is presented in Figure 3.3 for mature white cement paste. The solid grey line is the Gaussian fit giving the initial intensity of magnetized solid-like atoms: $A_{\text{solid}}(\tau = 0)$. The mobile part of the signal, $A_{\text{liquid}}(\tau = 0)$, supposed constant with variation of τ , is taken as the average of the fitted values (dashed line in Figure 3.3). The liquid intensity for the probed sample is found to be comparable to the total signal intensity using the CPMG pulse sequence (*cf.* next section). This gives confidence in the deconvolution between liquid- and solid-like hydrogen.

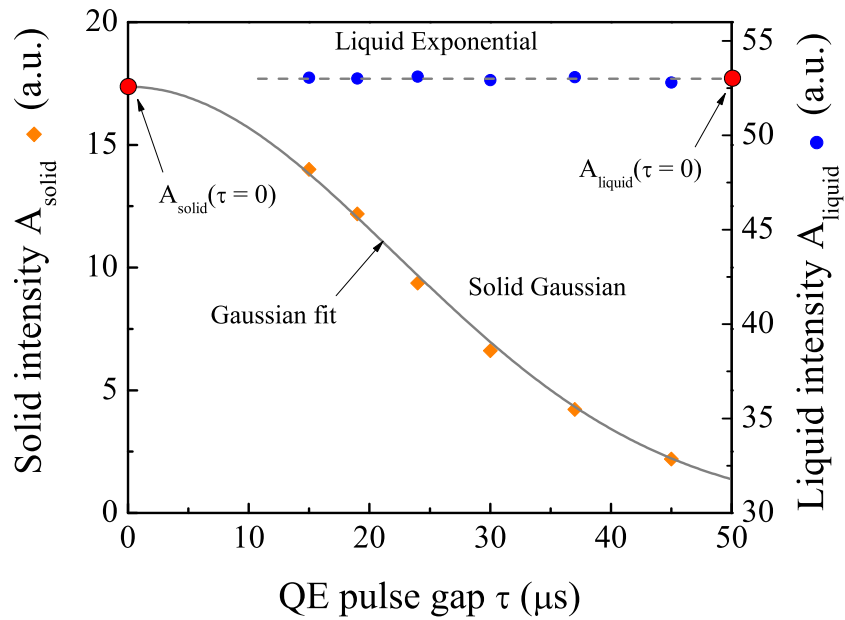


Figure 3.3 – QE solid and liquid amplitudes as a function of τ .

The fraction of hydrogen (so water) in crystalline phases ettringite and Portlandite, I_{solid} , is calculated as

$$I_{\text{solid}} = \frac{A_{\text{solid}}(\tau = 0)}{A_{\text{solid}}(\tau = 0) + A_{\text{liquid}}(\tau = 0)} \quad (3.3)$$

The liquid fraction of the signal, I_{liquid} , *i.e.* the fraction of evaporable water in the sample, is calculated by $I_{\text{liquid}} = (1 - I_{\text{solid}})$.

3.3.2 CPMG pulse sequence

The mobile part of the signal was separately resolved into different T_2 components using the CPMG pulse sequence (Figure 2.6, p. 25). Decays comprise typically 256 echoes logarithmically spaced from 50 μs to 12 ms. The logarithmic spacing was used to keep the total number of pulses low while covering ~ 5 orders of magnitude of relaxation times. The role of internal gradients caused by different magnetic susceptibilities [65, 66] notably for large pulse gaps (hence pores) is not considered critical to the measurement. For most of the pores in cement paste, the different T_2 are sufficiently close to each other (within 1 ms) that “diffusive attenuations” does not limit T_2 .

As samples were measured from mixing time up to 1 year of hydration, the time interval between two repetitions was progressively decreased from initially 1000 ms down to 500 ms beyond 1 day of hydration to ensure full recovery of spins between repetitions. Consequently, the number of averages (or *scans* in NMR terms) was increased from initially 512 to 1024 scans keeping an average measurement times of circa 15 minutes. As a result, the signal-to-noise ratio decreased from initially high values to lower values in mature pastes. The signal-to-noise ratio was typically 1500:1 as calculated by the signal intensity of the first echo point divided by the standard deviation of the last 20 echo amplitudes. The amplitude of the first echo point was comparable to that of liquid-like hydrogen (A_{liquid}) measured with parallel QE experiments. It needs to be specified that 15 minutes measurement time was sufficient to capture the changes happening during the first days of hydration.

Physics of NMR relaxation suggest that each different pore size contributes to a separated T_2 component. Different pores can be distinguished either if they are isolated from each other or if the exchange time between them is slow. If the spins diffuse rapidly between two pores, an overall average relaxation time for the two populations will be recorded. On the other hand, if little exchange of water occurs during the measurement time, two distinct rates are recorded and hence two pore sizes. For hydrating cement pastes, the exchange time between pores is slow [39] in comparison to the slowest relaxing T_2 component. That makes the different pore sizes resolvable without problems of diffusion.

The analysis of CPMG relaxation data from cement pastes remains the critical part of NMR experiments as it consists of a multi-exponential response difficult to deconvolute. To extract the information, three different methods exist:

- (1) A least squares fitting to a known number of components. The results can however have significant dependence on the “guess values” if all amplitudes and relaxation times are left variable. The results might also change according to whether the data are fitted as real data to exponential curves or as logarithmic data to straight lines as the noise weights differently.
- (2) A discrete method known as *curve peeling* consisting in a decomposition of the signal by an iterative fit of the longest T_2 component.

(3) A Laplace inversion method [67] using the CONTIN program [68].

Plassais *et al.* [57] studied the consistency of results between the two last methods and found similar results. In 2002, an inverse Laplace transform (ILT) algorithm was developed by Venkataramanan *et al.* [59] allowing more consistent analysis of multi-exponential curves. This latter was used in this work to analyse CPMG echo intensity decays. This algorithm contains a regularization parameter know as α which sets the sensitivity of the inversion. This parameter was optimized as described in [59] and a value of 1.5×10^{-6} was used. Special care was taken to identify the influence of the α parameter (*cf.* Annex A, section A.5.2, p. 151). While the widths of T_2 components depend upon it, the integrated peak intensities are robust to its variation. A typical T_2 CPMG decay for mature cement paste and the associated ILT result is presented in Figure 3.4. The assignment of the different peaks will be discussed in the next chapter.

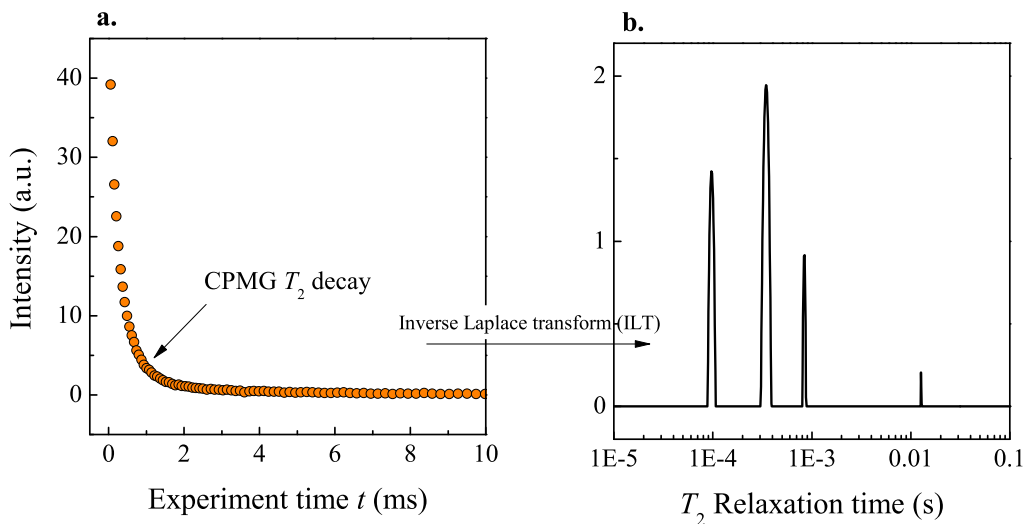


Figure 3.4 – (a) Example of T_2 decay for mature cement paste and (b) the associated inverse Laplace transform of the signal.

This section has introduced the way ^1H NMR is used to probe water in cement pastes. The aforementioned NMR methodology was applied to measure all pastes, for which the mix proportions and the curing conditions were varied. For more details about NMR experiments, the reader is referred to Annex A, p. 143.

3.4 Other methods

3.4.1 X-ray diffraction (XRD)

XRD measurements of as-prepared sealed pastes were first performed on slices right after cutting. This was done to properly quantify the ettringite, which partially dehydrates over drying. Hydration of other samples was stopped by immersion in isopropanol for 7 days. Such samples were then vacuum dried, crushed and measured as a powder. A Panalatical X'Pert Pro MPD diffractometer in a θ - θ configuration was used with a $\text{CuK}\alpha$ source (wavelength 1.54 Å) and a fixed divergence slit of 0.5°. Samples were scanned on a rotating stage between 7 and 70° (2θ) using a X'Celerator detector with a step size of 0.0167° (2θ) and a time step of 77.5 s.

3.4.2 Chemical shrinkage

Most of the pastes under study are kept sealed so empty voids not filled with water exist due to chemical shrinkage. The empty chemical shrinkage volume (and therefore not seen by NMR) was recorded by the conventional technique of following the water height in a pipette above saturated samples. Typically 3 g of paste was used. Extra water was added on the top of the sample a few minutes after mixing, being very careful not to dilute the cement paste under study. Coloured oil was used to highlight the water level in the pipette. The evolution of the chemical shrinkage level was recorded using a camera and the images were analysed using the in-house software ShrinkageSuite. This software was developed by Shashank Bishnoi, a former student of LMC. One image per minute was recorded.

Chemical shrinkage measurements require samples to be exposed to excess water. Therefore, the hydration may be different from sealed samples. Therefore, the degree of hydration of parallel underwater pastes was measured by XRD.

3.4.3 Isothermal calorimetry

The heat released from hydrating pastes was recorded with an isothermal calorimeter (TAM Air from TA Instruments). It consists of 8 parallel twin measurement channels maintained at a constant temperature: one for the paste sample (approximately 10 g), the other for the reference. Distilled water was used as the reference for which the mass was calculated according to mix proportions using Equation 3.4, to have the same thermal mass as the measured sample,

$$m_{H_2O} = \frac{(C_{H_2O} \times [w/(w+c)] + C_{\text{cement}} \times [c/(w+c)]) \times m_{\text{paste}}}{C_{H_2O}} \quad (3.4)$$

where C_{H_2O} and C_{cement} represent the calorific heat of water and cement respectively. For

a $w/c = 0.40$ paste, this corresponds to a water mass of approximately $m_{H_2O} = 4.14$ g. The instrument was maintained in a temperature-controlled room to ensure the stability of the baseline. Measurements were carried out at 20 °C.

3.4.4 Scanning electron microscopy (SEM)

For the microscopy, hydrating samples were cut into slices (≈ 2 mm thick) and immersed in isopropanol for 7 days followed by at least 7 days in a desiccator. Dried slices were then impregnated with an epoxy resin (EPO TEK[®] 301). The embedded samples were kept at 20 °C for 24 hours and then subsequently polished using a standard polishing machine with successively 9, 3 and 1 μm diamond sprays (STRUERS DP Spray M) with petrol as a lubricant.

A FEI Quanta 200 SEM equipped with a tungsten filament was used. It was operated at 15 kV with a spot size low enough to have a sufficient BSE image resolution (to allow the user to reasonably position the EDS points) and a relatively low beam current (0.7-0.8 nA), but high enough to achieve 12-15 kcts per second in hydrated phases. The detector was a Bruker AXS XFlash[®] Detector 4030 (with an active surface of 30 mm²) with a take-off angle of 35 °C, *i.e.* an optimal working distance of 12.5 mm.

In the experimental conditions, the interaction volume for the electrons is of the order of cubic micrometres. For EDX quantification, inner-C-S-H can therefore be influenced by the Ca from cement grains (mainly for early age pastes). In the same way, the quantification of outer-C-S-H can be influenced by Ca from surrounding Portlandite. Following the work of Rossen [69], the extreme Si edge of the distribution was considered to be more representative of the real Ca/Si ratio of the C-S-H.

3.4.5 Transmission electron microscopy (TEM)

The TEM experiments of this work were carried out by John Rossen, one of the PhD student at LMC, who did his research on the topic [70]. This was done in collaboration with the interdisciplinary centre for electron microscopy (CIME), at EPFL. The TEM was a FEI Technai Osiris[™]. It was operated at 80kV and adjusted to yield a low beam current in order to minimize damage. Imaging and EDS were done in STEM mode. Quantification of the spectra was done using a standardless Cliff-Lorimer method with a thickness chosen at 150 nm as a reasonable average, and assuming a density of 2.6 g/cm³ for the C-S-H layers [70].

3.4.6 Thermo-gravimetric analysis (TGA)

Hydrating samples were immersed 7 days in isopropanol, dried for 7 days in a desiccator and then crushed. To avoid interaction with solvent leading to extra mass loss at high temperatures [71], some samples were additionally freeze dried. TGA measurements were made on these dried powders with a Mettler Toledo TGA/SDTA 851 analyser operating between 30 and 950 °C at 10 °C/min under N₂ gas flow to prevent carbonation. The quantification of water loss from Portlandite was done using the tangent method as in [72].

3.4.7 Solid-state ²⁹Si MAS NMR

Solid-state ²⁹Si MAS NMR measurements were done by the Professor Jørgen Skibsted in the department of chemistry of Aarhus University, Aarhus, Denmark. Hydrating samples were cut into thin slices and immersed in isopropanol for 7 days. The samples were subsequently dried in a desiccator for 7 days and crushed. The solid-state ²⁹Si NMR measurements were carried out on this sample powder. Spectra were recorded at a magnetic field of 9.4 T on a Varian Unity INOVA-400 spectrometer, using a home-built CP/MAS probe for 7 mm *o. d.* rotors with sample volumes of 220 μL. The single-pulse experiments employed a spinning speed of $\nu_R = 6.0$ MHz, a 45° excitation pulse ($\tau_{pw} = 3.0$ μs) and a repetition delay of 30 s. Typically 1000 - 3000 scans were recorded for each spectrum. The ²⁹Si chemical shifts in the ²⁹Si MAS NMR spectra are reported in parts per million relative to an external sample of neat tetramethylsilane (TMS), using a sample of β-Ca₂SiO₄ ($\delta_{iso} = -71.33$ ppm) as a secondary reference material.

3.4.8 Relative humidity measurement

The internal RH development in hydrating cement pastes was measured with two Rotronic AW-DIO water-activity probes, equipped with high-precision RH and temperature sensors. The accuracy of the sensors was ±0.8% RH and ±0.1 °C. The temperature of the measuring chambers was controlled by means of water circulating in the casings. This allowed the temperature in the measuring chambers to be maintained at the level of 20 ± 0.07 °C. Samples were broken into mm pieces after 1 day of hydration and then placed into the chamber. RH measurements were taken at 1 min intervals. Before and after each measurement, the sensors were calibrated using saturated salt solutions in the range 81% to 98%.

3.4.9 Water dynamic vapour sorption (DVS)

Desorption measurements of cement pastes were done on a dynamic vapour sorption (DVS) analyser. At given hydration times, samples were broken and crushed in a 100% RH environment to avoid any drying. 30 mg of this water saturated powder were subsequently deposited in the sample holder in the chamber of the DVS. Desorption experiments were carried out applying several relative humidity steps. An initial step of 240 minutes at 100% RH was set to ensure the initial stability of the sample before starting the desorption. In the same way, a final

step (240 minutes at 0% RH) was set to ensure that the dry state had properly been reached. For all other relative humidity steps, a mass change criteria of $dm/dt = 0.00013 \text{ mg/min}$ was applied according to the sensitivity of the DVS analyser. The maximum time step was set at 1500 minutes. Data were recorded every second. The total measurement time was about 2 weeks.

Because sorption isotherm experiments rely on relative humidity sensors, a calibration is required. The calibration was done using different salt solutions following the procedure described in [73]. MgCl (32.78% RH), NaCl (75.30% RH), KCl (84.34% RH) and KNO₃ (93.58% RH) were used. Acquisitions of the salt solutions data were done before and after each experiment on cement pastes. To ensure that the sorption balance gives reliable data, a reference material was first studied: MCM41. MCM41 possesses a hexagonal array with one-dimensional pore size which can vary between 2-20 nm depending on the synthesis conditions. MCM41 has already been widely used as a calibration material [74, 75]. Figure 3.5 shows a full cycle of adsorption and desorption for the MCM41 material. The results are exactly similar to that obtained by Wu Min [76], the TRANSCEND student leading the project number 7 (*cf.* Figure 1.1,p. 2), who did similar testing on the same material in the Technical University of Denmark. The shape of the adsorption branch is comparable to the results of Llewellyn *et al.* [77] at $\pm 5\%$ and the hysteresis observed between the adsorption and the desorption branches has similar features as already published data [78].

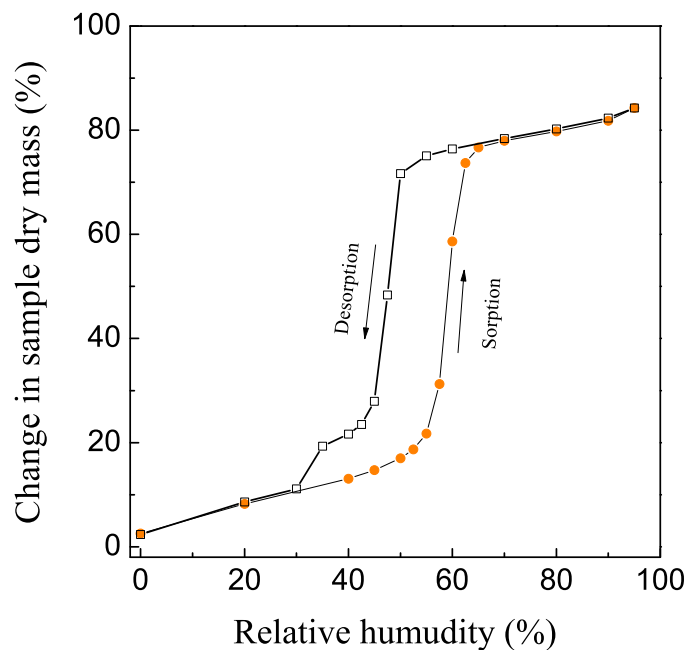


Figure 3.5 – Sorption and desorption branches for the reference material MCM41.

3.4.10 Mercury intrusion porosimetry

For MIP measurements, a porosimeter Porotec equipped with two devices was used. The first applies a low mercury pressure up to 400 kPa to introduce the mercury into the sample and to measure the macroporosity. The second applies a maximum pressure of 400 MPa for the measurement of the micro- and nano-porosity. The interpretation of the MIP data into pore volume versus pore size was done by the use of the Washburn equation (Equation 1.1, p. 15), for which the surface tension of mercury was $\gamma_{Hg} = 0.48 \text{ N/m}$ and the contact angle was $\theta = 140^\circ$. A planar pore model was used for comparison with the NMR.

For all pastes and sample treatments, samples were cut in slices and broken with a pincer into roughly cubic pieces of about 3 mm size. Circa 1.5 g of these pieces was used for each measurement (≈ 20 sample cubes). Three repetitions were done for each sample. As an example, Figure 3.6 shows the three repetitions obtained for the white cement paste mixed at $w/c = 0.32$ after 28 days of sealed hydration. There is a good reproducibility of the MIP measurements.

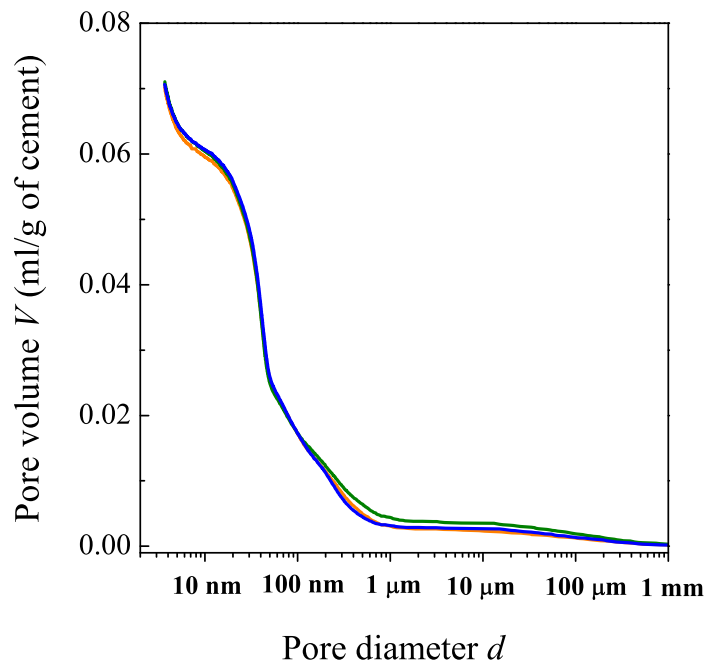


Figure 3.6 – Three MIP results for the white cement paste mixed at $w/c = 0.32$ after 28 days of sealed hydration.

4 NMR study of plain white cement pastes

Contents

4.1 Mixes under study	51
4.2 Experimental results	51
4.2.1 Isothermal calorimetry	51
4.2.2 ¹ H NMR signal assignment	52
4.2.3 ¹ H NMR experimental error	55
4.2.4 Evolution of NMR signal amplitude during the hydration (<i>w/c</i> = 0.40)	56
4.2.5 Evolution of <i>T</i> ₂ relaxation times during the hydration (<i>w/c</i> = 0.40)	57
4.2.6 Pore size interpretation	57
4.2.7 NMR responses for <i>w/c</i> = 0.32 and <i>w/c</i> = 0.48	59
4.2.8 Chemical shrinkage volume	62
4.3 Theory - calculations based on NMR signals	64
4.3.1 Mass and volume paste composition	64
4.3.2 C–S–H chemical composition	65
4.4 Analytical results - C–S–H characteristics	68
4.4.1 C–S–H density	68
4.4.2 C–S–H Chemical composition	73
4.4.3 Specific surface area of the C–S–H interlayer and gel pores	76
4.5 Mass and volume composition diagram	76
4.6 Sensitivity analysis	78
4.7 Desorption isotherm at 20 °C	79
4.7.1 Sample preparation and experimental procedure	79
4.7.2 Effective water-to-cement ratio	79
4.7.3 Solid and liquid NMR components after 28 days of underwater cure	79
4.7.4 Desorption isotherm results	80
4.7.5 Analysis of the results - C–S–H characteristics	82
4.7.6 Pore size by amplitude model	82

4.8 Sealed white cement paste cured at 10 °C	83
4.8.1 Experimental results	83
4.8.2 Analytical results - C-S-H characteristics	86
4.8.3 Discussion	87
4.9 General discussion	88

Most of the key results presented in this chapter were already published. A list of these publications can be found p. 179.

4.1 Mixes under study

White cement pastes mixed at $w/c = 0.32, 0.40$ and 0.48 sealed cured at $20\text{ }^\circ\text{C}$ were first studied. As a second step, the influence of under water cure and hydration at $10\text{ }^\circ\text{C}$ were investigated. For all these experiments, the white cement batch 1 was used (composition p. 36) and the pastes were cast according to the procedure described in the previous chapter.

^1H NMR measurements were done at intervals over the course of hydration from mixing up to a few 100 days. Additionally, experiments were performed by calorimetry, XRD and TGA.

4.2 Experimental results

4.2.1 Isothermal calorimetry

Figure 4.1a and b respectively show the differential heat flow and the cumulative heat flow for plain white cement pastes with $w/c = 0.32, 0.40$ and 0.48 as a function of time and normalized per gram of cement. The main peak of hydration between 2 hours and 16 hours is similar for all mixes. However, the cumulative heat plots at 10 days show the extra hydration which occurs with increased the w/c .

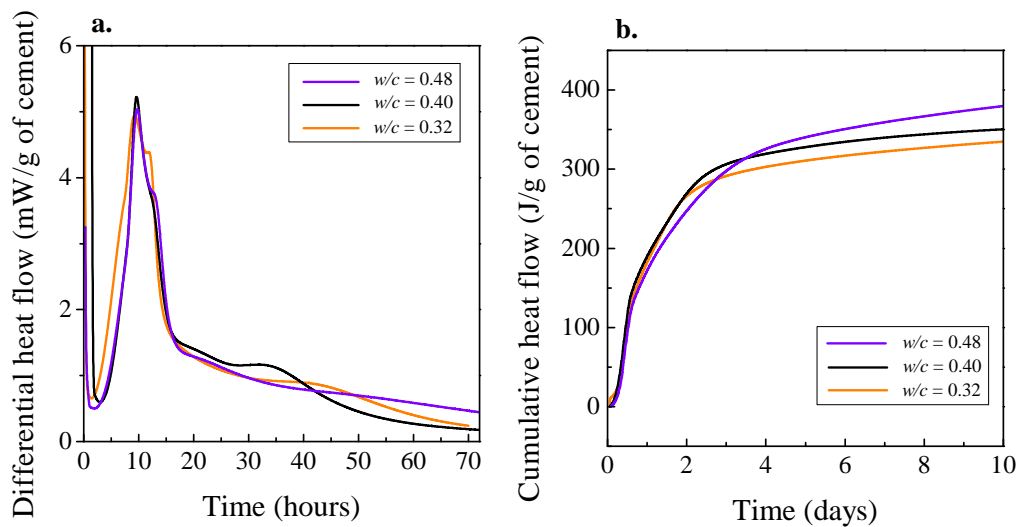


Figure 4.1 – Calorimetry results for white cement pastes with $w/c = 0.32, 0.40$ and 0.48 cured at $20\text{ }^\circ\text{C}$. (a) Differential heat flows in mW/g of cement and (b) cumulative heats in J/g of cement.

4.2.2 ^1H NMR signal assignment

NMR data were acquired for samples as a function of hydration time. Figure 4.2 shows the evolution of the NMR signal for the $w/c = 0.40$ paste. Combined QE and CPMG data are presented from 28 minutes after mixing to 62 days of hydration. The measurement time was kept at 15 minutes changing the time interval between repetitions to ensure full recovery of the spins. This 15 minutes measurement time is consider acceptable compared to the time scale of changes occurring in the early stages of hydration.

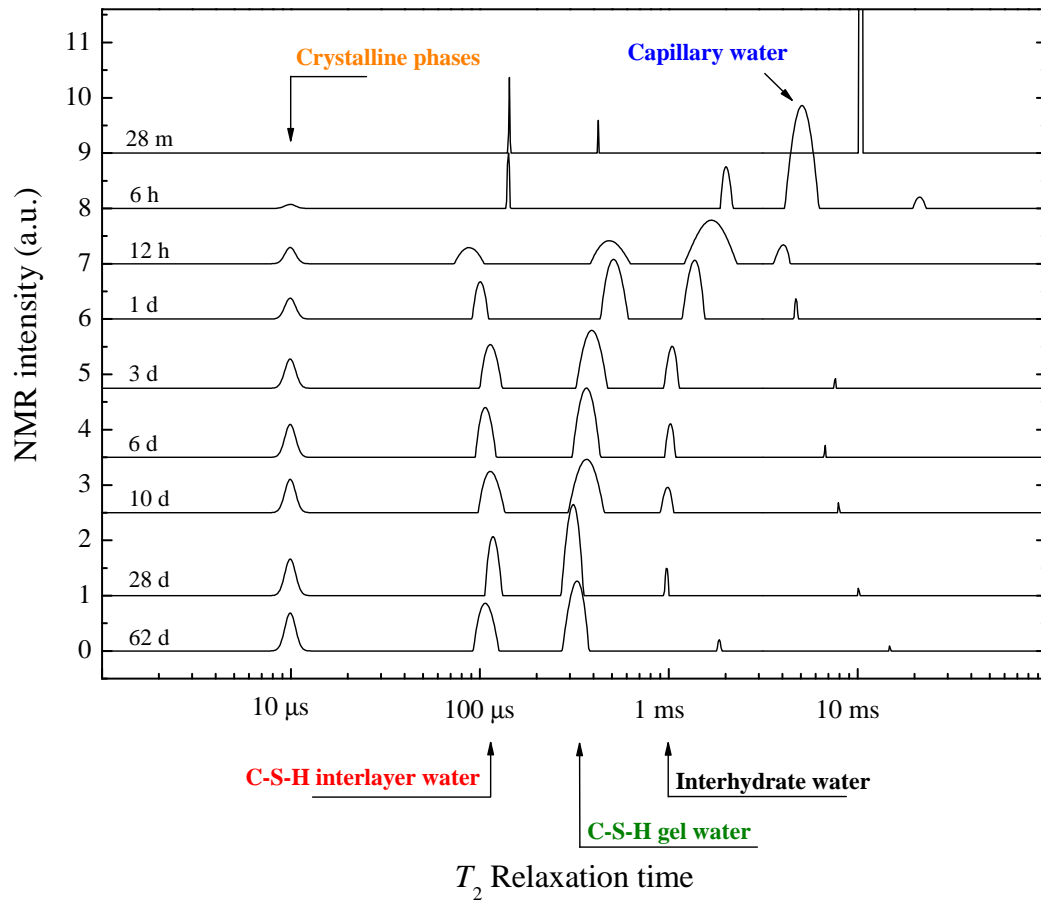


Figure 4.2 – Evolution of the NMR signal during hydration for the $w/c = 0.40$ paste. Combined QE and CPMG results.

At the beginning, the signal is dominated by that of “free water” with long T_2 . During the first day of hydration, relaxation times are shifted to smaller values and different populations can be distinguished. Taking the 10 days data as an example, the map shows five discrete components: $22.6 \pm 2\%$ at $10\ \mu\text{s}$; $25.7 \pm 2\%$ at $100 \pm 30\ \mu\text{s}$; $46.8 \pm 2\%$ at $340 \pm 10\ \mu\text{s}$; $4.6 \pm 2\%$ at $845 \pm 200\ \mu\text{s}$; and $< 0.5\%$ at $12 \pm 2\ \text{ms}$. The first is a fast relaxing component with a ^1H nuclear

spin-spin relaxation time T_2 of the order of 10 μs . It is assigned to ^1H chemically combined in solid crystalline phases calcium hydroxide and ettringite (defined as “solid signal”). Two further components have relaxation times of the order 80-120 μs and 300-500 μs . These are attributed to water in C–S–H interlayers and to gel pore water respectively. The fourth component rapidly displays a constant T_2 . It is speculated that this represents the spaces between the growing C–S–H needles and hence defined as “interhydrate pores”. The fifth component is associated to larger capillary pores and micro-cracks. The last two can be combined and defined as the free water within the paste, hereafter abbreviated simply to capillary water.

The signal assignment shown in Figure 4.2 is generally in accord with earlier observations of similar materials made with comparable equipment [58]. However, some other prior studies [51, 52] have lacked the temporal resolution to see the fastest relaxing components, in particular calcium hydroxide and ettringite while others have either failed to separately resolve the C–S–H layer and gel pore water [53]. Sometimes, the use of T_1 instead of T_2 was chosen to overcome “these difficulties” but a fast recovery machine is still needed to see the solid signal. Moreover, some earlier studies have lacked quantification of signal amplitudes and hence water mass in the different environments. The first important contribution of this work is that this last difficulty was overcome by use of combined QE and CPMG pulse sequences as described in the previous chapter.

The measured water signal intensities for each population can be expressed as signal fraction, noted I , of total signal intensity arising from mixing water. It hence represents absolute water fraction in the sample. Signals from solids (crystalline CH and ettringite, I_{solid}), C–S–H interlayer water (I_{CSH}), gel pore water (I_{gel}) and free water (I_{cap}) lead, for sealed pastes, to the statement $I_{\text{solid}} + I_{\text{CSH}} + I_{\text{gel}} + I_{\text{cap}} = 1$.

A key test that proper account has been taken of all the water in the sample is the comparison between the NMR solid signal fraction and an estimate of this value obtained by other means. To that end, parallel experiments were carried out using XRD and TGA for samples cured for 10 days and 28 days. At 10 days, the hydration was stopped by isopropanol exchange in one set of samples and freeze-drying in another, duplicate, set. At 28 days, only isopropanol exchange was used.

The ettringite mass fraction in each of the pastes was measured by XRD after 3, 6 and 10 days of hydration. As might be expected, it did not change appreciably during this time since calcium sulfates have all reacted by one day [79] and the small C_3A content does not allow a significant precipitation of AFm at later ages. As the precision of XRD for such low amounts of ettringite is not good, the average of all measurements, $m_{\text{ett}}^{\text{XRD}} = 0.066$ grams of ettringite per gram anhydrous cement, was taken as the value for all samples reported in Table 4.1.

The fractions of Portlandite measured by XRD and TGA at 10 days and 28 days of hydration are also shown in Table 4.1. From its known molecular compositions [80, 81], it is possible to evaluate the fraction of water consumed in Portlandite. Added to the one of ettringite, this

is directly comparable to the NMR signal attributed to the solid I_{solid} . Table 4.1 shows that the combined water in the CH and ettringite as determined by XRD/TGA is within 1% of that determined by NMR in all the samples. This degree of agreement is better than expected given the inherent uncertainties in each of the methodologies.

The water in Portlandite and ettringite measured by XRD fully accounts for the shortest T_2 component which support the assignment previously done. This result verifies that all the water is “seen” by the adopted NMR methodology. In addition is that upon sample drying, the NMR signal decreases linearly with sample mass as shown by Agata Gajewicz’s results in Figure 4.24a, p. 81. The trend is clear that no interlayer water or residual hydroxyl group of C–S–H is within the solid signal so that, the next shortest T_2 component must be attributable to the interlayer water in C–S–H. The degree to which the interlayer is protonated by OH groups remains a matter of contention and indeed such OH groups as exist in the interlayer may be associated with relatively (rotationally?) mobile Ca ions [9, 82].

Table 4.1 – CH and ettringite mass fractions measured by XRD and TGA, translated into water mass fraction for comparison with the NMR solid signal.

w/c	age (days)	Mass fraction (g/g anhydrous)						ett. XRD average	Fraction of water consumed			NMR I_{solid}
		isopr. exchange		freeze drying		average	CH		ett.	CH + ett.		
		XRD	TGA	XRD	TGA							
0.32	10	0.207	0.200	0.212	0.209	0.207	0.066	0.157	0.095	0.252	0.248	
	28	0.217	0.218	—	—	0.218	0.066	0.165	0.095	0.260	0.258	
0.40	10	0.260	0.231	0.255	0.238	0.246	0.066	0.150	0.076	0.225	0.226	
	28	0.266	0.286	—	—	0.276	0.066	0.168	0.076	0.243	0.241	
0.48	10	0.305	0.311	0.296	0.294	0.302	0.066	0.153	0.063	0.216	0.207	
	28	0.313	0.323	—	—	0.318	0.066	0.161	0.063	0.224	0.230	

4.2.3 ¹H NMR experimental error

As NMR signal amplitudes are used in this thesis to calculate water masses in the different pores of hydrating cement pastes, an estimation of the measurement error is required. For that, it is assumed that the ILT algorithm does not contribute to the error as perfect signal decay would lead to perfect deconvolution (see the study of artificially generated data, p. 154). For the experimental error, there are 4 ways of calculation.

(1) The first one is to take a mature sample (*i.e.* 28 days of hydration) and quantify the scatter of signal amplitudes between repetitive measurements. This was calculated based on 10 sets of results for white cement paste mixed at $w/c = 0.40$ and measured at 28 days of sealed hydration.

(2) The second option is to repeat the same experiment on the same sample after doing a calibration of the spectrometer (*cf.* Annex section A.2.1, p. 145 for the calibration details).

(3) The third option is to cast the same sample at different periods of the year and compare the NMR results at a given sample age.

(4) The final possibility is to measure the same sample on different spectrometers. In this case, the results acquired with the EPFL spectrometer were compared to the results from the spectrometer in University of Surrey.

The calculated errors for the aforementioned options are shown in Table 4.2 and expressed as percentages. The biggest error is for the reproducibility of measurement between different spectrometers. However, it needs to be specified that 4% difference might also arise through other factors such as the homogeneity of the cement, the sample preparation, etc..

Table 4.2 – Calculated errors in % for the four aforementioned options.

Option	Error on the NMR signal intensity (%)
(1)	±2.0%
(2)	±2.0%
(4)	±2.5%
(3)	±4.0%

4.2.4 Evolution of NMR signal amplitude during the hydration ($w/c = 0.40$)

Figure 4.3 shows the evolution of the different NMR signal amplitudes as a function of hydration time. The free water signal decreases rapidly during the first 2 days to just over 10% of the initial value, after which it decreases much more slowly. It is of negligible amplitude at circa 28 days. During the first 2 days, the signals attributed to crystalline solids, to C-S-H layers and to gel pores all increase. The volume ratio of interlayer water and gel water is approximately constant, 1:2. After two days the gel pore water signal stops increasing and stabilises at a constant value before eventually decreasing beyond 62 days. On the other hand, the water in the crystalline solids (CH and ettringite) and C-S-H interlayer water continues to grow throughout the entire experimental period (300 days). Hence, after two days, the volume ratio of interlayer water to gel water monotonically increases. It is speculated that the C-S-H growing in the very early stages, in parallel with gel pores, corresponds to the low density C-S-H and that which grows thereafter, devoid of corresponding new gel porosity, corresponds to the high density C-S-H that other authors have suggested/detected [83, 15, 16, 17, 84].

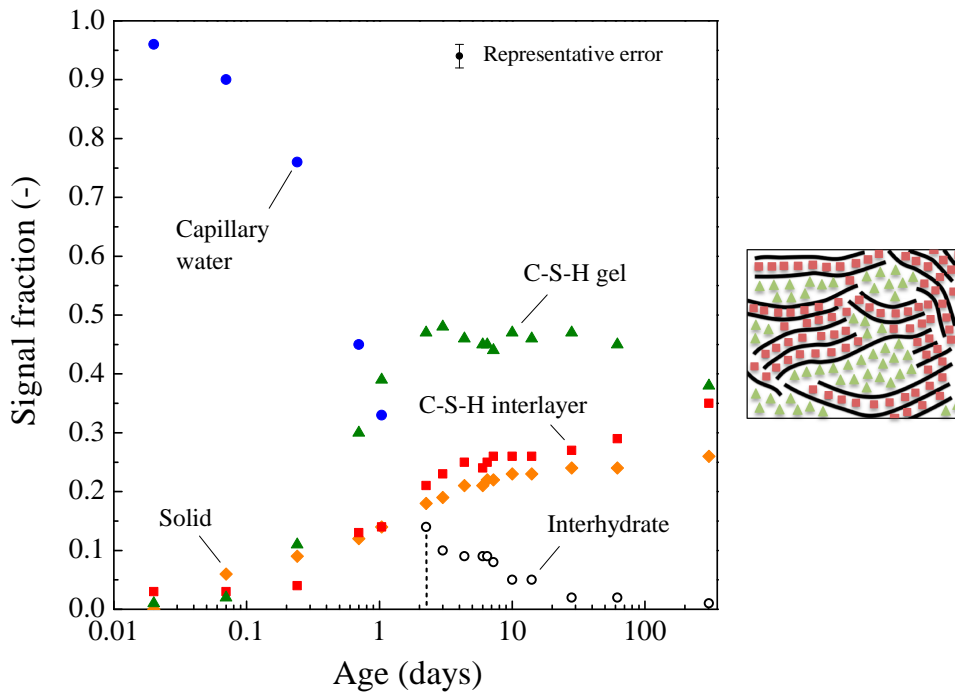


Figure 4.3 – Evolution of the different NMR signal fractions with hydration time ($w/c = 0.40$). These represent the fractional integrated peak areas shown in Figure 4.2. Blue circles are free water, becoming interhydrate water (empty black circles) beyond 2 days of hydration. The estimated error is $\pm 2\%$.

4.2.5 Evolution of T_2 relaxation times during the hydration ($w/c = 0.40$)

The corresponding T_2 relaxation times of the interlayer, gel and free water fractions are shown in Figure 4.4. Initially, while the signal is dominated by the single T_2 component corresponding to free water in the mix, the T_2 is long. However, it falls rapidly, along with the T_2 signal for the gel pores, approaching asymptotic values of $1000 \pm 200 \mu\text{s}$ and $300 \pm 10 \mu\text{s}$ respectively at 2 days of hydration. As might be expected, the values for the C–S–H interlayer are fairly constant at $\approx 100 \mu\text{s}$ from the time at which they first appear.

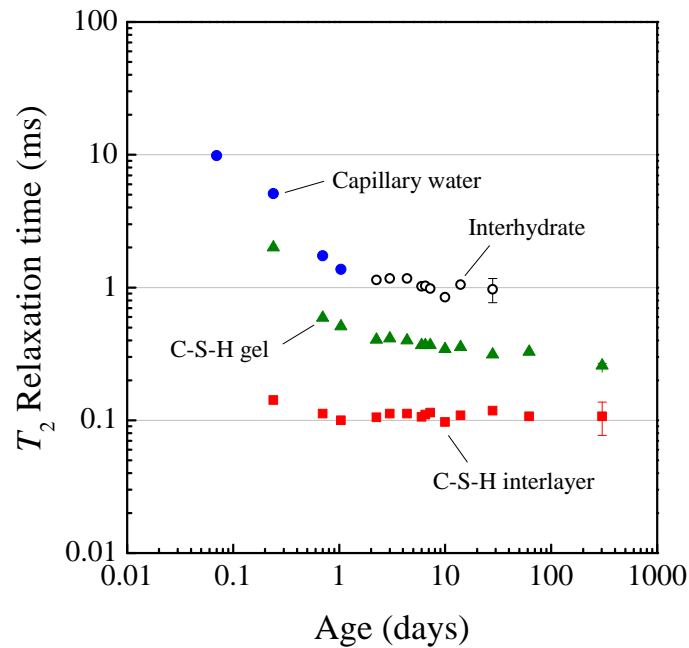


Figure 4.4 – Evolution of the T_2 relaxation times for the C–S–H interlayer water, the C–S–H gel water and the capillary water becoming interhydrate pores. The data points correspond to those presented in the previous figure.

4.2.6 Pore size interpretation

The relaxation times reported above may be interpreted in terms of pore sizes according to the fast exchange model of relaxation [39, 40, 46, 47, 49, 50] using

$$\frac{1}{T_2} \approx \frac{S\varepsilon}{V} \times \frac{1}{T_2^{\text{surf}}} \approx \frac{S}{V} \times \lambda \quad (4.1)$$

The key unknown here is the surface relaxivity λ . An empirical measurement of the surface

relaxivity was made on a very similar NMR spectrometer at University of Surrey by Agata Gajewicz. It is based on the asymptotic value of the relaxation time as the pore water is removed down to monolayer surface coverage. The NMR magnet, working at an NMR frequency of 20 MHz, gives $T_2^{\text{surf}} = 75 \mu\text{s}$. Combined with the diameter of a water molecule, 0.28 nm, this gives experimentally the surface relaxivity parameter $\lambda = 3.73 \times 10^{-3} \text{ nm}/\mu\text{s}$. The NMR frequencies of the two spectrometers are close enough to apply this value to the data generated here. Both spectrometers were used in combination to generate the NMR desorption isotherm in collaboration with Agata Gajewicz (section 4.7, p. 79).

Since the relaxation times rapidly approach constant values, it is concluded that the pores rapidly approach constant sizes. Application of Equation 4.1 with surface relaxivity $\lambda = 3.73 \times 10^{-3} \text{ nm}/\mu\text{s}$ gives average sizes of **2.5 nm** for the gel pores and **8.0 nm** for the interhydrate pores.

The size of the C–S–H interlayer spacing calculated by the fact exchange model is **0.85 nm**. This is a little larger than might be expected based on the mineral analogue of C–S–H, tobermorite 14 Å [6], for which the distance between opposite silicates in the interlayer is about 0.4 nm (see Figure 4.5d). However, the concept of mobile pore-water above an adsorbed layer that underpins the fast exchange model may not be valid in such a small space. Relaxation times also depend on what volume the water actually sees, for which there is no obvious answer (see blue arrows in Figure 4.5a and b). Ongoing simulations about relaxation times of water within tobermorite are currently in progress [85].

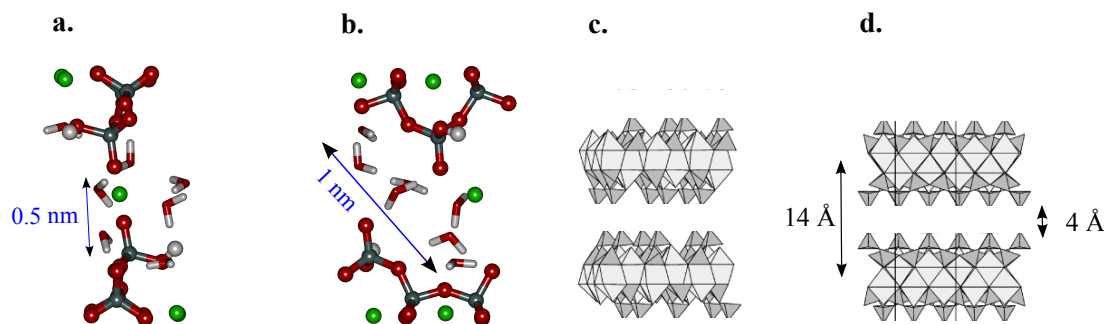


Figure 4.5 – Tobermorite structure viewed along (a and c) and perpendicular (b and d) to the silicate chains. (a) and (b) are atomistic modelling from [86]; (c) and (d) were taken from [6]. Tobermorite is a natural crystalline material made of a central calcium oxide layer on which are attached on both sides “dreierketten” silicate chains. The repeat distance for tobermorite 14 Å and it includes an interlayer space containing water molecules, hydroxyl groups and some calcium ions.

4.2.7 NMR responses for $w/c = 0.32$ and $w/c = 0.48$

Figure 4.6 shows the T_2 distribution map for the sealed cured cement pastes after 10 days of hydration with initial w/c ratios of 0.32, 0.40 and 0.48. Comparable populations are observed.

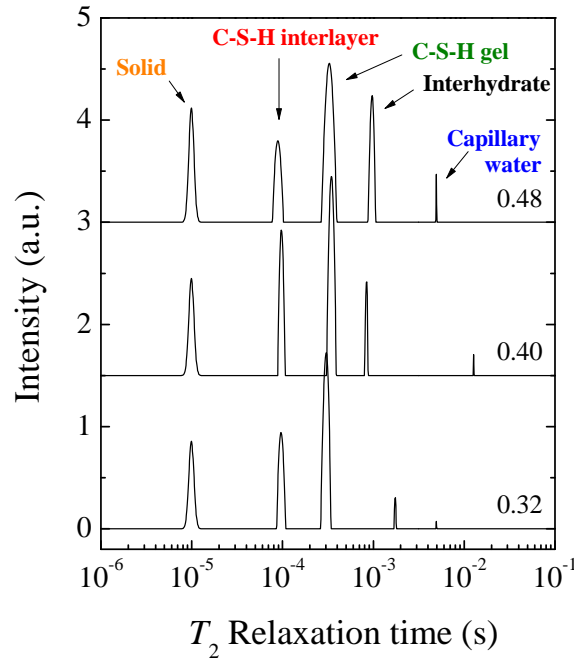


Figure 4.6 – T_2 distribution map of different pastes with $w/c = 0.32$, 0.40, and 0.48 at 10 days hydration.

Figure 4.7 and Figure 4.8 show respectively the evolution of the NMR response for the $w/c = 0.32$ and $w/c = 0.48$ pastes. As for the paste with $w/c = 0.40$, there is a fast consumption of capillary water during the first day of hydration. In the mean time, there is creation of solid crystalline phases (signal I_{solid}), C–S–H layers (signal I_{CSH}) and C–S–H gel (signal I_{gel}). This correlates with the heat flows presented in Figure 4.1.

The consumption of capillary water slows down at around two days for all w/c ratio pastes. However, the amount of capillary water left in the sample is higher when increasing the w/c ratio. Normalized per gram of cement, there is 0.03 g of capillary water at 2 days of hydration for $w/c = 0.32$, 0.06 g for $w/c = 0.40$ and 0.12 g for $w/c = 0.48$. While gel water effectively stops forming after 1 day for $w/c = 0.32$ and at 2 days for $w/c = 0.40$, gel pores are still created up to at least 10 days for the paste at $w/c = 0.48$. This phenomenon is related to the asymptotic T_2 relaxation time (1 ms) of the capillary water. It corresponds to the size of 8 nm previously described as the interhydrate porosity. It seems that C–S–H forms with gel pores only when the space is not restricted to 8 nm, independently of the capillary water content.

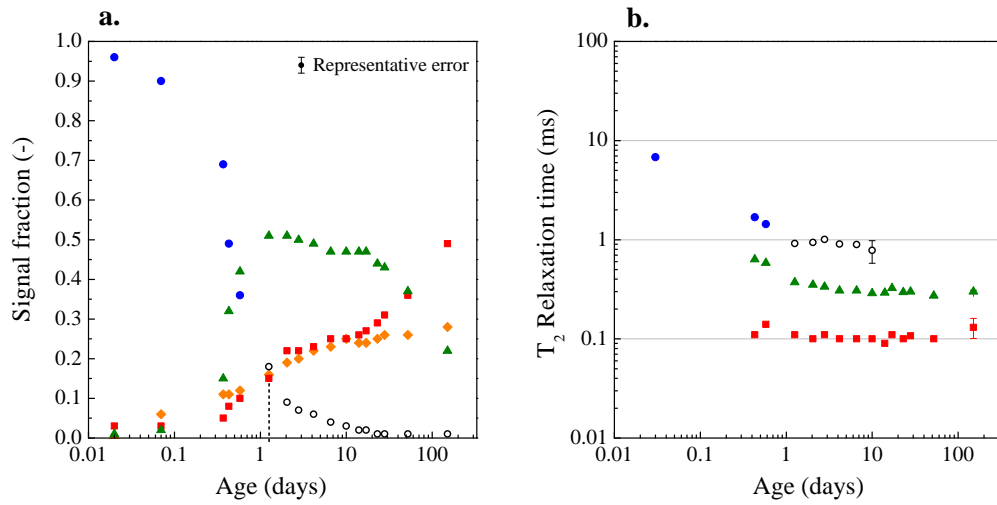


Figure 4.7 – (a) Evolution of the different NMR signal fractions with hydration time ($w/c = 0.32$). (b) associated T_2 relaxation times. Symbols are in accordance with the previous figure.

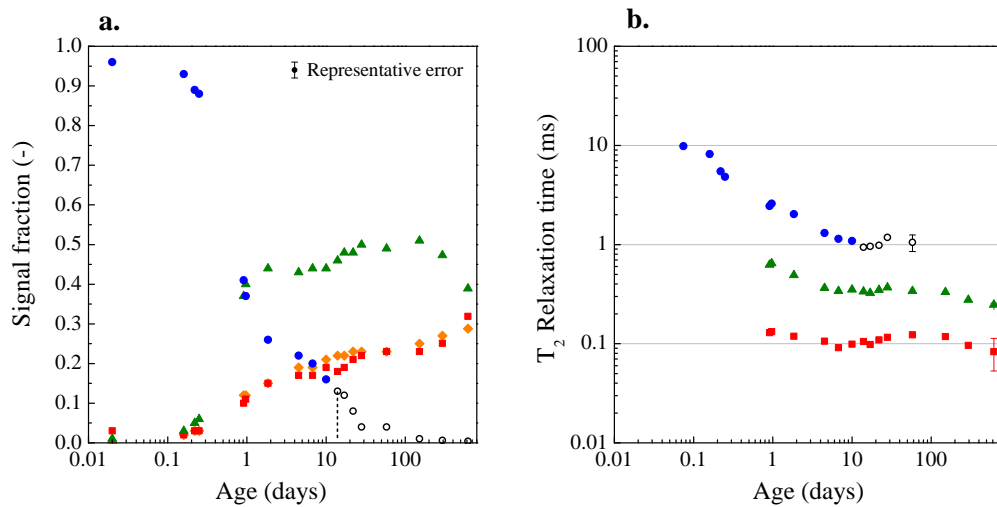


Figure 4.8 – (a) Evolution of the different NMR signal fractions with hydration time ($w/c = 0.48$). (b) associated T_2 relaxation times.

A decrease in the gel water content (signal I_{gel}) is observed at later ages for the three water-to-cement ratio pastes under study. It happens beyond 17 days, 62 days and 151 days for $w/c = 0.32$, 0.40 and 0.48 respectively. In parallel, the signal I_{CSH} increases and there is an almost equal signal decrease from I_{gel} as increase in I_{CSH} . This phenomenon starts to happen at the exact time when the capillary water content has become very low, almost at 0. The NMR desorption isotherm produced by Agata Gajewicz (*cf.* Figure 4.24, p. 81) showed that a monolayer coverage of water left on surfaces appears, in NMR relaxometry, within the C–S–H

interlayer signal. As the pastes are kept sealed, “internal” relative humidity measurements were carried out to see if the gel pores might eventually get empty. Figure 4.9 shows the evolution of the relative humidity monitored during the hydration of the $w/c = 0.40$ paste. Two repetitions are presented. At the end of the measurements, *i.e.* 38 days, the relative humidity is about 91%.

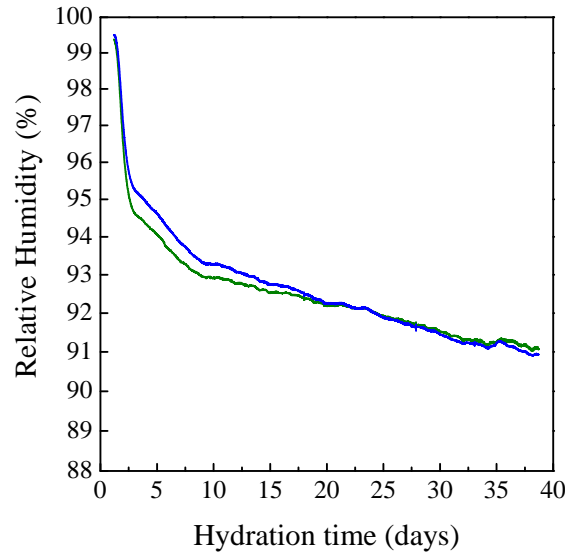


Figure 4.9 – Measure of the “internal” relative humidity in hydrating sealed white cement paste mixed at $w/c = 0.40$. Two measurement repetitions are presented.

Using the Kelvin equation for water in cylindrical pores

$$\ln \frac{P}{P_0} = \frac{2\gamma V_m}{rRT} \quad (4.2)$$

with a water surface tension of $\gamma = 0.07286$ N/m, a molar volume of the water $V_m = 0.00001801528$ m³/mol and the universal gas constant $R = 8.314$ J/kMol (all at 293.15 K *i.e.* 20 °C), size limits between empty pores and saturated pores can be reasonably estimated for $RH < 98\%$. 91% RH corresponds to a limit size for empty pores at 22.84 nm in diameter. For pores of 2.5 nm (gel pore size) to be empty, the relative humidity should be below 42%. For this reason, the conclusion is made that in the absence of remaining capillary water, the hydration continues to take place (creation of C–S–H layers) using the gel water, which then has become the biggest water reservoir in the paste. The creation of one or two C–S–H layers into a gel pore (Figure 4.10a→b) can result in a decrease in the signal fraction I_{gel} in favour of the signal fraction I_{CSH} .

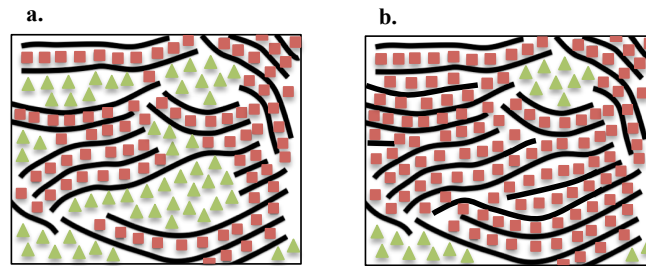


Figure 4.10 – Change in C–S–H water signals by the creation of solid layer(s) into gel pores. This is the suspected mechanism for long term hydration when the interhydrate water has been totally consumed.

4.2.8 Chemical shrinkage volume

Chemical shrinkage, due to the lower specific volume of the hydration products compared to the solid reactants and water, creates porosity that is expected to be of the order of 7–10% the total volume [3]. The sealed pastes of the present study therefore have empty voids not filled with water and hence invisible during ^1H NMR experiments. Figure 4.11 shows the chemical shrinkage volume as measured by the conventional capillary height method for different w/c ratios and sample ages (3, 10 and 28 days). A linear best fit to the data yields a chemical shrinkage of $0.075 \pm 0.003 \text{ cm}^3/\text{g}$ of reacted anhydrous white cement.

In addition to the conventional chemical shrinkage method, a test was carried out exposing sealed samples to extra water. Mature samples with different water-to-cement ratios were broken into mm pieces and immersed in water for 3 days in a low environmental pressure. This vacuum was used to favour water to penetrate into the empty chemical shrinkage volume. Neglecting the extra hydration due to water supply, mass increase and NMR signal increase were measured after 3 days of water exposure. The results are presented in Figure 4.11.

The sample voidage obtained by “re-wetting” experiments consistently under-estimates by circa 50% that by conventional chemical shrinkage method. This highlights the fact that some empty voids might be poorly, or simply not, connected to the exterior. Almost half of the chemical shrinkage volume was not accessible to external water on the time-scale and in the conditions of the experiment. For this reason, the sample voidage measured by the conventional method is considered to be more correct and was further used for calculations.

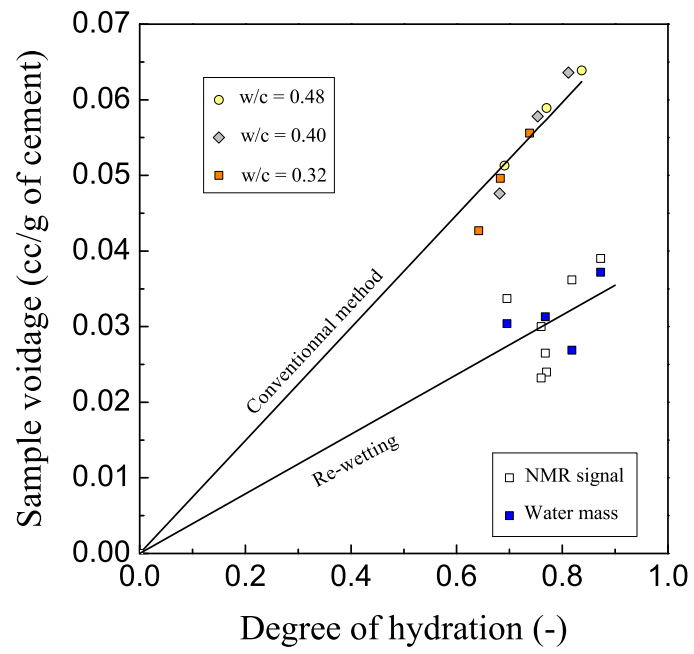


Figure 4.11 – Voidage volume measured by the conventional technique and by re-wetting experiments. Solid lines are linear least-squares fits to the data.

4.3 Theory - calculations based on NMR signals

4.3.1 Mass and volume paste composition

Based on the signal fractions of the different NMR populations, mass (Equation 4.3) and volume (Equation 4.4) balance equations can be written for the pastes per gram of anhydrous powder:

$$1 + \frac{w_{\text{mix}}}{c} = (1 - \alpha) + \frac{w_{\text{mix}}}{c} [\beta I_{\text{solid}} + \gamma I_{\text{CSH}} + \delta (I_{\text{gel}} + I_{\text{cap}})] \quad (4.3)$$

$$\frac{1}{\rho_{\text{uc}}} + \frac{w_{\text{mix}}}{c \rho_w} = \frac{(1 - \alpha)}{\rho_{\text{uc}}} + \frac{w_{\text{mix}}}{c} \left[\frac{\beta I_{\text{solid}}}{\rho_{\text{solid}}} + \frac{\gamma I_{\text{CSH}}}{\rho_{\text{CSH}}} + \frac{\delta (I_{\text{gel}} + I_{\text{cap}} + I_{\text{void}})}{\rho_w} \right] \quad (4.4)$$

The subscripts *uc*, *solid*, *CSH*, *gel*, *cap* and *voids* refer to unreacted cement, chemically combined water, C–S–H, gel pore water, capillary pore water and chemical shrinkage respectively. In Equation 4.3, the left hand side is the sum of the original anhydrous powder and the mix water mass (w_{mix}). The right hand side is the sum of the masses of the different products, written in terms of their respective water contents and NMR signals I . Equation 4.4 reworks Equation 4.3 for volumes by dividing by the product densities, ρ , and adding a term for the chemical shrinkage volume (I_{void}). The measured water signal intensities are expressed as a fraction of total signal intensity, I , arising from the original water of mixing as presented, for instance, in Figure 4.3. For sealed pastes, this leads to $I_{\text{solid}} + I_{\text{CSH}} + I_{\text{gel}} + I_{\text{cap}} = 1$. The signal fraction I_{void} takes the total above unity. It corresponds to the water which would occupy the chemical shrinkage volume. For sealed cured samples, as here, I_{void} is calculated from a separate measurement of the chemical shrinkage volume, which led to a linear relationship with the degree of cement reaction α . α is defined as the mass fraction of anhydrous powder consumed in the reactions. The parameters β , γ and δ are the inverse mass fractions of water in the solid, C–S–H and pore fluid respectively. The pore fluid is treated as water, so that $\delta = 1$. $\rho_{\text{uc}} = 3.15 \text{ g/cm}^3$ and $\rho_w = 1 \text{ g/cm}^3$ respectively.

The solid signal is assumed to comprise two parts, CH and ettringite: $I_{\text{solid}} = I_{\text{CH}} + I_{\text{ett}}$. The separation is done using XRD results with Rietveld quantification. There are two means by which the NMR CH content may be determined.

(1) One is to subtract the XRD ettringite mass, converted into water fraction with $I_{\text{ett}} = m_{\text{ett}}^{\text{XRD}} / (0.4\beta_{\text{ett}})$, from the NMR solid signal I_{solid} as $I_{\text{CH}} = I_{\text{solid}} - I_{\text{ett}}$.

(2) The other is to apportion the NMR solid signal between CH and ettringite in the same ratio

as measured by XRD.

The former is used for two reasons. First, beyond the early stages of hydration, the ettringite content is constant whereas the CH content is increasing. Thus, in principle, a measurement of the ettringite is only required at one time point. Second, the ettringite content is relatively difficult to measure, so an average content from multiple samples may be used. The total mass and volume of the solid products (CH and ettringite) per gram of anhydrous powder are given by respectively

$$\frac{w_{\text{mix}}}{c} \times \beta I_{\text{solid}} = \frac{w_{\text{mix}}}{c} \times (\rho_{\text{CH}} I_{\text{CH}} + \rho_{\text{ett}} I_{\text{ett}}) \quad \text{and} \quad \frac{w_{\text{mix}}}{c} \times \frac{\beta I_{\text{solid}}}{\rho_{\text{solid}}} = \frac{w_{\text{mix}}}{c} \left(\frac{\beta I_{\text{CH}}}{\rho_{\text{CH}}} + \frac{\beta I_{\text{ett}}}{\rho_{\text{ett}}} \right) \quad (4.5)$$

From the known composition of $\text{Ca}(\text{OH})_2$, $\beta_{\text{CH}} = 74/18$ [80, 81]. Similarly, $\beta_{\text{ett}} = 1255/576$ [87, 88]. Once I_{ett} is known, I_{CH} may be calculated from I_{solid} and known constants, as may β and ρ_{solid} . $\rho_{\text{CH}} = 2.24 \text{ g/cm}^3$ and $\rho_{\text{ett}} = 1.77 \text{ g/cm}^3$ respectively.

The unknowns are therefore α , I_{ett} , ρ_{CSH} and γ . A measurement of α and I_{ett} was made independently using XRD. Hence, two equations remain that enable the C–S–H density, ρ_{CSH} , and its inverse mass fraction of water, γ , to be found.

4.3.2 C–S–H chemical composition

The C–S–H chemical composition is expressed as



The parameters x , y and z may be determined from three further equations. First, γ is related to the number of water molecules x as

$$x = \frac{56z + 9y + 51}{18(\gamma - 1)} \quad (4.7)$$

where $y = n_{\text{Si}}^{\text{CSH}} / (n_{\text{Si}}^{\text{CSH}} + n_{\text{Al}}^{\text{CSH}})$ and $n_{\text{Si,Al}}^{\text{CSH}}$ are the molar content of Si and Al in the C–S–H. The numerical constants derive from the atomic masses of Ca, Si, Al, O and H. Second, a conservation equation can be written for the overall Ca/(Si+Al) ratio. If α' is defined as the mass of reacted ($\text{C}_3\text{S} + \text{C}_2\text{S}$) divided by the mass of the anhydrous powder, and ignoring minor

reactive components other than C_3A , then

$$\frac{3 \left(\frac{0.9\alpha'}{C_3S^{AMU}} \right) + 2 \left(\frac{0.1\alpha'}{C_2S^{AMU}} \right) + 1.5n_{Al}^{CSH}}{\left(\frac{0.9\alpha'}{C_3S^{AMU}} \right) + \left(\frac{0.1\alpha'}{C_2S^{AMU}} \right) + n_{Al}^{CSH}} = \frac{\frac{I_{CH}n_{Hyd}}{2} + \frac{I_{CSH}n_{Hyd}z}{2x} + 1.5n_{Al}^{CSH}}{\frac{I_{CSH}n_{Hyd}y}{2x} + n_{Al}^{CSH}} \quad (4.8)$$

The first term of the numerator of the left hand side of this expression expresses the fact that there are 3 moles of Ca per mole of C_3S ; $1/C_3S^{AMU}$ moles per gram of C_3S ; and that subject to the assumptions detailed below, $0.9\alpha'$ grams C_3S is consumed in reactions per gram of anhydrous cement. Similar arguments for Ca from C_2S and for Si from C_3S and C_2S lead to the second term of the numerator and the first two of the denominator respectively. Ca and Al derived from C_3A lead to the final term in the numerator and denominator respectively. On the right hand side, $n_{Hyd} = (w/c) \times (2/H_2O^{AMU})$ is the molar content of hydrogen in the paste per gram anhydrous powder. The moles of Ca and Si in the CH and C–S–H are written in terms of the signal fractions and n_{Hyd}^* . The Ca and Al contributions to the C–S–H from the C_3A are the same as on the left hand side. The further assumptions leading to Equation 4.8 as stated are as follows.

(1) It is known that in the hydration reaction, C_3S is consumed much more quickly than C_2S [89]. Hence, a consumption ratio of 9:1 in favour of C_3S is assumed until it has been used up. This implies that Equation 4.8 is valid in the range $0 < \alpha' \leq f_{C3S}/0.9$ where f_{C3S} is the fraction of C_3S in the anhydrous powder (assuming $f_{C3S}/9 < f_{C2S}$, the C_2S fraction). Equation 4.8 may be re-cast for $f_{C3S}/0.9 < \alpha' \leq 1$ by replacing α' in the first two terms in both the denominator and numerator of Equation 4.8 by $f_{C3S}/0.9$ and adding an additional term to the numerator of $2(\alpha' - f_{C3S}/0.9)/C_2S^{AMU}$ and of half this value to the denominator.

(2) X-ray analysis of samples at different ages showed that ettringite all forms early, at most within the first day. Since the analysis mainly focuses on data acquired after 1 day, the simplifying assumption that the ettringite forms at the start of the process is made and thereafter remain constant.

(3) The aluminium from the C_3A remaining after ettringite formation is assumed to be included in the C–S–H from the start. The factors determining the extent of aluminium uptake into the C–S–H are not well understood [90]. This hypothesis implies there is a negligible amount of alumina in the pore solution, which is in agreement with thermodynamics and experimental results [91]. It follows that $n_{Al}^{CSH} = 2(f_{C3A} - f_{C3A}^{ett})/C_3A^{AMU}$, where f_{C3A} and f_{C3A}^{ett} are the mass fractions of C_3A in the anhydrous powder and the C_3A mass fraction used to form ettringite respectively.

Finally, given the above assumptions concerning the formation of ettringite, the Si to (Si+Al)

*To avoid confusion with the cement notation representing water, atomic hydrogen is notated Hyd.

ratio, y , can be expressed as

$$y = \frac{n_{\text{Si}}^{\text{CSH}}}{n_{\text{Si}}^{\text{CSH}} + n_{\text{Al}}^{\text{CSH}}} = 1 - \frac{4x(f_{\text{C3A}} - f_{\text{C3A}}^{\text{ett}})}{I_{\text{CSH}} n_{\text{Hyd}} C_3 A^{\text{AMU}}} \quad (4.9)$$

The alternate C–S–H composition including gel water, $\text{Ca}_z \cdot (\text{Si}_y, \text{Al}_{(1-y)}) \cdot \text{O}_{(z+1/2y+3/2)} \cdot (\text{H}_2\text{O})_{x'}$ has

$$x' = x(I_{\text{CSH}} + I_{\text{gel}}) / I_{\text{CSH}} \quad (4.10)$$

In summary, the inverse water content of the C–S–H γ is found, from Equation 4.3, the NMR intensities and an XRD measurement of the degree of hydration and ettringite content. Hereafter is found the C–S–H density from Equation 4.4 knowing additionally the chemical shrinkage. Finally, using Equations 4.7, 4.8 and 4.9 and the anhydrous powder composition, the three C–S–H composition parameters, x , y and z are found. Of these, x gives the water molar content and z the Ca/(Si+Al) ratio of the C–S–H.

4.4 Analytical results - C-S-H characteristics

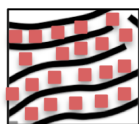
The statistical analysis of the error for the different C-S-H parameters calculated through the set of equations is difficult to make due to many different contributions. A sensitivity analysis is presented in section 4.6, p. 78. Indicative errors were however calculated based on the scatter; these are absolute errors on the presented values. Early NMR measurements have larger uncertainty as signals arising from C-S-H are weaker. For this reason, no calculation is done before 1 day of hydration.

4.4.1 C-S-H density

C-S-H density with time ($w/c = 0.40$)

The type of C-S-H structure most likely to explain the NMR data is presented in Figure 4.12. It depicts a continuous network of C-S-H layers and gel pores and closely resembles to the picture of C-S-H from Feldman and Sereda [12] (Figure 1.9b, p. 10). However, there are some differences. The primary difference between the picture of C-S-H morphology emergent from NMR and that proposed by Feldman and Sereda is that the latter proposed C-S-H with mainly interlayer water and physically adsorbed water but no larger intrinsic reservoirs. The picture of C-S-H coming from NMR relaxometry displays two distinct categories of pores: interlayer spaces of about 1 nm and gel pore spaces in the order of 2.5 nm.

a. Solid C-S-H



b. Bulk C-S-H

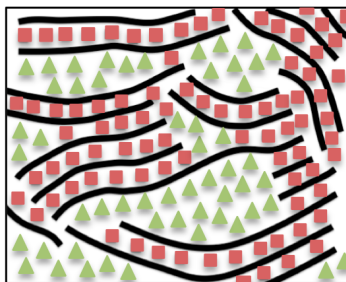


Figure 4.12 – Graphical representation of the C-S-H as seen by ^1H NMR. The solid lines are the calcium oxide layers with silicate tetrahedral attached on both sides; the red squares are the interlayer water and the green triangles represent the gel water. The figure illustrates what is defined as “solid C-S-H” and “bulk C-S-H”.

The data presented in the foregoing sections allows the calculation of C-S-H density and composition according to Equations 4.3 to 4.9. The way water is probed in both interlayer and gel pore spaces of C-S-H allows us to consider the C-S-H exclusive (called “solid C-S-H”) or inclusive (called “bulk C-S-H”) of the gel water. The NMR derived solid C-S-H density

excludes water (and surface hydrogen contacting water) on the surfaces of the agglomerates since such surface water is in rapid exchange with the gel pore fluid (longer T_2 of circa 300 μ s). The solid C–S–H then includes the Ca–O layers with SiO_2 tetrahedra and the interlayer water in between but specifically excludes the water and any hydroxyls on the outermost C–S–H surfaces. The bulk C–S–H stands for the overall C–S–H phase inclusive of the gel water. Solid and bulk C–S–H as envisaged and considered in calculations are schematically illustrated in Figure 4.12a and b.

Results for C–S–H density are presented in Figure 4.13. The NMR density at any one time is the average of all the C–S–H formed at that time.

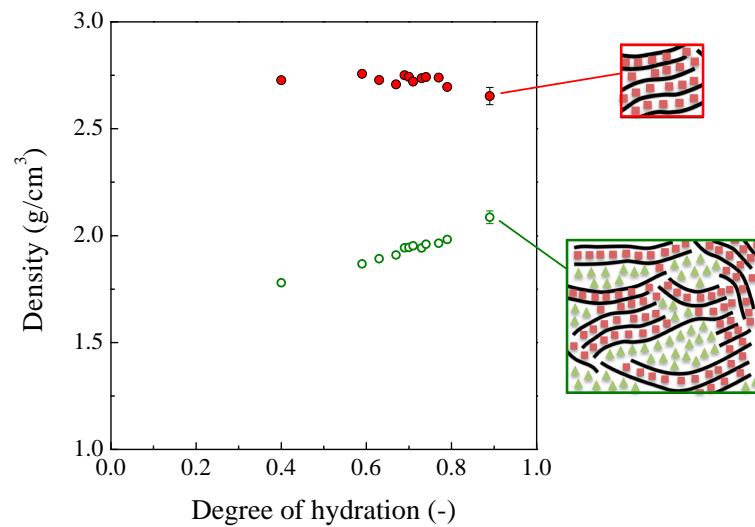


Figure 4.13 – C–S–H density as a function of the degree of hydration ($w/c = 0.40$). Solid symbols are the C–S–H solid density, exclusive of the gel water; empty symbols are for C–S–H bulk density, inclusive of the gel water.

The solid C–S–H density, exclusive of the gel pores, ρ_x , is largely independent of degree of hydration, decreasing only very slightly from $\rho_x = 2.73 \pm 0.04 \text{ g/cm}^3$ at 1 day ($\alpha = 0.4$) to $\rho_x = 2.69 \text{ g/cm}^3$ at 2 months ($\alpha = 0.8$) and on to $\rho_x = 2.65 \text{ g/cm}^3$ at 10 months ($\alpha = 0.9$). Perversely, the decrease arises due to “densification” of the C–S–H. As C–S–H densifies, the local number of aggregated layers increases. Hence, the ratio of calcium silicate layers (s) to interlayers of water ($s-1$) asymptotically decreases to 1. As the calcium silicate layer is denser than water, the average density falls.

The bulk C–S–H density, including the gel water, $\rho_{x'}$, behaves in opposite manner. It increases, and markedly so, during hydration. After 2 day, ($\alpha > 0.59$), the total volume of gel water plateaus but the hydrates continue to grow by consuming the interhydrate water. Hence, the bulk C–S–H density necessarily increases. Later, when the interhydrate water is fully

consumed (2 months, $\alpha = 0.8$), hydrates grow at the expense of gel water. The density rise continues and the values for the mature paste, $\rho_x \approx 1.96 \text{ g/cm}^3$ at 28 days, agree very well with the densities calculated by other methods: $\rho_x = 1.90 \text{ g/cm}^3$ by combined SEM/XRD [92]; between $\rho_x = 1.83 \text{ g/cm}^3$ and $\rho_x = 2.03 \text{ g/cm}^3$ from modelling and SANS measurements depending on the chosen volume and computing parameters [7, 16].

The plateau of the gel pore formation

The plateau of the gel pore formation was interpreted in this thesis as the creation of new C–S–H (layers) devoid of gel porosity. However, there is another way of interpreting the data saying that C–S–H hydrates still precipitate with gel porosity but in such a confined space that it pushes on the surrounding solids and generates, “by reciprocity”, the collapse of other gel pores elsewhere in the paste. This last explanation is not favoured for the following reasons.

- (1) The nucleation of C–S–H layers within gel pores (*cf.* long term NMR data) supports the hypothesis that C–S–H layers can nucleate on their own without gel pores (see Figure 4.10, p. 62 for the illustration of this phenomenon).
- (2) The second reason is that, based on SEM BSE images (an example is given in Figure 1.13, p. 16), outer-product (*i.e.* low density C–S–H) are rarely seen within the proximity of cement grains, where new C–S–H are more likely the have been formed.

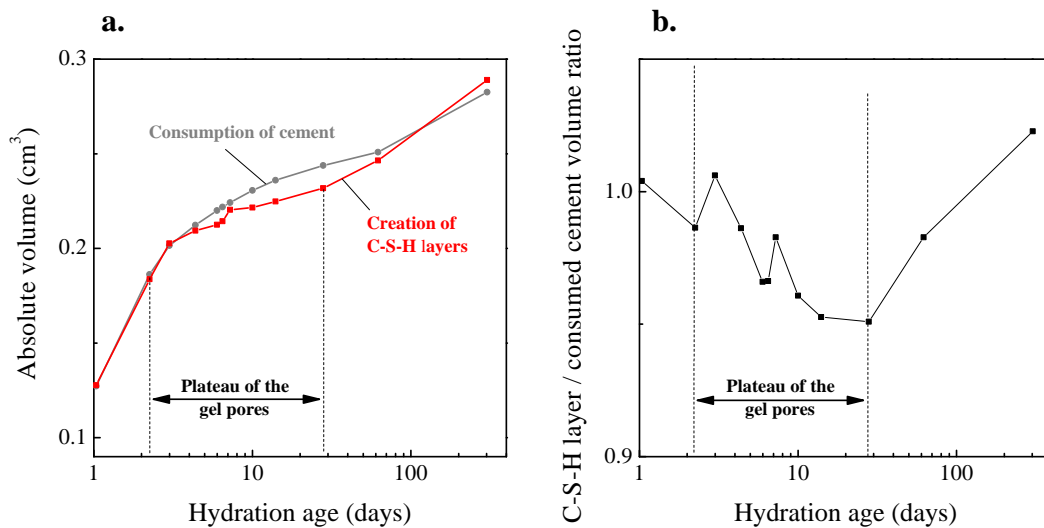


Figure 4.14 – Volume of cement consumed and volume of C–S–H layers created for the white cement paste mixed at $w/c = 0.40$ as a function of time.

Figure 4.14a shows the volume of cement consumed in parallel with the volume of C–S–H layers (including the interlayer water) that is created as a function of time. Figure 4.14b shows

the volume ratio of C–S–H layers over reacted cement as a function of time. A change in regime is observed at the beginning and at the end of the plateau of the gel pores formation. This clearly indicates that there might be different kinds of C–S–H nucleation processes which further supports the option (I). The conclusion is made that in restricted space, C–S–H layers are created devoid of gel pores.

Corrections to the density for C–S–H surface water

Measurements of the C–S–H density depend upon method and sample preparation and care must be taken when comparing the density and water fraction of C–S–H according to different models. Results of different studies and calculations have been reviewed by Jennings [7] in the context of the colloidal model and vary between 1.8 and 2.8 g/cm³. Much of this variability arises from the fraction of the gel pore water and other nanoscale confined or bound water that is, or is not, inferred to be included in the measurement. It also depends on whether or not the sample has been dried, a process that potentially damages the delicate nano-structure.

As explained earlier, the NMR solid C–S–H density excludes the adsorbed layer of water on the outer surface of agglomerates of C–S–H layers (Figure 4.12a). Taking tobermorite 14 Å [6] as a C–S–H analogue, then the layer repeat distance is 1.4 nm. If there are three layers as the NMR results suggest (*cf.* section 4.4.3, p. 76), then the NMR thickness is $3 \times 1.4 - 2 \times 0.28 = 3.64$ nm. If a monolayer coverage of water molecules is added on the outer surface of the C–S–H agglomerate, the NMR density ρ_x decreases to $\rho_x^m = (3.64\rho_x + 0.56)/4.2$. For example, for $\rho_x = 2.70$ g/cm³, the density reduces to $\rho_x^m = 2.47$ g/cm³ (Figure 4.15).

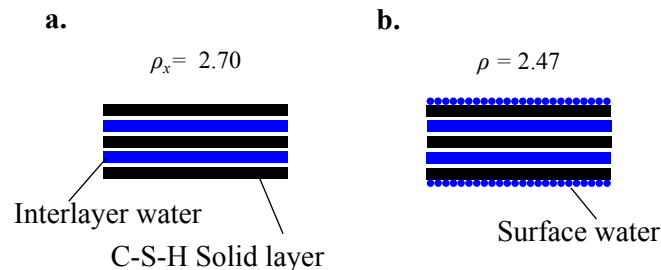


Figure 4.15 – Influence of surface water to the solid C–S–H density as calculated by NMR.

A recent and widely cited result [93] is the density obtained by small angle neutron scattering (SANS) for C–S–H in Portland cement hydrated for 28 days at 20 °C. This measurement is made in saturated material but is specifically for the solid nano-crystalline C–S–H excluding water on particle surfaces: $\rho = 2.604$ g/cm³. NMR gives a slightly larger average value of $\rho_x = 2.71$ g/cm³ between 7 and 300 days hydration. When the surface water correction is applied ($\rho_x = 2.47$ g/cm³), the density becomes identical to the value reported by Jennings [7], $\rho = 2.47$ g/cm³, for a saturated globule with a monolayer of water at 11% RH.

C–S–H density as a function of w/c

Figure 4.16 shows the calculated densities as a function of w/c for samples at 28 days of sealed hydration. Since the solid C–S–H density probes only the locally stacked C–S–H layers, ρ_x is constant as expected. The slight increase in ρ_x for $w/c = 0.48$ may be explained by a lower ratio of layers to interlayer spaces, $s/(s-1)$.

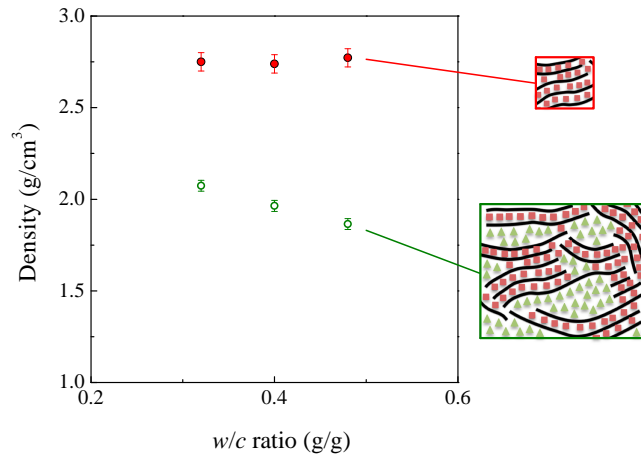


Figure 4.16 – C–S–H density as a function of w/c at 28 days of hydration.

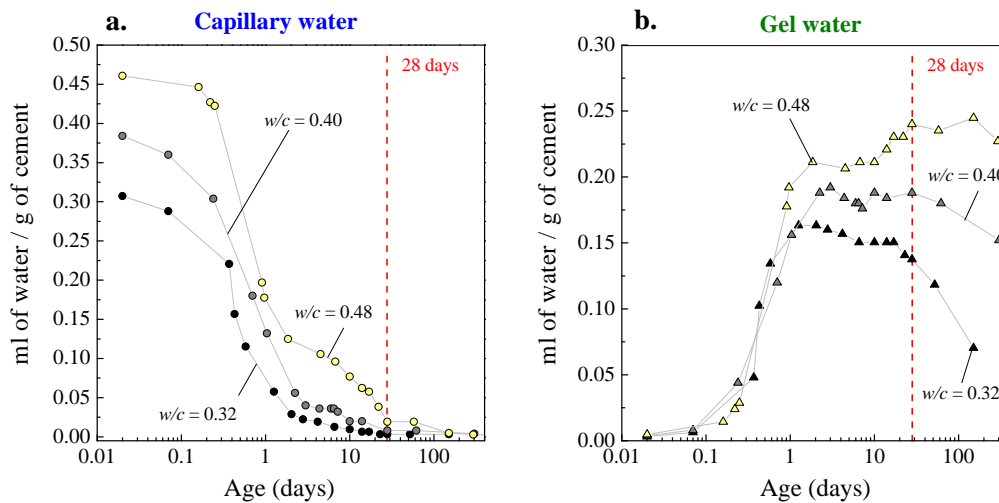


Figure 4.17 – Capillary and gel absolute water contents for $w/c = 0.32, 0.40$ and 0.48 .

To help interpreting bulk densities, Figure 4.17 shows the evolution of the absolute gel and capillary water contents for the three mixes as a function of time. At 28 days of hydration, the amount of capillary water is almost equal for all w/c . However the amount of gel water

increases with increasing the w/c . This has a direct influence on the bulk C–S–H density, $\rho_{x'}$, as more gel water has been formed for 1 gram of cement. In the range of w/c studied, there is a linear relationship between the C–S–H bulk density and the initial water content of the paste.

4.4.2 C–S–H Chemical composition

Evolution with time at $w/c = 0.40$

The results of the Ca/(Si+Al) ratio, z , of the C–S–H are shown as a function of degree of hydration in Figure 4.18a. Overall, z decreases with increasing degree of hydration. At 300 days, the Ca/(Si+Al) ratio of the C–S–H is 1.70 ± 0.04 , which is in good agreement with previous studies [94]. There is a clear difference in the calculated Ca/(Si+Al) ratio of the C–S–H during the first few days ($\alpha < 0.63$, $z \approx 1.84$) and that calculated later ($\alpha > 0.63$, $z \approx 1.70$). A transition in the rate of increase of gel porosity at around 2-3 days was previously identified to be a transition from growth of low to high density C–S–H. Some authors claimed that the Ca/(Si+Al) ratio may be different in the two types of product, as suggested by, for instance, Taylor *et al.* [94]. However, recent works made by Bazzoni [95] and Rossen [70] suggest that the Ca might leave the C–S–H layers rather than a clear change in compositions between different C–S–H. A decrease in the Ca/Si of the C–S–H with time was also observed by Bazzoni [95] for hydrating C_3S .

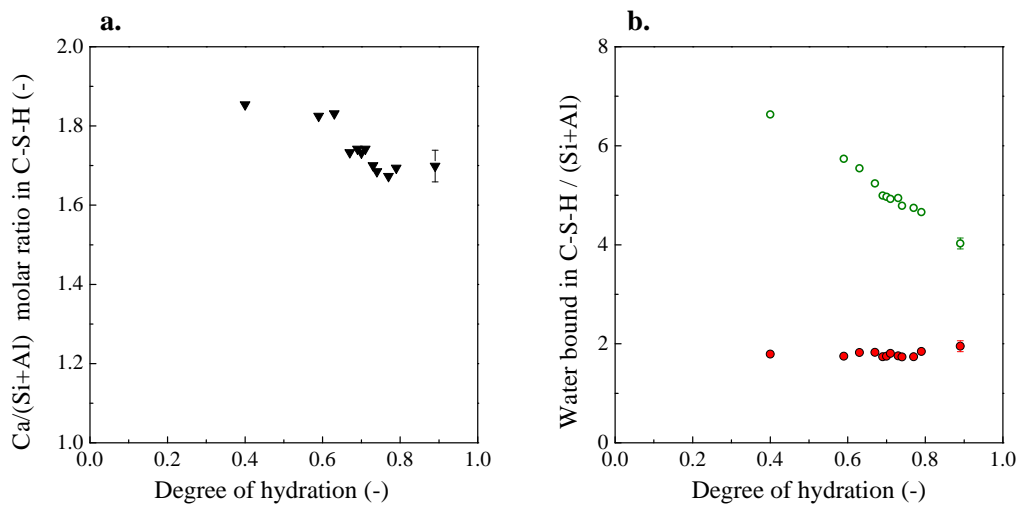


Figure 4.18 – (a) Ratio Ca/(Si+Al) and (b) the water in the C–S–H, excluding (x , solid circles) and including (x' , open circles) gel water as a function of degree of hydration for the $w/c = 0.40$ paste.

The water content of C–S–H without and with the gel water included, x and x' are shown in Figures 4.18b for the $w/c = 0.4$ paste as a function of degree of hydration. The value x for the water content excluding gel water follows the inverse trend of ρ_x . The slight increase in x

beyond 2 days ($\alpha \approx 0.6$), is attributed to densification and the increase of locally aggregated C–S–H sheets, and hence more water molecules, x , per Si or Al atom. The average value of x between 7 and 300 days is 1.80 ± 0.08 . On the other hand, the value of x' , that includes the gel water, decreases as the paste densifies. These results are entirely consistent with the changes in the densities.

The parameter $y = n_{\text{Si}}^{\text{CSH}} / (n_{\text{Si}}^{\text{CSH}} + n_{\text{Al}}^{\text{CSH}})$ ranges from 0.94 at 2 days hydration to 0.96 in the mature paste reflecting the fact that the Al is incorporated early in the process.

Evolution as a function of w/c

Figure 4.19a shows the dependence of Ca/(Si+Al) ratio on the w/c ratio after 28 days of hydration. The higher the water-to-cement ratio, the less calcium ions are incorporated into the C–S–H nano-structure. Figure 4.19b shows the associated water contents as a function of w/c . Again, the trends of water bound in the C–S–H microstructure, x and x' , follow the inverse behaviour of ρ_x and $\rho_{x'}$.

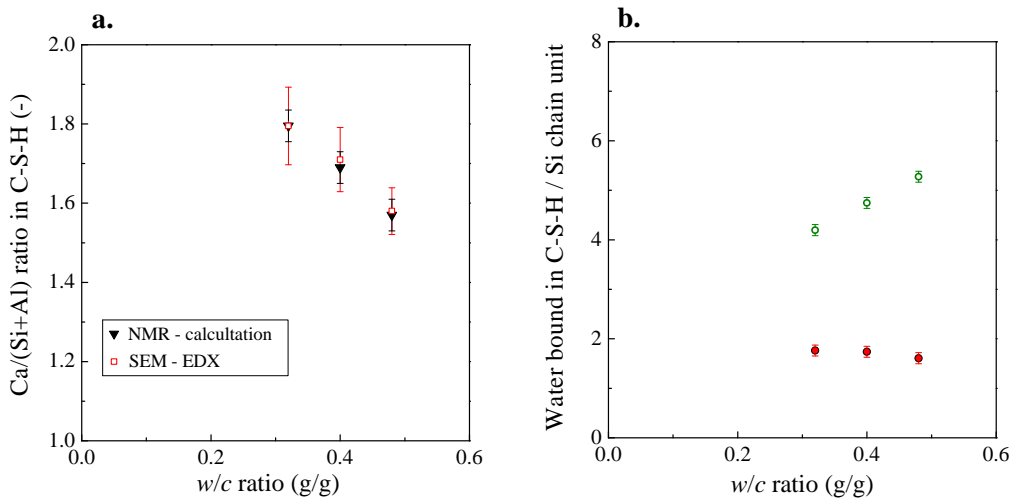


Figure 4.19 – (a) Ca/(Si+Al) ratio of the C–S–H and (b) the water in the C–S–H as a function of w/c ratio. Symbols are in accordance with previous figures.

In order to verify experimentally the NMR estimates for the Ca/(Si+Al) of the C–S–H, SEM-EDX experiments were carried out. Using backscattered images and point analysis, outer- and inner-C–S–H can be distinguished [14]. Outer-C–S–H have a brighter grey level while inner-C–S–H are mainly localized within the original cement grains. A BSE micrograph is presented in figure 4.20 showing a typical map of points for inner- and outer-C–S–H. The resulting SEM-EDX spectra are presented separately in Figure 4.21 for the different w/c ratio pastes. As discussed p. 45, the extreme Si edge of the distribution was considered to be more representative of the real Ca/Si ratio of the C–S–H.

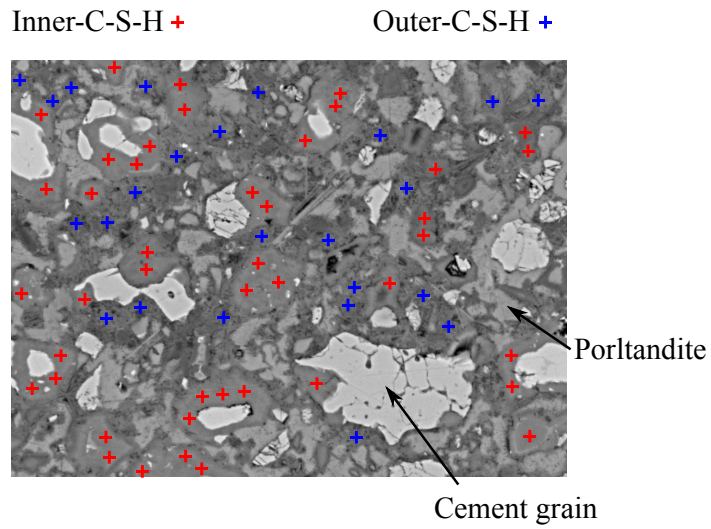


Figure 4.20 – SEM BSE micrograph of $w/c = 0.40$ paste after 28 days of hydration, showing the positioning of the points for the EDX-SEM analysis.

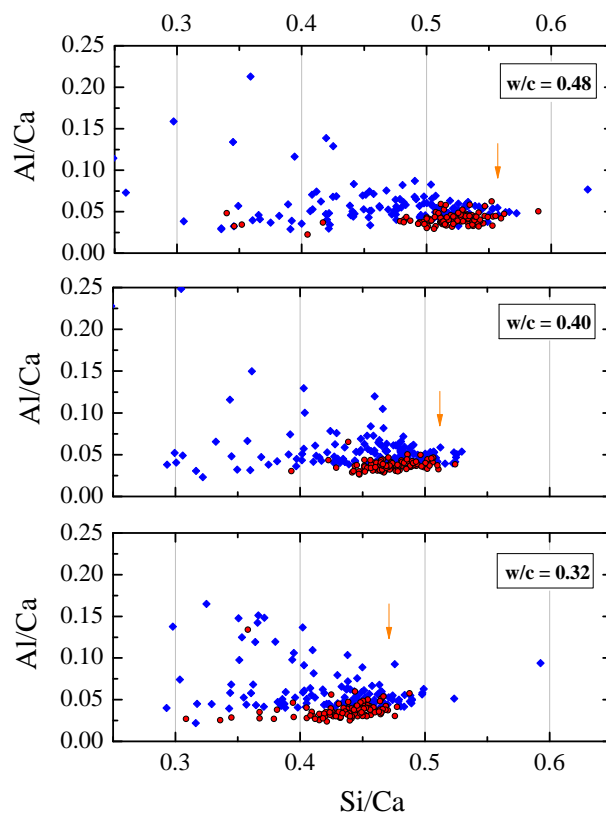


Figure 4.21 – SEM-EDX quantification of 28 days old pastes with different w/c . Inner-C-S-H are black circles and outer-C-S-H blue diamonds.

The calculated Ca/(Si+Al) ratios based on SEM-EDX analysis are reported in Figure 4.19a and compared to the values calculated from NMR. There is a good agreement between the two techniques. The important decrease in Ca/(Si+Al) ratio observed when increasing the w/c ratio is accompanied by a change in Portlandite content. Normalized per gram of cement and at a constant degree of hydration ($\alpha = 0.74$), the Portlandite contents are 0.221, 0.271 and 0.324 ± 0.01 g/g of cement for $w/c = 0.32, 0.40$ and 0.48 respectively. So the calcium not in Portlandite ends up in C–S–H and *vice versa*.

4.4.3 Specific surface area of the C–S–H interlayer and gel pores

The NMR signal intensities can be recalibrated as volume of water per unit volume of paste. Given the pore sizes, the specific surface area of the C–S–H interlayer spaces and of the gel pores may be calculated. They are $171 \text{ m}^2/\text{cm}^3$ and $111 \text{ m}^2/\text{cm}^3$ of paste respectively for the $w/c = 0.4$ paste at 28 days of hydration. These are close to the values usually reported using water sorption measurements [28]. The total, $282 \text{ m}^2/\text{cm}^3$ or $393 \text{ m}^2/\text{g}$ of cement, is comparable to the NMR value reported by Korb *et al.* [96] for a 4 days old white cement paste using field cycling relaxometry. They reported around $400 \text{ m}^2/\text{g}$.

Given the specific surface area and sizes of the interlayer and gel pores, the number of locally stacked layers comprising a region of C–S–H can only be two or three.

4.5 Mass and volume composition diagram

Figure 4.22(a-c) brings all the data together and shows revised composition diagrams of cement with $w/c = 0.32, 0.40$ and 0.48 , in a manner akin to the well known results of Powers and Brownyard [4]. The phase compositions are presented both in terms of mass and volume fractions. Two differences are immediately apparent.

First, there is a clear non-linearity in the growth of the gel water with degree of hydration. This feature was, in fact, not present in the Powers and Brownyard's proposal as they did not examine early age properties. The gel porosity of C–S–H develops mainly at early age when the volume of capillary water still remains significant. The gel water volume then plateaus and does not increase after, $\alpha = 0.33$ for $w/c = 0.32$, $\alpha = 0.56$ for $w/c = 0.40$ and $\alpha = 0.79$ for $w/c = 0.48$. Despite the differences in the gel/capillary water volumes at early age between NMR and the Powers and Brownyard model, the latter produces good result at later ages / larger degrees of hydration and therefore that it remains a powerful tool to predict long term paste composition.

The second difference between the two methods is that NMR subdivides the hydration products into crystalline phases and C–S–H. The colours shown in Figure 4.22 indicate the underlying NMR signal as presented in Figure 4.3, p. 56.

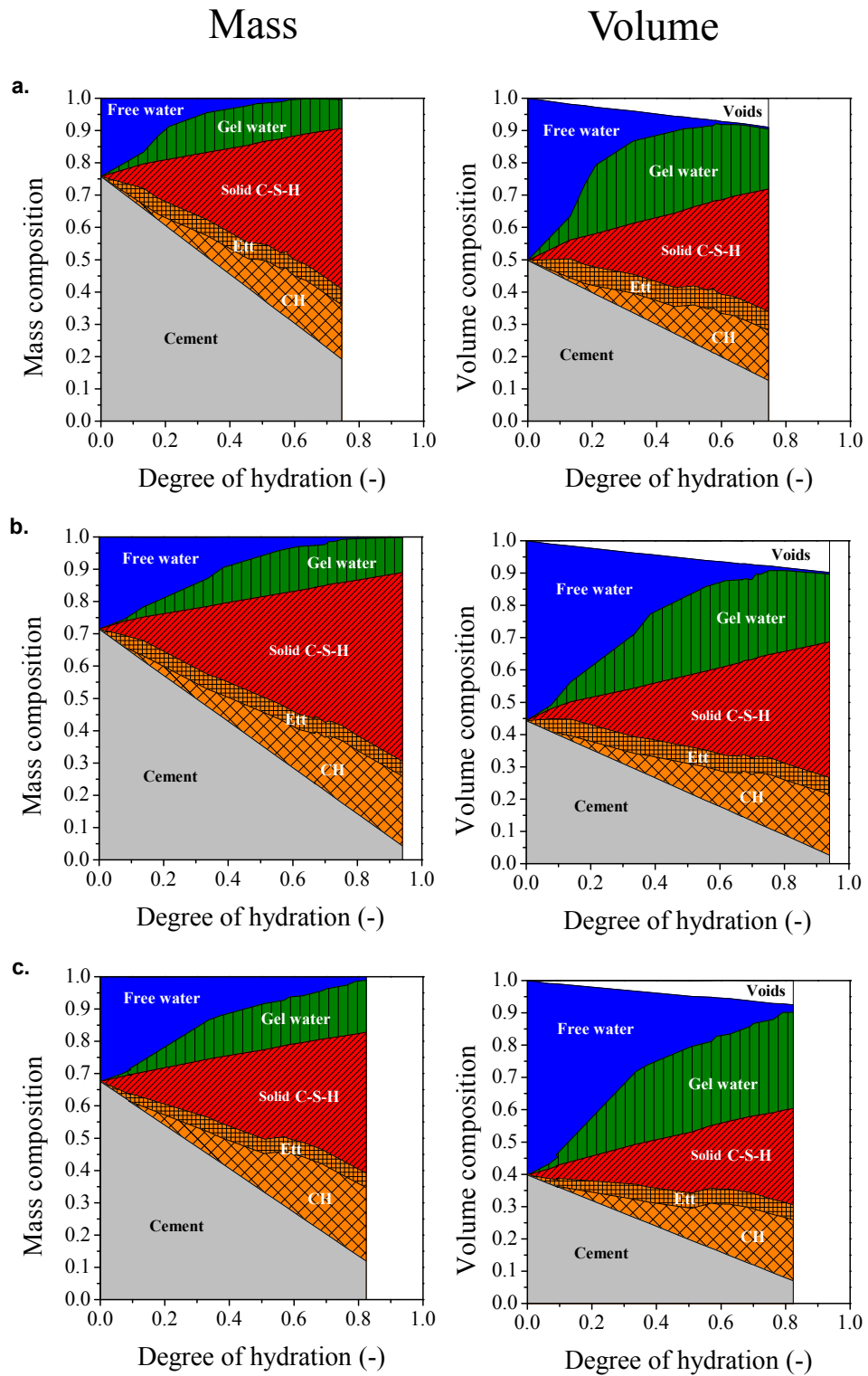


Figure 4.22 – Mass and volume composition of cement paste for (a) $w/c = 0.32$, (b) $w/c = 0.40$, and (c) $w/c = 0.48$. These results are calculated from the NMR signal intensities of samples measured as prepared throughout hydration. Colours indicate the underlying NMR water populations as presented in Figure 4.3.

4.6 Sensitivity analysis

The C–S–H parameters presented above depend on many different measured values through the system of Equations 4.3 to 4.9. In Table 4.3 is shown the sensitivity of these parameters to variations in the experimental values. While the ettringite and the voidage fraction have little impact on the calculations, a 5% change in the degree of reaction of cement affects all results by 2.5% to 5%. The total ^1H NMR signal is kept constant. A 5% change in the I_{solid} ^1H NMR signal compensated by a weighted change of the ^1H NMR liquid signals seems to have an important effect on the Ca/(Si+Al) ratio of the C–S–H as Portlandite contains a lot of Ca. A 5% decrease of the gel fraction, I_{gel} , with a compensating increase to the benefits of the interlayer signal, I_{CSH} , has the stronger effect and impacts the solid water content of the C–S–H up to 12%. However, the fact that different parameters are followed throughout the hydration and between different samples allows to better capture the paste variations. In addition, the comparison with other measurements gives confidence in the absolute input values and hence in the C–S–H results.

Table 4.3 – Sensitivity study of C–S–H density, water content and Ca/(Si+Al) calculation at 28 days of hydration.

Parameter changed by -5%	Solid C–S–H density	Solid H ₂ O/Si	Ca/(Si+Al)	Bulk C–S–H density
Initial values	2.74	1.74	1.67	1.96
Ettringite (g/g of cement)	-0.06%	-0.32%	-1.55%	-0.14%
DOH cement (α_c)	-2.65%	4.94%	-3.05%	-2.64%
Voidage (cm ³ /g of cement)	-1.06%	0.00%	-0.01%	-0.57%
NMR I_{solid} (with change in I_{liquid})	0.15%	1.69%	4.48%	0.44%
NMR I_{gel} (with change in I_{CSH})	-2.69%	12.14%	0.13%	0.00%

4.7 Desorption isotherm at 20 °C

4.7.1 Sample preparation and experimental procedure

All the NMR experiments of this section, apart from 100% RH sample, were performed by Agata Gajewicz using the NMR magnet in the physics department of Surrey University (Guildford, UK). However, the desorption results are important for the discussion of NMR signal analysis in the present document. Agata is one of the 15 TRANSCEND students who also worked with ^1H NMR relaxometry. The following of this section was jointly published with Agata Gajewicz in “*Microporous and Mesoporous Materials*” journal (*cf.* p.179).

Similar white cement as for sealed pastes was mixed with water in a w/c mass ratio 0.40. Aliquots, $\approx 0.35\text{ cm}^3$, were inserted into moulds and covered with a small quantity of saturated CH solution (less than 10% sample volume) for underwater curing, all at 20 °C. Samples were then measured by NMR after 28 days of underwater cure, removing the surface water before NMR experiments. Measurements of fully saturated samples were done at EPFL on the Bench-top spectrometer operating at 7.5 MHz. For the desorption isotherm measurements made by Agata, saturated samples were broken into millimetre sized pieces and equilibrated at constant relative humidity (RH) to constant mass in a moisture sorption analyser using N_2 gas. At every significant stage, samples were weighed with a microbalance. A Bench-top spectrometer operating at 20 MHz was used.

4.7.2 Effective water-to-cement ratio

As for sealed cured pastes, critical to the analysis is verification that the NMR measurements sense all the water in the sample. Figure 4.24a shows the total NMR intensity at 20 MHz as a function of sample mass during controlled drying of the underwater cured paste. The plot is linear. The intercept with the mass axis implies an effective $w_{\text{paste}}/c = 0.463$. The increase reflects that the sample is cured underwater and further proves that there is no “hidden” water.

4.7.3 Solid and liquid NMR components after 28 days of underwater cure

The QE solid signal fraction at 100% RH was $I_{\text{solid}} = 24.3 \pm 2\%$ and the mass of ettringite per gram of anhydrous detected by XRD was 0.083 g/g anhydrous cement. The solid signal then splits into that from CH and ettringite as 0.185 and 0.096 respectively. The average mass of Portlandite between XRD and TGA was $m_{\text{CH}} = 0.34 \pm 0.01$ g/g of cement, in good agreement with the NMR. The CPMG experiment subdivides the mobile water fraction into components with T_2 of $126 \pm 30\ \mu\text{s}$ ($I_{\text{CSH}} = 25.5 \pm 2\%$), $420 \pm 10\ \mu\text{s}$ ($I_{\text{gel}} = 44.1 \pm 2\%$), $1.4 \pm 0.2\text{ ms}$ and $12 \pm 2\text{ ms}$ ($I_{\text{cap}} = 6.1 \pm 2\%$ taken together). These populations are similar in amplitudes and T_2 to the ones recorded for sealed pastes (section 4.2.2, p. 52) and so is the signal assignment. The distribution of the liquid water populations is shown in Figure 4.23.

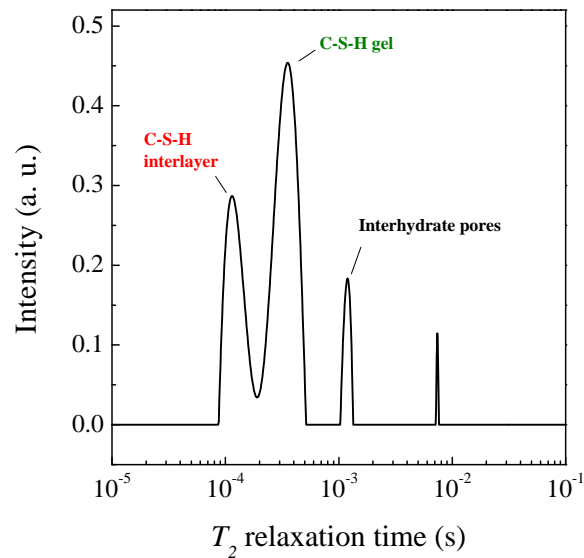


Figure 4.23 – Spectrum of the different liquid water populations measured by the CPMG pulse sequence on white cement paste after 28 days of underwater cured hydration.

4.7.4 Desorption isotherm results

Figure 4.24b. shows the amplitude of the four NMR components as a function of relative humidity. The data point at 100% RH was generated at EPFL. All points during the desorption (RH < 100%) were measured and analysed by Agata Gajewicz at University of Surrey. As such, it is the pore-size resolved desorption isotherm. The total signal loss closely resembles the first-drying weight-loss isotherm as reviewed by Jennings [7].

The capillary pore water dries above 90% RH. The gel pore water decreases from 50% of the total to practically zero between 100% and 25% RH. In the same range, the interlayer water apparently increases. This is because water associated with surface sites in a full gel pore rapidly exchanges with the pore fluid and therefore has the same T_2 . However, as the pore empties, so surface water is left as a less mobile monolayer that, in NMR terms, more resembles interlayer water with shorter T_2 . Below 25% RH, water is rapidly lost from the C–S–H interlayer spaces with a noticeable acceleration around 10% RH. At low RH there is an increase in the solid signal. Similar to the gel, as interlayer water is lost, so hydrogen in, for example, residual silanol groups appear solid-like. Figure 4.25 is a pictorial representation of C–S–H morphology and water placement consistent with the results.

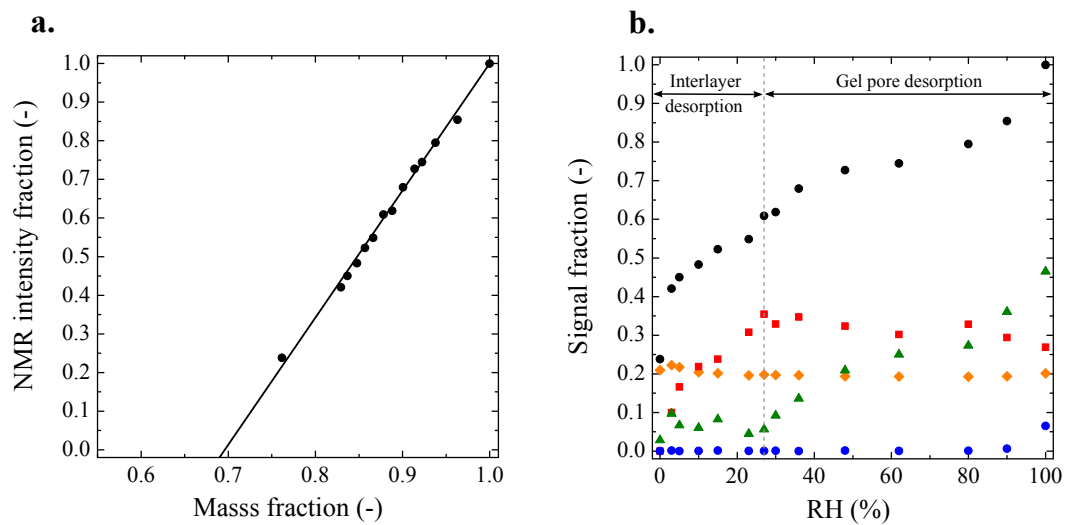


Figure 4.24 – (a) The total normalised NMR signal against relative sample mass in progressively dried white cement paste. (b) The total signal plotted against relative humidity (black circles) and de-composed into the different water populations. Symbols are similar as other NMR graphs.

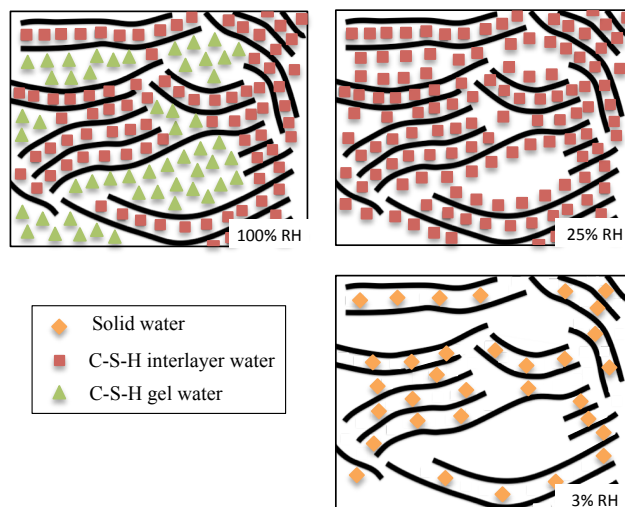


Figure 4.25 – A schematic of C-S-H morphology at 100, \approx 25, and \approx 3% RH. Solid lines are C-S-H sheets of Ca ions and SiO₂ tetrahedra.

4.7.5 Analysis of the results - C–S–H characteristics

Density and chemical composition of the C–S–H for the present saturated sample are calculated as for sealed systems using Equations 4.3 to 4.9. However, underwater curing introduces slight changes. I_i , the measured NMR signal fractions, become normalised to the total signal before chemical shrinkage (*i.e.* the creation of filled voids). Each signal fraction is then recalculated by $I_i^n = I_i \times (w_{\text{paste}} / w_{\text{mix}})$ and $I_{\text{void}}^n = (w_{\text{paste}} - w_{\text{mix}}) / w_{\text{mix}}$. In such, the statement $I_{\text{solid}}^n + I_{\text{CSH}}^n + I_{\text{gel}}^n + I_{\text{cap}}^n = 1$ still remains valid and the signal fraction I_{void}^n takes to total above unity. The normalized signal intensities of the solid, C–S–H interlayer, C–S–H gel, capillary and void water at 100% RH are $I_{\text{solid}}^n = 0.281$, $I_{\text{CSH}}^n = 0.295$, $I_{\text{gel}}^n = 0.510$, $I_{\text{cap}}^n = -0.086$ and $I_{\text{void}}^n = 0.157$, respectively. The negative sign implying that some water drawn into the sample has been used for hydration products.

Even though the sample was dried to determine the actual, as opposed to mix, water-to-cement ratio, density and chemical composition of the C–S–H can be calculated for “never-dried” material using the intensities at 100% RH. Solving Equations 4.3 to 4.9, the resultant solid C–S–H density after 28 days of underwater curing is $\rho_x = 2.68 \pm 0.04 \text{ g/cm}^3$, with composition $\text{Ca}_{1.53} \cdot (\text{Si}_{0.96}, \text{Al}_{0.04}) \cdot \text{O}_{3.51} \cdot (\text{H}_2\text{O})_{1.92}$. The calculated density and composition are for the calcium–oxygen layers and silicate of C–S–H with the interlayer space fully saturated. If gel water is included in the composition, the bulk density and water content are $\rho_{x'} = 1.89 \pm 0.02 \text{ g/cm}^3$ and $x' = 5.25 \pm 0.04$, respectively.

4.7.6 Pore size by amplitude model

From the NMR desorption isotherm, pore sizes may be calculated using the amplitude model [44] (*cf.* p. 29). The change in signal amplitudes with drying yields 1.6 nm, 3.4 nm and 10 nm for C–S–H interlayer, C–S–H gel and capillary pores respectively. The pore size values are fractionally bigger than calculated for sealed pastes based on the fast exchange model (0.85 nm for the interlayer, 2.5 nm for the gel and 8 nm for the interhydrate pores, p. 58). However, sealed measurements in this work were made at 7.5 MHz while the surface relaxivity parameter used in the fast exchange model was taken from the desorption experiment made by Agata Gajewicz at 20 MHz. This may cause this discrepancy as the surface relaxivity parameter is frequency dependent [41, 97].

Given the pore widths, the specific surface area (SSA) can be evaluated. From fast exchange, it is $91 \text{ m}^2/\text{cm}^3$ of paste for gel pores and $175 \text{ m}^2/\text{cm}^3$ for interlayer spaces in accord with earlier undifferentiated estimates [50, 56].

4.8 Sealed white cement paste cured at 10 °C

As discussed in the previous section, the effect of underwater curing slightly changed the density and the chemical composition of C–S–H at 28 days. The aim of this section is to apply a different type of cure to the same material, namely a change in temperature from 20 °C to 10 °C.

White cement pastes were cast at $w/c = 0.40$ following the same procedure as for the other sealed pastes in this work (*cf.* section 3.2, p. 36). Samples were measured by ^1H NMR relaxometry throughout the hydration at 10 °C. In parallel, XRD and TGA experiments were carried out at 10 days and 28 days of sealed hydration. The degree of cement reaction, the ettringite and Portlandite contents were calculated by Rietveld analysis. The chemical shrinkage volume at 10 °C was recorded as for pastes cured at 20 °C.

4.8.1 Experimental results

NMR signal amplitudes and T_2 relaxation times

Figure 4.26 shows the evolution of the different NMR signal fractions with time for the paste cured at 10 °C (coloured symbols); the data are compared to that cured at 20 °C (grey lines). For unexplained reasons, the scatter of the NMR results at 10 °C is higher than when the paste was measured at 20 °C. This will have a repercussion on the calculated density and chemical composition of the C–S–H.

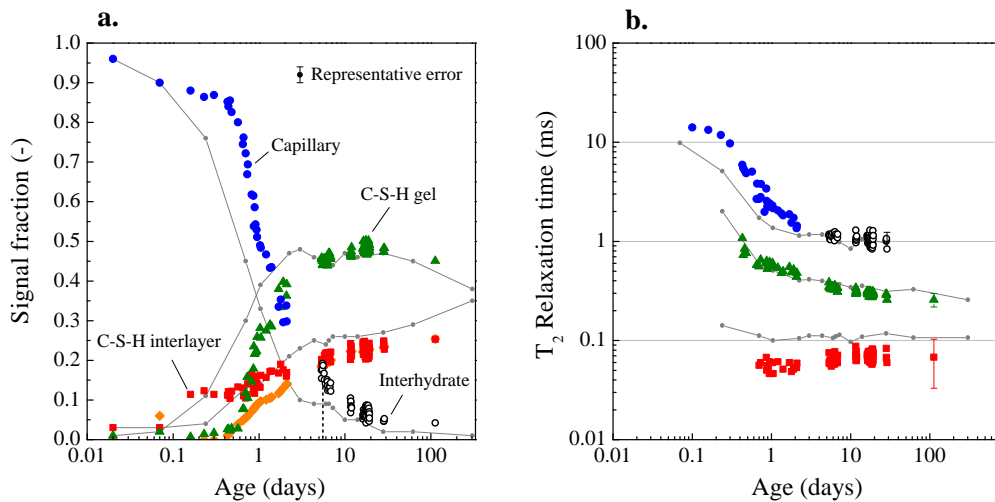


Figure 4.26 – (a) Evolution of the different NMR signal amplitudes with hydration time for sealed white cement paste mixed at $w/c = 0.40$ and cured at 10 °C. The error of the different signal amplitudes is $\pm 4\%$. (b) associated T_2 . Grey lines show the evolution of the paste cured at 20 °C.

The main difference for the curing at 10 °C compared to the paste cured 20 °C is that the amount of capillary water decreases much more slowly when the paste is cured at low temperature. This correlates with the smaller degrees of cement hydration reported in Table 4.4 at 10 and 28 days of hydration. The slowing down of the cement reactions at low temperature is a well-known effect.

As for the paste cured at 20 °C, a plateau in the formation of gel pore is observed. The maximum content of gel water remains however almost equivalent for both curing temperature. As previously observed when varying the *w/c* ratio (*cf.* section 4.2.7, p. 60), the plateau of the gel pore happens when the capillary water volume has reached a T_2 of 1 ms, at around 5-6 days.

Another difference between the two curing temperature is that after 2 days of hydration, the C–S–H interlayer signal fraction becomes smaller than when cured at 20 °C. The C–S–H layers also seem to appear earlier in the hydration process. These observations will not be further discussed in this document.

The T_2 of the C–S–H gel water are similar as when cured at 20 °C. However, the C–S–H interlayer space has an average T_2 of $70 \pm 40 \mu\text{s}$, which is smaller than the value reported at 20 °C ($T_2 \approx 100 \mu\text{s}$). This lower value could be interpreted as a smaller interlayer space according to the fast exchange model [46, 47]. However, this is difficult to substantiate. The fast exchange model of relaxation pre-supposes the existence of a surface water layer and bulk pore water. In such a small space, this is clearly of limited application. On-going molecular simulations and calculations of T_1 in nanoscopic planar pores [98, 99] suggest that the observed relaxation times are very sensitive to the details of surface chemistry and may not be solely related to a change in spaces.

Crystalline phases content

XRD and TGA results are shown in Table 4.4. The CH content is compared to that calculated from NMR solid signal (and the average content of ettringite) at 10 days and 28 days of hydration. The three estimates, TGA, XRD and NMR are, within the error ($\pm 1\%$), in good agreement.

Table 4.4 – TGA and XRD results for the plain white cement paste sealed cured at 10 °C, normalized per gram of cement. The error of these techniques is $\pm 1\%$; Portlandite contents calculated from NMR; and the Ca/(Si+Al) ratio of the C–S–H measured by SEM-EDX and calculated by NMR.

Time (days)	DOH	Ettringite XRD	CH			Ca/(Si+Al)	
	XRD		XRD	TGA	NMR	SEM-EDX	NMR
10	0.619	0.085	0.225	0.212	0.206	1.89 ± 0.04	1.80 ± 0.10
28	0.651	0.085	0.213	0.210	0.222	1.75 ± 0.04	1.77 ± 0.10

Compared to the paste cured at 20 °C, slightly more ettringite precipitates at 10 °C. However, for the same α , the CH content is equivalent.

Chemical Shrinkage

The chemical shrinkage results are presented in Figure 4.27 and compared to the results obtained at 20 °C. The chemical shrinkage at 10 °C, $0.046 \pm 0.003 \text{ cm}^3/\text{g}$ of reacted anhydrous powder, is significantly smaller than for the same paste cured at 20 °C ($0.075 \text{ cm}^3/\text{g}$). This is a first evidence that cement hydrates occupy a bigger volume when the curing temperature is lowered.

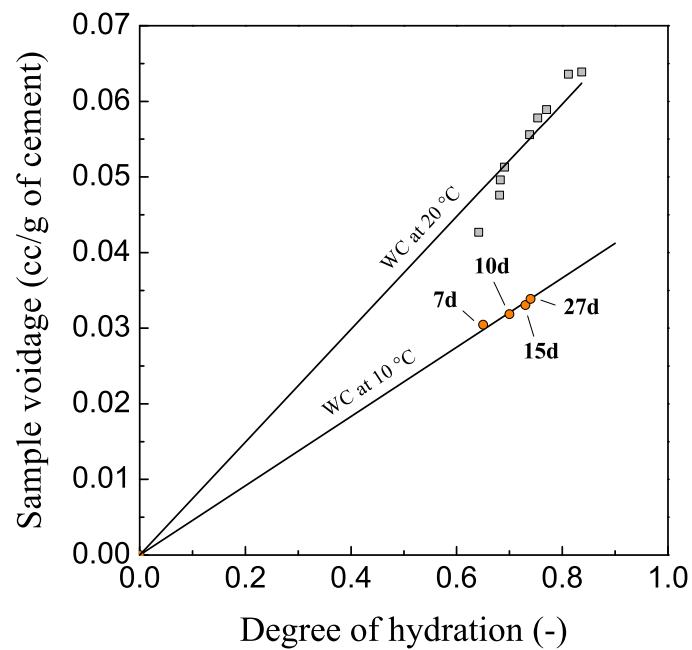


Figure 4.27 – Chemical shrinkage as measured by the conventional method (*cf.* section 3.4.2, p. 44) for the paste with $w/c = 0.40$ cured at 10 °C.

4.8.2 Analytical results - C-S-H characteristics

Using Equations 4.3 to 4.9, C-S-H density and chemical composition can be calculated from 10 days to 28 days of hydration. The results of density and water contents are shown in Figure 4.28 and compared to the results obtained at 20 °C. The scatter of the calculated C-S-H parameters is higher than for the paste measured at 20 °C due to higher uncertainties in the the different NMR signal fractions.

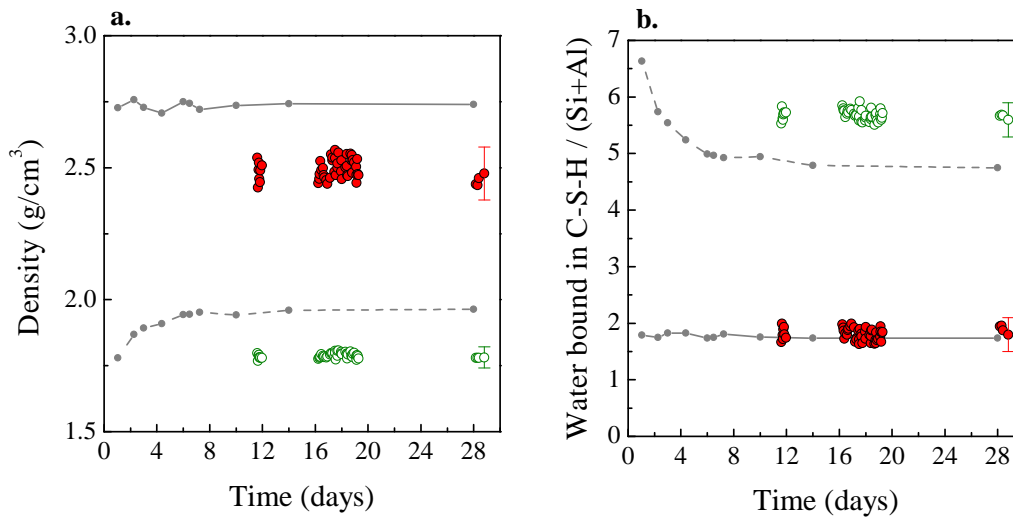


Figure 4.28 – (a) C-S-H density as a function of time at 10 °C. Solid symbols are the C-S-H solid density, exclusive of the gel water; empty symbols are for C-S-H bulk density, inclusive of the gel water and (b) associated water contents. The grey lines show the results for the same paste cured at 20 °C.

The Ca/(Si+Al) ratio of the C-S-H is found, within the scatter, roughly constant with time oscillating between 1.70 and 1.80. The values calculated for 10 days and 28 days of hydration are presented in Table 4.4 and compared to quantifications made by SEM-EDX. Again, the agreement of the NMR with undifferentiated techniques is good.

At 28 days, C-S-H solid density is $\rho_x = 2.45 \pm 0.10 \text{ g/cm}^3$ and bulk density is $\rho_{x'} = 1.78 \pm 0.04 \text{ g/cm}^3$. These values are lower than the densities calculated at 20 °C ($\rho_x = 2.74$ and $\rho_{x'} = 1.96$ at 28 days), which correlates with the lower chemical shrinkage reported in Figure 4.27. For bulk densities, the results are consistent with the values calculated by Galluci *et al.* [92] who found $\rho = 1.79$ at 5 °C compared to $\rho = 1.90$ at 20 °C. Galluci *et al.* speculated, based on BSE-SEM micrographs, that the C-S-H layers themselves must somehow have a lower density at low temperature and that the decrease in the overall density does not only originate from a change in gel pore content/size.

Water contents of solid C-S-H are similar for both curing temperature. However, bulk C-S-H binds more H₂O/(Si+Al) when the paste is cured at 10 °C.

4.8.3 Discussion

To help interpreting the data, Table 4.5 shows different variables of the solid C–S–H for both 10 °C and 20 °C at almost equivalent mass (in bold). This corresponds to 28 days for 10 °C and to 3 days for 20 °C.

Table 4.5 – Comparison of different C–S–H variables between 10 °C and 20 °C when the solid C–S–H mass is approximatively equivalent.

Curing Temp.	Age (days)	Solid C–S–H			Ca/(Si+Al)	H ₂ O/(Si+Al)	H ₂ O/Ca
		mass (g)	vol. (cc)	density			
10 °C	28	0.544	0.222	2.73	1.768	1.893	1.071
20 °C	3	0.567	0.209	2.45	1.733	1.827	1.054

For approximatively the same mass of solid C–S–H (including the water in the interlayer), the atomic amounts of Ca, Si and H₂O are almost equivalent within the measurement error (last three columns of Table 4.5). The associated volume of solid C–S–H is however smaller when the paste is cured at 10 °C. From this, the conclusion can be made that the decrease in C–S–H density (solid and bulk) arises from different structural order of the C–S–H layers. C–S–H might reach a different degree of crystallinity for different curing temperatures.

In the two cases presented in Table 4.5, the gel pore content is almost equivalent. The bulk water contents are also equivalent when comparing 3 days at 20 °C and 28 days at 10 °C. The reason why the bulk water contents are higher at later ages for 10 °C is related to the fact that gel pores are created on a much longer period of time (up to 5-6 days).

The study of low temperature in this work showed a change in the C–S–H primary parameters. The impact of higher temperatures on NMR water distributions and C–S–H density can be found in Agata Gajewicz's thesis [100].

4.9 General discussion

A feature of the data is that, for all pastes studied, the content of the capillary water become rapidly small. The lack of capillary water is significant as it strongly affects transport properties of cement. It implies that the finer gel pores must play a correspondingly greater role in controlling the rate of ingress of dissolved, aggressive ions such as chlorides and sulfates. Recent lattice Boltzmann simulations made by Zalzale *et al.* [101, 102] showed that the permeability of cement paste is strongly affected by the fraction of capillary pores that is, or not, filled with water. Zalzale *et al.* introduced an intrinsic C–S–H permeability in order to explain some experimental results taken from literature.

The ^1H NMR signal assignment showed that the solid signal arises predominantly from CH and ettringite, and in particular does not contain any component of C–S–H. Likewise, the interhydrate pores does not seem to be an intrinsic part of the C–S–H hydrate, because the total porosity in this category decreases with the degree of hydration rather than increasing.

The C–S–H is first growing in the free water space rapidly becoming interhydrate spaces. Since the interhydrate pores do not decrease much in size below about 8 nm, it is speculated that it represents the spaces between the C–S–H needles. SFEG micrographs of hydrated C_3S grains a few hours after mixing are presented in Figure 4.29. It shows, as an example, needle-like C–S–H growing from the C_3S surfaces and filling the surrounding space. As the interhydrate size remains constant while its amount diminishes, it is as if the interhydrate spaces are either present, or filled with C–S–H. There is no evidence for a halfway house. Only when all of interhydrate water is consumed (beyond 2 months), is there any evidence that the C–S–H grows within the gel pore space.

The rapid small size of the capillary porosity (8 nm) impacts the way the C–S–H fills the space in a second stage. The strong dependence between the capillary pore size and the gel pore formation illustrates one parameter controlling the “long term” hydration. A “space filling” theory was previously proposed by Bishnoi and Scrivener in 2009 [103] to model numerically hydration kinetics based on the distances between growing particles. However, the purpose of this model was to explain the deceleration period observed by calorimetry (between 10 and 20 hours) and hence does not compare with the mechanism discussed here.

As explained earlier, the proposed C–S–H structure (schematic in Figure 4.29) closely resembles to the picture from Feldman and Sereda [12]. The main difference is that NMR measures two water population intrinsic to the C–S–H: the interlayer and the gel pore water. A colloidal model “CM-II” was recently proposed by Jennings in 2008 [7]. As well as the interlayer water, Jennings suggested three nanoscale pore sizes associated with C–S–H: intra-globular pores associated with stacking heterogeneities of the calcium silicate layers (circa 1 nm), small globule pores between particles (circa 1-3 nm) and large globule pores between particle flocs (3-12 nm). In here, there are just two nano-scale pore types intrinsic to the C–S–H: the interlayer spaces between the calcium silicate sheets and the gel pores of comparable size to the small globule pores. The large globule pores reported by Jennings are comparable in

size to what has been called the interhydrate spaces (8 nm). However, the interhydrate pores that NMR sees are not integral to the C–S–H since they always decrease in volume as C–S–H grows. What is interesting, however, is that NMR suggests that C–S–H aggregates of layers are approximately three layers thick. Based on the analogue tobermorite 14, this leads to a stack thickness of 4.2 nm, close to the CM-II globule size.

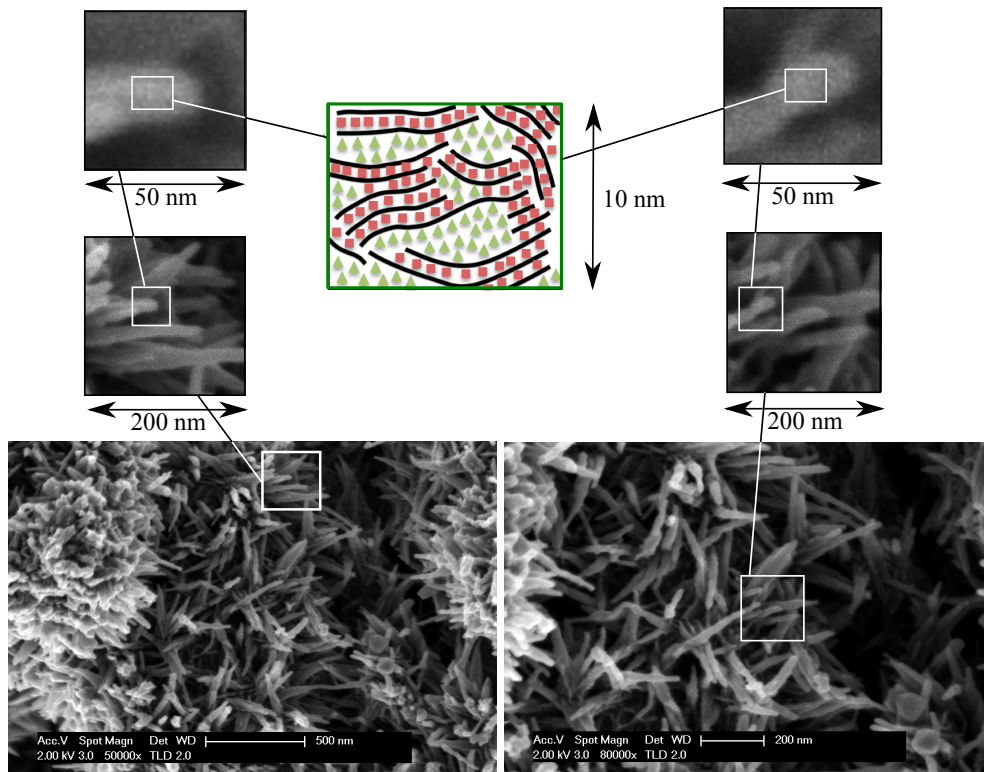


Figure 4.29 – SFEG micrographs showing the C–S–H growing as needles. The pictures were provided by Dr. Emmanuelle Boehm-Courjault from EPFL and show hydrating C_3S grains. The size of the needles is compared to the schematic size of the C–S–H as seen by 1H NMR.

Although it seems easy to represent the C–S–H (with its pore populations) in a 2D space, it becomes more difficult to imagine the C–S–H structure in 3 dimensions. Etzold *et al.* recently proposed a growing sheet model [104] to generate model structures for C-S-H. In their model, they grow planar sheets made of elementary blocks from a given number of seeds in a confined space. The gel pores in their model are located at two places. One is at defects created by the impingement of sheet stacks. The other one is caused by the misalignment of sheets between themselves. How the gel pores take part of the C–S–H structure is still an open question. According to NMR data, the features drawn in Figure 4.29 should be, somehow, included within the needles seen on the micrographs. The comparison between the size of the proposed C–S–H structure and the size of the needles (cross section) suggest that the needles could contain several gel pores and tens of C-S-H layers.

5 NMR study of blended systems

Contents

5.1 The influence of 10% of silica fume	92
5.1.1 Introduction on silica fume	92
5.1.2 Mix under study	92
5.1.3 Theory - modifications of the calculation for the silica fume	93
5.1.4 NMR results	94
5.1.5 Hydration kinetics	95
5.1.6 Degree of reaction of alite and belite	98
5.1.7 Degree of reaction of silica fume	99
5.1.8 Crystalline phases: ettringite and Portlandite content	102
5.1.9 Chemical shrinkage	104
5.1.10 Calculation of the C-S-H parameters	104
5.1.11 SEM and TEM microscopy	107
5.1.12 Discussion and conclusions	109
5.2 The addition of slag	111
5.2.1 Mixes under study	111
5.2.2 Experimental results	111

5.1 The influence of 10% of silica fume

5.1.1 Introduction on silica fume

Silica fume is a by-product from the production of elemental silicon and its alloys. Silica fume is typically used at replacement levels of 5-10% in high performance concrete to improve strength and durability. It can react pozzolanically with calcium hydroxide to produce C-S-H, but also modifies the microstructure of the cement paste due to its fine particle size. Many studies describe changes due to addition of silica fume. Skibsted *et al.* [105] used the ^{29}Si MAS NMR technique to quantify the reaction degree of 10% of silica fume in white cement pastes at water-to-cement ratio, $w/c = 0.5$. They found 65% of silica fume reaction by 100 days. Justnes *et al.* [106] investigated the hydration of C_3S and C_2S with condensed silica fume. Mixes with silica fume had an increased C-S-H mean chain length compared to mixes without silica fume. Justnes *et al.* [107] also found an acceleration of the cement reaction at early age in the presence of silica fume and estimated a lower Ca/Si of the C-S-H in mixes with silica fume knowing additionally the non-evaporable water content measured by TGA. However, despite these studies, there is no description of the changes affecting the nanostructure of C-S-H and its evolution with time in never dried systems. Moreover, the C-S-H density has not been reported for Portland cement with silica fume addition.

5.1.2 Mix under study

The white cement batch 2 was used in this study (composition p. 36). Condensed silica fume was provided by Elkem under the name “Microsilica 983 U”; it is made of 98.6% amorphous silica (Annex B) and has an absolute density of 2.27 g/cm^3 .

Pastes with 10% cement mass replacement by silica fume were made according to the following procedure. The silica fume was first pre-dispersed in distilled water for 8 minutes at 15,000 rpm in an ultrasonic bath. No superplasticizer was used for rheological or dispersive purposes in order not to introduce hydrogen other than that in water which might affect the ^1H NMR experiments. Then the water with suspended silica fume was added to the cement to achieve a water-to-binder ratio of $w/b = 0.4$ by weight. All components were mixed together for 5 minutes at 1,600 rpm.

As for plain white cement pastes, small amounts of paste ($\approx 0.35 \text{ cm}^3$) were deposited at the bottom of glass ^1H NMR tubes and sealed with parafilm[®]. Multiple samples cast at different times were intermittently measured in by ^1H NMR. Other samples were cast in larger containers and parallel experiments were carried out throughout the hydration using XRD, isothermal calorimetry, SEM-EDX, TEM-EDX, solid-state ^{29}Si MAS NMR and TGA. All samples were measured and cured under sealed conditions at $20 \text{ }^\circ\text{C}$.

For the study of silica fume addition, the plain white cement paste with $w/c = 0.4$ is used as a reference for comparison.

5.1.3 Theory - modifications of the calculation for the silica fume

Mass and volume paste composition

Mass and volume balance equations for the paste in terms of NMR signal intensities were previously written for the plain white cement pastes (section 4.3, p. 64). For this work, the calculations are modified to incorporate the contribution of 10% of silica fume. The revised equations for one gram of binder (cement + silica fume) are written as

$$1 + \frac{w_{\text{mix}}}{b} = 0.9(1 - \alpha_c) + 0.1(1 - \alpha_{sf}) + \frac{w_{\text{mix}}}{b} [\beta I_{\text{solid}} + \gamma I_{\text{CSH}} + \delta(I_{\text{gel}} + I_{\text{cap}})] \quad (5.1)$$

$$\frac{0.9}{\rho_c} + \frac{0.1}{\rho_{sf}} + \frac{w_{\text{mix}}}{b\rho_w} = \frac{0.9(1 - \alpha_c)}{\rho_c} + \frac{0.1(1 - \alpha_{sf})}{\rho_{sf}} + \frac{w_{\text{mix}}}{b} \left[\frac{\beta I_{\text{solid}}}{\rho_{\text{solid}}} + \frac{\gamma I_{\text{CSH}}}{\rho_{\text{CSH}}} + \frac{\delta(I_{\text{gel}} + I_{\text{cap}} + I_{\text{void}})}{\rho_w} \right] \quad (5.2)$$

The left hand side of Equation 5.1 (mass) and Equation 5.2 (volume) correspond to the state of the paste at time of mixing. The right hand sides represent the sum of the different components of the paste at any subsequent hydration time. Most of the parameters are similar as in Equations 4.3 and 4.4. In addition, the subscript *b* and *sf* refer to binder and silica fume respectively. The *w/b* of the paste remains constant over time due to the sealing of the sample.

In the same manner, the solid water signal, I_{solid} , can be decomposed into $I_{\text{solid}} = I_{\text{CH}} + I_{\text{ett}}$. The mass of crystalline phases in the sample, per gram of binder, is then decomposed as in Equation 4.5. I_{ett} is measured by XRD, allowing the deconvolution of the I_{solid} signal. The chemical shrinkage is normalized per gram of binder (cement + silica fume). At any given time, $I_{\text{void}} = V_{\text{void}}/(w/b)$, where V_{void} is the chemical shrinkage volume, or voidage, in cm^3 per gram of binder.

For density calculation, the degrees of reaction of cement and silica fume are required. For cement, careful XRD Rietveld quantifications were done sufficiently frequently to capture the consumption kinetics of C_3S and C_2S . In parallel, ^{29}Si MAS NMR quantifies the degree of reaction of the 10% of silica fume initially incorporated into the mix. Combined XRD and isothermal calorimetry are used to confirm the trends.

C–S–H chemical composition

The C–S–H composition is, in the same way as for the plain white cement pastes, expressed as $\text{Ca}_z \cdot (\text{Si}_y, \text{Al}_{(1-y)}) \cdot \text{O}_{(z+1/2y+3/2)} \cdot (\text{H}_2\text{O})_x$. However, the Ca/(Si+Al) ratio is now balanced with:

$$\frac{0.9 \left[3 \left(\frac{f_{C_3S} \alpha_{C_3S}}{C_3S^{\text{AMU}}} \right) + 2 \left(\frac{f_{C_2S} \alpha_{C_2S}}{C_2S^{\text{AMU}}} \right) \right] + 1.5 n_{\text{Al}}^{\text{CSH}}}{0.9 \left[\left(\frac{f_{C_3S} \alpha_{C_3S}}{C_3S^{\text{AMU}}} \right) + \left(\frac{f_{C_2S} \alpha_{C_2S}}{C_2S^{\text{AMU}}} \right) \right] + 0.1 \left[\frac{\alpha_{\text{sf}}}{\text{SiO}_2^{\text{AMU}}} \right] + n_{\text{Al}}^{\text{CSH}}} = \frac{\frac{I_{\text{CH}} n_{\text{Hyd}}}{2} + \frac{I_{\text{CSH}} n_{\text{Hyd}}^z}{2x} + 1.5 n_{\text{Al}}^{\text{CSH}}}{\frac{I_{\text{CSH}} n_{\text{Hyd}}^y}{2x} + n_{\text{Al}}^{\text{CSH}}} \quad (5.3)$$

The degrees of C_3S and C_2S reaction are now considered as two separated parameters. Silica fume is taken as 100% SiO_2 . Following the same method of calculation as previously, the number of moles of alumina in the C–S–H, $n_{\text{Al}}^{\text{CSH}}$, per gram of binder, is expressed as $n_{\text{Al}}^{\text{CSH}} = 2 \cdot 0.9 (f_{C_3A} - f_{C_3A}^{\text{ett}}) / C_3A^{\text{AMU}}$. n_{Hyd} represents the number of hydrogen moles per gram of binder.

Calculations for water contents work similarly as for plain pastes (*cf.* Equation 4.7 and Equation 4.10).

5.1.4 NMR results

Figure 5.1a shows the evolution of the different ^1H NMR water signal fractions as a function of hydration time for white cement with 10% silica fume (coloured symbols) and for plain white cement (grey symbols), for comparison. The addition of 10% of silica fume in the white cement paste did not cause the appearance of any other population of water, according to ^1H NMR relaxometry data, compared to the plain white cement. The I_{solid} signal arises from crystalline phases; two water reservoirs are found within the C–S–H (interlayer and gel water) and the “free water” volume is seen as longer components.

The evolution of the pore populations with hydration of the cement with silica fume is similar to plain white cement. However, there are important differences. The first is that the end of gel pore formation happens at around 1 day for the silica fume blend compared to 2 days previously observed for plain white cement paste. The second difference is that the fraction of C–S–H interlayer water (I_{CSH}) is much lower in the presence of silica fume. On the other hand, the fraction of C–S–H gel becomes higher and I_{gel} rapidly represents more than 50% of all water within the cement paste. Despite this redistribution between the two C–S–H water populations, the “free water” content I_{cap} is very similar, almost identical from 2 days to 28 days of hydration, to the white cement paste without silica fume. An increase of the capillary water signal is however observed by ^1H NMR at later ages in the presence of silica fume. The reasons for this are not clear but multiple repetitions have confirmed this trend. It might be that the pozzolanic reaction of silica fume leaves water behind in sealed systems where some parts of the porosity are disconnected from each other.

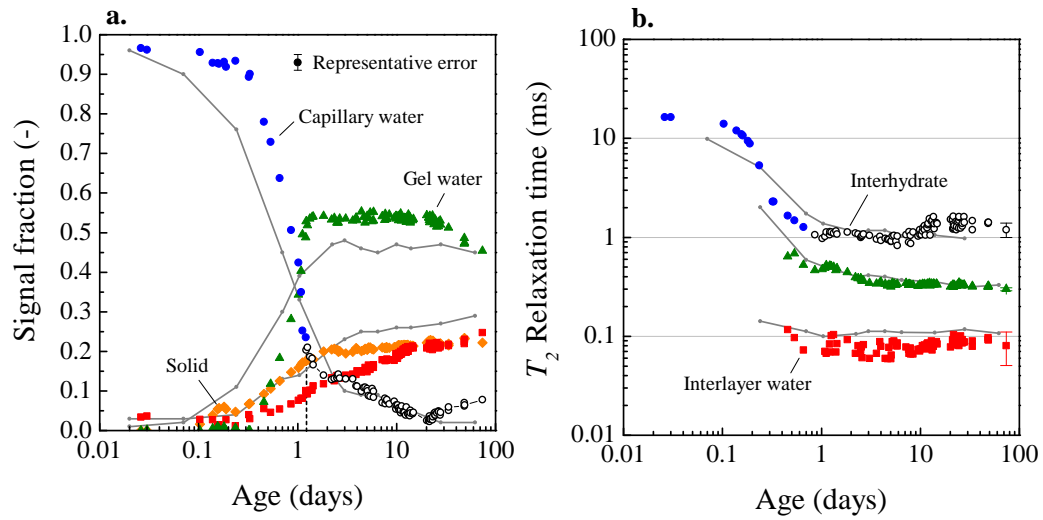


Figure 5.1 – (a) Evolution of the different water populations as a function of hydration time for white cement with 10% silica fume (colours) and for the plain white cement (grey lines), all at $w/b = 0.4$. (b) Evolution of the associated T_2 relaxation times.

Concerning T_2 relaxation times (Figure 5.1b), the different water populations have very similar magnitudes as for plain white cement. T_2 of the capillary water reservoir rapidly reaches an asymptotic value of 1 ms. The reservoir of capillary water reaches the interhydrate size at about 1 day of hydration for the silica fume mix. The T_2 of the gel pores are almost equal for both mixes with a slight decrease with time to $320 \pm 10 \mu\text{s}$. The T_2 relaxation times of the C–S–H interlayer are however slightly shorter in the case of white cement with silica fume ($80 \pm 30 \mu\text{s}$). As discussed in the previous section, the T_2 of the interlayer space is highly sensitive to the surface chemistry and hence the interpretation to a smaller pore size is difficult to substantiate.

5.1.5 Hydration kinetics

Figure 5.2a shows the heat flow measured by isothermal calorimetry for white cement paste with 10% of silica fume (solid line) and plain white cement (dashed line), as a function of hydration time. There is a clear enhancement of the heat released during the first 10 hours of hydration when 10% of the cement is replaced by silica fume. The acceleration period is highly impacted and shows a higher heat flow rate. This reflects the acceleration of the cement reaction at early age due to the important and well-known filler effect of silica fume [108]. XRD gives $\alpha_c = 0.52$ for the silica fume mix at 1 day compared to $\alpha_c = 0.40$ previously observed for plain white cement.

Figure 5.2b shows the cumulative heats, H , calculated from the end of the induction period for the same two mixes, expressed in Joules and normalized per gram of cement. The heat released

for white cement with 10% of silica fume becomes significantly higher than plain white cement early in the hydration process. Following previous work in this field [109, 110, 111, 112], both cumulative curves were extrapolated to infinite time using two-components, three-parameters, exponential functions as in Equation 5.4.

$$H = H_1 \cdot e^{-\left(\frac{B_1}{t}\right)^{C_1}} + H_2 \cdot e^{-\left(\frac{B_2}{t}\right)^{C_2}} \tag{5.4}$$

This function was first introduced in 1977 by Hansen and Pedersen to estimate the strength development of concretes [109]. Since then, it has been extensively used by various researchers for fitting of: heat flow of blended cements [111], degree of hydration [112], tensile strength and elastic modulus [110]. It is a reasonable fit to the data as processes in cement reaction have a rate constant that increases exponentially. The introduction of a second exponential term is essential to the fit when a secondary reaction takes place: silica fume in this case. The six fitting parameters H_1 , B_1 , C_1 , H_2 , B_2 and C_2 for the cumulative heats are given in Table 5.1.

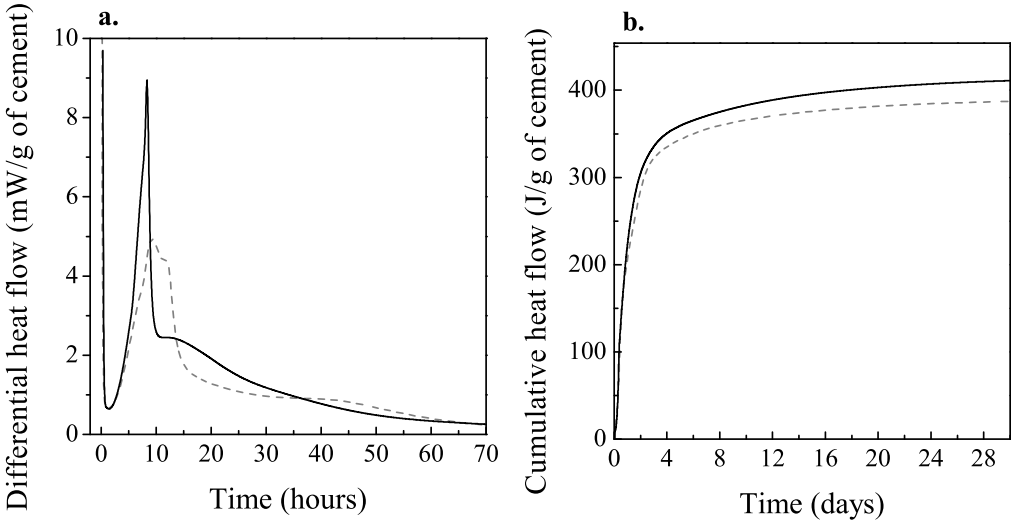


Figure 5.2 – (a) Heat flows measured during the first 70 hours after mixing for white cement with 10% silica fume (solid line) and for plain white cement (dashed line). (b) Cumulative heat flows for the same two mixes.

Table 5.1 – Fitting parameters based on Equation 5.4 for the cumulative heat flows of white cement and white cement with 10% of silica fume.

	Heat flow WC	Heat flow WC/SF
H_1 (J/g of cement)	112	199
B_1 (days)	17.2	14.2
C_1	0.15	0.22
H_2 (J/g of cement)	350	288
B_2 (days)	0.63	0.56
C_2	1.0	1.2

The results of the fitting give the total heat that can be released per gram of binder for both mixes at infinity. For plain white cement, $H_c^\infty = 461$ J/g of cement. A theoretical value can also be calculated based on the heat properties of each reactive component of the cement using the different heat values given by Riding *et al.* [112]. From the composition of the white cement, $H_c = 457$ J/g of cement. The calorimetry curve for the paste with silica fume extrapolates to $H_{c+10\%sf}^\infty = 487$ J/g of binder. The difference allows to calculate the heat associated with the reaction of silica fume by $H_{sf} = (H_{c+10\%sf}^\infty - 0.9 \cdot H_c^\infty)/0.1 = 714$ J/g of silica fume. Some data for the heat released by the silica fume reaction are available in the literature. Many have been reviewed by Kamyab [113], who stated that the only reliable values were found by Waller [114]. They were measured by performing adiabatic test on mixes having silica fume, water and excess $\text{Ca}(\text{OH})_2$. For comparison, Waller found 798 J/g, for a silica fume similar to that used in this study.

5.1.6 Degree of reaction of alite and belite

Figure 5.3 shows the respective degree of hydration of alite (C_3S) and belite (C_2S) calculated from XRD measurements and Rietveld quantification for the paste which incorporates 10% of silica fume. The XRD data points presented at each age are average values between samples measured as a slice and samples measured after drying as a powder; the measurement error is presented in the figure. According to the XRD patterns, no other cement phases are left unreacted after 1 day of hydration – *i.e.* C_3A is completely reacted. Figure 5.3 reveals that alite reacts mainly during the first 3 days of hydration and reaches $\alpha_{C_3S} = 0.84$ at this time. Belite does not show any reaction before 12 days and seems to start dissolving only when the alite reaction has slowed down significantly. At 28 days, $\alpha_{C_2S} = 0.15$. The grey lines are fits to the data using

$$\alpha = \alpha_1 \cdot e^{-\left(\frac{B_1}{t}\right)^{C_1}} + \alpha_2 \cdot e^{-\left(\frac{B_2}{t}\right)^{C_2}} \quad (5.5)$$

for which the parameters are shown in Table 5.2.

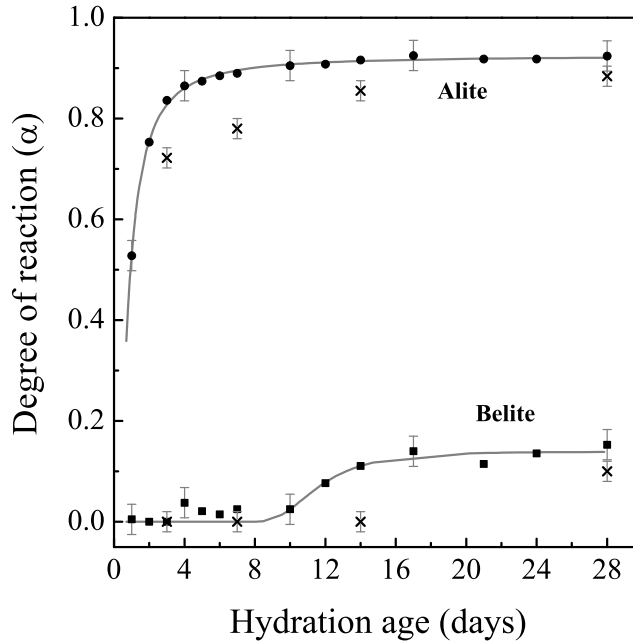


Figure 5.3 – Degree of reaction of alite (circles) and belite (squares) calculated from XRD and Rietveld quantification as a function of hydration time. The solid grey lines are fits to the data used in the calculation. Crosses are the corresponding values calculated from ^{29}Si MAS NMR.

Table 5.2 – Fitting parameters based on Equation 5.5 for the degree of reaction of alite and belite from XRD; and for the degree of silica fume reaction from ^{29}Si MAS NMR.

	α_{C3S}	α_{C2S}	α_{sf}
α_1	0.92	0.14	1.85
B_1 (days)	0.67	11.0	27.3
C_1	1.5	6.0	0.26
α_2	2.0	7.1	—
B_2 (days)	87	87	—
C_2	3.0	3.0	—

The two fitted behaviours are used as an input for α_{C3S} and α_{C2S} in Equation 5.3. The overall degree of cement reaction cement can be calculated as

$$\alpha_c = 1 - [f_{\text{C3S}}(1 - \alpha_{\text{C3S}}) + f_{\text{C2S}}(1 - \alpha_{\text{C2S}})] \quad (5.6)$$

The degree of hydration of alite and belite as calculated from ^{29}Si MAS NMR (*cf.* Table 5.3) are also presented in Figure 5.3. While both techniques show similar values at later ages, there is a larger discrepancy for the alite reaction during the first 10 days of hydration. At 28 days of hydration, $\alpha_{\text{C3S}} = 0.92 \pm 0.04$ by XRD whereas ^{29}Si MAS NMR gives $\alpha_{\text{C3S}} = 0.88 \pm 0.02$. The reasons for this discrepancy are not clear, but highlight the errors present in the different measurement techniques [115].

5.1.7 Degree of reaction of silica fume

Knowing the degree of hydration of cement at every age (from the data presented in Figure 5.3), it is possible to calculate the heat released by the cement itself and hence estimate the additional heat due to silica fume reaction. Using $H_{\text{sf}} = 714 \text{ J/g}$ of silica fume and $H_c^\infty = 461 \text{ J/g}$ of cement, the degree of reaction of silica fume can be estimated by $\alpha_{\text{sf}}(t) = [H_{\text{c}+10\%\text{sf}}^t - 0.9 \cdot \alpha_c(t) \cdot H_c^\infty] / (0.1 \cdot H_{\text{sf}})$, where $\alpha_{\text{sf}}(t)$ and $\alpha_c(t)$ are respectively the degree of reaction of silica fume and cement at time t . The results are presented in Figure 5.4 (open triangles) and compared to the degree of reaction of silica fume obtained by ^{29}Si MAS NMR (filled circles). Both methods give the same trend for the silica fume reaction. The scatter of the combined calorimetry and XRD results gives an idea of the uncertainty using this indirect method of calculation. The absolute values between the two methods are in relatively good agreement with each other even if there are slightly lower estimates for calorimetry/XRD compared to the ^{29}Si MAS NMR results (partly a consequence of the higher values for alite reaction by XRD identified above). This may also be attributed to the fact that the cumulative heat flow starts from the end of the induction period and does not include the dissolution heats. For these reasons, the ^{29}Si MAS NMR results are considered as more accurate and thus

these data were exclusively used in a fit with one three parameters exponential component (Figure 5.4, grey line) that was subsequently used for α_{sf} in Equations 5.1, 5.2 and 5.3. The details of the fit for α_{sf} are reported in Table 5.2. As an indicative value, the degree of reaction for silica fume is calculated to be 76% at 120 days by combined calorimetry/XRD.

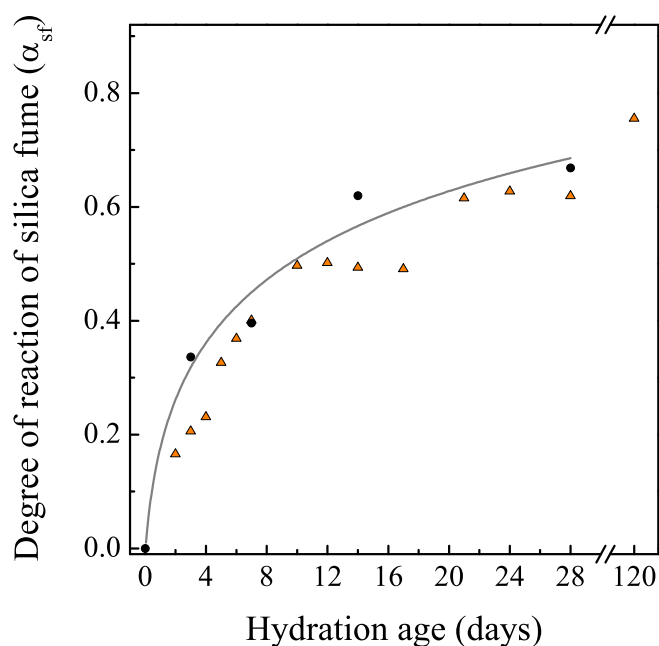


Figure 5.4 – Degree of reaction for silica fume measured by ^{29}Si MAS NMR (filled circles) and as calculated from combined calorimetry and XRD Rietveld analysis (orange triangles). The grey line is a fit to the ^{29}Si MAS NMR data (*cf.* Table 5.2).

Analysis of the ^{29}Si MAS NMR spectra presented in Figure 5.5 provides information about the alite and belite degree of reaction based on intensities of deconvoluted spectra. These analysis were performed by Jørgen Skibsted in the department of chemistry of Aarhus University, Aarhus, Denmark. The data are presented in Table 5.3 and reported in Figure 5.3. Estimated error limits for α_{C3S} and α_{C2S} are ± 0.02 and ± 0.04 respectively. Based on the work of Richardson *et al.* [116] and Andersen *et al.* [117], it is possible to calculate from ^{29}Si MAS NMR data the mean aluminosilicate chain length (MCL), the chain length of pure SiO_4 tetrahedra (CL_{Si}) and the Al(IV)/Si ratio of the C–S–H. These data, summarized in Table 5.3, reveal that both MCL and CL_{Si} increase with the time of hydration, showing that the C–S–H incorporates more Si in its structure. The Al(IV)/Si ratio of the C–S–H is almost invariant with the hydration time, in agreement with earlier ^{29}Si MAS NMR studies of C–S–H phases formed in hydrated white Portland cement [118]. The error limits for MCL and CL_{Si} are ± 0.15 and for Al(IV)/Si it is estimated to ± 0.01 .

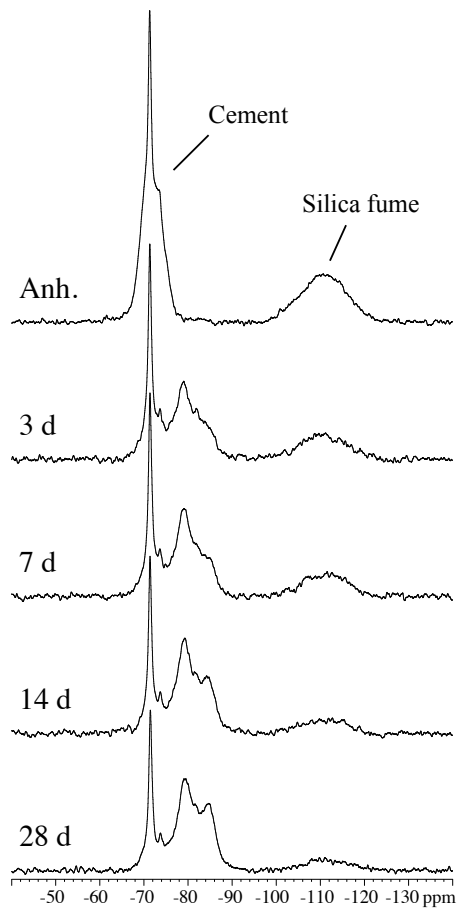


Figure 5.5 – ^{29}Si MAS NMR spectra (9.4 T, $\nu_R=6.0$ kHz) of the anhydrous white cement with silica fume and of the blend after hydration for 3, 7, 14 and 28 days.

Table 5.3 – ^{29}Si MAS NMR results: degree of reaction for alite and belite ($\alpha_{\text{C}_3\text{S}}$ and $\alpha_{\text{C}_2\text{S}}$), C–S–H mean chain length (MCL), chain length of silicate tetrahedra (CL_{Si}) and the Al(IV)/Si ratio of the C–S–H as a function of hydration time.

	$\alpha_{\text{C}_3\text{S}}$	$\alpha_{\text{C}_2\text{S}}$	MCL	CL_{Si}	Al/Si
3 days	0.72	0.00	2.98	2.51	0.055
7 days	0.78	0.00	3.02	2.51	0.059
14 days	0.86	0.00	3.20	2.67	0.059
28 days	0.88	0.10	3.29	2.80	0.052

5.1.8 Crystalline phases: ettringite and Portlandite content

The amount of ettringite for the white cement paste with silica fume, as determined by XRD and Rietveld analysis, is presented as a function of time in Figure 5.6. The data are normalized per gram of cement. As for plain white cement pastes, ettringite is formed in the first day and stays constant through the analysis (1-28 days). There is any transformation of ettringite into tricalcium-monosulfo-aluminate (AFm) as the white cement contains a low amount of C_3A . The average ettringite content is $m_{ett} = 0.089 \pm 0.010$ g/g of cement, corresponding to $I_{ett} = 0.092$.

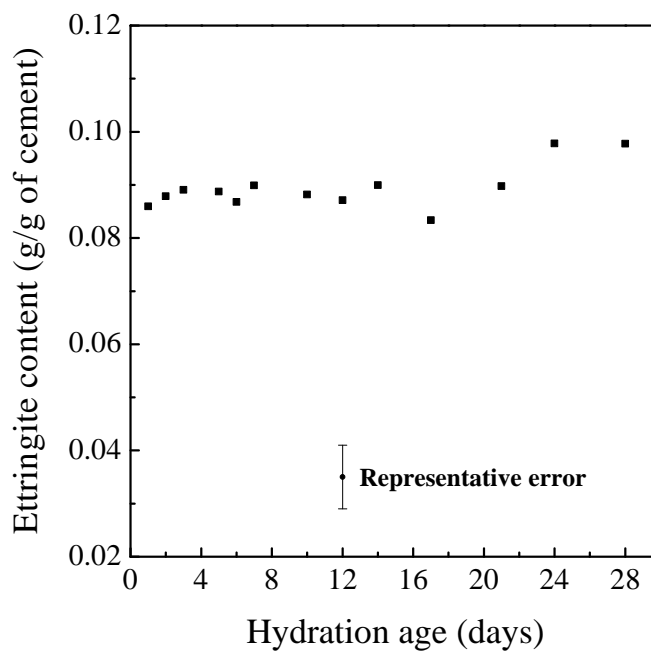


Figure 5.6 – Mass of ettringite as a function of time, in g/g of anhydrous cement, measured by XRD and Rietveld analysis.

The results of CH content based on 1H NMR are presented in Figure 5.7, in gram of Portlandite per gram of cement, and compared to the results obtained by both XRD and TGA; the relative error bar on the figure indicates the uncertainty. The kinetic of CH formation is similarly captured by the three techniques. The jumps in the 1H NMR data are due to the fact that different samples were scanned at different times. Nevertheless, these small shifts stay within the error of the other techniques (around $\pm 1\%$ of the absolute value) and are not considered critical to the analysis.

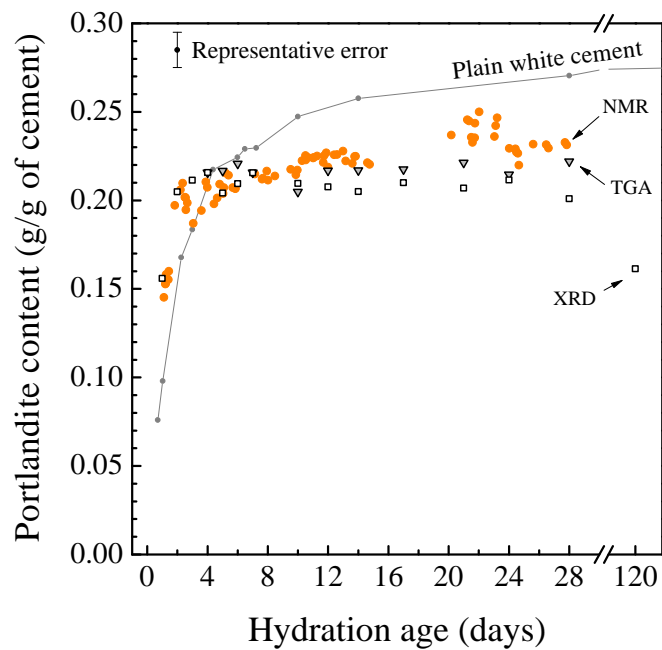


Figure 5.7 – Mass of Portlandite as a function of time, in g/g of anhydrous cement, measured and calculated by ^1H NMR (black diamonds), XRD (empty squares) and TGA (grey inverted triangles). The grey line shows the CH content of plain white cement.

The Portlandite content reaches a plateau after 3 days of hydration with an average value of 0.21 ± 0.01 g/g of cement between both XRD and TGA. For comparison, the grey line on Figure 5.7 tracks the behaviour of the plain white cement where there is a continuous increase of the Portlandite content with time. The faster increase at early age for the silica fume mix is due to the acceleration of the cement hydration by the filler effect of silica fume noted by calorimetry. The apparent consumption of CH by the pozzolanic reaction with silica fume at 28 days of hydration is 0.05 g/g of cement. A further decrease is observed at 120 days when $m_{\text{CH}} = 0.16$ g/g of cement measured by XRD. This is a decrease of 25% compared to the 28 days CH content. In the meantime, the degree of hydration of silica fume goes up from $\alpha_{\text{sf}} = 62\%$ at 28 days to $\alpha_{\text{sf}} = 76\%$ at 120 days as calculated from combined calorimetry/XRD (Figure 5.5). All measurements were performed on sealed systems with empty pores due to chemical shrinkage so there might be a chemical isolation of the calcium hydroxide. As discussed below it is also seen that the calcium content of the C–S–H is lower in the silica fume system, indicating that this calcium is also available for the pozzolanic reaction.

5.1.9 Chemical shrinkage

The chemical shrinkage results, in cm^3 per gram of cement, are presented in Figure 5.8 as a function of degree of cement hydration. The evolution of voidage with the degree of hydration of cement is not linear due to the contribution of silica fume to the total chemical shrinkage volume. The data were fitted as shown in the figure using a polynomial function (written in Figure 5.8). Only the part between the dashed lines is used for C–S–H density calculation.

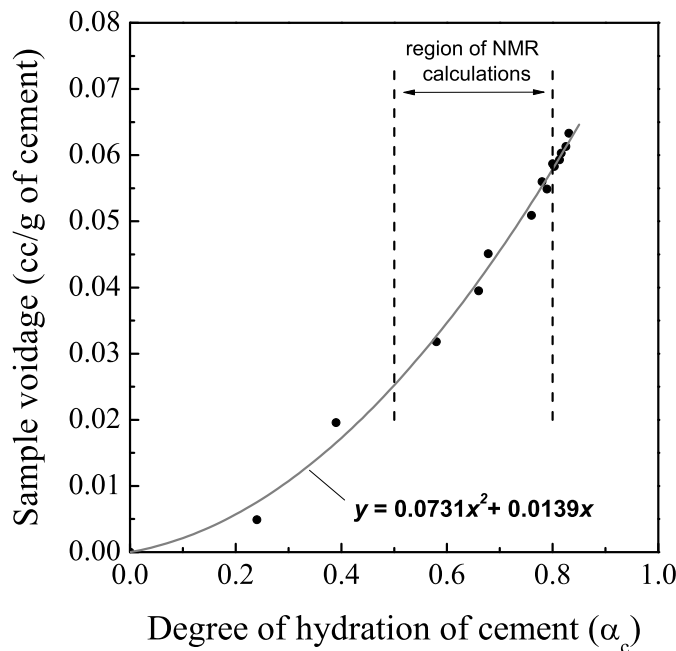


Figure 5.8 – Chemical shrinkage volume in cm^3/g of cement as a function of cement hydration for the white cement and 10% silica fume mix. The solid line is a polynomial fit to the data. The “region of NMR calculations” illustrates the part of the curve used for the density calculation.

5.1.10 Calculation of the C–S–H parameters

The data presented above allow the calculation of the C–S–H characteristics according to Equations 5.1 to 5.3. The calculated C–S–H solid and bulk densities are shown in Figure 5.9a; the $\text{Ca}/(\text{Si}+\text{Al})$ ratio of the C–S–H in Figure 5.9b; and the solid and bulk C–S–H water contents in Figure 5.9c and Figure 5.9d respectively. Taken together these results give a complete description of hydrating white cement paste with 10% of silica fume from 1 day to 28 days. The results are interdependent as all equations are solved together. The data are compared to the plain white cement results (grey lines).

To study the impact of potential errors, extra points in these graphs were calculated using the degrees of alite reaction from ^{29}Si MAS NMR at 3 days (cross symbols). The sensitivity of the

results to the measured values is discussed further below. Nevertheless, it is interesting to note that this alternate analysis has a major impact on some values and little on others.

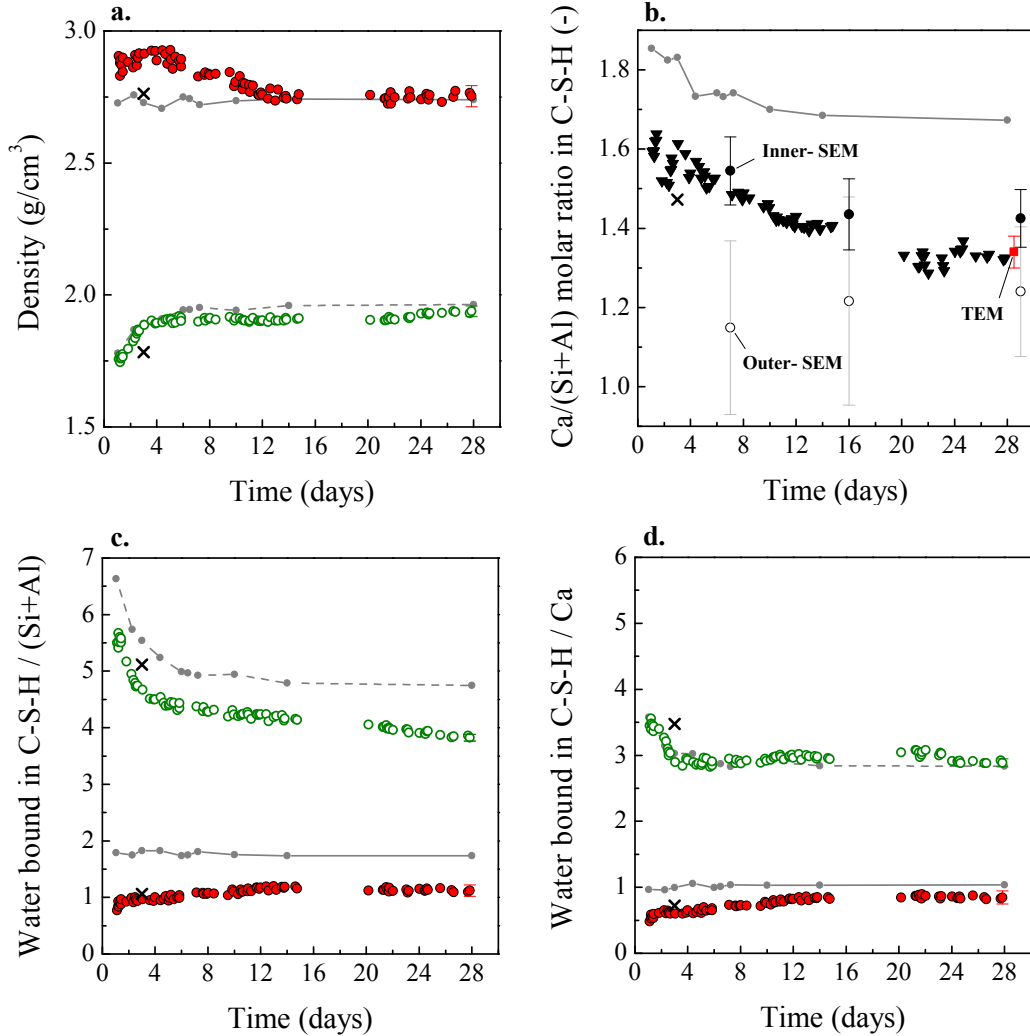


Figure 5.9 – Calculation results for the white cement paste including 10% silica fume prepared with $w/b = 0.4$ as a function of hydration time. (a) C–S–H density: solid symbols are C–S–H solid density, exclusive of the gel water; empty symbols are for C–S–H bulk density, inclusive of the gel water. (b) Average Ca/(Si+Al) ratio of the C–S–H calculated from ¹H NMR (black inverted triangles); estimated by SEM-EDX for inner-C–S–H (solid circles) and outer-C–S–H (empty circles) and by TEM-EDX (red square). (c) and (d) associated water contents for the solid and bulk C–S–H. The crosses in all figures show the results when the degree of alite reaction was taken from ²⁹Si MAS NMR instead of XRD. In addition, the grey lines show the behaviour of plain white cement.

The average bulk density of the C–S–H increases with time between 1 day and 28 days of

hydration. This densification of the average C–S–H material reflects the fact that no more gel pore is created beyond 1 day. Two densification regimes are observed. The end of the first regime of fast densification corresponds to the slow down of the alite reaction (Figure 5.3). The C–S–H bulk density calculated at 28 days, $\rho_{x'} = 1.94 \pm 0.02 \text{ g/cm}^3$, is close to the values usually reported in the literature [7] and similar to the one calculated for plain white cement at the same hydration age: $\rho_{x'} = 1.96 \text{ g/cm}^3$. In the same way, the solid C–S–H density at 28 days, $\rho_x = 2.75 \pm 0.04 \text{ g/cm}^3$, is almost the same as the one reported for plain white cement, $\rho_x = 2.74 \text{ g/cm}^3$. There is a higher solid C–S–H density observed initially at 1 day with $\rho_x = 2.91 \pm 0.01 \text{ g/cm}^3$ compared to $\rho_x = 2.73 \text{ g/cm}^3$ for plain white cement. However, this early age difference is difficult to substantiate as early age properties are more difficult to capture experimentally. This discrepancy does not occur for the value calculated when using, at 3 days, the α_{C3S} estimated by ^{29}Si MAS NMR.

For the C–S–H water contents, inclusive x' and exclusive x of the gel water (Figure 5.9c), the inverse trends to the densities are observed. The slight increase of x and the decrease of x' with time are a result of densification. The main differences compared to plain white cement are the absolute water contents. The values normalised per silicon and aluminium moles are significantly lower than without incorporation of silica fume. There is an average solid C–S–H water content of $x = 1.10 \pm 0.08 \text{ H}_2\text{O}/(\text{Si}+\text{Al})$ beyond 20 days of hydration. This is a decrease of 39% compared to $x = 1.80$ for plain white cement. As for the plain paste, a decrease in $\text{H}_2\text{O}/(\text{Si}+\text{Al})$ ratio with time is also observed in the case of bulk C–S–H: the total water content of C–S–H goes down from circa $x' = 5.50 \text{ H}_2\text{O}/(\text{Si}+\text{Al})$ at 1 day of hydration to $x' = 3.84 \pm 0.04$ at 28 days. However, when the water contents are normalized by calcium in C–S–H (Figure 5.9d), the two mixes present much more similar values. Solid C–S–H nonetheless shows slightly lower $\text{H}_2\text{O}/\text{Ca}$ than for the plain white cement.

There is an average $\text{Ca}/(\text{Si}+\text{Al}) = 1.60 \pm 0.04$ for the C–S–H produced during the first 2 days of hydration. This is lower than for plain white cement with $\text{Ca}/(\text{Si}+\text{Al}) > 1.80$ at early age (grey line in Figure 5.9b). This is related to the fact that $\approx 15\%$ of the silica fume has already reacted after 2 days (Figure 5.4) and that this silicon is incorporated in the C–S–H structure. As the hydration of cement and silica fume proceeds, this average ratio goes progressively down to $\text{Ca}/(\text{Si}+\text{Al}) = 1.33 \pm 0.04$ at 28 days. The calculated $\text{Ca}/(\text{Si}+\text{Al})$ values are in good agreement with TEM analyses as discussed below.

The complete chemical composition for the bulk C–S–H inclusive of the gel water, at 1 day, is $\text{Ca}_{1.60} \cdot (\text{Si}_{0.94}, \text{Al}_{0.06}) \cdot \text{O}_{3.57} \cdot (\text{H}_2\text{O})_{5.50}$. At the other end of the range, the solid C–S–H chemical composition exclusive of the gel water, at 28 days, is $\text{Ca}_{1.33} \cdot (\text{Si}_{0.97}, \text{Al}_{0.03}) \cdot \text{O}_{3.33} \cdot (\text{H}_2\text{O})_{1.10}$. This shows that C–S–H is characterized by various compositions dependent on whether the gel water is included, and on the hydration time at which C–S–H is probed. There is some uncertainty in these values, particularly for the Al/Si ratio. The Al/Si values calculated from the ^1H NMR data decreases with time due to the assumption that all the C_3A (only alumina containing component) has reacted at one day whereas in fact the alite and belite phases also contain some alumina in solid solution which is not accounted for and is released later. The

Al/Si ratios calculated at early age (0.06 at 1 day) are consistent with the ^{29}Si MAS NMR values (0.052-0.059) reported in Table 5.3.

Using the C–S–H density and chemical composition as calculated above, the evolution of the mass and volume composition of the paste with silica fume can be drawn, for instance, as a function of hydration time as shown in Figure 5.10.

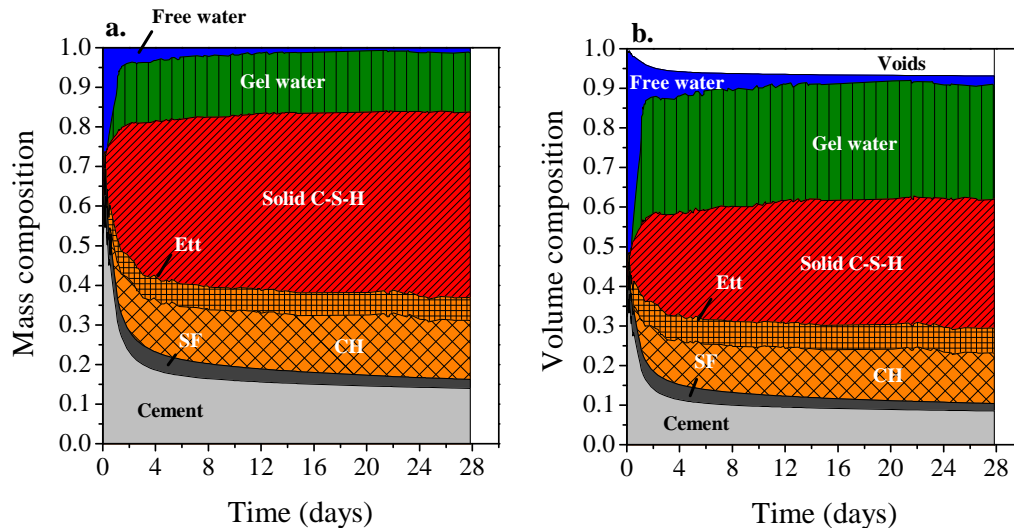


Figure 5.10 – The mass (a) and volume (b) compositions of the paste as a function of time. The different populations are shown on the graphs.

5.1.11 SEM and TEM microscopy

The calculation gives substantially lower Ca/(Si+Al) ratios for white cement mixed with 10% of silica fume compared to plain white cement (Figure 5.9b). In order to confirm experimentally the decrease in Ca/(Si+Al) ratio of the silica fume blend, SEM-EDX quantifications were carried out at 7, 16 and 29 days of hydration. Using backscattered images and point analysis, outer- and inner-C–S–H can be distinguished [14] and quantified separately. The results for both the inner- and outer-C–S–H Ca/(Si+Al) ratios are reported in Table 5.4 and compared to the ^1H NMR results in Figure 5.9b (solid and empty circles). In the experimental conditions, the interaction volume for the electrons is of the order of cubic micrometres. For this reason, a reliable quantification of outer-C–S–H becomes difficult due to intermixing with fine silica fume particles. Inner-products, localized within the original cement grains, are less sensitive to this effect [69].

The SEM data for the inner-C–S–H show slightly higher Ca/(Si+Al) values than the ^1H NMR calculation. However, the ^1H NMR values are average chemical compositions and no dis-

inction is possible between inner- and outer-products. A decrease of Ca/(Si+Al) ratio with time is still observed for both ^1H NMR and inner-C-S-H by SEM. On the other hand, the estimated Ca/(Si+Al) of outer-C-S-H appears to increase with time. This reflects the artefact of intermixing with unreacted silica fume. As silica fume reacts, the outer-C-S-H quantification approaches the ^1H NMR value.

Table 5.4 – SEM-EDX and TEM-EDX Ca/(Si+Al) ratios at different hydration ages. The values are compared to the ^1H NMR Ca/(Si+Al) estimates.

Age (days)	Outer-CSH by SEM	Inner-CSH by SEM	TEM	Average ^1H NMR
7	1.15 ± 0.22	1.54 ± 0.09	—	1.48 ± 0.04
16	1.22 ± 0.26	1.43 ± 0.09	—	1.40 ± 0.04
28 / 29	1.24 ± 0.16	1.42 ± 0.07	1.34 ± 0.04	1.33 ± 0.04

A TEM-EDX quantification of the C-S-H Ca/(Si+Al) at 28 days of hydration was carried out (red square in Figure 5.9b). TEM experiments were performed by John Rossen at the CIME laboratory at EPFL. It is easier to avoid interaction with either cement grains or unreacted silica fume by TEM-EDX analysis as it probes thin sections of C-S-H where the interaction volume is much smaller. The results give $\text{Ca}/(\text{Si}+\text{Al}) = 1.34 \pm 0.04$, which is in between the SEM inner- and outer- quantification and almost identical to the ^1H NMR estimate at 28 days.

The second advantage of the TEM is the possibility of seeing C-S-H morphology. Figure 5.11 shows a TEM bright field electron image of one of the thin sections under study. It is clear from the image that the C-S-H displays a more fine, foil-like structure than fibrils. Richardson [18] reports that this feature is representative of a $\text{Ca}/\text{Si} < 1.5$. This was further confirmed by the recent work of Rossen [70] when studying various blended systems. In this work, the foil-like morphology observed by TEM is then consistent with the Ca/(Si+Al) ratios reported in Table 5.4 (1.34 ± 0.04 measured by TEM and 1.33 ± 0.04 measured by ^1H NMR at 28 days).

The difference in the values obtained based on the degree of reaction of alite by XRD and ^{29}Si MAS NMR shown in Figure 5.3 highlights the possible discrepancies particularly at early age. Nevertheless at later ages the values seem to be highly self-consistent, in particular with excellent agreement in the C-S-H composition measured by TEM and that calculated from the ^1H NMR. This gives confidence in the absolute values from around 12 days.

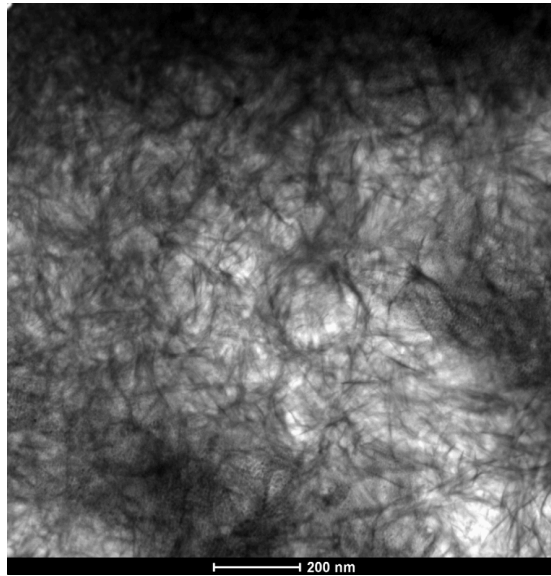


Figure 5.11 – TEM micrograph of white cement paste with 10% of silica fume at 28 days of hydration. The image displays the foil-like structure of C–S–H.

5.1.12 Discussion and conclusions

This study has confirmed the impact of silica fume on hydration kinetics. There is an enhancement of the cement reaction at early age due to the small size and high surface area of the silica fume which increases the C–S–H nucleation. However, the evolution of the different water populations follows a very similar pattern in the system with silica fume to those without, indicating no fundamental change in the underlying mechanisms.

Several phenomena occur simultaneously at 1 day. In addition to the plateau of the gel pores intensity, there is an important change in the rate of consumption of capillary water. This moment coincides with the time at which the capillary pore size reaches 8 nm, the interhydrate specific size. This behaviour, previously observed for the plain white cement, suggests at this stage that the hydration processes in cement paste are affected by the lack of water filled space for C–S–H growth.

The changes in the C–S–H due to the pozzolanic reaction also confirm previous findings of a decrease in the Ca/(Si+Al) ratio of the C–S–H. Based on the C–S–H analogue structure of tobermorite, this decrease may be thought of the addition of silicon bridging tetrahedra in between silicon dimers as a replacement of calcium. However, the ^{29}Si MAS NMR data reported in Table 5.3 shows only a slight rise of the average chain length of SiO_4 tetrahedra (CL_{Si}) from 2.51 to 2.80. It is suggested that there is also a loss of calcium from the interlayer of the C–S–H, which participates in the pozzolanic reaction and explains that the decrease in the Portlandite content is lower than expected. Kocaba [119] also found for slag blends that the Ca/Si lowers before consumption of Portlandite.

The analysis of ^1H NMR signals allows to take the analysis further by quantifying the different water populations and calculating C–S–H characteristics. It indicates a growth of C–S–H similar to that observed for plain white cement when gel pores stop forming within the first days. Densities and the overall water content of the C–S–H are very similar at 28 days and no major structural difference is observed. Pore sizes between plain white cement and white cement with silica fume are also very similar. However there is an indication that there is less interlayer water in the C–S–H. Furthermore, the ratio $I_{\text{gel}}/I_{\text{CSH}}$ goes from 1.7 for plain white cement up to 2.4 for the silica fume mix at 28 days of hydration. One might relate the change in this value with different C–S–H morphology: foils or fibrils. However, more systems need to be explored and no definitive conclusions can be drawn at this stage.

5.2 The addition of slag

5.2.1 Mixes under study

Slag is one of the common SCMs used in the field and hence an important material to study. Following the study of Berodier [120] who studied slag systems by MIP and SEM, the influence of the addition of 10, 20, 30 and 40% of slag by mass was investigated. For all slag mixes, the cement mass was kept at 60% of the solid content and quartz was used as replacement of the slag. Table 5.5 shows the 5 mixes under study. White cement batch 3 was used (composition p. 36). The detailed chemical composition of the slag is given in Annex B, p. 163. The quartz is supposed to be inert and has the same particle size distribution as the cement and the slag (Annex C, p. 165).

Table 5.5 – The different mixes under study with slag contents ranging from 0 to 40 mass %.

Mix	w/s	WC	Slag	Quartz
1	0.40	60%	40%	0%
2	0.40	60%	30%	10%
3	0.40	60%	20%	20%
4	0.40	60%	10%	30%
5	0.40	60%	0%	40%

The water-to-solid ratio, w/s , was kept at 0.40 to keep a similar space available for hydrates to grow. It was previously shown that the w/c ratio has an influence on the growth of C–S–H gel pores (section 4.2.7, p. 59).

Pastes were mixed according to the procedure used for all other pastes. Samples were kept sealed at 20 °C for 28 days. At 28 days, ^1H NMR and XRD with Rietveld analysis were carried out.

5.2.2 Experimental results

XRD and Rietveld quantification

Figure 5.12a shows the XRD results after 28 days of sealed hydration. The degree of cement reaction decreases linearly when increasing the amount of slag, from $\alpha_c^{0\%S} = 0.88$ to $\alpha_c^{40\%S} = 0.78$ for 0% and 40% of slag respectively. In that sense, there is a competition between slag and cement reaction.

For the crystalline phases, the Portlandite and ettringite amounts decrease with addition of slag. This is related to the fact that both arise from cement reaction. As α_c decreases with addition of slag, so do Portlandite and ettringite contents. On the other hand, the hydrotalcite content increases due to the supply of aluminium from the reacting slag.

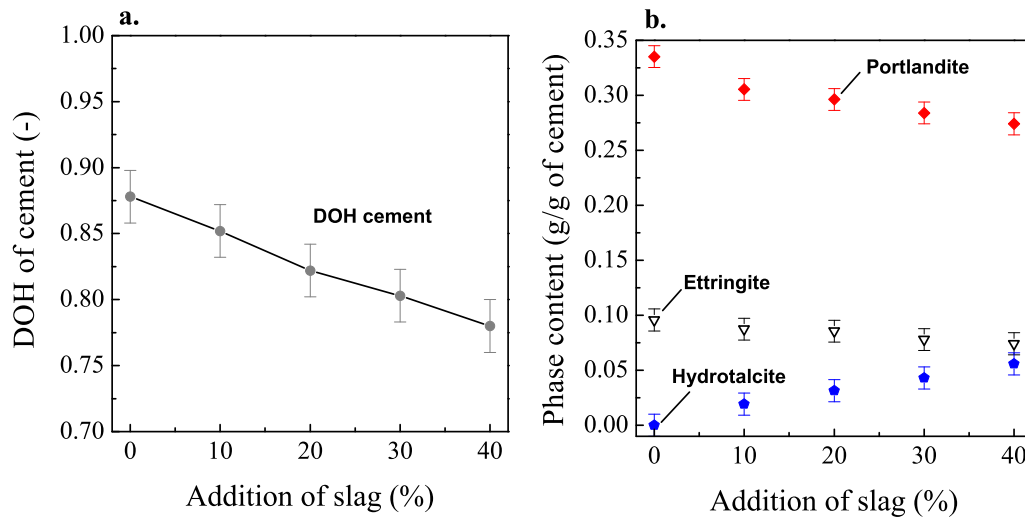


Figure 5.12 – XRD Rietveld quantification results. (a) Degree of cement reaction and (b) Portlandite, ettringite and hydrotalcite contents, all normalized per gram of cement.

¹H NMR results

Figure 5.13 shows the corresponding ¹H NMR results after 28 days of sealed hydration for all mixes. Signal amplitudes and signal T_2 are presented.

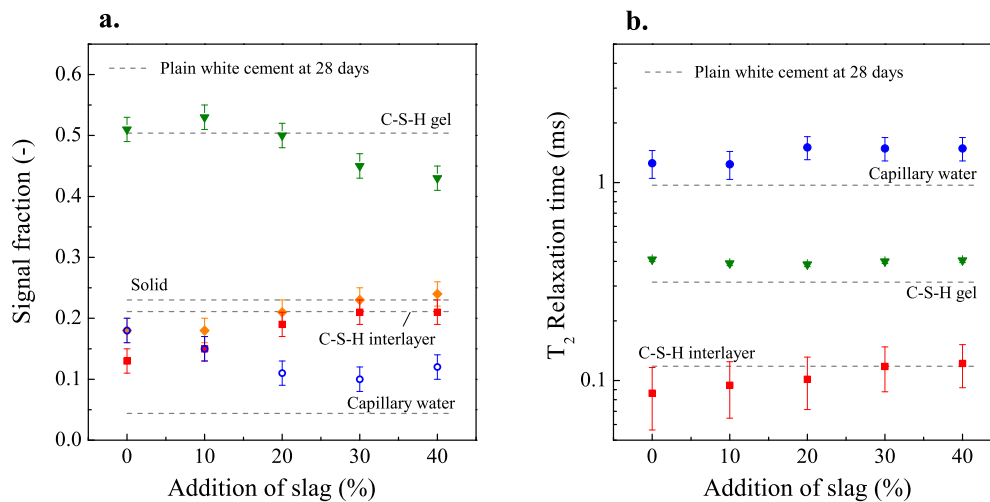


Figure 5.13 – (a) The different NMR signal fractions as a function of slag addition and (b) associated T_2 relaxation times. Symbols are similar to other sections. The dashed grey lines show the NMR characteristics of the comparable plain white cement paste at 28 days of hydration.

As slag is added as a replacement of quartz, the solid signal I_{solid} and signal from C–S–H interlayer I_{CSH} increase. Despite the lower degree of cement hydration, it reflects the fact that more reactive material is present in the mixes and hence more C–S–H and hydrotalcite precipitate. As more hydrates precipitate when adding slag instead of quartz, the amount of capillary water I_{cap} is lower from $I_{\text{cap}} = 0.18$ for 0% of slag to $I_{\text{cap}} = 0.12$ for 40% of slag.

The bigger impact due to the addition of slag concerns the gel water signal I_{gel} , which decreases from $I_{\text{gel}} = 0.51$ for 0% of slag down to $I_{\text{gel}} = 0.43$ for 40% of slag. Even though the interlayer signal increases, the presence of slag does not favour the formation of gel pores. The ratio $I_{\text{gel}}/I_{\text{CSH}} = 2.1$ for 40% of quartz compared to $I_{\text{gel}}/I_{\text{CSH}} = 4.0$ for 40% of slag.

Compared to the plain white cement paste at 28 days, all mixes with the different amounts of slag and quartz have a higher amount of filled capillary pores. However, significantly less material has reacted at 28 days when part of the cement was replaced by either slag or quartz.

Concerning the T_2 relaxation times, T_2 values are of the same order of magnitude as for plain white cement pastes. The T_2 of the gel pores does not vary with addition of slag and stays at an average value of $400 \pm 10 \mu\text{s}$. This is slightly higher than in plain white cement pastes. There is a higher T_2 for the capillary water compared to plain white cement paste with a further increase for replacement levels of slag $> 20\%$. Interestingly, the T_2 of the interlayer water monotonically increases with addition of slag. It is difficult to draw any conclusion on this behaviour as extra ferrite from slag ($\approx 1\%$ of Fe_2O_3 by weight) may end up in iron rich phase and influence relaxation phenomena.

The content of water in crystalline phases from XRD is compared to the NMR signal fraction I_{solid} in Figure 5.14. There is a good agreement between both methods for low slag contents. However, the NMR signal gets progressively higher than the one calculated from XRD when more slag is added. This is accounted by some AFm phases, seen by NMR but hardly detectable by XRD. This would correspond to a AFm content of $m_{\text{AFm}} = 0.154 \text{ g/g}$ of cement for 40% of slag.

Kocaba [119] in 2009 studied similar materials. For the combination 60% white cement / 40% slag, the degree of slag reaction at 28 days was approximatively 35%. Based on this value, calculations were done using the thermodynamic model GEMS [121]. Taken the cement and slag compositions and $\alpha_c = 0.78$ and $\alpha_{\text{slag}} = 0.35$, the software GEMS predicts, per gram of cement, a precipitation of 0.211 g of Portlandite, 0.061 g of Hydrotalcite and 0.177 g of AFm. This last results is close to what was calculated based on combined XRD/NMR. The Portlandite content calculated by GEMS may be smaller than expected because the simulation, for $\alpha < 1$, intrinsically assumes that all phases react proportionally.

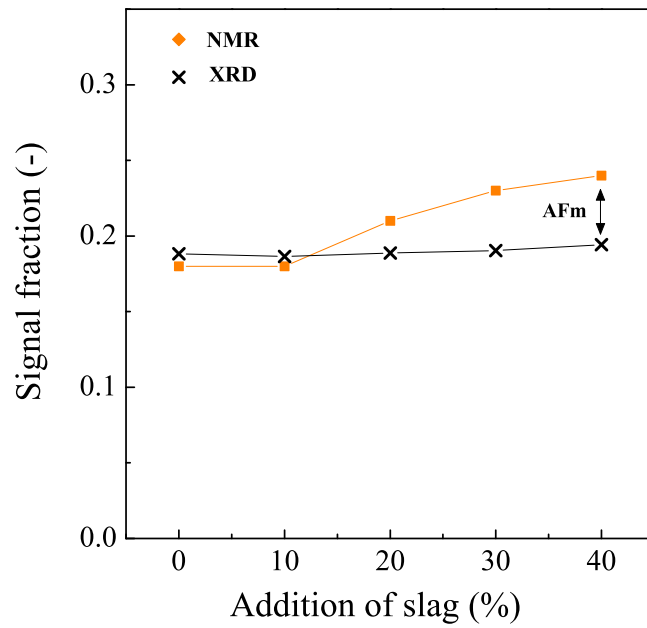


Figure 5.14 – Comparison between NMR I_{solid} and the one calculated based on XRD quantification of crystalline phases.

This study showed that slag has a great influence on the different water population seen by ^1H NMR at 28 days of hydration. To calculate the associated C–S–H densities and chemical compositions, the degree of slag reaction is required. Measurements at later ages are still in progress and the full analysis of the slag systems is not included in this document.

6 Comparison with other measurement techniques

Contents

6.1 Desorption isotherms	116
6.1.1 Experimental procedure	116
6.1.2 Results	116
6.1.3 Discussion	119
6.2 Scanning electron microscopy	120
6.2.1 Experimental procedure	120
6.2.2 Image analysis	121
6.2.3 Results	124
6.2.4 Discussion	124
6.3 Mercury intrusion porosimetry	126
6.3.1 Experimental procedure	126
6.3.2 White cement pastes with different w/c at 28 days of sealed hydration .	126
6.3.3 White cement paste at w/c as a function of hydration time	132
6.3.4 White cement paste cured under water for 28 days	134
6.3.5 The influence of drying on MIP results	136
6.3.6 Conclusions	138

In this project, ^1H NMR was used to measure and characterize the porosity of white cement pastes with different water-to-cement ratios and incorporating different SCMs. Unlike other techniques, ^1H NMR probes never dried pore structures and shows distinct pore populations. In this section, the NMR response is compared to the porosity as assessed by other techniques. Water sorption experiments, scanning electron microscopy and mercury intrusion porosimetry were investigated.

6.1 Desorption isotherms

6.1.1 Experimental procedure

Desorption isotherm experiments were carried out on 28 days old white cement and white cement with 10% of silica fume pastes, both mixed at $w/b = 0.40$ and cured under water for 28 days. The measurements were done on a dynamic vapour sorption (DVS) analyser according to the procedure described in section 3.4.9, p. 46.

6.1.2 Results

Figure 6.1a shows the desorption curves for the white cement and the white cement with silica fume pastes after 28 days of underwater cure. Both shapes resemble classic desorption data for mature cement paste [122]. The two materials show similar results with an important desorption step at high relative humidities and between 40% RH and 30% RH.

For comparison, Figure 6.1b shows the NMR pore type resolved desorption isotherm previously discussed in section 4.7.4, p. 80. The water loss above 90% RH corresponds to the emptying of both capillary and C-S-H gel pores. The important decrease observed further between 40% RH and 30% RH for the DVS corresponds to the final loss of liquid water from the C-S-H gel pores. In the NMR experiments, the C-S-H interlayer pores empty below 30% RH which corresponds to the linear part of the DVS isotherm usually attributed to surface coverage.

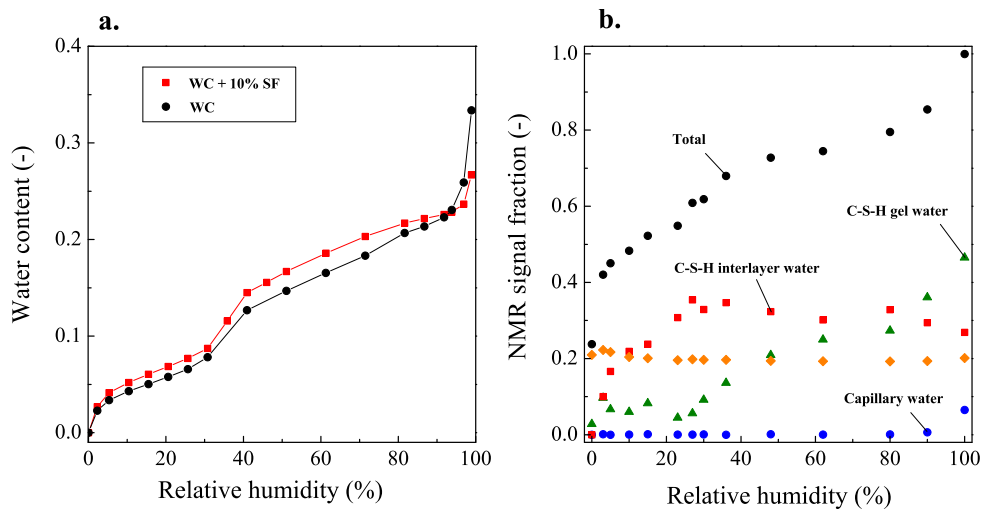


Figure 6.1 – (a) Desorption isotherm for the white cement paste and the white cement with 10% of silica fume paste, carried out after 28 days of under water cure. (b) NMR resolved desorption isotherm for the corresponding paste.

For the plain white cement paste, it is possible from the DVS desorption data to calculate the effective water-to-cement ratio of the paste using additionally the amount of crystalline

phases from XRD. Taking $m_{\text{CH}} = 0.34$ g/g of cement and $m_{\text{ett}} = 0.083$ g/g of cement obtained in the context of the NMR study (*cf.* p. 79), the water-to-cement ratio calculated from DVS is $w_{\text{paste}}/c = 0.455$. This is close to the value obtained upon drying by NMR, 0.463.

Specific surface area (SSA)

The linear region of the desorption isotherm between 30% RH and 10% RH can be used to calculate the BET SSA of the material. Assuming a water molecule thickness ≈ 0.28 nm and its effective adsorbed area $\approx 10.6 \times 10^{-20}$ m², 1 g of water covers a surface ≈ 3500 m². The SSA of the material can then be calculated by $S = 3500 \times u_m$, where u_m is the monolayer moisture ratio. u_m is calculated by

$$u_m = \frac{1}{s + i} \quad (6.1)$$

where s is the desorption slope (between 10% and 30% RH) and i the intercept of this slope with the y -axis.

The results are **198 m²/g of cement** for the plain white cement paste and **226 m²/g of binder** for the silica fume paste. This accounts for all available surfaces, being mostly C–S–H hydrates. The values obtained by NMR for the plain paste were 91 m²/cm³ of paste for the C–S–H gel pores and 175 m²/cm³ of paste for the C–S–H interlayer pores (p. 82). These can be combined and normalized per gram of cement for a total of 190 m²/g of cement. It is close to the DVS result, 198 m²/g, which also takes into account additional surfaces associated with Portlandite and unreacted cement grains for instance.

Pore size interpretation

Desorption isotherms can be interpreted in terms of pore volume versus pore diameter. To that end, the Barrett-Joyner-Halenda (BJH) [23] method using a t -curve from Hagymassy *et al.* [123] was applied to the desorption data. A BET constant of $c = 10-14.5$ was used as in [76]. The results are presented in Figure 6.2. Both pastes show a similar pore size distribution with one major peak corresponding to a pore diameter of circa 2.5 nm.

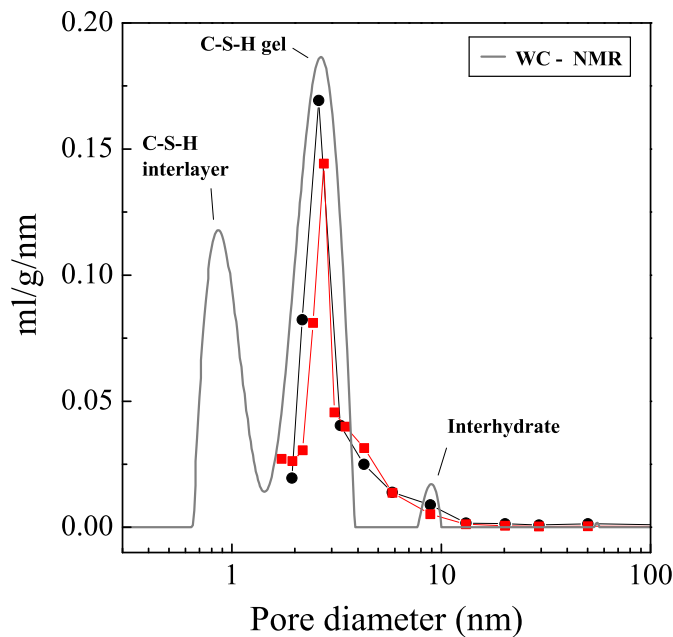


Figure 6.2 – Pore size distribution calculated with the BJH method for the white cement and the white cement with silica fume pastes. Symbols are in accordance with the previous figure. The results are compared to the NMR pore size distribution of the plain white cement paste.

The desorption results for the plain white cement paste can be compared to the NMR pore size distribution (*cf.* p. 80). The main peak of the desorption result corresponds to the second NMR peak previously associated with the C–S–H gel pores. However, the amount of gel porosity is slightly lower when measured by DVS. The interhydrate volume observed by NMR (at 8 nm in diameter) is not resolved as a distinct pore population by the analysis of the desorption data, for which pore cavities are calculated for sizes between 3.0 nm and 10.3 nm in diameter. The C–S–H interlayer pores as seen by NMR are not captured by the DVS analysis.

6.1.3 Discussion

For small pores such as the interlayer space of the C–S–H (≈ 1 nm), the coalescence of water molecules into a liquid phase is unrealistic. Hence, in sorption experiments, the C–S–H interlayer water is desorbed mainly at relative humidities $< 30\%$. In the absence of coalescence in small pores, this quantity of adsorbed water cannot be included in the pore size versus pore volume calculation.

The volume of gel pores is calculated at $0.20 \text{ cm}^3/\text{g}$ of cement by NMR and at $0.14 \text{ cm}^3/\text{g}$ of cement by DVS. These two results both include any potential adsorbed water onto the gel pore surfaces. For the NMR, the adsorbed water is in fast exchange with the bulk pore fluid and hence is included in the total signal intensity for any given saturated pore. The experimental evidence of this phenomenon is the increasing NMR interlayer signal as the gel pores progressively empty (already discussed p. 80). For the DVS, the adsorbed layers were taken into account through the t -curve required in the BJH model. The main reason for the discrepancy between the two methods is that, during desorption experiments, the gel pores do not desorb in one single step. The NMR data reported in Figure 6.1b, p. 116 show a continuous decrease of the gel pore content over a wide range of relative humidities. Some of the gel water already desorbs at high relative humidity ($> 90\%$) while the final loss of water from the gel pores occurs at relative humidity between 40% and 30% . This fact might suggest that not all gel pores are accessible to drying at the same relative humidity pointing out the known “ink bottle” effect during sorption experiments [124].

6.2 Scanning electron microscopy

6.2.1 Experimental procedure

For the microscopy, plain white cement pastes mixed at water-to-cement ratio of 0.40 were studied after 1, 10 and 28 days of sealed hydration. At the desired hydration times, samples were cut in slices of about 2 mm thick, immersed in a large volume of isopropanol for 7 days and then vacuum dried for the same period of time. Samples were subsequently impregnated with epoxy resin and polished following the procedure described in section 3.4.4, p. 45.

Critical to the analysis is the magnification used. This parameter was studied on an OPC paste after 3 days of sealed hydration. The magnification was varied between 1600×, 2400×, 6000× and 10,000× for which the brightness and the contrast were calibrated similarly. At each magnification, a grid of 20 × 20 images was taken. For the analysis, the area associated with the porosity was separated from the cementitious matrix using the same grey level for all magnifications. The total porosity was estimated using the average grey level histogram (of the 400 images). The results are presented in Figure 6.3 and expressed as percentages of the sample surface. The error on these values was calculated by $\text{Error} = \text{Std} / \sqrt{N}$, where N is the number of images.

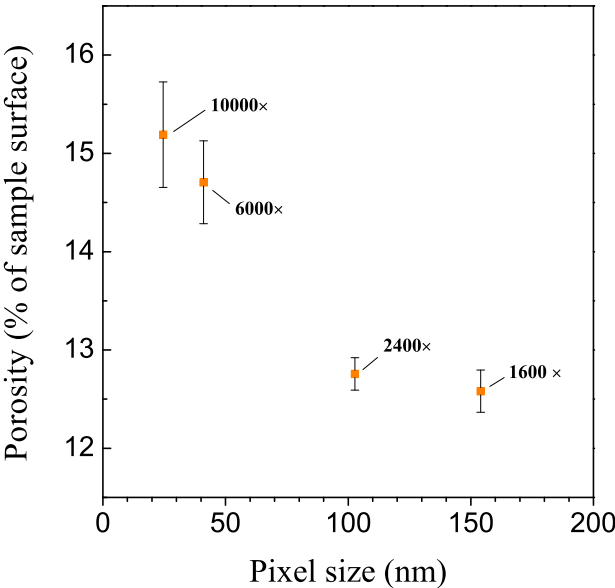


Figure 6.3 – Change in porosity and measurement error with change of magnification for an OPC paste after 3 days of sealed hydration.

The higher the magnification is, the higher the estimated porosity becomes. As the same number of images was used for all magnifications, the error increases for high magnifications.

On the other hand, when very low magnifications are used, the resolution does not allow a good quantification of small features as porosity may be.

For the following study of white cement pastes, a magnification of $2400\times$ (≈ 100 nm of pixel size) was chosen. This magnification has the smallest representative error while the area covered by 400 images (≈ 3 mm²) is still high enough to be representative of the whole sample, within a reasonable measurement time (≈ 5 hours). Using a magnification of $2400\times$, a spot size of 5.5, a working distance of 10 mm and a voltage of 15 kV, a grid of 400 images (20×20 at 16 bits resolution; 1024 per 768 pixels per image) were acquired for each sample.

6.2.2 Image analysis

For pore quantification, the difficult part is the choice of the grey level threshold between the porosity, in black, and the C–S–H hydrates with greyer colours. The grey level histograms of the 400 images taken together for the sealed pastes at 1, 10 and 28 days are presented in Figure 6.4. Peaks corresponding to each phase are shown on the graph. There are 2^{16} grey levels (notated gl) in the exported images. As an example, one image of each paste is shown. While the peak associated to cement grains goes down with hydration time, the one of the C–S–H becomes higher and progressively merges with that of CH. The histogram at 10 days is less wide compared to the two other ones due to the brightness and contrast settings. This further highlights the difficulties of choosing an appropriate threshold for pore quantification.

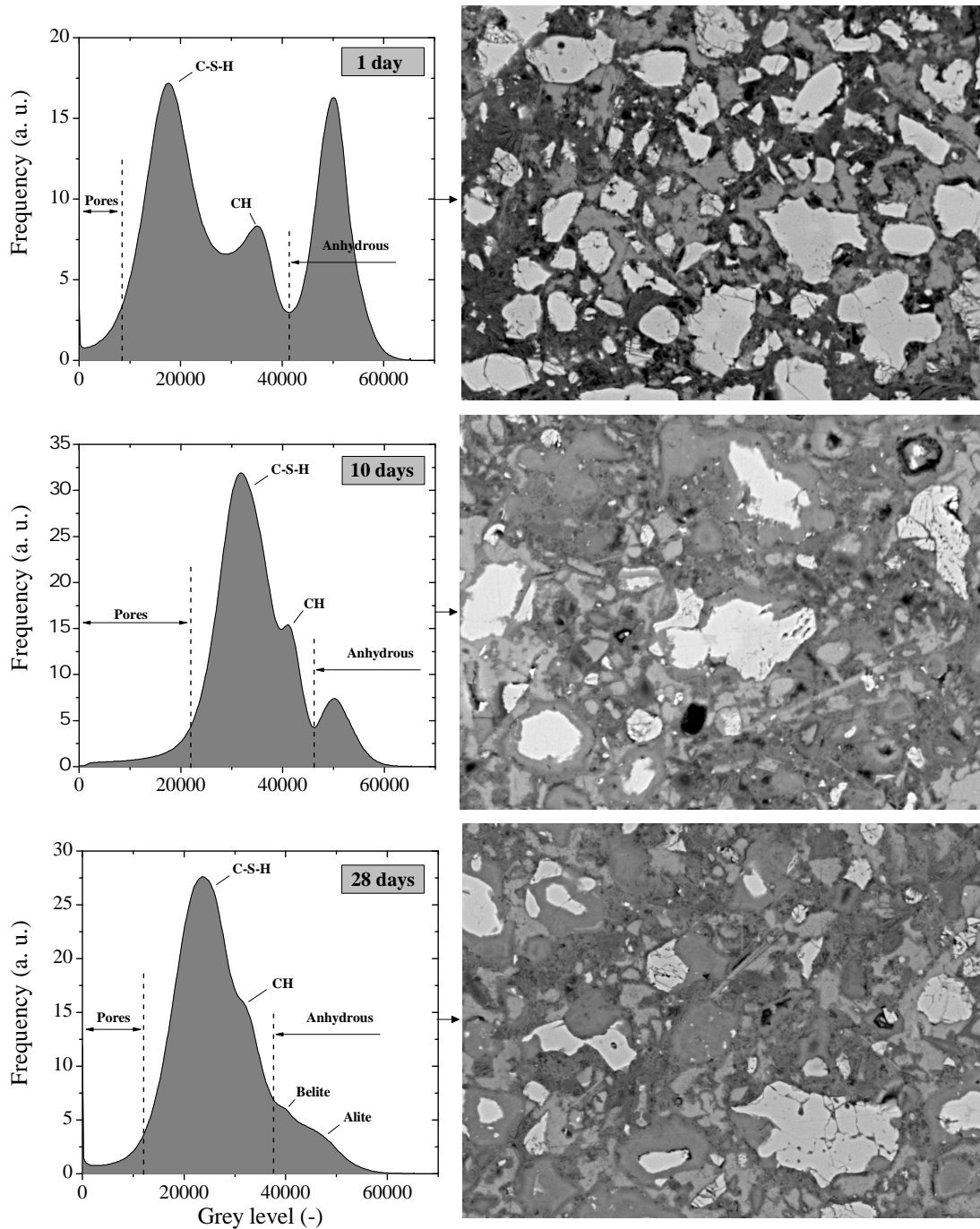


Figure 6.4 – Average grey level histograms for the sealed white cement pastes at 1, 10 and 28 days of hydration with one associated BSE image.

To be consistent in the choice of the threshold for pore quantification between the different images and moreover between the different samples, the following methodology was followed. The total porosity was first quantified for $\pm 5\ 000\ \text{gl}$ around the range of interest, and

normalized to the higher porosity value, notated P_{max} . The results are shown in Figure 6.5 and highlight the sensitivity of the chosen “ gl threshold” on the quantification of the total pore volume. A criteria $d(P)/d(gl)/P_{max} = 0.025$ was chosen and applied to all images and all samples.

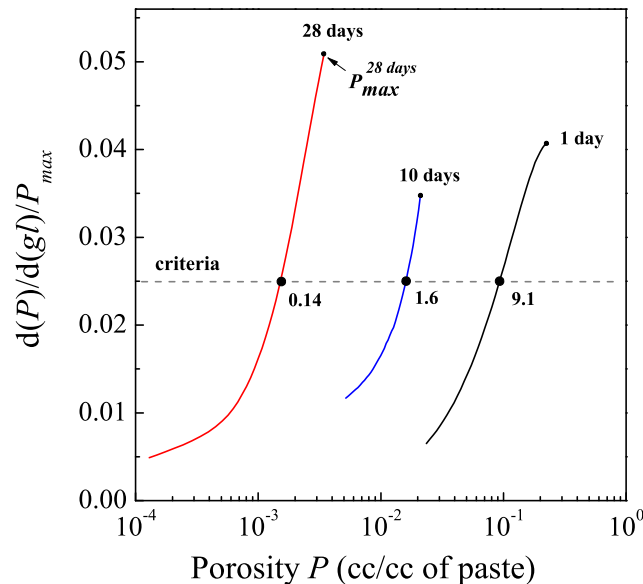


Figure 6.5 – Derivative plot of the estimated porosity with variation of the grey level (notated gl). A criteria of 0.025 was chosen for the pore thresholding.

For the image analysis, the procedure was as follows. Images were translated into binary with the aforementioned thresholding criteria. An “erode” procedure of 2 pixels was carried out and the eroded area was counted as “small pores” (< 2 pixels, *i.e.* < 200 nm in diameter). This procedure allows removing cracks and elongated pores. The rest of the porosity falls in the second category called “big pores” (> 2 pixels, *i.e.* > 200 nm in diameter). As a consequence of the erosion step, big pores are more of rounded shapes. This image analysis procedure was applied following the work of Dunant [125], who used it to quantify damage caused by the alkali silica reaction. No pre-processing filter was applied. This 2D analysis was extended to 3D considering that surface fractional areas are equal to that of volumes. This is valid if there is no preferential orientation and if the probed surface is wide enough to be representative of the sample average characteristics. The results of the following sections are therefore presented in cc/cc of paste.

6.2.3 Results

Following the procedure previously described, Figure 6.6a shows the evolution of the porosity as a function of hydration age. As discussed, the total porosity is divided between small and big pores. The total porosity goes from 9.1% by volume at 1 day down to 1.6% at 10 days and further down to 0.14% at 28 days of hydration. The relative fraction of small pores also goes down over the course of hydration. The division between small and big pores for the 28 days old sample is not discussed as the measured porosity has become very small (< 0.5 %).

One might want to compare the porosity measured by SEM with the one obtained by NMR (cf. Figure 4.22, p. 77). Figure 6.6b shows the total porosity estimated by SEM, the NMR capillary water volume (signal I_{cap}) and the chemical shrinkage volume (previously expressed as I_{void}) as a function of hydration time. At every hydration age, the quantification by SEM at a magnification of 2400× detects less capillary pores than what was measured by NMR. When the chemical shrinkage volume is added to the NMR capillary water volume, the comparison shows similar trends but different magnitudes.

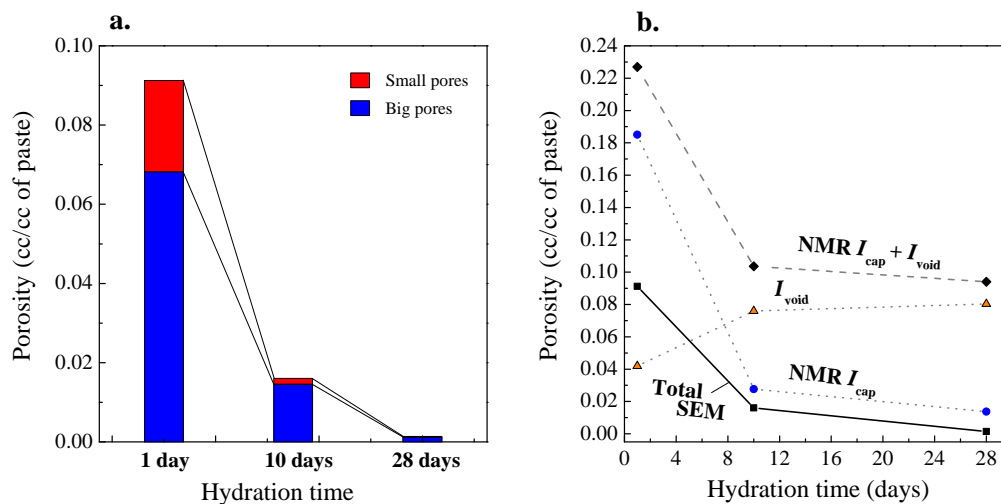


Figure 6.6 – (a) Pore volume calculated by SEM for plain white cement pastes at 1, 10 and 28 days of sealed hydration. Big pores are pores > 200 nm in diameters, small pores < 200 nm in diameter. (b) Comparison between the total porosity estimated by SEM (black squares), the capillary water volume measured by NMR (blue circles), the chemical shrinkage volume (orange triangles), and the sum of the two previous quantities (black diamonds), as a function of hydration time and normalized as a volume percentage of paste.

6.2.4 Discussion

Figure 6.7 show a SEM image at 10,000× magnification and a TEM bright field image both for mature cement pastes. The TEM image was provided by John Rossen and shows the C–S–H in a mature white cement paste. While inner- and outer-C–S–H can be distinguished in both

images, only the high resolution of the TEM allows to see the spaces between the tightly packed C-S-H needles. The common scale of 2 μm between the two images indicates that the finest capillary porosity cannot be captured by the SEM technique. For this reason, there will always be an underestimation of the porosity measured by SEM.

In conclusion, the SEM measures both chemical shrinkage and capillary pore volume, but the resolution of the technique leads to an underestimation of their combined quantity. A calibration would be required to use the SEM quantitatively.

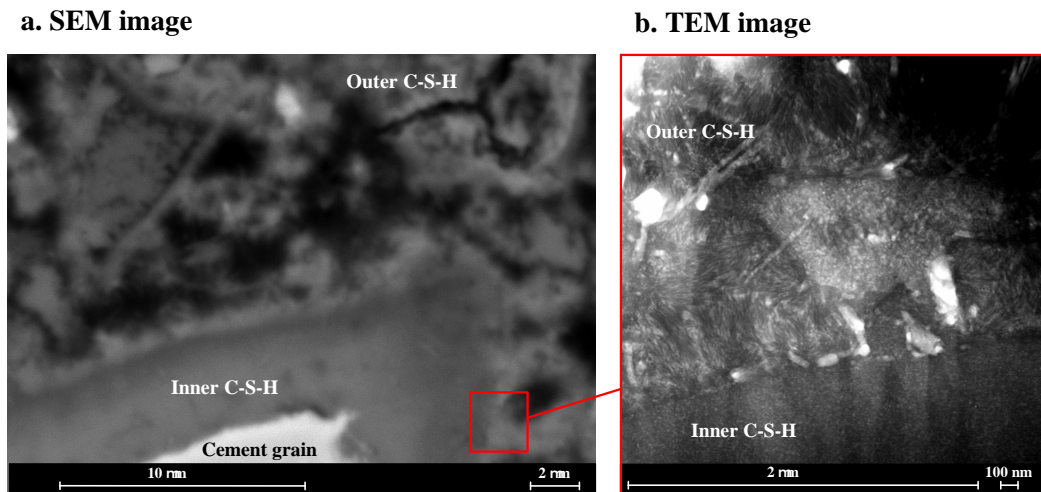


Figure 6.7 – (a) SEM image at 10,000 \times magnification and (b) a TEM bright field image of the C-S-H, both for mature cement pastes.

6.3 Mercury intrusion porosimetry

6.3.1 Experimental procedure

For most of the cement pastes studied by MIP, isopropanol exchange method was used as the sample preparation. The influence of other drying methods on MIP results was further investigated and is presented in section 6.3.5, p. 136.

At the desired hydration age, MIP measurements were carried out according to the procedure described in section 3.4.10, p. 48. Three repetitions were done for each sample and the results presented are average MIP data. The contact angle between the solid surface and the mercury is taken at $\theta = 140^\circ$. For comparison with NMR results, a planar pore model was used for the interpretation of MIP pore volumes versus pore diameters. It did not change appreciably compared to the commonly used cylindrical model.

6.3.2 White cement pastes with different w/c at 28 days of sealed hydration

Plain white cement pastes mixed at $w/c = 0.32$, 0.40 and 0.48 were first studied. The sample preparation was done by solvent exchange. Figure 6.8 shows the average MIP cumulative pore volumes for each paste.

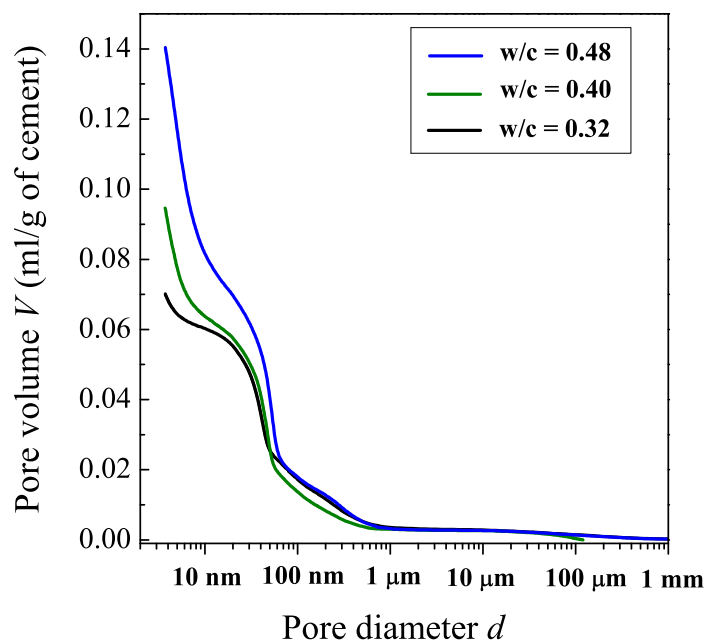


Figure 6.8 – MIP cumulative pore volumes at 28 days of sealed hydration for $w/c = 0.32$, 0.40 and 0.48.

A common intrusion threshold is observed at around 600 nm pore diameter. Hereafter, two main intrusion steps can be observed. The total accessible porosity during the MIP experiment goes down with decreasing the water-to-cement ratio with approximately 0.141 ml/g of cement, 0.095 ml/g of cement and 0.070 ml/g of cement for $w/c = 0.48$, 0.40 and 0.32 respectively.

Interpretation of MIP data into pore populations

To help the interpretation of the MIP data, derivatives were calculated with respect to the logarithm of the pore entry diameter d . The results are shown in Figure 6.9 and plotted versus pore entry diameter. As suggested by the cumulative plots, two main peaks can be distinguished. The first peak on the left hand side arises almost certainly from the C–S–H gel pores (grey areas on the figure). The second main peak at a few tens of nm in diameter is assumed to be part of the capillary pore volume.

The volume associated with the C–S–H peak becomes smaller when decreasing the water-to-cement ratio as well as the content of capillary porosity. The reason why less C–S–H are being measured for low w/c is related to the decrease in intrusion capacity for tinier or “less connected” pore networks. Evidences of this phenomenon are the shift of the C–S–H peak toward smaller size and the reduction of the neck between the C–S–H peak and the rest of the intruded volume. Therefore, the measurement of this C–S–H peak is certainly not a reliable estimate of the C–S–H porosity. The current peak assignment is further discussed in the next sections.

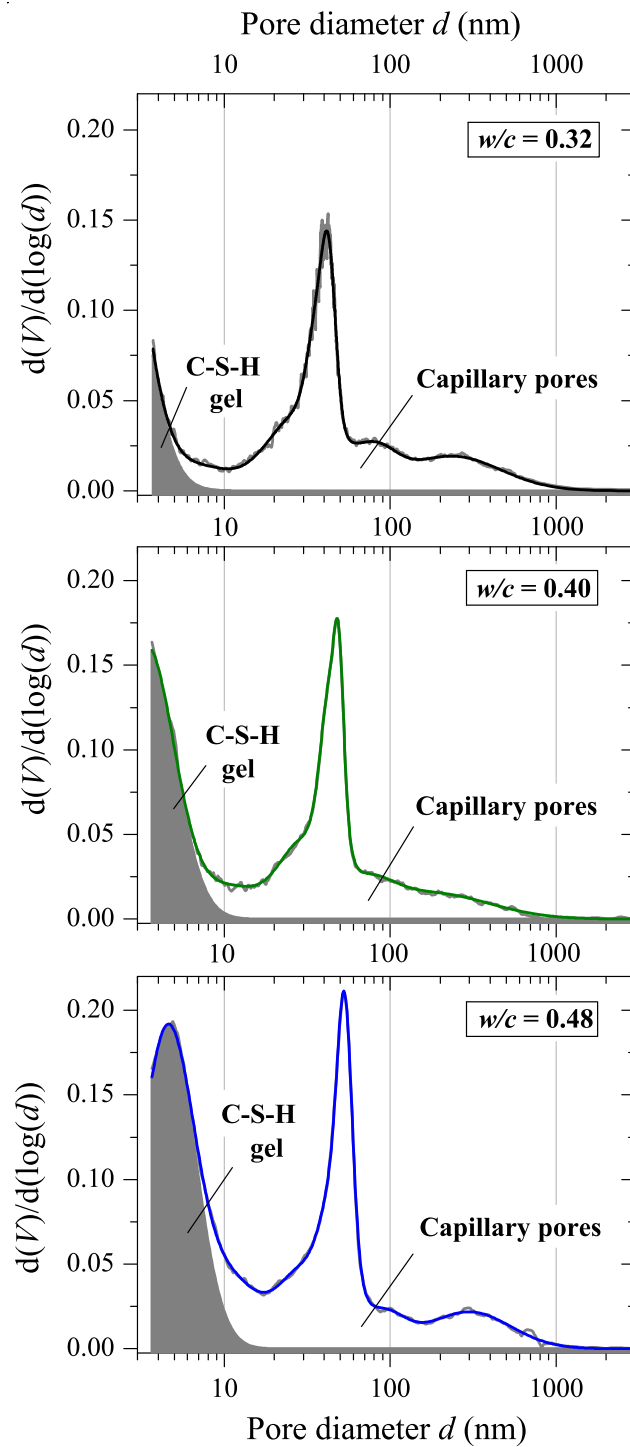


Figure 6.9 – First derivative of the MIP pore volumes as a function of $\log(d)$ for $w/c = 0.32$, 0.40 and 0.48 pastes.

Comparison with the NMR results

It first needs to be pointed out that there might be some limitations comparing MIP results with the pore volumes obtained by NMR, especially for the fact that the sample preparation for the MIP might generate irreversible changes to the existing pore structure. Nevertheless, this section compares both methods disregarding these problematic.

The derivative curves presented in Figure 6.9 can be recalculated into pore volume for the two populations previously mentioned. As C–S–H peaks are not complete, they cannot be quantified. The volume of capillary porosity can however be calculated as the total pore volume minus the fraction within the C–S–H peak. The results for the three pastes under study are presented in Figure 6.10 as a function of water-to-cement ratio and compared to the porosity results obtained in the context of the NMR study (*cf.* Figure 4.22 ,p. 77). To that end, the NMR signal I_{cap} was converted into ml/g of cement and added to the associated chemical shrinkage volume I_{void} .

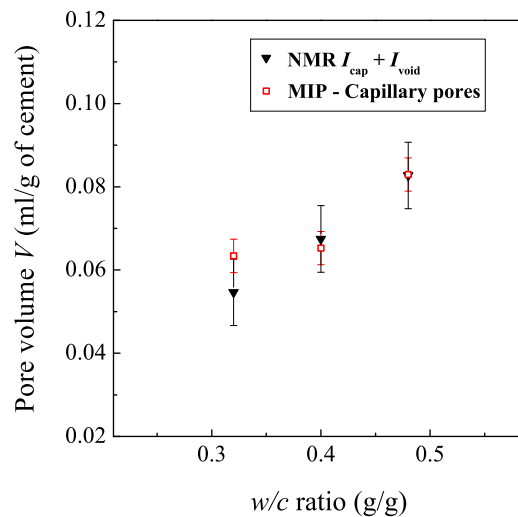


Figure 6.10 – Comparison between the capillary porosity as quantified by MIP and the “NMR $I_{\text{cap}} + I_{\text{void}}$ ” volumes.

The analysis of the MIP data gives very similar capillary pore volumes compared to the combined “NMR $I_{\text{cap}} + I_{\text{void}}$ ”. The absolute volume error estimated for the MIP and the NMR is $\pm 0.008 \text{ cm}^3$ and $\pm 0.004 \text{ cm}^3$ respectively. For the $w/c = 0.32$ paste, the discrepancy of the results between both methods might arise from the poor workability of the paste and the difficulties to remove air bubbles out of the in-place material.

Now that the peak assignment has been verified quantitatively, it is interesting to compare pore sizes (Figure 6.11). It can be seen that the pore sizes calculated for both techniques are not comparable. The C–S–H gel pore size by MIP ranges between 3.6 nm and 10 nm in diameter

which is bigger than the size calculated from NMR (2.5 nm for the C–S–H gel pores). In the same way, the capillary porosity by MIP is located at sizes between 30 and 60 nm compared to 8 nm for the NMR interhydrate.

The "Ink-bottle" effect [30, 126] was often mentioned to justify the discrepancies of pore sizes between the MIP and other methods. In this work, "ink-bottle" pores do slightly influence pore sizes as seen by the small shift of the main capillary peak when decreasing the w/c . However, this theory does not explain the difference with the NMR as it would have shifted pore size to smaller values rather than bigger. Given the good agreement between the amount of capillary porosity between the MIP and the NMR, the question about using $\theta = 140^\circ$ in the Washburn equation (Equation 1.1, p 15) is raised. Researchers often use $\theta = 140^\circ$ (as here) for the intrusion contact angle between the mercury and the solid surface and a $\theta = 107^\circ$ is used when the mercury is receding.

Figure 6.11 (bottom graph) shows what would be the impact of changing the contact angle θ on the MIP pore size distribution of the $w/c = 0.40$ data set (dashed lines). The contact angle needs to be changed from 140° to 125° in order to align approximately the MIP gel pore size onto the NMR results. On the other hand, to get the interhydrate size right, the value of θ needs to be further decreased to $\theta = 100^\circ$. This last value is quite low but values as small as 117° can be found in the literature [127]. Additionally, the θ parameter may depend on many factors such as the sample age, the surface composition, the pre-treatment used and the purity of the mercury [128]. The present study suggests that the C–S–H surface might be more mercuriphilic than expected but furthermore that different θ must be used for the mercury entering capillary pores and the mercury entering C–S–H pores.

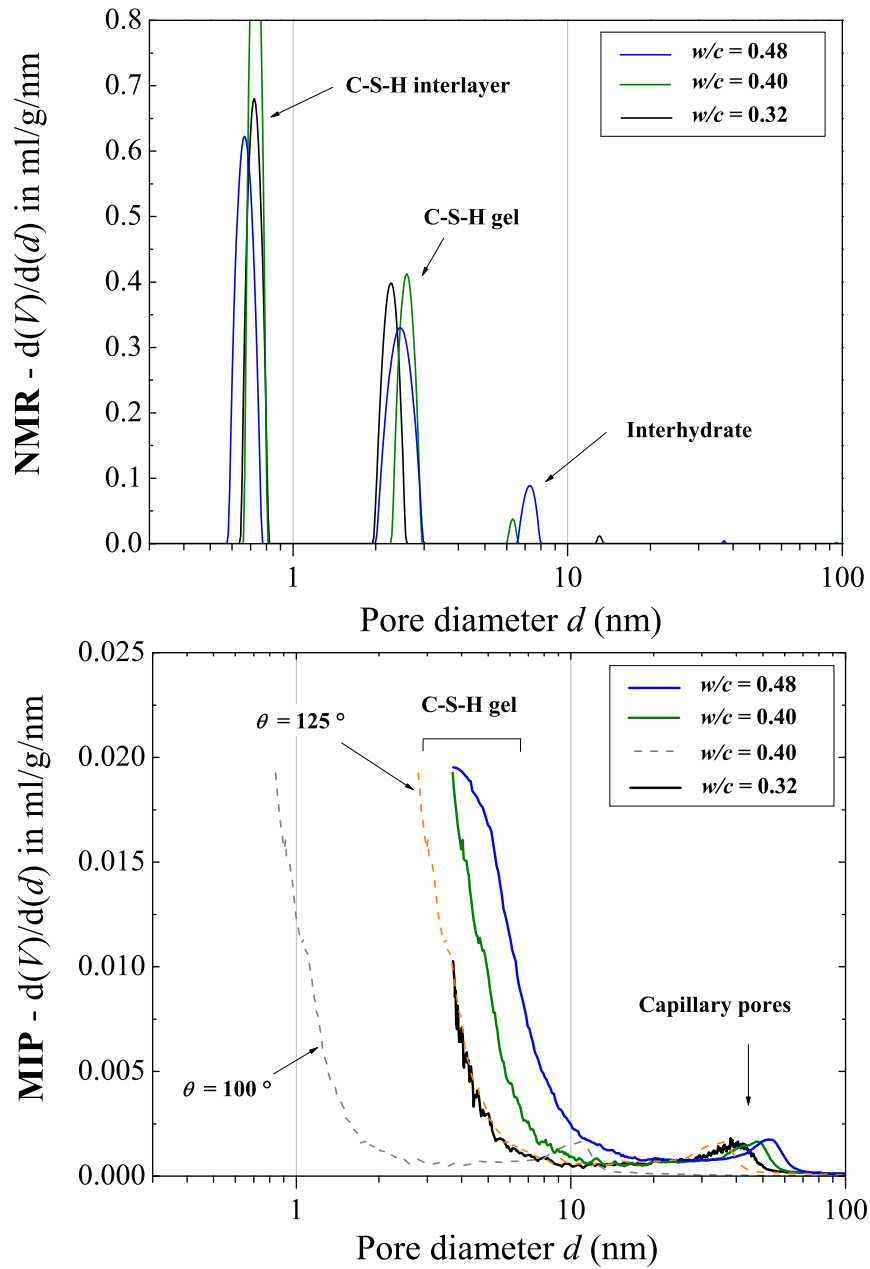


Figure 6.11 – Comparison between the MIP pore size distribution and the NMR pore size distribution for $w/c = 0.32, 0.40$ and 0.48 .

6.3.3 White cement paste at w/c as a function of hydration time

The methodology used to calculate the content of capillary porosity from MIP data was applied to track the porosity changes as a function of hydration time. Sealed white cement paste mixed at $w/c = 0.40$ was cast for MIP experiments after 1, 2, 2.5, 3.5, 6.5, 10 and 28 days of hydration. The sample preparation was done by solvent exchange. The cumulative MIP results are presented in Figure 6.12a using $\theta = 140^\circ$. Three derivatives are shown in Figure 6.12b for the paste after 1 day, 3.5 days and 28 days of sealed hydration.

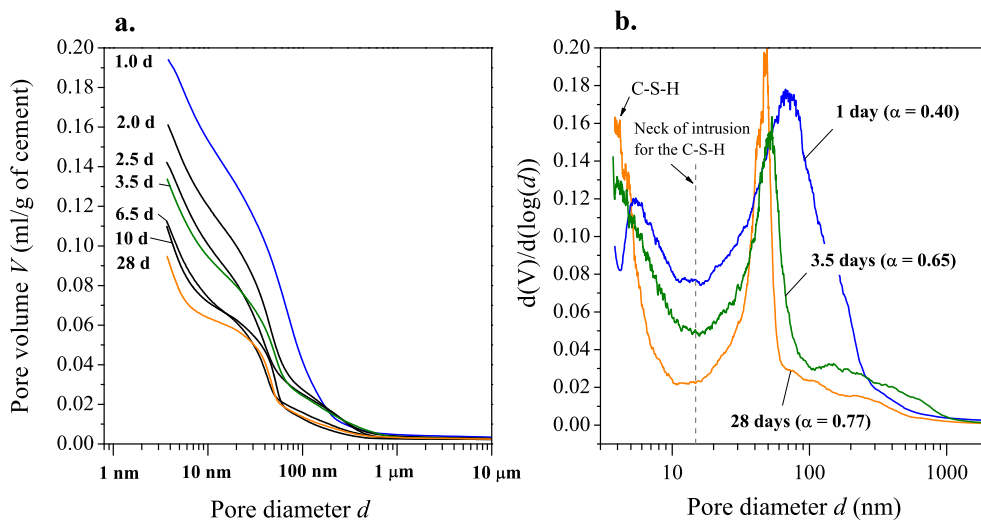


Figure 6.12 – (a) Cumulative pore volumes as a function of hydration time and (b) the associated derivative for 1 day, 3.5 days and 28 days of hydration.

Except for the 1 day sample, comparable intrusion steps are observed while the total accessible porosity goes down with increasing hydration. When looking at the derivative curves, the main peak of the capillary porosity goes down in amount and in size from 1 day to 28 days of hydration. On the other hand and as for the study of different w/c , the C–S–H peak and the volume of its “neck of intrusion” (dashed line in Figure 6.12b) become smaller.

As previously, the MIP capillary pore volume can be obtained by subtracting the porosity associated with the C–S–H peak from the total intruded pore volume. The results are presented in Figure 6.13 and compared to the combined “NMR $I_{\text{cap}} + I_{\text{void}}$ ”. There is a good agreement between both techniques which further supports the methodology of quantification and the peak assignment of MIP spectra.

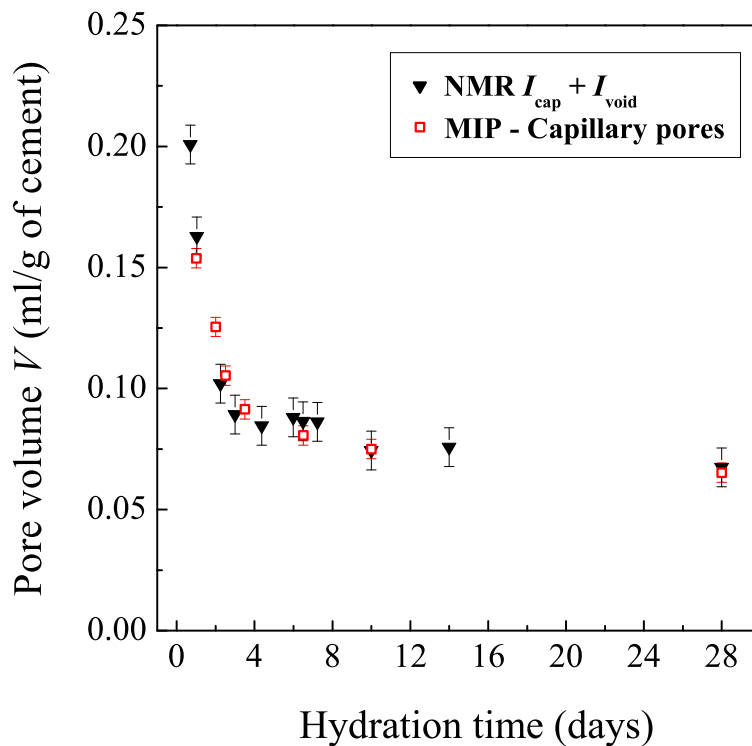


Figure 6.13 – Comparison between the capillary content between the MIP technique and the NMR analysis as a function of hydration age for the $w/c = 0.40$ paste.

As an illustration, Figure 6.14 shows what the MIP technique is able to measure of the porosity detected by NMR. For the latter, the cumulative bar charts show the different categories of NMR pore water plus additionally the chemical shrinkage volume (Voids). From 1 day to 28 days, there is a progressive redistribution of the water from the capillary porosity to the C–S–H pores.

Concerning the MIP, only a small fraction of gel porosity is being measured for the different samples studied. This highlights the difficulties to push the mercury into the small C–S–H pores. A collapse of these structures also might have occurred over drying or as a result of the high mercury pressures. Approximately the same amount of the gel porosity is measured from 1 day to 28 days of hydration which indicates that the measurable C–S–H gel pores remain accessible even when the volume of capillary porosity diminishes. Because of that, the MIP total pore volume is a good indicator of the changes occurring to the capillary porosity. The total MIP pore volume needs, in fact, to be defined as the volume accessible for the mercury at the maximum applied pressure which includes all capillary pores plus a part of the gel pores.

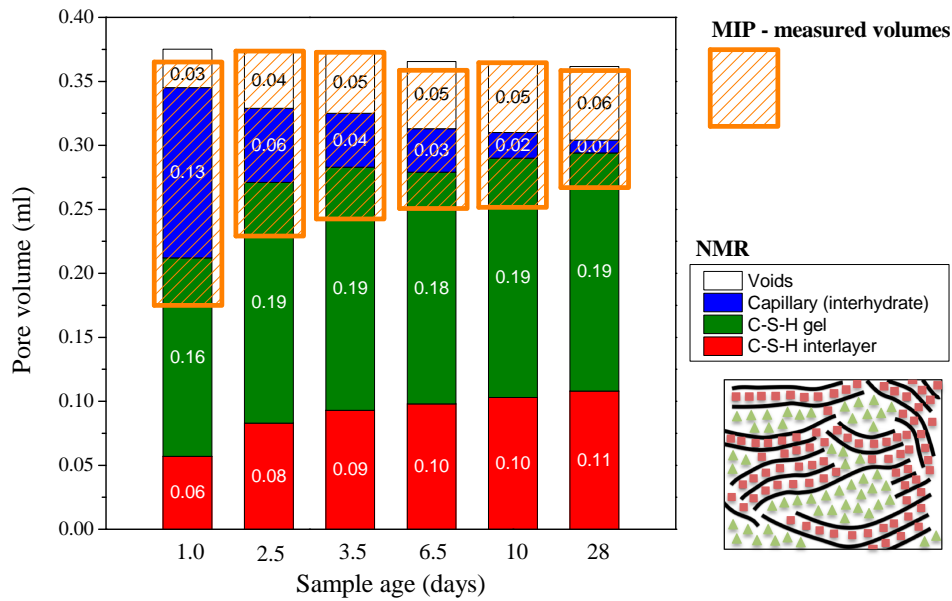


Figure 6.14 – Comparison between the volumes of liquid water measured by NMR for the different pores and the porosity as measured by MIP. The division of the MIP pore volume between the capillary pores and the C–S–H gel pores was done by quantifying the respective C–S–H peaks.

6.3.4 White cement paste cured under water for 28 days

White cement paste after 28 days of under water cure was prepared by the solvent exchange method and measured by MIP according to the procedure previously described.

Figure 6.15a shows two repetitions of the MIP measurements. The threshold pore diameter observed at 600 nm for sealed pastes is located at 50 nm when the paste is cured under water. Two main intrusion steps are still observed for a total porosity of about 0.085 ml/g of cement.

Figure 6.15b shows the first derivative of the average MIP data which is directly comparable to the NMR pore size distribution taken from Figure 4.23, p. 80. As for sealed pastes, the same size discrepancy is observed between the NMR and MIP pore size distribution when $\theta = 140^\circ$ is used. $\theta = 125^\circ$ for the C–S–H gel pores and $\theta = 100^\circ$ for the interhydrate pores must be used respectively in order to obtain similar sizes as the NMR.

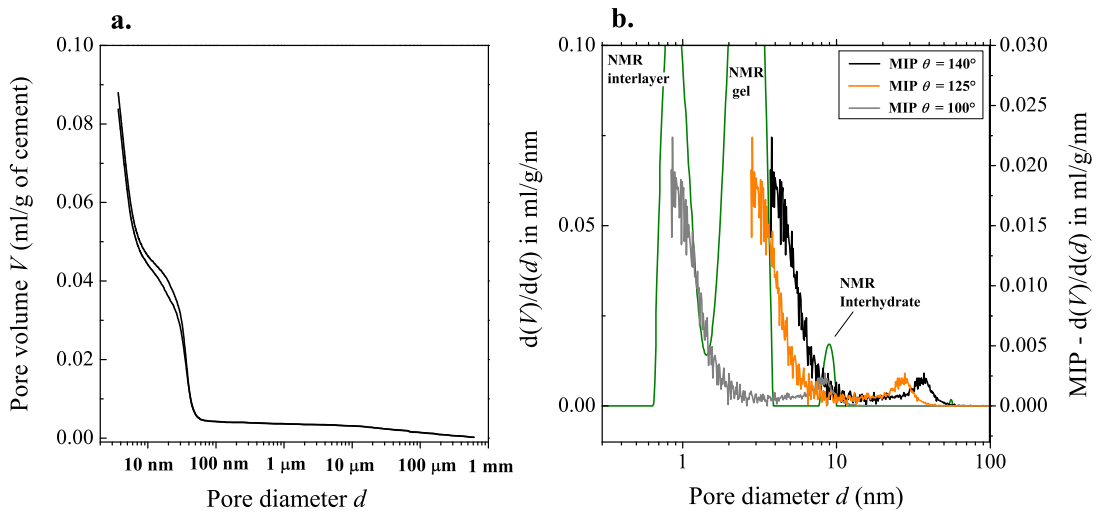


Figure 6.15 – (a) Cumulative pore volumes for the $w/c = 0.40$ paste cured under water for 28 days and (b) the comparison of the pore size distribution with the NMR.

The first derivative of the MIP pore volume with respect to the logarithm of the pore diameter is shown in Figure 6.16. Again, the left hand side peak is associated with the C-S-H gel pores, being only partially measured.

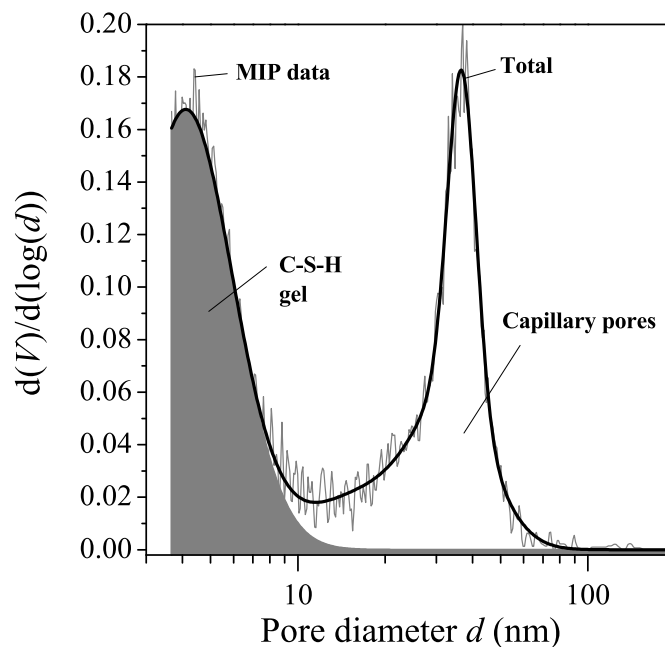


Figure 6.16 – First derivative of the MIP data as a function of $\log(d)$ for the underwater cured paste at 28 days.

Contrary to sealed pastes (Figure 6.9), the underwater cured paste shows no pores with size above 100 nm in diameter. This highlights that the bigger porosity in cement paste arises from chemical shrinkage and self-dessication of the sample. When the MIP capillary pore volume is quantified as the total pore volume minus the C–S–H peak, it leads to 0.043 ± 0.004 ml/g of cement. The amount of capillary pores (called interhydrate pores) measured by NMR was 0.028 ± 0.008 ml/g of cement. This is in reasonable good agreement considering the error of both techniques. However, the difference may eventually come from the curing condition. Small samples were cured under water for the NMR measurements while bigger samples were cast for the MIP. The curing water might not have percolate through the whole sample thickness for the MIP leading to partial self-dessication.

6.3.5 The influence of drying on MIP results

The previous sections showed MIP results obtained on cement pastes dried by solvent exchange method. Other drying methods are often used such as oven drying, freeze drying or vacuum drying. The aim of this section is to quantify the impact of different drying methods on the MIP results for the sealed white cement paste mixed at $w/c = 0.40$ after 28 days of sealed hydration. The results are presented in Figure 6.17a for the cumulative pore volumes and in Figure 6.17b for the derivative pore volumes. The solvent exchange method is the reference for comparison.

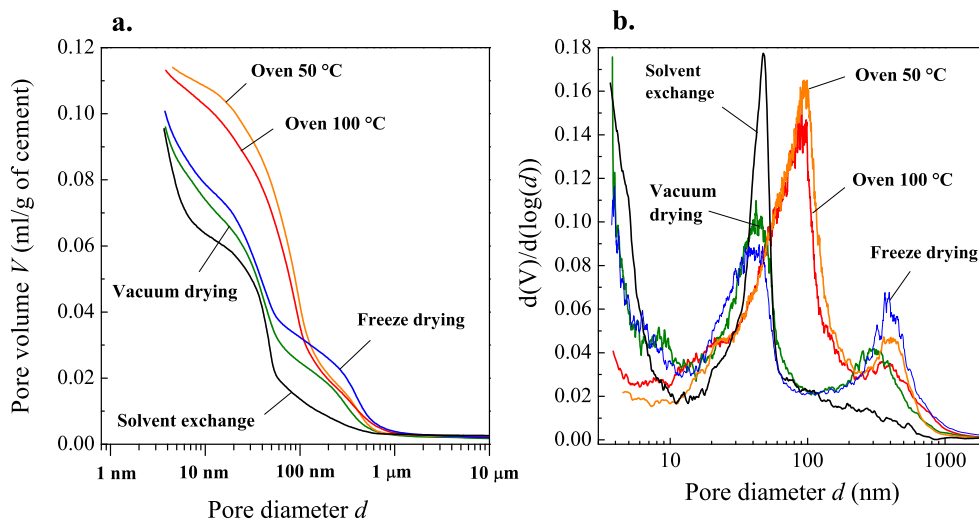


Figure 6.17 – (a) MIP results for different drying methods for the paste $w/c = 0.40$ paste at 28 days of sealed hydration and (b) the associated derivative pore volumes.

The oven drying at 50 °C and 110 °C give a significant higher amount of total porosity compared to the other drying techniques and C–S–H gel pores are not measured anymore. In addition, the main capillary pore peak is broader and shifted to bigger sizes. There is the appearance of a big pore population between 200 nm and 1 μ m which might result from the cracking of the

sample.

Freeze drying and the direct water removal in a desiccator (*i.e.* “Vacuum drying”) have a comparable total porosity to the solvent exchange method. However, the main capillary water peak becomes wider. As for the oven drying methods, there is the appearance of a population of big pores between 200 nm and 1 μm in size.

The total porosity measured by MIP are summarized in Figure 6.18 for the different drying methods with additionally the associated capillary porosity calculated by the total minus the C–S–H peak. As previously stated, the oven drying methods lead to higher total porosity. The freeze drying and the desiccator drying show similar total porosity as the solvent exchange method but solely the latter preserves the microstructure in a way to quantify properly the capillary pore volume.

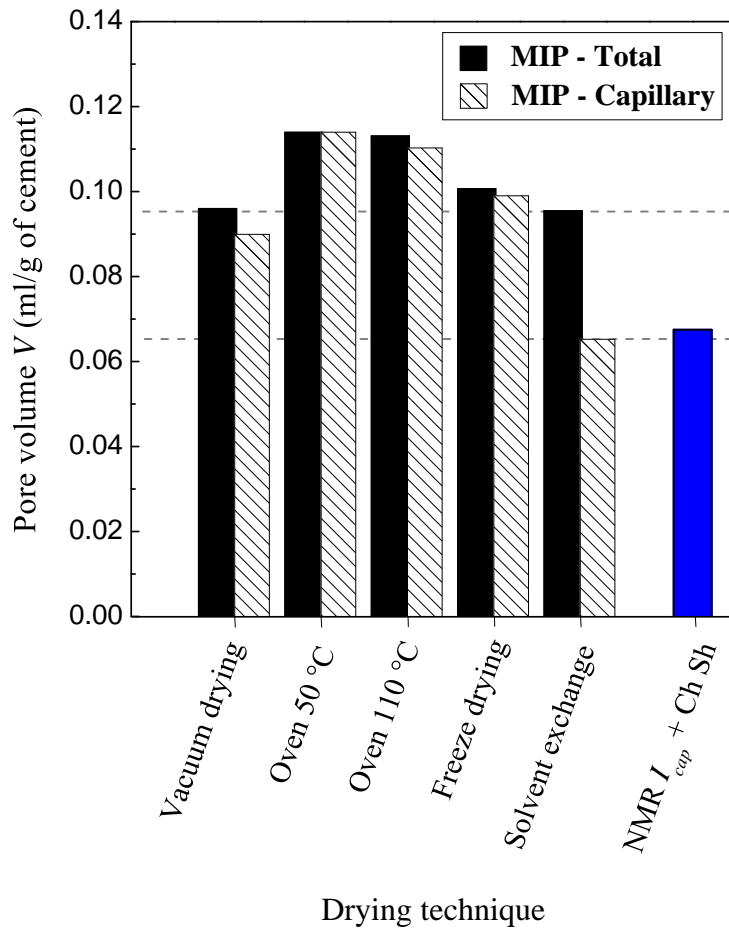


Figure 6.18 – Comparison between the MIP volume across different sample pre-treatments.

6.3.6 Conclusions

The MIP technique is able to adequately quantify the capillary porosity of hydrated samples as long as the sample was dried by the solvent exchange method. Almost no information can be extracted on the porosity of C-S-H hydrates. The different pore sizes obtained by MIP are overestimated by a factor of 3-4. This could be due to wrong assumptions for the contact angle between the mercury and the solid surface. There are evidences that the contact angle might vary depending on the type of pore intruded.

7 Conclusions and perspectives

The aim of this work was to investigate porosity of cementitious binders and the different means to measure it. In that respect, the main contribution was the development of a methodology to measure water in cement paste by ^1H NMR. By a combination of two pulse sequences, water in all the different pores and in crystalline phases can be distinguished. The important point was the support of the signal assignment by a quantitative analysis of water mass.

Once NMR signals were understood, the methodology was routinely applied to follow the evolution of the water in hydrating cement pastes. Plain white cement pastes cured at 20 °C were first studied. During the first days of hydration, water associated with crystalline phases (CH and ettringite) and C–S–H hydrates develop together and the free water volume diminishes. This is the classic picture of cement hydration. However, after a few days, a plateau of the gel porosity was observed for all the mixes studied. This results in a densification of the cementitious matrix over time. The gel water, intrinsic to the C–S–H hydrates, holds approximately half of the total water after a few days of hydration and is one of the important water reservoirs of the solid material. On the other hand, the content of capillary water rapidly becomes small, although large capillary pores may still exist due to the chemical shrinkage of the cement reaction.

A revised Powers and Brownyard type diagram was produced based on NMR signals. Mass and volume compositions were calculated. In comparison with the Powers Brownyard's version, NMR subdivides the hydration products into crystalline phases and "solid C–S–H". There is a very good agreement between Powers and Brownyard's model and the NMR results for their combined quantity. However, early age measurements showed the non-linear behaviour of the gel water that forms during the first day(s) and then plateaus.

The quantification of water mass in the different pores allowed, in combination with XRD, to calculate several parameters of C–S–H for both "solid" (nanocrystalline regions) and "bulk" (including the gel porosity). Some of them are summarized in Table 7.1. While solid C–S–H density was similar for the different mixes studied, a range of chemical compositions was found. The main changes were in the $\text{Ca}/(\text{Si}+\text{Al})$ which varied as a function of w/c and time.

The different results were remarkably consistent with data reported in the literature and when compared to the results obtained by other undifferentiated methods. ^1H NMR provides a unique inexpensive laboratory based method to calculate the density of the delicate nano-scale C–S–H, in contrast to synchrotron based methods [129].

Table 7.1 – C–S–H parameters as a function of w/c at 28 days of hydration.

w/c	Solid C–S–H		Ca/(Si+Al)	Bulk C–S–H	
	Density	H ₂ O/(Si+Al)		Density	H ₂ O/(Si+Al)
0.32	2.75	1.76	1.79	2.07	4.19
0.40	2.74	1.74	1.67	1.96	4.74
0.48	2.77	1.61	1.53	1.86	5.27

The full analysis through ^1H NMR experiments was extended to pastes including SCMs. Silica fume and slag were investigated. Both impact the hydration kinetics and also influence the distribution of water in the paste. Silica fume enhances the formation of C–S–H gel over C–S–H interlayer water while slag does the opposite.

The only major change in the C–S–H structure was observed when the paste was cured at 10 °C instead of 20 °C. A significant drop in C–S–H density was reported. Nevertheless, all pore sizes based on the different relaxation times were similar. The origin of this density change merits further investigation.

The picture emerging from NMR on never dried material is an important step to put in perspective results of other characterisation methods. The comparison with dynamic vapour sorption (DVS), scanning electron microscope (SEM) and mercury intrusion porosimetry (MIP) highlights the difficulties to measure the C–S–H pores experimentally other than with ^1H NMR. Only the desorption isotherm is able to capture properly the C–S–H gel pores. The quantification of capillary porosity suffers from the interpretation of the DVS data for big pores and from the resolution by image analysis of SEM polished sections. However and despite the fact that it measures pore entry size rather than pore size, the study of MIP derivative pore volume showed a good quantification of the capillary porosity if the pastes were gently dried by solvent exchange.

Perspectives

In this work ^1H NMR has been developed as a routine technique to measure water in cement pastes. It has brought a full picture of hydrating cement pastes and it opens further perspectives to understand hydration mechanisms. However, the measurement parameters and the signal analysis vary between different spectrometers and the use of ^1H NMR requires training, and practice (*cf.* Annex A, p. 143). A joint project between the UK National Physical laboratory (NPL) and University of Surrey is currently running to develop a standard for use of

^1H NMR applied to cement. Reference materials are being developed and the measurement and analysis protocols are being documented in detail.

Fundamental research on the relaxation mechanisms of water in cement pastes is currently very active (sister projects in TRANSCEND plus EPSRC sponsored project at University of Surrey). Water exchange between pores and NMR cryoporometry are two of the promising experiments that can lead to further understanding of cementitious materials. In particular, the connectivity of the porosity and the dynamics of water movement between the different pores are studied. Regarding water environments, the used of lower magnetic fields could allow water in Portlandite and aluminate phases to be further subdivided.

From a general standpoint on this work, C–S–H hydrates showed similar features for different mixes. However, the creation of gel pores was governed by the changes in w/c and the addition of SCMs. An interesting and potential study would be to relate the amount of gel pores to the strength properties of the material. Elise Berodier from LMC, EPFL showed, using ^1H NMR, that the gypsum content highly influences the formation of gel pores during the first stages of hydration. High dosages of gypsum drastically reduced the formation of gel pores. This point need to be further investigated. Prior studies focused mainly on capillary pores as a relation with mechanical properties. The study of the C–S–H gel pores might, somehow, be important.

The ^1H NMR study indicates how the hydration at later ages is governed by the space available for hydrates to grow. The capillary water is used first and then, eventually, the gel pores become filled with C–S–H layers (Figure 7.1a→b). In sealed systems, capillary pores are mainly empty due to chemical shrinkage and the capillary water does not represent a large volume after a few days of hydration. The curing under water showed a better space filling than sealed pastes and, *de facto*, a better material. The use of water retaining agent, already utilized in the field for later water supply, could be study by ^1H NMR, understood and potentially better used.

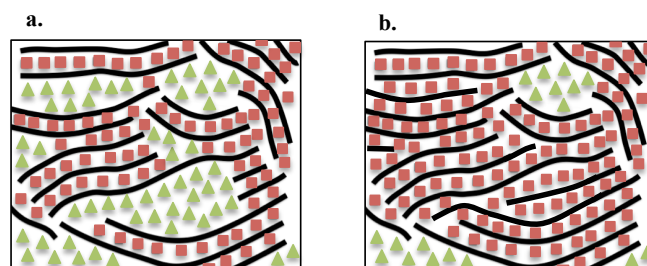


Figure 7.1 – Change in C–S–H water signals by the creation of solid layer(s) into gel pores.

In cement pastes, C–S–H can have two types of morphology, a fibril-like and a foil-like. The fibril-like morphology is dominant and the foil-like features only appear in blended systems

[130]. Rossen [70] recently studied various cementitious systems by TEM. He suggested that the fibril- or foil-like morphology in cement paste tends to persist with time even though its chemical composition may evolve. This suggests that the morphology is an intrinsic property of the C–S–H being formed. For the present work, the slag and the silica fume mixes certainly contain different C–S–H morphologies. Unfortunately, these different types of C–S–H could not be probed separately.

Synthetic preparations for C–S–H have been developed over the last 20 years to better understand the morphology and the growth of this material. C–S–H is produced either mechanochemically [131] or by the hydration of C_3S under controlled lime concentration [132]. Both foil-like and fibril-like C–S–H can be produced [133] but past trials of measuring synthetic C–S–H by 1H NMR encountered difficulties due to the longer relaxation times and the significant amount of free water surrounding the C–S–H. These problems could eventually be solved by adding some iron into the synthesis process and by reducing the high w/s ratio used for the synthesis. Nevertheless, other methods showed that the C–S–H obtained from synthesis often do not compare well with that formed in cement pastes.

The MIP study showed how important is the sample preparation for the quantification of the porosity. However, an important number of studies still use damaging drying methods prior to testing. 1H NMR has the advantage of measuring never-dried cement pastes. NMR studies made by Noemi Fisher, one of the 15 TRANSCEND students, showed a swelling of the C–S–H upon drying and wetting cycles. Kowalczyk *et al.* [134] recently studied the way isopropanol progressively replace water in pores. The picture provided by the 1H NMR technique can be used to look in more details at different drying methods. This could enable damage upon drying to be identified and moreover quantified.

1H NMR was applied successfully in this work to different cementitious systems. The research possibilities now seem very vast as cement hydration is sensitive to all kind of changes. In particular the study of other binders like calcium sulfo-aluminate cements (CSA) or calcium aluminate cements (CACs) for which other kinds of structure develop, would be interesting. It would also be interesting to extend the study of blended systems started in this work to related the changes in porosity to durability related behaviour. In this respect, ternary blends like cement-metakaolin-limestone or paste with reactive glass would be a good topic of study. If the main porosity features do not change, NMR water exchange experiment could elucidate the reasons of improved durability. If many researchers start to use routinely 1H NMR relaxometry, progress will be made in the fundamental understanding of cement hydration and 1H NMR could be the means to characterize novel, potentially improved, cements.

A Appendix - ^1H NMR experimental details

Contents

A.1 Before starting	144
A.1.1 Casting	144
A.1.2 Sample weight	145
A.2 Signal acquisition	145
A.2.1 Calibration of the spectrometer	145
A.2.2 Operating pulse sequences	146
A.3 What can affect the acquisition?	146
A.3.1 Sample position	146
A.3.2 Cooling bath	147
A.3.3 Empty probe signal	147
A.4 What ways of testing do we have?	148
A.4.1 Probing pulses by oscilloscope	148
A.4.2 Using copper sulfate solutions	149
A.5 Signal processing	150
A.5.1 Fitting QE signals back to $\tau=0$	150
A.5.2 Inverse Laplace transform - sensitivity and parameters	151
A.6 Issues with the measurement of	156
A.6.1 Synthetic C-S-H	156
A.6.2 Under water cured samples	156
A.6.3 Pure C_3S and Alite samples	157
A.7 Matlab codes	158
A.7.1 Fitting the QE	158
A.7.2 FID generator	160

The aim of this annex is to complement the thesis with more details about NMR experiments. This section discusses difficulties encountered during experiments and special care taken throughout the measurements and the analyses. This annex is divided in sections with important details to be communicated.

A.1 Before starting

A.1.1 Casting

There are two ways to cast NMR samples.

(1) The first one is to cast the paste in special cylindrical moulds that have a diameter comparable (slightly smaller) to that of the NMR tubes. The sample is then unmoulded and inserted into the NMR tube at the time of the measurement.

(2) The second option is to cast the paste directly into NMR tubes. This latter has different advantages. It allows measurements to be made during the first day of hydration; during which the paste is not solid enough to be unmoulded. It also keeps the sample undisturbed and provides a high sample-to-volume ratio within the probe (useful for low magnitude signals such as cement paste samples measured at low frequency).

Casting a cement paste directly into a deep NMR tube of 8 mm diameter is not an easy task. For that, a home-made syringe was developed. It is made of a normal pumping device on the top of which was adapted a long metallic tube (Figure A.1). The paste was deposited at the bottom of the NMR tube while being very careful not to dirty the tube wall around the sample location.



Figure A.1 – Home made syringe for inserting cement paste at the bottom of NMR tubes.

NMR tubes need to be manipulated with gloves to prevent any physiological grease to disrupt the measurements. The external part of the NMR tubes was cleaned with isopropanol before insertion into the probe.

A.1.2 Sample weight

Each time a paste was cast, the sample and the associated empty tube were weighed. This was done to follow the evolution of the sample mass over time and, eventually, to calculate the mass of hydrogen being probed. NMR tubes need to be weighed each time as there is a slight variation of weight between them.

Sample masses were rarely used in this thesis as most pastes were kept sealed. In addition, the NMR methodology developed allowed the measurement of all the water within the paste. For sealed pastes, the different NMR signal fractions (I_i) were then applied to an ideal paste containing 1 gram of cement and x gram of water for which $x = w/c$. The weighing of the sample was however important when the state of the sample within the tube was not accurately known. This was the case when measuring samples at different relative humidities and for the study of synthetic C–S–H (*cf.* section A.6.1).

The amount of water within the sample was obtained by ignition in an oven reaching 1000 °C for a few hours. In NMR experiments, the sample mass is tiny so a great care must be taken weighing the sample before and after ignition. Because cement samples have high specific surface areas, water can quickly be adsorbed by the sample once removed from the oven. To prevent measuring adsorbed water on the ignited sample, specimens were removed from the oven and weighed at 100 °C.

NMR signal is not proportional to the number of hydrogen atoms

In NMR experiments, the signal intensity for a given number of hydrogen atoms might change according to the susceptibility of the sample. The type of binder and the sample age are some parameters that can affect the spin response intensity. Hence, signal intensity cannot be directly related to hydrogen mass. That is why in some case the sample mass is needed.

A.2 Signal acquisition

A.2.1 Calibration of the spectrometer

^1H NMR relaxometry is a sensitive technique which requires some calibration to be made frequently. The spectrometer used was a Bruker Minispec sold with an software interface called “The Minispec”. In it, there is an automatic procedure to calibrate the parameters of the spectrometer on demand, such as the receiver dead time, the receiver gain, the magnetic field, detection angles, pulse lengths, and the magnetic field homogeneity. Having the parameters right is essential, particularly the pulse lengths, as miss-set values result in incomplete inver-

sion. The calibration was done once a month using a saline solution with approximately 1.25 g/L $\text{CuSO}_4 \cdot 5\text{H}_2\text{O}$.

In addition to monthly calibrations, a “daily check” was carried out every day to make sure that the spectrometer behaves properly. On demand, the software automatically checks the power supply, the receiver, the modulator, etc.

A.2.2 Operating pulse sequences

Quad-echo

For QE experiments, the signal must be acquired for several values of τ for which the responses look like the data presented in Figure 3.2, p. 40. In order to simplify the experiments and the handling of several data files, the QE pulse sequence was coded to run all τ values one after each other and save all decay data in one single file. The total time for running all QE τ experiments was about 15 minutes. The recovery time between the different runs of τ was adjusted from initially 1000 ms to 500 ms for samples at later ages. The same settings were used for the CPMG pulse sequence.

Changing pulse sequence

As explained in the thesis, measuring all the water in hydrating cement pastes requires the use of combined CPMG and QE pulse sequences. This can be done by first running the CPMG pulse sequence on one set of samples and then the QE on another. The other option (chosen in this thesis) is to switch between the two pulse sequences scanning the same sample.

As the solid signal arising from Portlandite and Ettringite evolves far more slowly than the change occurring in the liquid water populations, the CPMG pulse sequence was run more frequently. During the first few days, 2 hours of CPMG were carried out for respectively 45 minutes of QE.

A.3 What can affect the acquisition?

A.3.1 Sample position

It is very important to ensure the proper positioning of the sample in the probe head to stay in the homogeneous field region of the magnet. A wrong positioning weakens the sample signal and might lead to further difficulties in the analysis.

On the NMR spectrometer used in this thesis, there is the possibility to set the position of the sample by the use of a plastic screw at the bottom of the probe. This device is easy to move and might, over sample manipulations, change position. Therefore, the position of the sample in the probe was calibrated each year by the use of straight FID decay. The sample was moved

in the probe to get the highest signal intensity.

A.3.2 Cooling bath

The spectrometer used was equipped with a cooling circuit running around the sample for temperature control (see Figure A.10, p. Figure 157). Water was used as a coolant either at 20 °C or at 10 °C depending on the curing condition. It needs here to be pointed out that the cooling bath must be taken away from the spectrometer as its electric system (and notably the way it switches the condenser on and off) causes magnetic disturbances. This was found to have a great influence on the recorded signal.

A.3.3 Empty probe signal

It was mentioned in the “Chapter 3 - materials and methods” that a blank (*i.e.* an empty probe signal) was subtracted from the signals obtained with cement paste samples. This drastically improved the analysis by yielding better precision and better deconvolutions (*cf.* section A.5.2, p. 153). As the signal from the empty probe is very weak, high statistic is required and both CPMG and QE blank signals were taken as an average of signals acquired for, at least, a week long.

Figure A.2 shows the CPMG empty probe signal, in comparison with the signal when a sample is being additionally measured. The empty probe signal is important in the first few echoes.

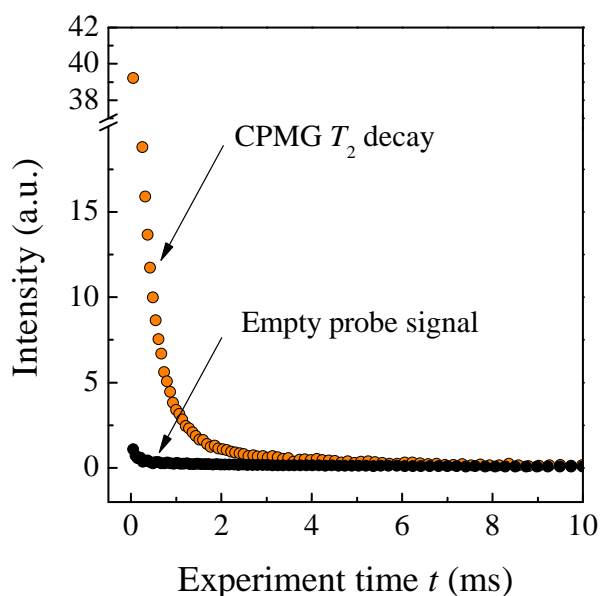


Figure A.2 – Empty tube signal in comparison with the signal when a sample is being measured.

A.4 What ways of testing do we have?

^1H NMR is a sensitive technique where small disturbances difficult to detect might affect the results. In case the user has some doubts about the results, there are possibilities for testing the proper functioning of the spectrometer.

A.4.1 Probing pulses by oscilloscope

It is possible to look at the pulses by the use of an oscilloscope. To that end, a coil needs to be made, inserted into the NMR probe and connected to an oscilloscope.

During the time of this thesis, the length of the P_{90} and P_{180} pulses was verified (Figure A.3a). The beginning of the CPMG sequence as recorded by the oscilloscope is shown in Figure A.3b. Only the first three pulses are shown here. This method was used to check the length of pulse gaps in the middle and at the end of the CPMG pulse sequence.

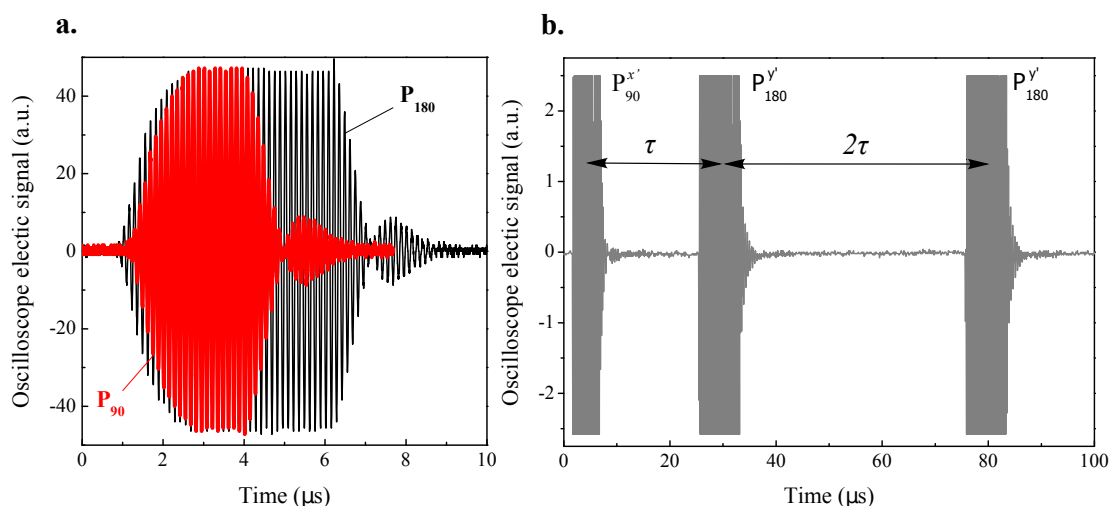


Figure A.3 – (a) P_{180} and P_{90} as seen by an oscilloscope. (b) The first three pulses of the CPMG pulse sequence.

To check the proper functioning of the coil, pulse gaps needs to be known. The CPMG pulse sequence was designed to logarithmically increase τ between an initial value (τ_{\min}) and a final value (τ_{\max}) for a given number of echoes (n_{echoes}). This was done using

$$\tau_i = \exp \left[\frac{n_i \times \ln \left(\frac{\tau_{\max}}{\tau_{\min}} \right)}{n_{\text{echoes}}} + \ln(\tau_{\min}) \right] \quad (\text{A.1})$$

where τ_i is the τ value used for the echo n_i . Common values used as parameters when measuring cement samples were $\tau_{\min} = 25 \mu\text{s}$, $\tau_{\max} = 6 \text{ ms}$ and $n_{\text{echoes}} = 256$. The resulting τ values are summarized in Table A.1. 256 echoes make 256 τ values as τ is doubled between the different P_{180} peak of the CPMG pulse sequence. Only the beginning and the ending τ values are shown in the table.

Table A.1 – τ values as calculated with Equation A.1 and the aforementioned parameters.

n_i	τ_i (μs)
1	25.00
2	25.54
3	26.10
4	26.67
5	27.24
}	}
252	5505.73
253	5625.34
254	5747.55
255	5872.42
256	6000.00

A.4.2 Using copper sulfate solutions

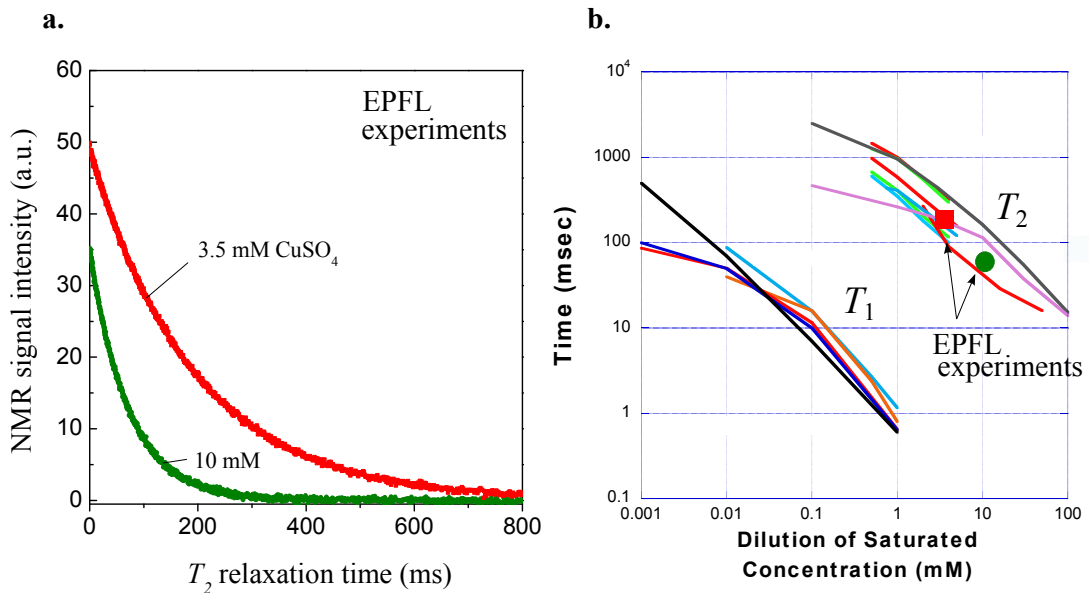


Figure A.4 – (a) CPMG decay for solutions at 3.5 mM and 10 mM CuSO_4 . (b) Literature data for the influence of the CuSO_4 concentration on the T_1 and T_2 relaxation times. Results of the experiments presented in (a) are reported.

One possible way to check if the correct T_2 are being measured is to use copper sulfate solutions. In the context of this thesis, 3.5 mM and 10 mM of copper sulfate in distilled water were measured. The raw data are presented in Figure A.4a. The fit of one exponential decay for each of the curve led to $T_2 = 193$ ms and $T_2 = 71$ ms for 3.5 mM and 10 mM of CuSO_4 respectively. The data are compared to the literature on Figure A.4b. More information can be found in [135] and associated references.

A.5 Signal processing

A.5.1 Fitting QE signals back to $\tau=0$

The aim of the QE pulse sequence is to quantify the fraction of solid-like hydrogen protons within cement pastes. All the details about the protocol of analysis is reported in section 3.3.1, p. 38. As explained in section A.2.2, all τ signals were saved together in one data file. These raw QE data were fitted according to Equation 3.2 for different values of τ . For the analysis, a Matlab code was written to fit all τ values in one go and to store the final results in a *.txt* file. The code is given in section A.7.

In this work, τ was varied between 15, 19, 24, 30, 37 and 45 μs . The choice of these values was done to capture the solid signal decay. Most of the time, all data were used. However, questions were raised about using the $\tau = 15$ μs results. The issue is that, for such small τ value, the top of the Gaussian might be (sometimes) located within the dead zone of the spectrometer. In this case, the Gaussian fit becomes hazardous and the 15 μs data point not reliable. In this case, the $\tau = 15$ μs solid signal intensity often diverges from the Gaussian shape as shown in Figure A.5 and the resulting A_{solid} intensity is changed.

Seeing or not the top of the Gaussian peak for $\tau = 15$ μs QE signal depends on the sensitivity of the machine at the time of the measurement. The intrinsic dead time of the spectrometer itself might vary between 15.0 μs and 16.5 μs at different periods of the year.

Using a Gaussian law for extrapolating the solid signal to $\tau = 0$ might be the subject of debate [136]. However, this gave the best results when comparing the solid signal with crystalline water calculated by XRD/TGA, for different ages and across a wide range of samples. Moreover, the Gaussian shape was better seen using the spectrometer at University of Surrey, for which the dead time was much shorter. τ values such as 9 μs were used. The Gaussian shape was found to be the optimum for bound hydrogen in cement pastes. However, it needs to be specified that this is not necessarily the case for hydrogen bound in other organic or inorganic materials.

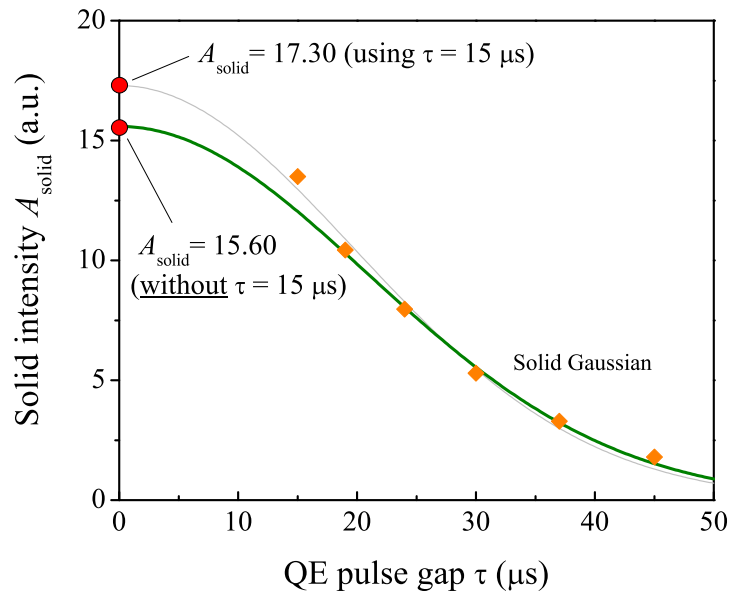


Figure A.5 – Effect of including or not the $\tau = 15 \mu\text{s}$ data point for extrapolating the solid signal to $\tau = 0$.

A.5.2 Inverse Laplace transform - sensitivity and parameters

α parameter

As explained in the thesis, the ILT program used to deconvolute CPMG decays into different populations contains a regularization parameter, called α . This parameter sets the sensitivity of the inversion and helps to adapt the algorithm to the noise in the data. If α is too high, the different peaks might not be fully resolved. If α is too small, the ILT becomes too sensitive to the noise. The program possesses an automatic procedure to find the best α parameter for the input data (details are given in [59]). However, a fixed α was used in this work because the automatic procedure for α did not give robust results with large variations from one sample to another.

Figure A.6 shows the influence of α on the ILT deconvolution of a CPMG decay for a sealed white cement paste mixed at $w/c = 0.40$ after 28 days of hydration. The α parameter was varied by factors of ten. It can be seen that the α parameter influences the width of the different peaks and, to some extent, on the way they become separately resolved.

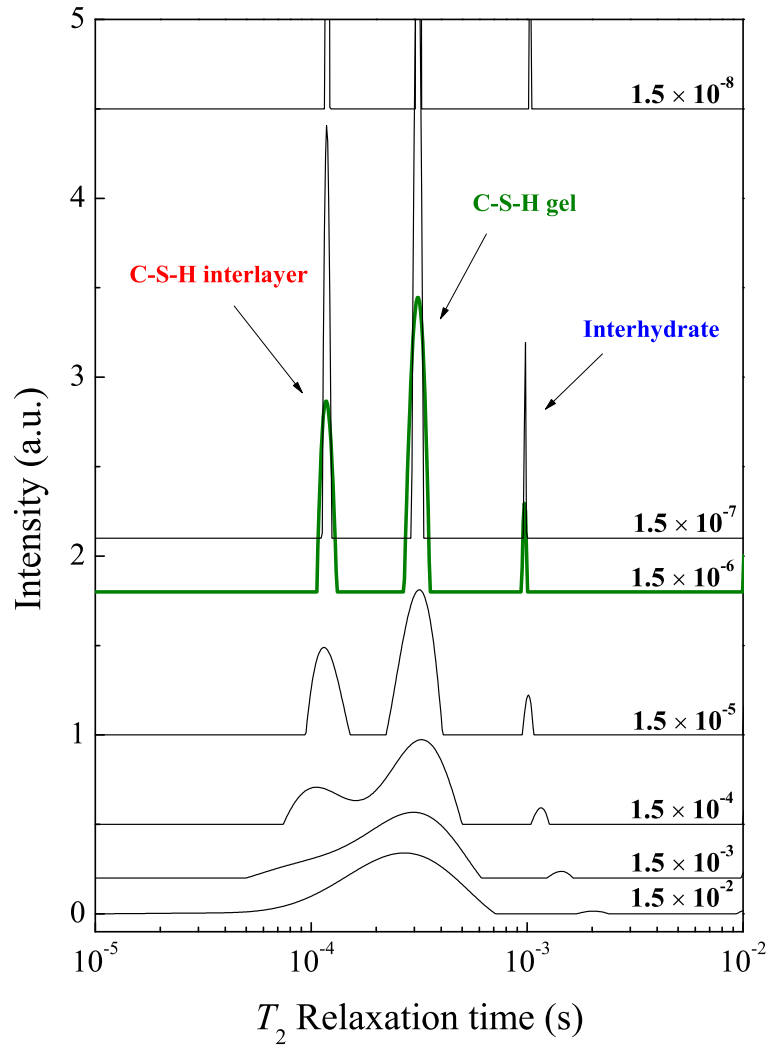


Figure A.6 – Effect of the parameter α on the ILT peak deconvolution. The chosen α for the cement samples measured in this thesis was $\alpha = 1.5 \times 10^{-6}$ (green curve).

For cement samples measured in this thesis $\alpha = 1.5 \times 10^{-6}$ was chosen (in green). It can be seen that from $\alpha = 1.5 \times 10^{-4}$, the C–S–H interlayer peak and C–S–H gel peak start to merge together. As α is further increased, the merging increases and the two C–S–H populations appear progressively as one single peak. On the other hand, when α is set too small, the peaks become very tiny leading sometimes to additional peaks. 50'000 iterations was chosen as parameter for the ILT and the smaller the α is, the longer the deconvolution takes.

Even though the width of the peaks are changing when changing α , their area does not vary significantly. Table A.2 shows the different peak areas for the data presented in Figure A.6. For $\alpha = 1.5 \times 10^{-6}$ and $\alpha = 1.5 \times 10^{-7}$, there is no much change in the different peak areas. The intensities of the different peaks become however slightly different when $\alpha = 1.5 \times 10^{-5}$ was used, for which it can be seen in Figure A.6 that the two C–S–H populations slightly interfere

with each other. By $\alpha = 1.5 \times 10^{-8}$, the peaks become very narrow and the analysis is limited by the digital resolution (*i.e.* not enough points to resolve the peak properly). For this specific sample, $\alpha = 1.5 \times 10^{-6}$ or $\alpha = 1.5 \times 10^{-7}$ seem good values to be used.

Table A.2 – Peak area for the different populations presented in Figure A.6.

α	Interlayer peak area	Gel peak area	Interhydrate peak area
1.5×10^{-8}	13.74	25.74	1.80
1.5×10^{-7}	13.24	25.85	1.95
1.5×10^{-6}	13.12	25.99	1.94
1.5×10^{-5}	12.75	26.57	1.74

Artefact peak

The data presented in Figure A.7 shows the kind of result that often comes out of ILT analysis for cement pastes. The peaks seen at very low relaxation times are artefact peaks as no information can be extracted from the CPMG pulse sequence before $50 \mu\text{s}$, time when the first echo is recorded.

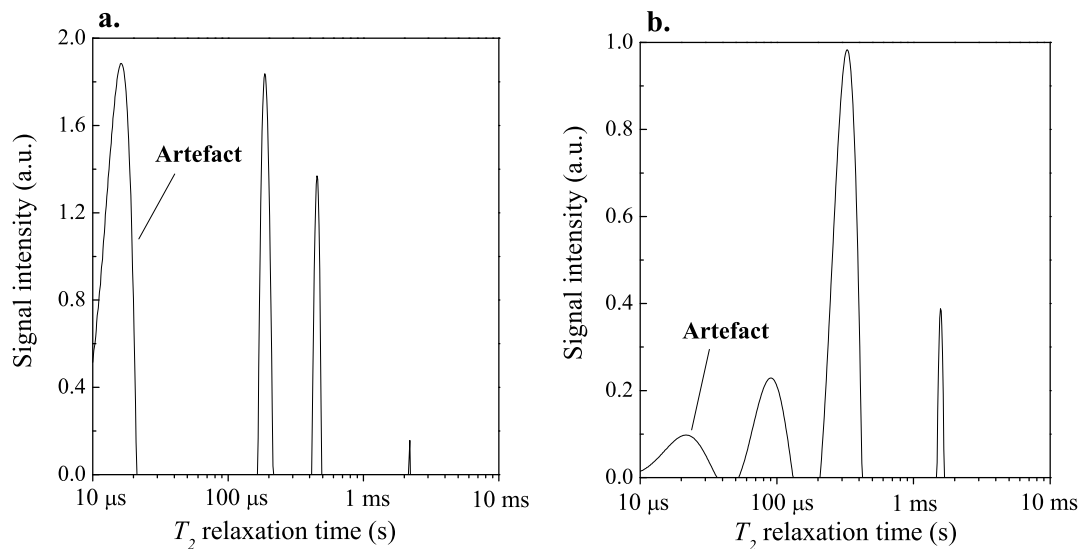


Figure A.7 – Example of “wrong” deconvolution. (a) and (b) are typical data having an artefact peak.

Some tests were conducted trying to understand this artefact peak phenomenon. It was concluded that this depends on the noise in the first data point. The first echo point should however not be removed because a lot of information, particularly about the interlayer population, lies within it. To illustrate this, Figure A.8 shows a CPMG decay for mature paste deconvoluted into the different exponential components obtained by the ILT. It can be seen

that the first data point is important for fitting the fast decaying interlayer signal. Unusable dataset as shown in Figure A.7 was something common and it could not be avoided.

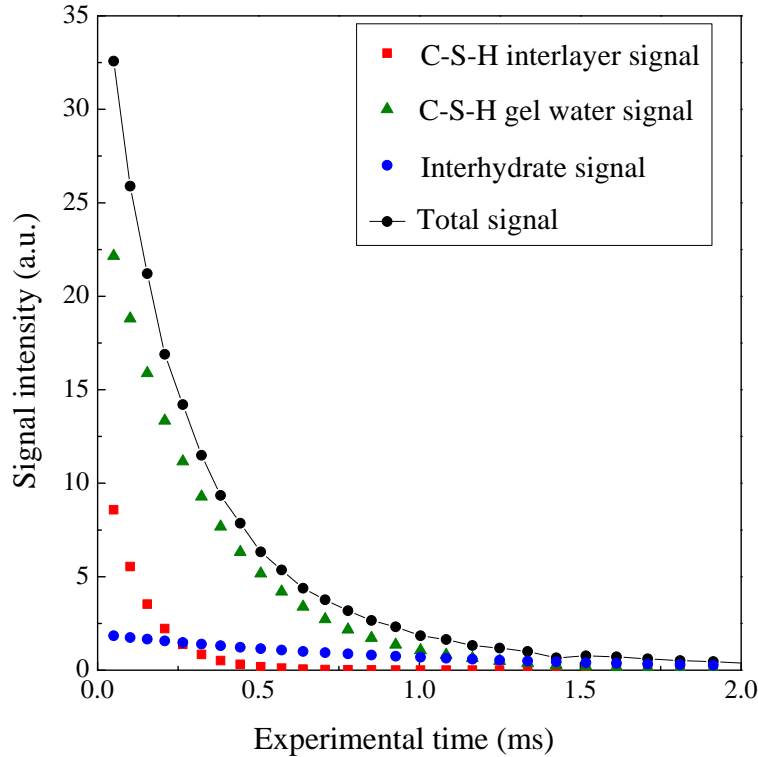


Figure A.8 – Deconvolution of the CPMG decay between the different water populations for the white cement paste after 28 days of hydration.

The conclusion here is that several spectra are needed at a given time to ensure having enough usable data when no artefact peak is present. For a sample at 28 days, 10 CPMG decays were acquired for which $\frac{1}{3}$ of them were not usable due to peak at low relaxation times.

Test on artificial data

During the course of the thesis, the ILT algorithm was tested with artificially generated data. For that, CPMG decays were generated artificially using the program reported in section A.7, p. 160. Figure A.9a shows two examples of generated data. The first one is made of three peaks well separated from each other and with increasing intensity (from left to right: 2.000, 3.000 and 5.000 respectively). The second data set is made of two first peaks very close to each other with intensity 3.000 and 1.000 and a peak at long relaxation times with intensity 3.000. The associated decays are shown in Figure A.9b. There are made of 256 echo points as for real data obtained on cement pastes.

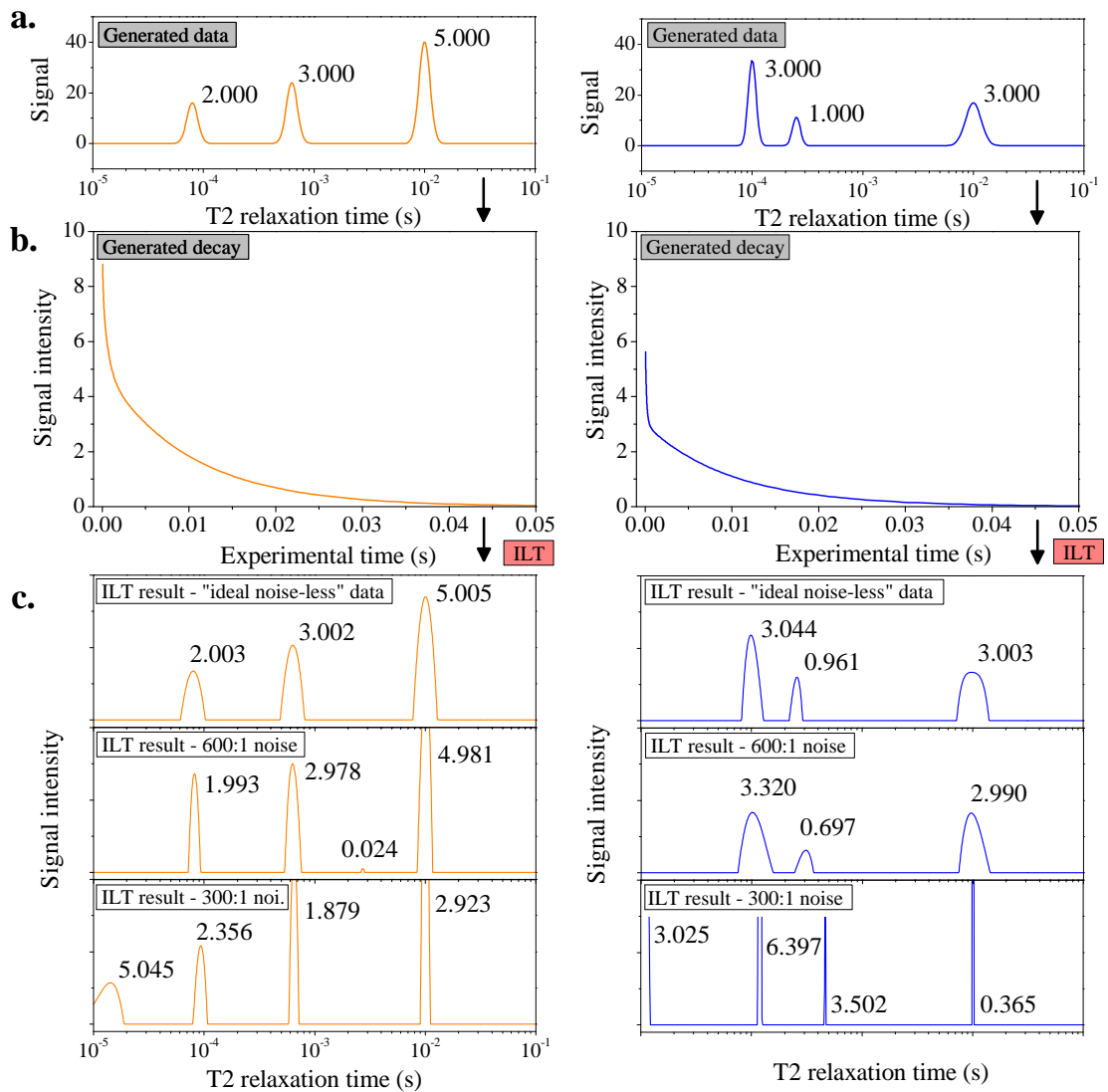


Figure A.9 – (a) Generated data and (b) its Fourier transform. (c) ILT deconvolution of the data presented in (b) for different signal-to-noise ratios.

The inversion of the generated decays using the ILT algorithm is shown in Figure A.9c. An $\alpha = 1.5 \times 10^{-6}$ was used. The first spectra are for the ideal noise-less data. For the second and third one, a noise was artificially generated with a Gaussian distribution to obtain 600:1 and 300:1 signal-to-noise ratio, respectively.

At first, it can be seen that even without noise, the two peaks on the right hand side which are close to each other are not perfectly resolved. Probably increasing the α parameter will make the deconvolution closer to the generated data. For noisy data, it can be seen that even with a signal-to-noise ratio of 600:1, the initial generated peaks are still well recovered through the ILT algorithm. In comparison, a common signal-to-noise ratio for the experiments carried out

in this thesis was of at least 1000:1.

For very noisy data (bottom graphs in Figure A.9, signal-to-noise ratio 300:1), there is the appearance of a peak at very low relaxation times. This was already discussed in section A.5.2 and this kind of results depends on how the noise weights in the first few echoes.

A.6 Issues with the measurement of

A.6.1 Synthetic C–S–H

Other experiments (not presented in this thesis) were carried out on synthetic C–S–H. A first batch of samples was provided by Elena Tajuelo Rodriguez, the TRANSCEND student leading the project number 8 on C–S–H morphology (*cf.* Figure 1.1, p. 2) in University of Leeds, UK. The second batch was provided by Emilie L'Hopital, a student working at EMPA, Switzerland. Different C–S–H samples with different Ca/Si and Al/Si ratios were measured.

The synthesis of C–S–H was done in both cases at high water-to-solid ratio and the resulting C–S–H often looked like a white gel. In fully saturated conditions, this makes them very difficult to measure experimentally. The issue is that a lot of “free water” is surrounding the C–S–H structures of interest for which the signal becomes very tiny in comparison (< 2% of the total signal). To adequately characterize synthetic C–S–H by ^1H NMR, the solution would be to increase the volume of C–S–H per sample volume and hence remove a maximum of the surrounding free water. An unsuccessful trial was done by pressing the water out to make pellets of “condensed” C–S–H.

In a second attempt the water surrounding the synthetic C–S–H was removed using controlled environments. However, the choice of an appropriate relative humidity is not easy. The RH should be low enough to remove most of the free water but high enough not to empty the C–S–H gel pores. Samples were equilibrated at 81% RH and 93% RH but none of these conditions did help reducing drastically the free water content of the samples. The best results from synthetic C–S–H came from samples equilibrated at 11% RH. In this state, the gel porosity of the C–S–H is certainly empty but based on the results presented in Figure 4.24b (p. 81), the C–S–H interlayer can be considered as still almost full. The interlayer content of the C–S–H was quantified for different samples and the results will eventually be published.

The lesson of these experiments on pure C–S–H is that it is not easy to measure water content of synthetic C–S–H (especially for the gel pores) due to the excess of the surrounding free water.

A.6.2 Under water cured samples

For samples cured under water, there are two ways of proceeding. Either the samples can be cast in a separate mould, unmoulded after one day and then immersed in saturated lime

water up to the measurement time. The second option is to cast the sample directly into NMR tubes and introducing a little drop of water on the top. Both were tried and gave similar NMR results after 28 days of hydration.

There had been some issues measuring underwater cured samples on the spectrometer at EPFL. Some condensation occurred at the surface of the tube wall just on the top of the section which was temperature controlled (Figure A.10). This led to the progressive drying of the sample. This problem was solved by changing a little bit the temperature of the “cooling water”. This issue of condensation in the tube for water saturated samples did not occur on the spectrometer in University of Guilford as the temperature control of the sample was done by ventilated air.

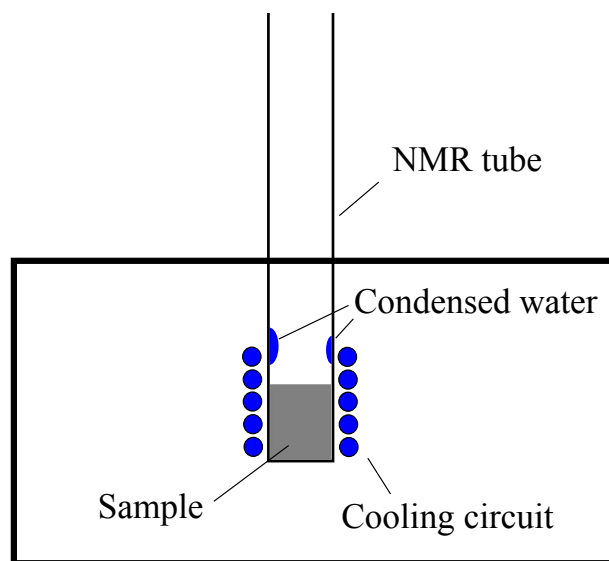


Figure A.10 – Illustration of the condensation issue for saturated sample.

It needs to be specified that for underwater cured samples, the water surrounding the specimen needs to be removed before ^1H NMR experiments. This was done by using tissue and quickly making the surface of the sample dry. Therefore, following the course of hydration of underwater cured samples requires many samples to be cast because the removal of the curing water during the time of measurement might influence the sample condition.

A.6.3 Pure C_3S and Alite samples

Pure C_3S and Alite samples have much longer relaxation times compared to white cement pastes due to the very low iron content of these materials. As a consequence, experiments take a much longer time and it becomes very difficult to measure the evolution of C_3S or Alite samples during the first weeks of hydration. Long measurement times become less problematic for mature samples at for instance 28 days of hydration. A common CPMG

acquisition time for a C₃S paste sample is about 50 minutes.

A.7 Matlab codes

A.7.1 Fitting the QE

This Matlab code is composed of two files. One called *main* and the second one called *fitting*.

main

Here is just shown the lines for the $\tau = 15 \mu\text{s}$ data. This just needs to be copied and adjusted for the other values of τ .

```
load 'QE_Cavity.txt';

[LoadName1,LoadPath1]=uigetfile('*.dps','Select raw data file');
cd(LoadPath1);
Test1 = load(LoadName1);

% ----- Tau = 15 μs -----

start = [14.40,45,-0.01,0.15] ;

global x y Center;

index1 = QE_Cavity(11:258,1) ;
index = Test1(11:258,1) ;
x = Test1(index,2) ;
y = Test1(index,3)- QE_Cavity(index1,3) ;
Center = 0.032 ;

final15 = fminsearch(@fitting, start) ;

Gaussian = final15(1) ;
Exponential = final15(2) ;
Width = final15(3) ;
T2star = final15(4) ;

fitted = Gaussian*exp(-((x-Center) .^2)/(Width .^2))+Exponential*exp(-x/T2star) ;

subplot(3,2,1)
plot(x,y,'ko',x,fitted) ;
```



```

xlabel('
fontname{Times}
fontsize{13} T_2 Relaxation Time (ms)');
ylabel('
fontname{Times}
fontsize{13} Intensity');
legend('
fontname{Times}
fontsize{11} Raw data',...
,
fontname{Times}
fontsize{11} Fitting')
title('
fontsize{15}
bf 15  $\mu$ s')
text(0.25, 30, ['Agaussian = ', num2str(final15(1),'% 10.2f')]);
text(0.25, 25, ['Aexponential = ', num2str(final15(2),'% 10.2f')]);
set(gca,'xlim',[0 0.35],'ylim',[0 60])

% ----- Saving -----

temp = [final15; final19; final24; final30; final37; final45] ;

save (LoadName1(1:end-4), 'temp', '-ascii');

```

fitting

```

function f = fitting(param)

global x y Center ;

Gaussian = param(1) ;
Exponential = param(2) ;
Width = param(3) ;
T2star = param(4) ;

f = 0 ;
for i = 1:size(x)
g = Gaussian*exp(-((x(i)-Center) $\hat{2}$ )/(Width $\hat{2}$ ))+Exponential*exp(-x(i)/T2star) ;
f = f + (g - y(i)) $\hat{2}$  ;
end
end

```

A.7.2 FID generator

% ILT test data generator

*clear all
clc*

*n=128; % number of points in the FID
t1=50.0e-6; % initial echo time, tau_1 in second
tn=0.1; % final echo time in second*

*m=128; % number of points in the test distribution
T21=50.0e-6; % initial T20 for ditribution
T2n=0.1; % multiplier for T2 distribtion*

*rms_noise=0; % FID rms_noise
base_offset=0; % FID baseline offset*

%%%%%%%% distribution paramters: Area; log(T2); width(log(T2) %%%%%%%%%

*a=[1, -3.9, 0.05; ...
2, -3, 0.15; ...
1, -2, 0.18];
kmax=size(a,1);*

%%%%%%%% generate the noise %%%%%%%%%

*noise=base_offset+rms_noise*rand(n,1);*

*fid=zeros(n,2);
T2=zeros(m,3);*

*i=1:n;
j=1:m;*

fid(i,1)=10.^(log10(t1)+(log10(tn)-log10(t1))(i-1)/n); % log of the FID times
T2(j,2)=(log10(T21)+(log10(T2n)-log10(T21))*(j-1)/m); % log of the T2 times
T2(j,1)=10.^(T2(j,2));*

*for k=1:kmax;
T2(j,3)=T2(j,3)+(a(k,1)./a(k,3)/sqrt(pi)).*exp(-(((T2(j,2)-a(k,2))./a(k,3)).^2));*

```

end

Area=0;
for j=2:m
Area=Area+0.5*(T2(j,2)-T2(j-1,2))*(T2(j,3)+T2(j-1,3));
end

%%%%%%%%% generate the FID %%%%%%%%%%

for i=1:n
fid(i,2)=sum(T2(2:m,3).*(T2(2:m,2)-T2(1:m-1,2)).*exp(-fid(i,1)./(T2(2:m,1))));
end
fid(:,2)=fid(:,2)+noise(:,1);

%%%%%%%%% Plotting %%%%%%%%%%

figure (2);
semilogx(T2(1:m,1),T2(1:m,3));
title('T2 distribution vs T2 (log plot)');

q = 10â(1,2);
w = 10â(2,2);
e = 10â(3,2);
text(q, 2, [' ', num2str(a(1,1), '% 10.1f')]);
text(w, 2, [' ', num2str(a(2,1), '% 10.1f')]);
text(e, 2, [' ', num2str(a(3,1), '% 10.1f')]);

figure (3)
plot(fid(1:n,1),fid(1:n,2));
title('FID intensity vs time');

%%%%%%%%% Saving data %%%%%%%%%%

save FID.txt fid /ascii
save T2.txt T2 /ascii

```


B Appendix - Oxides composition of white cements, silica fume and slag

Table B.1 – Oxides composition of the three batches of white cement, silica fume and slag obtained by XRF analysis. Numbers are expressed in percentages.

Oxides	White cement			Silica fume	Slag
	Batch 1	Batch 2	Batch 3		
CaO	71.58	69.30	69.48	0.15	41.38
SiO ₂	21.79	24.73	24.89	98.70	35.72
Al ₂ O ₃	1.47	2.15	2.20	0.31	11.94
SO ₃	2.05	2.11	1.98	—	1.38
MgO	0.87	0.60	0.57	0.04	7.45
Fe ₂ O ₃	0.36	0.34	0.33	0.02	0.84
P ₂ O ₅	0.40	0.31	0.20	0.02	0.00
Na ₂ O	—	0.15	0.06	0.09	0.26
TiO ₂	0.08	0.08	0.07	0.39	0.51
K ₂ O	0.09	0.07	0.07	0.30	0.27
MnO	0.02	0.02	0.02	0.01	0.23
SrO	0.14	0.13	0.12	—	—
LOI*	0.75	0.70	0.66	0.67	0.66

*LOI = loss on ignition

C Appendix - Particle size distribution (cement, slag and quartz)

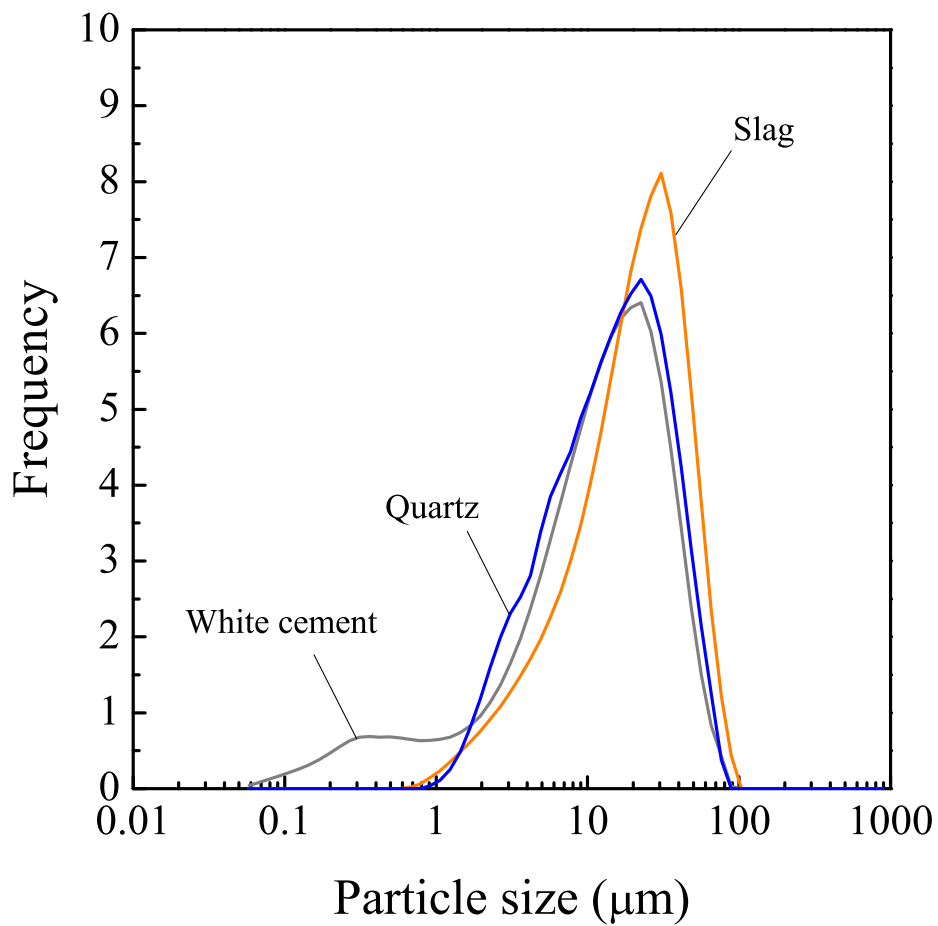


Figure C.1 – Typical particle size distribution for white cement, slag and quartz.

Bibliography

- [1] S. Mindess, J. Young, *Concrete*, Prentice-Hall, Englewood Cliffs, N.J., 1981.
- [2] K. L. Scrivener, Backscattered electron imaging of cementitious microstructures: understanding and quantification, *Cement and Concrete Composites* 26 (8) (2004) 935–945.
- [3] D. P. Bentz, A review of early-age properties of cement-based materials, *Cement and Concrete Research* 38 (2) (2008) 196–204.
- [4] T. C. Powers, T. L. Brownyard, *Studies of the physical properties of hardened portland cement paste*, bulletin 22 Edition, Research Laboratories of the Portland Cement Association, Chicago, 1948.
- [5] T. C. Powers, Structure and Physical Properties of Hardened Portland Cement Paste, *Journal of the American Ceramic Society* 41 (1) (1958) 1–6.
- [6] E. Bonaccorsi, S. Merlino, A. R. Kampf, The crystal structure of tobermorite 14 Å (plombierite), a c-s-h phase, *Journal of the American Ceramic Society* 88 (3) (2005) 505–512.
- [7] H. M. Jennings, Refinements to colloid model of c-s-h in cement: Cm-ii, *Cement and Concrete Research* 38 (3) (2008) 275–289.
- [8] W.-S. Chiang, E. Fratini, P. Baglioni, D. Liu, S.-H. Chen, Microstructure determination of calcium-silicate-hydrate globules by small-angle neutron scattering, *The Journal of Physical Chemistry C* 116 (8) (2012) 5055–5061.
- [9] I. G. Richardson, The calcium silicate hydrates, *Cement and Concrete Research* 38 (2) (2008) 137–158.
- [10] J. J. Thomas, J. J. Biernacki, J. W. Bullard, S. Bishnoi, J. S. Dolado, G. W. Scherer, A. Luttge, Modeling and simulation of cement hydration kinetics and microstructure development, *Cement and Concrete Research* 41 (12) (2011) 1257–1278.
- [11] A. R. Barron, *Portland Cement in the Energy Industry*, 2007.
- [12] P. J. Feldman, R F; Sereda, A new model for hydrated portland cement and its practical implications, *Engineering Journal (Canada)* 53 (8/9) (1970) 53–59.

- [13] F. H. Wittmann, Grundlage eines Modells zur beschreibung charakteristischer Eigenschaften des betons, Wilhelm Ernst and Sohn, 1978.
- [14] K. L. Scrivener, The microstructure of concrete (1989).
- [15] J. Thomas, H. Jennings, A. Allen, The surface area of cement paste as measured by neutron scattering: evidence for two C-S-H morphologies (1998).
- [16] H. M. Jennings, A model for the microstructure of calcium silicate hydrate in cement paste, *Cement and Concrete Research* 30 (1) (2000) 101–116.
- [17] P. D. Tennis, H. M. Jennings, A model for two types of calcium silicate hydrate in the microstructure of portland cement pastes, *Cement and Concrete Research* 30 (6) (2000) 855–863.
- [18] I. G. Richardson, The nature of c-s-h in hardened cements, *Cement and Concrete Research* 29 (8) (1999) 1131–1147.
- [19] K. K. Aligizaki, Determination of pore structure parameters in hardened cementitious materials, Ph.D. thesis, The Pennsylvania State University (1995).
- [20] K. V. Breugel, Simulation of hydration and formation of structure in hardening cement-based materials, Ph.D. thesis, Delft University of Technology (1991).
- [21] Y. Xi, Z. P. Bazant, L. Molina, H. M. Jennings, Moisture diffusion in cementitious materials moisture capacity and diffusivity, *Advanced Cement Based Materials* 1 (6) (1994) 258–266.
- [22] S. Brunauer, P. H. Emmett, E. Teller, Adsorption of gases in multimolecular layers, *Journal of the American Chemical Society* 60 (2) (1938) 309–319.
- [23] E. P. Barrett, L. G. Joyner, P. P. Halenda, The determination of pore volume and area distributions in porous substances. i. computations from nitrogen isotherms, *Journal of the American Chemical Society* 73 (1) (1951) 373–380.
- [24] L. Nielsen, Moisture sorption in porous materials: A best fit from experimental data, Tech. rep., Technical University of Denmark (2007).
- [25] O. Kadlec, M. M. Dubinin, Comments on the limits of applicability of the mechanism of capillary condensation, *Journal of Colloid and Interface Science* 31 (4) (1969) 479–489.
- [26] R. F. Feldman, H. Cheng-Yi, Properties of portland cement-silica fume pastes i. porosity and surface properties, *Cement and Concrete Research* 15 (5) (1985) 765–774.
- [27] G. G. Litvan, Variability of the nitrogen surface area of hydrated cement paste, *Cement and Concrete Research* 6 (1) (1976) 139–143.
- [28] R. M. Selim, S.A., Adsorption of organic vapors in relation to the pore structure of hardened cement pastes (1966).

- [29] J. Van Brakel, S. Modry, M. Svata, Mercury porosimetry: state of the art, *Powder Technology* 29 (1) (1981) 1–12.
- [30] S. Diamond, Mercury porosimetry: An inappropriate method for the measurement of pore size distributions in cement-based materials, *Cement and Concrete Research* 30 (10) (2000) 1517–1525.
- [31] D. N. Winslow, S. Diamond, A mercury porosimetry study of the evolution of porosity in Portland cement, Purdue University. Indiana State Highway Commission United States Bureau of Public Roads Joint Highway Research Project, Lafayette, 1968.
- [32] J. Zhou, G. Ye, K. van Breugel, Characterization of pore structure in cement-based materials using pressurization/depressurization cycling mercury intrusion porosimetry (pdc-mip), *Cement and Concrete Research* 40 (7) (2010) 1120–1128.
- [33] H. S. Wong, M. K. Head, N. R. Buenfeld, Pore segmentation of cement-based materials from backscattered electron images, *Cement and Concrete Research* 36 (6) (2006) 1083–1090.
- [34] C. Galle, Effect of drying on cement-based materials pore structure as identified by mercury intrusion porosimetry: A comparative study between oven-, vacuum-, and freeze-drying, *Cement and Concrete Research* 31 (10) (2001) 1467–1477.
- [35] M. Moukwa, P. Aictin, The effect of drying on cement paste pore structure as determined by mercury porosimetry, *Cement and Concrete Research* 18 (1988) 745–752.
- [36] P. C. Fonseca, H. M. Jennings, The effect of drying on early-age morphology of c-s-h as observed in environmental sem, *Cement and Concrete Research* 40 (12) (2010) 1673–1680.
- [37] C. Hunt, L. Tomes, R. Blaine, Some effects of aging on the surface area of portland cement paste, *J. Res. Natl. Bur. Stand. A* 64 (1960) 163–169.
- [38] J. P. Korb, M. Whaley-Hodges, R. G. Bryant, Translational diffusion of liquids at surfaces of microporous materials: Theoretical analysis of field-cycling magnetic relaxation measurements, *Physical Review E* 56 (2) (1997) 1934–1945.
- [39] L. Monteilhet, J. P. Korb, J. Mitchell, P. J. McDonald, Observation of exchange of micropore water in cement pastes by two-dimensional $t(2)$ - $t(2)$ nuclear magnetic resonance relaxometry, *Physical Review E* 74 (6) (2006) 061404.
- [40] P. J. McDonald, J. P. Korb, J. Mitchell, L. Monteilhet, Surface relaxation and chemical exchange in hydrating cement pastes: A two-dimensional nmr relaxation study, *Physical Review E* 72 (1) (2005) 011409.
- [41] A. Valori, P. J. McDonald, K. L. Scrivener, The morphology of c-s-h: Lessons from ^1H nuclear magnetic resonance relaxometry, *Cement and Concrete Research* 49 (0) (2013) 65–81.

- [42] H. Y. Carr, E. M. Purcell, Effects of diffusion on free precession in nuclear magnetic resonance experiments, *Physical Review* 94 (3) (1954) 630–638.
- [43] S. Meiboom, D. Gill, Modified spin-echo method for measuring nuclear relaxation times, *Review of Scientific Instruments* 29 (8) (1958) 688–691.
- [44] P. J. McDonald, V. Rodin, A. Valori, Characterisation of intra- and inter-c-s-h gel pore water in white cement based on an analysis of nmr signal amplitudes as a function of water content, *Cement and Concrete Research* 40 (12) (2010) 1656–1663.
- [45] J. G. Powles, J. H. Strange, Zero time resolution nuclear magnetic resonance transient in solids, *Proceedings of the Physical Society* 82 (1) (1963) 6.
- [46] K. R. Brownstein, C. E. Tarr, Importance of classical diffusion in nmr studies of water in biological cells, *Physical Review A* 19 (6) (1979) 2446–2453.
- [47] M. H. Cohen, K. S. Mendelson, Nuclear magnetic relaxation and the internal geometry of sedimentary rocks, *Journal of Applied Physics* 53 (2) (1982) 1127–1135.
- [48] S. D. Senturia, J. D. Robinson, Nuclear spin-lattice relaxation of liquids confined in porous solids.
- [49] F. D’Orazio, S. Bhattacharja, W. P. Halperin, K. Eguchi, T. Mizusaki, Molecular diffusion and nuclear-magnetic-resonance relaxation of water in unsaturated porous silica glass, *Physical Review B* 42 (16) (1990) 9810–9818.
- [50] W. P. Halperin, J.-Y. Jehng, Y.-Q. Song, Application of spin-spin relaxation to measurement of surface area and pore size distributions in a hydrating cement paste, *Magnetic Resonance Imaging* 12 (2) (1994) 169–173.
- [51] R. Blinc, M. Burgar, G. Lahajnar, M. Rožmarin, V. Rutar, I. Kocuvan, J. Uršič, Nmr relaxation study of adsorbed water in cement and c3s pastes, *Journal of the American Ceramic Society* 61 (1-2) (1978) 35–37.
- [52] L. J. Schreiner, J. C. Mactavish, L. Miljković, M. M. Pintar, R. Blinc, G. Lahajnar, D. Lasic, L. W. Reeves, Nmr line shape-spin-lattice relaxation correlation study of portland cement hydration, *Journal of the American Ceramic Society* 68 (1) (1985) 10–16.
- [53] D. D. Lasic, J. M. Corbett, J. Jian, J. C. MacTavish, M. M. Pintar, R. Blinc, G. Lahajnar, Nmr spin grouping in hydrating cement at 200 mhz, *Cement and Concrete Research* 18 (4) (1988) 649–653.
- [54] L. Miljkovic, D. Lasic, J. C. MacTavish, M. M. Pintar, R. Blinc, G. Lahajnar, Nmr studies of hydrating cement: A spin-spin relaxation study of the early hydration stage, *Cement and Concrete Research* 18 (6) (1988) 951–956.

- [55] J. Greener, H. Peemoeller, C. Choi, R. Holly, E. J. Reardon, C. M. Hansson, M. M. Pinar, Monitoring of hydration of white cement paste with proton nmr spin–spin relaxation, *Journal of the American Ceramic Society* 83 (3) (2000) 623–627.
- [56] F. Barberon, J. P. Korb, D. Petit, V. Morin, E. Bermejo, Probing the surface area of a cement-based material by nuclear magnetic relaxation dispersion, *Physical Review Letters* 90 (11) (2003) 116103.
- [57] A. Plassais, M. P. Pomiès, N. Lequeux, J. P. Korb, D. Petit, F. Barberon, B. Bresson, Microstructure evolution of hydrated cement pastes, *Physical Review E* 72 (4) (2005) 041401.
- [58] R. Holly, E. J. Reardon, C. M. Hansson, H. Peemoeller, Proton spin–spin relaxation study of the effect of temperature on white cement hydration, *Journal of the American Ceramic Society* 90 (2) (2007) 570–577.
- [59] L. Venkataramanan, S. Yi-Qiao, M. D. Hurlimann, Solving fredholm integrals of the first kind with tensor product structure in 2 and 2.5 dimensions, *Signal Processing, IEEE Transactions on* 50 (5) (2002) 1017–1026.
- [60] A. Valori, V. Rodin, P. J. McDonald, On the interpretation of 1h 2-dimensional nmr relaxation exchange spectra in cements: Is there exchange between pores with two characteristic sizes or fe³⁺ concentrations?, *Cement and Concrete Research* 40 (9) (2010) 1375–1377.
- [61] J. Y. Jehng, D. T. Sprague, W. P. Halperin, Pore structure of hydrating cement paste by magnetic resonance relaxation analysis and freezing, *Magnetic Resonance Imaging* 14 (7–8) (1996) 785–791.
- [62] R. M. E. Valckenborg, L. Pel, K. Kopinga, Combined nmr cryoporometry and relaxometry, *Journal of Physics D: Applied Physics* 35 (3) (2002) 249.
- [63] N. Boden, Y. K. Levine, R. T. Squires, Nmr dipolar echoes in solids containing spin-1/2 pairs, *Chemical Physics Letters* 28 (4) (1974) 523–525.
- [64] G. E. Pake, Nuclear resonance absorption in hydrated crystals: Fine structure of the proton line, *The Journal of Chemical Physics* 16 (4) (1948) 327–336.
- [65] J. Mitchell, T. C. Chandrasekera, L. F. Gladden, A general approach to measurements in the presence of internal gradients, *Microporous and Mesoporous Materials* 178 (0) (2013) 20–22.
- [66] M. Hurlimann, K. Helmer, T. Deswiet, P. Sen, Spin Echoes in a Constant Gradient and in the Presence of Simple Restriction, *Journal of Magnetic Resonance, Series A* 113 (2) (1995) 260–264.

- [67] P. Claverie, A. Denis, E. Yeramian, The representation of functions through the combined use of integral transforms and pade approximants: Pade-laplace analysis of functions as sums of exponentials, *Computer Physics Reports* 9 (5) (1989) 247–299.
- [68] S. W. Provencher, Contin: A general purpose constrained regularization program for inverting noisy linear algebraic and integral equations, *Computer Physics Communications* 27 (3) (1982) 229–242.
- [69] K. S. J. Rossen, Optimization of sem-edx to determine c-s-h composition in matured cement paste samples, paper in preparation for *Materials characterization journal*.
- [70] J. Rossen, Stability of c-a-s-h in pastes of alite and cement blended with supplementary cementitious materials, Ph.D. thesis, EPFL, Lausanne, Switzerland (2014).
- [71] J. Zhang, G. W. Scherer, Comparison of methods for arresting hydration of cement, *Cement and Concrete Research* 41 (10) (2011) 1024–1036.
- [72] B. K. Marsh, R. L. Day, Pozzolanic and cementitious reactions of fly ash in blended cement pastes, *Cement and Concrete Research* 18 (2) (1988) 301–310.
- [73] L. Wadsö, A. Anderberg, I. Åslund, O. Söderman, An improved method to validate the relative humidity generation in sorption balances, *European Journal of Pharmaceutics and Biopharmaceutics* 72 (1) (2009) 99–104.
- [74] J. R. Olaf Franke, Gunter Schulz Ekloff, J. Starekb, A. Zukalb, Unusual type of adsorption isotherm describing capillary condensation without hysteresis, Royal Society of Chemistry, Cambridge, United Kingdom, 1993.
- [75] R. Schmidt, E. W. Hansen, M. Stoecker, D. Akporiaye, O. H. Ellestad, Pore size determination of mcm-51 mesoporous materials by means of ^1H nmr spectroscopy, n_2 adsorption, and hrem. a preliminary study, *Journal of the American Chemical Society* 117 (14) (1995) 4049–4056.
- [76] M. Wu, B. Johannesson, M. Geiker, Application of water vapor sorption measurements for porosity characterization of hardened cement pastes, *Construction and Building Materials* 66 (2014) 621–633.
- [77] P. L. Llewellyn, F. Schueth, Y. Grillet, F. Rouquerol, J. Rouquerol, K. K. Unger, Water sorption on mesoporous aluminosilicate mcm-41, *Langmuir* 11 (2) (1995) 574–577.
- [78] S. Kittaka, S. Ishimaru, M. Kuranishi, T. Matsuda, T. Yamaguchi, Enthalpy and interfacial free energy changes of water capillary condensed in mesoporous silica, mcm-41 and sba-15, *Physical Chemistry Chemical Physics* 8 (27) (2006) 3223–3231.
- [79] K. L. Scrivener, A. Nonat, Hydration of cementitious materials, present and future, *Cement and Concrete Research* 41 (7) (2011) 651–665.

- [80] H. Petch, The hydrogen positions in portlandite, $\text{Ca}(\text{OH})_2$, as indicated by the electron distribution, *Acta Crystallographica* 14 (9) (1961) 950–957.
- [81] L. Desgranges, D. Grebille, G. Calvarin, G. Chevrier, N. Floquet, J.-C. Niepce, Hydrogen thermal motion in calcium hydroxide: $\text{Ca}(\text{OH})_2$, *Acta Crystallographica Section B* 49 (5) (1993) 812–817.
- [82] A. Nonat, The structure and stoichiometry of c-s-h, *Cement and Concrete Research* 34 (9) (2004) 1521–1528.
- [83] K. L. Scrivener, P. L. Pratt, Backscattered electron images of polished cement sections in the scanning electron microscope, 1984, pp. 145–155.
- [84] G. Constantinides, F.-J. Ulm, The nanogranular nature of c-s-h, *Journal of the Mechanics and Physics of Solids* 55 (1) (2007) 64–90.
- [85] S.-H. Cachia, Water dynamics modeling in cement pastes at nanoscale, Ph.D. thesis, University of Surrey, UK (2014).
- [86] S. Galmarini, Atomistic simulation of cementitious systems, Ph.D. thesis, Ecole Polytechnique Fédérale de Lausanne (2013).
- [87] F. A. Bannister, M. H. Hey, J. D. Berna, Ettringite from scawt hill, co. antrim, *Mineralogical Magazine* 24 (153) (1936) 324–329.
- [88] A. Moore, H. F. W. Taylor, Crystal structure of ettringite, *Nature* 218 (5146) (1968) 1048–1049.
- [89] H. Taylor, *Cement Chemistry*, Academic Press: London, 1997.
- [90] R. Brydson, I. Richardson, G. Groves, Determining the local coordination of aluminium in cement using electron energy loss near-edge structure, *Microchimica Acta* 114-115 (1) (1994) 221–229.
- [91] B. Lothenbach, F. Winnefeld, Thermodynamic modelling of the hydration of portland cement, *Cement and Concrete Research* 36 (2) (2006) 209–226.
- [92] E. Gallucci, X. Zhang, K. L. Scrivener, Effect of temperature on the microstructure of calcium silicate hydrate (c-s-h), *Cement and Concrete Research* 53 (0) (2013) 185–195.
- [93] A. J. Allen, J. J. Thomas, H. M. Jennings, Composition and density of nanoscale calcium-silicate-hydrate in cement, *Nat Mater* 6 (4) (2007) 311–316.
- [94] R. Taylor, I. G. Richardson, R. M. D. Brydson, Composition and microstructure of 20-year-old ordinary Portland cement-ground granulated blast-furnace slag blends containing 0 to 100% slag, *Cement and Concrete Research* 40 (2010) 971–983.
- [95] A. Bazzoni, Study of early hydration mechanisms of cement by means of electron microscopy, Ph.D. thesis, EPFL, Lausanne, Switzerland (2014).

- [96] J. P. Korb, L. Monteilhet, P. McDonald, J. Mitchell, Microstructure and texture of hydrated cement-based materials: A proton field cycling relaxometry approach, *Cement and Concrete Research* 37 (3) (2007) 295–302.
- [97] J. P. Korb, M. Whaley Hodges, R. Bryant, Translational diffusion of liquids at surface of microporous materials: new theoretical analysis of field cycling magnetic relaxation measurements, *Magnetic resonance imaging* 16 (5) (1998) 575–578.
- [98] D. A. Faux, P. J. McDonald, N. C. Howlett, J. S. Bhatt, S. V. Churakov, Nuclear magnetic resonance relaxometry of water in two and quasi-two dimensions, *Physical Review E* 87 (6) (2013) 062309.
- [99] J. S. Bhatt, P. J. McDonald, D. A. Faux, N. C. Howlett, S. V. Churakov, Nmr relaxation parameters from molecular simulations of hydrated inorganic nanopores, *International Journal of Quantum Chemistry* (2014) n/a–n/a.
- [100] A. Gajewicz, Characterisation of cement microstructure and pore – water interaction by ¹h nuclear magnetic resonance relaxometry, Ph.D. thesis, University of Surrey (2014).
- [101] M. Zalzal, P. J. McDonald, Lattice boltzmann simulations of the permeability and capillary adsorption of cement model microstructures, *Cement and Concrete Research* 42 (12) (2012) 1601–1610.
- [102] M. Zalzal, P. McDonald, K. Scrivener, A 3d lattice boltzmann effective media study: understanding the role of csh and water saturation on the permeability of cement paste, *Modelling and Simulation in Materials Science and Engineering* 21 (8) (2013) 085016.
- [103] S. Bishnoi, K. L. Scrivener, uic:a new platform for modelling the hydration of cements, *Cement and Concrete Research* 39 (4) (2009) 266–274.
- [104] M. A. Etzold, P. J. McDonald, A. F. Routh, Growth of sheets in 3D confinements - A model for the C-S-H meso structure, *Cement and Concrete Research* 63 (2014) 137–142.
- [105] J. Skibsted, O. M. Jensen, H. J. Jakobsen, J. Skibsted, O. M. Jensen, H. J. Jakobsen, Hydration kinetics for the alite, belite, and calcium aluminate phase in portland cements from ²⁷al and ²⁹si mas nmr spectroscopy (1997).
- [106] H. Justnes, I. Meland, J. Bjoergum, J. Krane, A ²⁹si mas nmr study of the pozzolanic activity of condensed silica fume and the hydration of di- and tricalcium silicates, *Advances in Cement Research* 3 (11) (1990) 111 –116.
- [107] H. Justnes, E. J. Sellevold, G. Lundevall, High strength concrete binders. part a: reactivity and composition of cement pastes with and without condensed silica fume, 4th International Conference on Fly Ash, Silica Fume, Slag and Natural Pozzolans in Concrete (1992) 873–889.

- [108] W. A. Gutteridge, J. A. Dalziel, Filler cement: The effect of the secondary component on the hydration of portland cement: Part i. a fine non-hydraulic filler, *Cement and Concrete Research* 20 (5) (1990) 778–782.
- [109] P. F. Hansen, J. Pedersen, Maturity computer for controlled curing and hardening of concrete, *Nordisk Betong* 1 (1977) 19–34.
- [110] J. Zhang, D. Cusson, L. Mitchell, T. Hoogeveen, J. Margeson, The maturity approach for predicting different properties of high-performance concrete, *Proc. 7th International Symposium on the Utilization of High-Strength/High-Performance Concrete* (2005) 135–154.
- [111] I. Pane, W. Hansen, Investigation of blended cement hydration by isothermal calorimetry and thermal analysis, *Cement and Concrete Research* 35 (6) (2005) 1155–1164.
- [112] K. Riding, J. Poole, K. Folliard, M. Juenger, A. Schindler, Modeling hydration of cementitious systems, *ACI Materials Journal* 109 (2) (2012) 225.
- [113] M. K. Kamyab, Autogenous Shrinkage and Hydration Kinetics of SH-UHPFRC under Moderate to Low Temperature Curing Conditions, Ph.D. thesis, EPFL (2013).
- [114] V. Waller, Relation entre composition des bétons, exothermie en cours de prise et résistance en compression, Ph.D. thesis, Ecole Nationale des Ponts et Chaussées (1999).
- [115] S. L. Poulsen, V. Kocaba, G. Le Saoût, H. J. Jakobsen, K. L. Scrivener, J. Skibsted, Improved quantification of alite and belite in anhydrous portland cements by ^{29}Si mas nmr: Effects of paramagnetic ions, *Solid State Nuclear Magnetic Resonance* 36 (1) (2009) 32–44.
- [116] I. G. Richardson, A. R. Brough, G. W. Groves, C. M. Dobson, The characterization of hardened alkali-activated blast-furnace slag pastes and the nature of the calcium silicate hydrate (c-s-h) phase, *Cement and Concrete Research* 24 (5) (1994) 813–829.
- [117] M. D. Andersen, H. J. Jakobsen, J. Skibsted, Characterization of white portland cement hydration and the c-s-h structure in the presence of sodium aluminate by ^{27}Al and ^{29}Si mas nmr spectroscopy, *Cement and Concrete Research* 34 (5) (2004) 857–868.
- [118] M. D. Andersen, H. J. Jakobsen, J. Skibsted, Incorporation of aluminum in the calcium silicate hydrate (csh) of hydrated portland cements: A high field ^{27}Al and ^{29}Si mas nmr investigation, *Inorganic Chemistry* 42 (7) (2003) 2280–2287.
- [119] V. Kocaba, Development and evaluation of methods to follow microstructural development of cementitious systems including slags, Ph.D. thesis, Ecole Polytechnique Federale de Lausanne (2009).
- [120] E. Berodier, Impact of additions on hydration of cementitious materials, Ph.D. thesis, EPFL, Lausaane, Switzerland (2015).

- [121] D. Kulik, Software gems-psi 2.1 [http://les.web.psi.ch/ software/gems-psi/](http://les.web.psi.ch/software/gems-psi/) (2005).
- [122] A. Korpa, R. Trettin, The influence of different drying methods on cement paste microstructures as reflected by gas adsorption: Comparison between freeze-drying (f-drying), d-drying, p-drying and oven-drying methods, *Cement and Concrete Research* 36 (4) (2006) 634–649.
- [123] J. Hagymassy Jr, S. Brunauer, R. S. Mikhail, Pore structure analysis by water vapor adsorption: I. t-curves for water vapor, *Journal of Colloid and Interface Science* 29 (3) (1969) 485–491.
- [124] S. Brunauer, *The adsorption of gases and vapors*, Princeton University Press, Princeton, NJ, 1943.
- [125] C. Dunant, Experimental and modelling study of the alkali-silica-reaction in concrete, Ph.D. thesis, École polytechnique federale de Lausanne (EPFL) (2009).
- [126] F. Moro, H. Böhni, Ink-bottle effect in mercury intrusion porosimetry of cement-based materials, *Journal of Colloid and Interface Science* 246 (1) (2002) 135–149.
- [127] D. Winslow, S. Diamond, A mercury porosimetry study of the evolution of porosity in portland cement, *Journal of Materials* 5 (3) (1970) 564–585.
- [128] D. N. Winslow, The validity of high pressure mercury intrusion porosimetry, *Journal of Colloid and Interface Science* 67 (1) (1978) 42–47.
- [129] S. Chae, J. Moon, S. Yoon, S. Bae, P. Levitz, R. Winarski, P. M. Monteiro, Advanced nanoscale characterization of cement based materials using x-ray synchrotron radiation: A review, *International Journal of Concrete Structures and Materials* 7 (2) (2013) 95–110.
- [130] I. G. Richardson, Tobermorite/jennite- and tobermorite/calcium hydroxide-based models for the structure of c-s-h: applicability to hardened pastes of tricalcium silicate, beta-dicalcium silicate, portland cement, and blends of portland cement with blast-furnace slag, metakaolin, or silica fume, *Cement and Concrete Research* 34 (9) (2004) 1733–1777.
- [131] K. Garbev, G. Beuchle, M. Bornefeld, L. Black, P. Stemmermann, Cell dimensions and composition of nanocrystalline calcium silicate hydrate solid solutions. part 1: Synchrotron-based x-ray diffraction, *Journal of the American Ceramic Society* 91 (9) (2008) 3005–3014.
- [132] A. Nonat, X. Lecoq, *The Structure, Stoichiometry and Properties of C-S-H Prepared by C3S Hydration Under Controlled Condition*, Springer Berlin Heidelberg, 1998, Ch. 14, pp. 197–207.
- [133] E. Tajuelo, I. Richardson, L. Black, J. Skibsted, A. Nonat, Comparison of morphology and chemical structure of c-s-h synthesized by silica-lime reaction and by the controlled hydration of c3s, TRANSCEND final conference.

- [134] R. M. Kowalczyk, A. M. Gajewicz, P. J. McDonald, The mechanism of water-isopropanol exchange in cement pastes evidenced by nmr relaxometry, *RSC Advances* 4 (40) (2014) 20709–20715.
- [135] J. Pope, N. Repin, A simple approach to T2 imaging in MRI, *Magnetic Resonance Imaging* 6 (6) (1988) 641–646.
- [136] N. Boden, M. Mortimer, An NMR “solid” echo experiment for the direct measurement of the dipolar interactions between spin- pairs in solids, *Chemical Physics Letters* 21 (3) (1973) 538–540.

List of publication

Journal papers

- A.C.A. Muller, K.L. Scrivener, A.M. Gajewicz and P.J. McDonald, "Use of bench-top NMR to measure the density, composition and desorption isotherm of C-S-H in cement paste", *Microporous and Mesoporous Materials*, ISSN 1387-1811.
- A.C.A. Muller, K.L. Scrivener, A.M. Gajewicz and P.J. McDonald, "Densification of C-S-H measured by ^1H NMR relaxometry", *Journal of Physical Chemistry C*, 117 (2013) 403-412.
- A.C.A. Muller, K.L. Scrivener, J. Skibsted, A.M. Gajewicz, P.J. McDonald, "The influence of silica fume on the state of water in cement pastes measured by ^1H NMR relaxometry", submitted to *Cement and Concrete Research*, June 2014.
- H.K. Kamyab, A.C.A. Muller, E. Denarié, K.L. Scrivener, E. Brühwiler, "Kinetics of water repartition in UHPFRC using ^1H NMR", in preparation for *Cement and Concrete Research*, 2014.

Conference papers

- K.L. Scrivener, A.C.A. Muller, M. Zalzale, Q.H. Do, P. McDonald, "New Insights on mechanisms controlling kinetics and implications for pore structure", *Workshop celebrating Professor Erik. J. Sellevold's 75th birthday*, Apr. 25-26, 2013, Trondheim, Norway
- A.M. Gajewicz, A.C.A. Muller, P.J. McDonald, K.L. Scrivener, "Study of the nano-structure of the C-S-H using nuclear magnetic resonance, extended abstract, *Final TRANSCEND conference "Water transport in cementitious materials"*, Nov. 3-6, 2013, Guildford, UK
- A.C.A. Muller, K.L. Scrivener, P.J. McDonald, "The use of ^1H NMR: a new method to address the properties of concretes", *Concrete Innovation Conference - CIC 2014*, Jun. 11-14, Oslo, Norway



Arnaud Muller

Born on 15th May 1985,
French,
Single

7b avenue du Censuy
Apartement 32
1020, Renens
SWITZERLAND

Tel: (+41) 77 479 80 47

arnaud.mu@gmail.com

Dynamic

Curious

Social

Contentious

Open minded

ACADEMIC BACKGROUND

- From 11/2010 **PhD thesis:** ¹H-NMR study of the porosity of cementitious materials. Marie-Curie Transcend European PhD fellow studying moisture in concrete, EPFL, Lausanne (Switzerland)
- 2008/2009 **Master in Science and Engineering (MSc)**
Research topic: calcium aluminate cements; strengths development
Laval University, Québec (Canada)
- 2006/2008 **Master 1 and 2 IUP "Génie civil et infrastructures"**
Joseph Fourier University, Grenoble (France)
- 2003/2006 **Bachelor's Degree in Civil Engineering**
Robert Schuman University, Strasbourg (France)

PROFESSIONAL EXPERIENCE

- From 11/2010 **PhD Thesis:** Development of a new methodology (non-invasive and simple to carry out) to quantify water in the different environment of cement pastes based on ¹H NMR. This advance allows C-S-H density and chemical composition to be founds and is of great interest to understand new materials. Experience with supplementary cementitious materials (SCMs) such as silica fume, slag, quartz, limestone and metakolin.
- 2010 **Research Engineer**
Responsible of the shotcrete group, facilities care and tutoring students, CRIB, Laval University, Québec (Canada)
- 2008 **Research internship** (24 weeks): calcium aluminate cements
CRIB, Laval University, Québec (Canada)
- 2006 **Construction management internship** (7 weeks): COGEOR
Monitoring and construction site coordination, Grenoble (France)
- 2005 **Works supervisor internship** (7 weeks) ZIMMER company
Site of the Albert Schweitzer Hospital, Colmar (France)

SCIENTIFIC JOURNAL PUBLICATIONS

A.C.A. Muller, K.L. Scrivener, A.M. Gajewicz and P.J. McDonald, "Use of bench-top NMR to measure the density, composition and desorption isotherm of C-S-H in cement paste", 2013, Microporous and Mesoporous Materials. () ISSN 1387-1811.

Muller et al. "Densification of C-S-H measured by ¹H NMR relaxometry", 2013, Journal of Physical Chemistry C, 117, 403-412.

Muller et al. "The influence of silica fume on the state of the water in cement pastes measured by ¹H NMR relaxometry", 2014, submitted to Cement and Concrete Research

COMMUNICATION SKILLS

Spoken & written languages:

Fluent: French, English

Basic: German, Spanish

- from 2010 **Representing 15 PhD students** in the Marie-Curie Transcend European project. Link between head of the project and students
- 2012 **Project: "Science outreach to the public"** taught by prof Jim Al Khalili. Interaction with school classes about concrete.
- 2012 **Project management course**, 2 days, EPFL, Switzerland

181

HOBBIES

Sports

Running, Tennis, Soccer, Capoeira, Hiking, Snowboard

